Secular Variation Prediction of the Earth's Magnetic Field Using Core Surface Flows

Ciarán D. Beggan

Thesis submitted for the Degree of

Doctor of Philosophy

University of Edinburgh

2009

Abstract

The Earth's magnetic field is generated by fluid motion of liquid iron in the outer core. Flows at the top of the outer core are believed to be responsible for the secular variation (SV) observed at the surface of the Earth. Modelling of this flow is open to considerable ambiguity, though methods adopting different physical assumptions do lead to similar flow velocity regimes. Some aspects of the ambiguities are investigated in this thesis.

The last decade has seen a significant improvement in the capability to observe the global field at high spatial resolution. Several satellite missions have been launched, providing a rich new set of scalar and vector magnetic measurements from which to model the global field in detail. These data complement the existing record of ground-based observatories, which have continuous temporal coverage at a single point. I exploit these new data to model the secular variation (SV) globally and attempt to improve the core flow models that have been constructed to date.

Using the approach developed by Mandea and Olsen (2006) I create a set of evenly distributed 'Virtual Observatories' (VO), at 400km above the Earth's surface, encompassing satellite measurements from the CHAMP satellite over seven years (2001-2007), inverting the SV calculated at each VO to infer flow along the core-mantle boundary. Direct comparison of the SV generated by the flow model to the SV at individual VO can be made. Thus, the residual differences can be investigated in detail. Comparisons of residuals from flow models generated from a number of VO datasets provide evidence that they are consistent with internal and external field effects in the satellite data. I also show that the binning and processing of the VO data can induce artefacts, including sectorial banding, into the residuals.

By employing the core flows from the inversion of SV data it may be possible to forecast the change of the present magnetic field (as measured) forwards in time for a short time period (e.g. less than five years) within an acceptable error budget. Using simple advection of steady or non-steady flows to forecast magnetic field change gives

reasonably good fit to field models such as GRIMM, POMME or xCHAOS (< 50nT root mean square difference after five years).

The forecast of the magnetic field change can be improved by optimally assimilating measurements of the field into the forecast from flow models at discrete points in time (e.g. annually). To achieve this, an Ensemble Kalman Filter (EnKF) can be used to the capture non-linearity of the model and delineate the error bounds by means of a Monte Carlo representation of the field evolution over time. In the EnKF model, an ensemble of probable state vectors (Gauss coefficients) evolve over time, driven by SV derived from core flows. The SV is randomly perturbed at each step before addition to the state vectors. The mean of the ensemble is chosen as the most likely state (i.e. field model) and the error associated with the estimate can be gauged from the standard deviation from the mean.

I show an implementation of the EnKF for steady and non-steady flows generated from 'Virtual Observatory' field models, compared to the field models GRIMM and xCHAOS over the period 2002–2008. Using the EnKF, the maximum difference never exceeds 25nT over the period. This promising approach allows measurements to be included into model predictions to improve the forecast.

Contents

1 Introduction **4**

1.1 Planetary Magnetic Fields 4

1.2 Measuring the Magnetic Field 8

1.3 Field Modelling 11

1.4 Secular Variation 16

1.5 Other Measurable Fields 19

1.6 Recent Developments 22

1.7 Thesis Structure 23

2 Background **25**

2.1 The Outer Core 25

2.2 The Inner Core 29

2.3 Modelling Secular Variation 31

2.4 Core Flow Modelling 34

2.4.1 Representation of flow inversion 36

2.4.2 Reducing non-uniqueness of Flow Models 38

2.4.3 One-Norm Iterative Inversion 48

2.5 Core Flow Models and Length of Day 51

2.6 Entering the Satellite Era 53

2.7 Magnetic Field Forecasting 56

3 Core Flow Modelling Assumptions **59**

3.1 Overview 59
3.2 Examining Flow Constraints 60
3.3 Observatory Data 62
3.4 Comparison of Flow Models 64
3.5 Flow Spectra 79
3.6 Primary Controls on Flow Models 84
3.7 Summary 87

4 Core Flows from 'Virtual Observatories' 88
4.1 Overview 88
4.2 Virtual Observatories 89
4.2.1 VO Method 92
4.3 Flow Modelling 97
4.4 Biased Residuals 99
4.5 Analysis 106
4.5.1 Influence of Fields External to Satellite Orbit 109
4.5.2 Influence of Fields Internal to Satellite Orbit 112
4.5.3 Influence from the VO method 113
4.6 Correction Strategies 118
4.6.1 Removal of fields using the Comprehensive Model 119
4.6.2 Spherical Harmonic Analysis of the VO datasets 124
4.6.3 Covariance Rotation of the VO dataset 129
4.6.4 Smoothing using Steady Flow 139
4.6.5 Smoothing using B-Splines 140
4.7 Comparison 144
4.8 Summary 145

5 Forecasting using Core Flow Models 149
5.1 Simple Flow Modelling 150
5.1.1 Steady Flow Model 151

5.1.2 Forecasting using Steady Flow models? . . . 157
5.1.3 Non-steady Flow Models . . . 157
5.2 Comparison to Ground Obs . . . 167
5.3 Flow Model Hindcasting . . . 172
5.4 Forecasting: 2010–2015 . . . 174
5.5 Summary . . . 176

6 Forecasting and Assimilation 177
6.1 Motivation . . . 178
6.2 Background . . . 178
6.3 Kalman Filtering . . . 180
6.3.1 Representation of State, Process and Noise . . . 181
6.3.2 Extended Kalman Filtering . . . 184
6.4 Ensemble Kalman Filtering . . . 185
6.4.1 Stochastic Dynamic Prediction . . . 185
6.4.2 Approximating the Kalman Filter . . . 187
6.4.3 Practical Implementation . . . 189
6.4.4 Efficient Computational Implementation . . . 190
6.5 EnKF: One-Dimensional Example . . . 192
6.5.1 EnKF: Three Dimensional Example . . . 197
6.6 Application of EnKF Forecasting . . . 199
6.7 EnKF Flow Modelling . . . 203
6.7.1 EnKF using a Steady Flow Model . . . 204
6.7.2 EnKF using Non-steady Flow Models . . . 205
6.7.3 Dataset 1 . . . 205
6.7.4 Dataset 2 . . . 207
6.7.5 Dataset 1 with CM4 Correction . . . 207
6.8 Summary . . . 210

7 Discussion **212**

7.1 Core Processes 212

7.2 Field and Flow Modelling 215

7.3 Data Processing 217

7.4 Forecasting the Change of the Magnetic Field 219

7.5 Future of Magnetic Field Studies 222

7.6 Recommendations for Future Work 223

8 Conclusions **225**

Bibliography **227**

A Table of Crustal Fields **247**

B EnKF code **251**

C Table of CD contents **257**

List of Figures

1.1 Earth Section 5
1.2 Reversal Rate 8
1.3 Dipole and 3D field 10
1.4 Measurement Reference Frame 12
1.5 Surface Harmonic functions 14
1.6 Magnetic Field Strength 2005 15
1.7 Magnetic Field Strength (F) from GUFM1 18
1.8 Geomagnetic Storm 21
1.9 External Current Systems 22

2.1 $\alpha\omega$ Dynamo 27
2.2 Schematic Core Section 29
2.3 Tangent Cylinder 31
2.4 Plaque to Edmond Halley 32
2.5 Flow Ambiguity 40
2.6 Example Flow Types 46
2.7 One-Norm Algorithm 49
2.8 Two-Norm and One-Norm Flow Models 50
2.9 Core-Mantle Interaction 52
2.10 Error Estimate of IGRF 58

3.1 Ground Observatory Locations 64
3.2 Iteration Metrics 65

3.3 Coefficients contribution from toroidal-poloidal flow 66
3.4 Flow Model with 'strong' velocity norm (Dataset 4) 71
3.5 Flow Model with 'strong' velocity norm (Dataset 4) 72
3.6 Residual Distributions 73
3.7 Flow Model with minimum RMS SV norm (Dataset 4) 77
3.8 Histograms with minimum RMS SV norm (Dataset 4) 78
3.9 Flow Spectra 'strong' norm 80
3.10 Flow Spectra RMS SV norm 81
3.11 Flow Spectra balanced RMS SV norm 82
3.12 SV Spectra 83

4.1 CHAMP Satellite Orbital Altitude 91
4.2 Example Orbital Trace and VO data 94
4.3 NGK: VO and Ground station comparison 95
4.4 Equal Lat/Lon Grid and Equal Area Grid 96
4.5 VO Field Model Z component 97
4.6 SV for November 2001 98
4.7 L_1 norm iterative solution for VO data 99
4.8 VO Flow Models: Dataset 1 EqLL 102
4.9 Geographic distribution of the residual: Dataset 1 eqLL 103
4.10 VO Flow Models: Dataset 2 Eqarea 104
4.11 Geographic distribution of the residual: Dataset 1 eqarea 105
4.12 Geographic distribution of the residual: Dataset 2 eqLL 108
4.13 Geographic distribution of the residual: Dataset 3 eqLL 110
4.14 VO Dataset 3: data distribution 111
4.15 Dst Index vs. Bias in $\dot{X}$ 113
4.16 Geographic distribution of the residual: Dataset 4 eqLL 116
4.17 Geographic distribution of the residual: Dataset 4 Eqarea 117
4.18 Comparison of Flow Model Fit to VO SV Data 120
4.19 Comparison of Flow Model Fit to VO SV Data 121

4.20 Geographic distribution of the residual: Dataset 1 eqLL 122
4.21 Geographic distribution of the residual: Dataset 2 eqLL 123
4.22 Internal SV: Core Flow Model 125
4.23 External SV: Core Flow Model 126
4.24 Toroidal SV: Core Flow Model 127
4.25 SAV metric for Internal SH Datasets 130
4.26 VO Flow Models: Dataset 1 EqLL Covariance rotated 132
4.27 Geographic distribution of the residual: Dataset 1 Covariance rotated . 133
4.28 VO Flow Models: Dataset 2 EqLL Covariance rotated 134
4.29 Geographic distribution of the residual: Dataset 2 Covariance rotated . 135
4.30 Geographic distribution of the residual: Dataset 1 CM4 + Covariance rotated 136
4.31 Geographic distribution of the residual: Dataset 2 CM4 + Covariance rotated 137
4.32 SAV metric for Covariance rotated Datasets 138
4.33 Steady Flow 2001-2005 139
4.34 B-Spline Fit to Flow Coefficients 142
4.35 Geographic distribution of the residual: B-Spline 143
4.36 SAV metric for B-spline 143
4.37 SAV Metrics: Summary 145

5.1 Steady Flow Model 2001-2005 152
5.2 Steady Flow Model Forecast (GRIMM, xCHAOS, IGRF10) 155
5.3 Steady Flow Model Forecast (POMME) 156
5.4 Steady Flow Model Forecasts 158
5.5 Non-Steady Flow Models D1 160
5.6 POMME/xCHAOS Non-Steady Flow D1 161
5.7 Non-Steady Flow Model D2 162
5.8 POMME/xCHAOS Non-Steady Flow D2 163
5.9 Non-Steady Flow Model D1 CM4 164

5.10 POMME/xCHAOS Non-Steady Flow D1 CM4 165
5.11 ABK comparison 169
5.12 AQU comparison 169
5.13 HAR comparison 170
5.14 HON comparison 170
5.15 RES comparison 171
5.16 TSU comparison 171
5.17 Hindcast vs. CM4 173
5.18 Hindcast vs. IGRF 174
5.19 Steady Flow 2004.5–2007.5 175
5.20 Forecast 2010-2015 175

6.1 Discrete Kalman Filter 181
6.2 Kalman Filter Algorithm 184
6.3 Phase space evolution 187
6.4 Scalar EnKF example 194
6.5 Scalar EnKF example with smoothing 195
6.6 Scalar EnKF example with white noise 196
6.7 EnKF 3D vector example 198
6.8 Initiation of Ensemble 200
6.9 Forecasting of Ensemble 201
6.10 Assimilitation in Ensemble 202
6.11 EnKF Steady Flow Model Forecast 206
6.12 EnKF Dataset 1 Flow Model Forecast 208
6.13 EnKF Dataset 2 Flow Model Forecast 209
6.14 EnKF Dataset 1 + CM4 Flow Model Forecast 211

7.1 Inner Core Anisotropy 214
7.2 Hindcast from Maus et al. (2008) 220

List of Tables

3.1 Ordering of the first sixteen flow coefficients in Figure 3.3. 67

3.2 Fit of flow models minimising 'strong' norm 69

3.3 Fit of flow models using RMS SV norm 75

3.4 Fit of flow models using RMS SV norm with matched solution norm . . 76

4.1 VO Datasets summary 107

4.2 Correlation of Dst Index and $\dot{X}$ 120

4.3 Correlation of Dst Index and separation of Flow Models 128

4.4 Variance Ratio of flow models 129

4.5 Correlation Matrix of Steady Flows 140

4.6 SAV Metrics Summary 146

5.1 Description of Field Models 153

5.2 Crustal Bias CM3 172

5.3 Prediction of Gauss coefficients 175

A.1 Crustal Bias 250

C.1 Images & Animations 258

Acknowledgements

I would like to thank Kathy Whaler for being helpful, positive and very quick to respond to my queries and questions over the past three-and-a-half years. I would like to thank her, in particular, for all the time she has spent correcting my written work and mangling of equations. I have used most of her original FORTRAN code, converted into MATLAB to perform the experiments for the thesis. I am very grateful for her sponsorship of all the opportunities I had to travel about Europe and the world to talk to other members of the community. She also left me to do my own work at my own pace, in my own time and undertake a host of other activities from conference organising to papers in other research areas – I couldn't ask for a better supervisor.

I would like to thank Susan Macmillan for her advice on my progress and for finding time to discuss the many aspects of forecasting and field modelling over the past few years.

I would like to thank Ingo Wardinski for initial datasets and Richard Holme for advice and code for the covariance correction method and temporal splines. Richard kindly let me stay for a week in Liverpool which was very useful to the project.

I wish to thank Nils Olsen for his advice, for the Virtual Observatory code and for providing certain CHAMP data. He also provided help for the analysis of the internal, external and toroidal parts of the field – the basis for much of the study in Chapter 4.

I would like to thank Andy Jackson and Chris Finlay for code and help with flow modelling and general chats about magnetic field modelling over the many GEOSPACE meetings.

I also thank Alan Thomson at the British Geological Survey for the provision of

Ørsted and CHAMP satellite data and for taking the time to turn the data into a useful format for me. The CHAMP data used in this study were supplied by GFZ Potsdam. Stefan Maus provided help on reproducing results from one of his papers.

Thanks to all the people in the Attic (Gillian, Caroline, Dan, Jenny, Rich, Ruth, Louise, Emma, Tim(s), Pete etc.), the Grant Institute (Lisa, Andy R., Joan, Simon, Roger, Sue etc.) and the School of GeoSciences in Edinburgh who have helped me over the years (including the nice IT people, Justin, Shane, Allister and Fay who keep the system going flawlessly). Thanks to all the members of staff who let me come on the various fieldtrips and teach or demonstrate. I've certainly learned about much more than the Earth's magnetic field. I hope I have given back as much as I have received from the postgraduate and School community!

This thesis was written in LaTeX 2_ε. Images using map projections were generated using Generic Mapping Tools from Wessel & Smith (1991). All other graphs were plotted using MATLAB.

Finally, this research is part of the NERC GEOSPACE programme, funded under grants NER/O/S/2003/00674 and NER/O/S/2003/00677. I have been funded under NERC studentship award NER/S/J/2005/13496.

Chapter 1

Introduction

1.1 Planetary Magnetic Fields

The Earth is a heterogenously differentiated planetary body with an average radius of 6371 km and average density of 5515kg/m^3 (Lowrie, 1997). Accreted from the accumulation of planetessimals approximately 4.567 Ga (billion years) ago, gravity and compositional differentiation have created a layered body which is still cooling from its initial formation temperatures. There are four primary layers (see Figure 1.1): the low density silicic crust (0–30km thick, density = $\sim$ 2800kg/m^3), the denser silicic mantle (30–2885km depth, density = $\sim$ 3800kg/m^3), the liquid iron-rich outer core (2885–5150km depth, density = $\sim$ 8500kg/m^3) and the solid iron-rich inner core (5150–6370km).

It is believed, from the study of meteorites, that the concentration and accumulation of dense elements such as iron and siderophiles in the centre of the planet arose from the density contrast between the silicate minerals and lithophile elements, with pooling of the densest material being a natural consequence of gravitational instability (e.g. Beatty et al., 1999, see Wood, p13). Large amounts of potential energy (in the form of heat) would have been released as the denser material migrated to the centre of the planet. In addition, the decay of short-lived (generally $\lambda_{\frac{1}{2}}$ <10Ma) radiogenic isotopes would have increased the temperature within the newly formed planet. Approximately 100Ma (million years) after the formation of the planet a large bolide, believed to

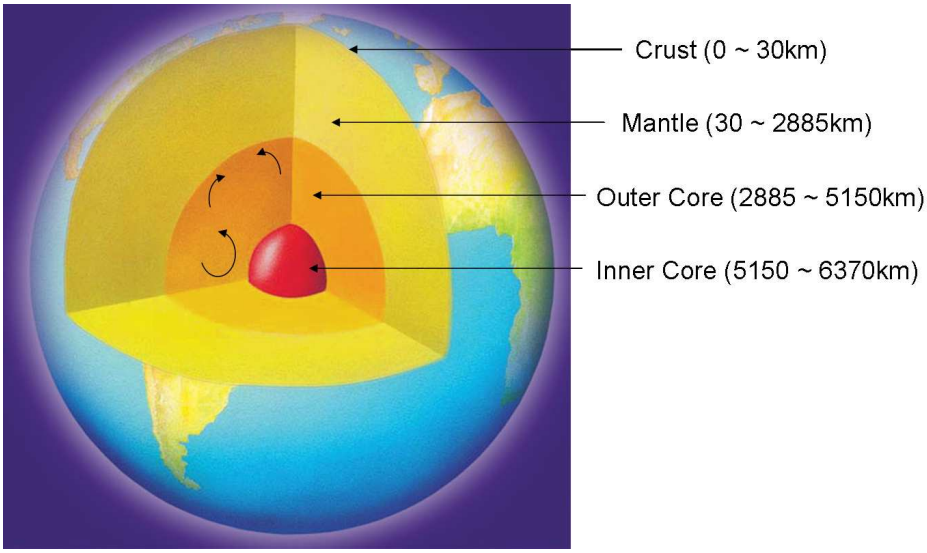

Figure 1.1: Idealised Section through the layered Earth, after Stevenson (2003a)

be about the size of Mars, collided with the proto-Earth (e.g. Stevenson, 1987). This event vapourised the early crust and upper mantle, initiated the formation of the Moon and added to the energy budget of the planet, increasing temperatures and altering the geochemical differentiation of the planet (Stevenson, 2008). It is assumed that the liquid core developed fully within a few tens of million years of this event. The timing of the development of the solid inner core, at the expense of the liquid core, is still an area of active research.

The internal magnetic field of the Earth (and other planets) is generated by dynamo action within the liquid outer core (e.g. Stevenson, 2003b; Christensen & Wicht, 2007). Large electrical currents are generated from an initial (perhaps solar?) magnetic field and sustained by convection of the liquid within the core (c.f. Merrill et al., 1996). These electrical currents, in turn, generate a magnetic field. The poloidal (radial) part of the field permeates to the surface of the Earth and into space. The toroidal (contained within the core) part of the field is twisted and the field lines are re-connected within the liquid core, regenerating the poloidal field. Thus, flow of the liquid within the outer core is critical to sustaining and maintaining the geodynamo (e.g. Russell, 1999).

In the Earth, there are three driving convection forces: *(a)* thermal convection as a

consequence of the decay of radiogenic isotopes, *(b)* the release of heat (from the latent heat of crystallisation) as the liquid iron freezes in the centre and *(c)* compositional bouyancy from the release of light incompatible elements (entrained during planetary differentiation) from the freezing of the inner core. It is currently thought that compositional bouyancy is the dominant process (Labrosse et al., 1997; Lister & Buffett, 1998; Gubbins, 2004).

Other planets known to have a magnetic field, such as Jupiter and Saturn and the gas giants are assumed to have regions of liquid metallic hydrogen deep within, where a dynamo can operate (Beatty et al., 1999, see Van Allen & Bagenal, p39). Uranus and Neptune have unusual non-dipolar fields which may be due to dynamo action in a confined shell within the upper regions of their conductive fluid 'ice' interiors (Stanley & Bloxham, 2004). The field of Mercury is as yet unexplained. Due to its small size it was supposed to have cooled sufficiently to freeze its liquid core. However, recent radar and spaceborne probe measurements suggest otherwise (e.g. Solomon, 2007). Mars and the Moon have remanent (residual) magnetic fields, primarily recorded by the igneous rocks on the planetary surfaces, indicating that they may have once had viable internal dynamos. Measurements from space probes have allowed initial models of their remanent crustal fields to be realised (e.g. Whaler & Purucker, 2005; Purucker, 2008). With these models, it is hoped that a better understanding of the magnetic and planetary history will be gained. From a survey of the solar system, it appears that planetary magnetic fields are ubiquitous and to be expected when large planets form. The individual details of their evolution and eventual decay depend largely on the size and composition of the planet, and may also be influenced by other events such as large impacts.

The timing of formation of the Earth's core and its internal magnetic field is still unknown, but rocks collected on the Moon during the Apollo programme suggest that a lunar field existed some 3.9Ga ago (Goswami, 1976; Runcorn, 1978; Garrick-Bethell et al., 2009). Currently, the oldest known magnetised minerals are found in the 3.2Ga Archaean Kaapvaal craton, South Africa (Tarduno et al., 2007). These indicate that the

field was approximately 50% of its modern-day strength, suggesting that the internal magnetic field was well established. Tarduno et al. (2007) propose, based on this and the lunar evidence, that the geomagnetic field had been formed by 3.9Ga.

The main magnetic field of the Earth is constantly changing. The rate of change and indeed the most extreme form of change – magnetic field reversals – are not constant in time. The rate of reversal is currently about four times per million years but has varied widely in the past 200Ma, as records from the magnetised oceanic floor reveal (Merrill & McFadden, 1990). For example, the Cretaceous 'quiet period' when there were no recorded reversals, can be seen in Figure 1.2. It is currently unknown why no reversals occurred during this period or the reason for the abrupt resumption at ∼82Ma. (Muller (2002), for example, suggests an extraterrestrial impact destabilised the flow regime of the core.) The longest frequency timescales for the change in reversal rate is on the order of 10^8 years, similar to those of mantle convection, prompting research into the influence and control of the overlying mantle on the thermal regime within the core (e.g. Buffett, 1999; Glatzmaier et al., 1999; Gubbins et al., 2007). Biggin et al. (2008) demonstrate that the magnitude and direction of the field varied during the period 2.82–2.45Ga. This change, loosely termed palaeosecular variation, indicates that the processes cause spatial and temporal changes of the magnetic field must have been in operation early in its history. Currently, the decadal change of the main field is termed *secular variation*.

Reversals and excursions (weakening and diminishing) of the main field are poorly understood, but in a highly non-linear system such behaviour is not suprising (Hollerbach, 1996; Hide et al., 2004, and references therein). Non-linear dynamic systems are not, in general, predictable but can be described mathematically and statistically in terms of chaos. States or regimes of stability in dynamical systems are referred to as 'strange attractors', as the system may spend most of the time in one of a fixed number of states, and only a short time transitioning between them. If the geodynamo system is viewed as a dynamic, chaotic and non-periodic one, then (analogous to climate systems) stable states can exist for very long periods of time but can change or evolve

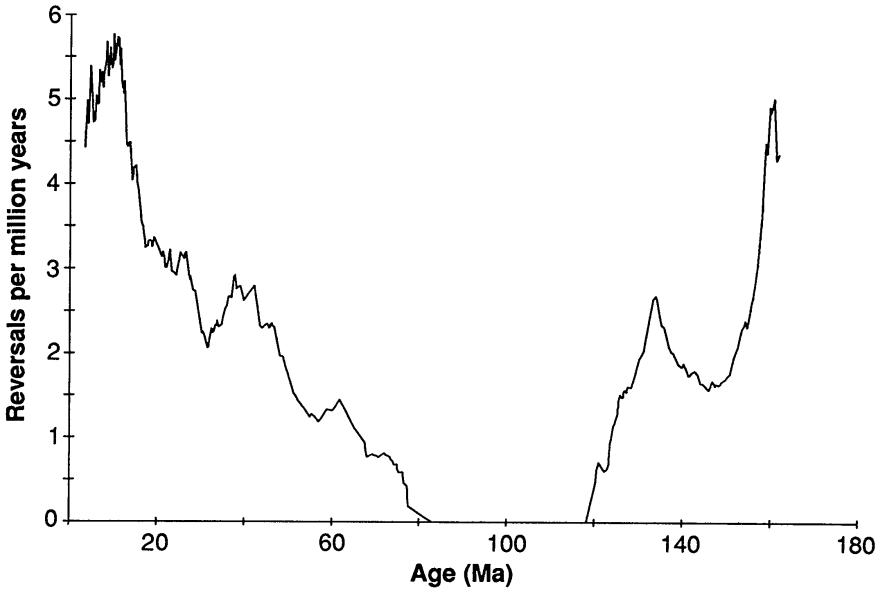

Figure 1.2: Rate of magnetic field reversals over the past 200Ma, after Merrill & McFadden (1990)

rapidly to other states from seemingly small fluctuations (Lorenz, 1963; Glatzmaier & Roberts, 1995a; Dormy & Courtillot, 2000; Ryan & Sarson, 2007). It appears the Earth's magnetic field has two stable regimes of normal and reversed polarity – and despite the infinite number of possible intermediate states – spends only a relatively short period of time in transition (e.g. Herrero-Bervera & Valet, 1999). For these reasons, precise prediction of the long term state and detailed behaviour of the magnetic field will remain unobtainable.

1.2 Measuring the Magnetic Field

The earliest known form of the magnetic compass (as a specially shaped lodestone) is recorded in China, from the 1st century A.D., though older versions are thought to have existed in the 2nd century B.C. (Needham, 1978). The use of compasses for navigation in Europe was first recorded in 1190 AD and by the 16th century were commonly used. The scholar Peregrinus published a treatise in 1269 AD on his experiments with lodestones, and was the first to recognise the dipolar nature of all magnets, that the

field is strongest at the poles and that opposite poles attract (Merrill et al., 1996). Jonkers (2000) has undertaken a thorough examination of the history of the compass in navigation in Europe and its impact on safety and efficiency of transport and hence commerce and trade.

Needham (1978) cites the work of Shen Kuo, a 11th century Chinese polymath whose book, entitled *Dream Pool Essays*, describes his observation that compass needles always pointed 'east of south', thus recognising the offset of magnetic south from true south. In 1600 AD, William Gibert correctly identified that the Earth's magnetic field behaves approximately like that of a large dipolar bar magnet, offset from the rotation axis. For most casual compass users in the United Kingdom this assumption works well. However, in detail the magnetic field structure is far more complex than the simple image shown in Figure 1.3 (a), generally found in science books in primary and secondary education. The field contains higher order features, referred to as the quadropole, octopole etc. The dipole consists of about 80% of the energy of the field, while the non-dipole components contain the remainder of the energy (Campbell, 2003). Figure 1.3 (b) shows the magnetic field lines at the core-mantle boundary generated by a computer simulation of a geodynamo from Glatzmaier & Roberts (1995a). It illustrates intricate and complicated entanglement of the field lines, required to maintain and generate the electrical activity of the core. (More recently, Aubert et al. (2008b) have developed an improved method of visualising the fields generated by geodynamo simulations, allowing detailed analysis of geodynamo behaviour.)

Magnetic fields are vector fields. On the Earth, the magnetic field has both direction and magnitude (see Figure 1.4). Compass users in the northern hemisphere are familiar with accounting for the Declination of the field, that is the angle between true or grid North (for example, as marked on Ordnance Survey maps) and geomagnetic North. To effectively use a compass with a grid-orientated map, the declination of the user's position must be known and compensated for. Typically, compasses for professional navigation have an adjustable arrow to correct for the offset (currently $\sim 3°$W in Scotland). At the geomagnetic equator, a compass needle will be aligned roughly

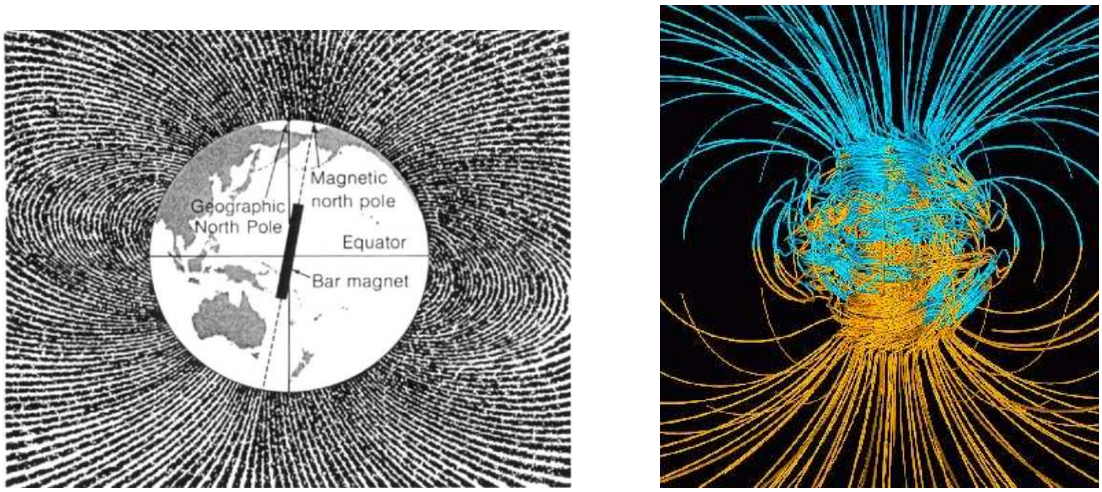

(a) Simple Bar Magnet Dipole (b) 3D Model Geomagnetic Field

Figure 1.3: (a) Simple approximation for the dipolar nature of the Earth's magnetic field illustrating magnetic field lines. (b) Visualiation of the field lines from a fully 3D geodynamo model, from Glatzmaier & Roberts (1995a). Blue field lines are pointing into Earth, red lines are point out of the Earth.

horizontally. At the geomagnetic poles, the needle will point vertically into the ground (see Figure 1.3 (a)). The angle between the horizontal plane and the needle is referred to as Inclination of the field and is measured downwards.

Technically, there are several definable magnetic poles. The principle pole definitions used are: *(a)* the Centred dipole (geomagnetic pole) which passes through the centre of the Earth, *(b)* the Eccentric axis dipole (the dipole-only field) which is the dipole moment of the field and *(c)* the Eccentric Dip poles (where the magnetic field lines are perpendicular to the Earth's surface) which are not anti-podal. However, the pole defined by the Centred dipole is considered to be the primary position of interest used in magnetic field research. It is currently offset (tilted) at an angle of $\sim 10^{\circ}$ from the planetary rotation axis (Macmillan & Maus, 2005). The complexity of the magnetic field means a compass does not actually point directly at the Centred dipole.

A more convenient method of representation of the vector direction than (the non-orthogonal) Declination and Inclination is the North-East-Down (NED) or XYZ reference frame, shown in Figure 1.4. The measurement vector can be resolved into three orthogonal Cartesian components. The North (X) vector component points towards

the geographic North pole, while the Down (Z) component points toward the centre of the Earth. The East (Y) component is orthogonal to these directions in the sense of a right-handed set and is undefined at the poles.

To measure the magnitude (F) of the field (rather than just the direction), a device such as a flux-gate (vector) or proton-precession (scalar) magnetometer is required. These instruments can measure the strength of the field to better than 0.1nT (nanoTesla) (e.g. Gilles et al., 2001). Typical field strength at the surface of the Earth varies in the range of 25,000–60,000nT, which is $\mathcal{O}(10^4)$ times weaker than magnets used for industrial purposes (or even fridge magnets). It was Carl Friedrich Gauss who invented the first method for measuring the total intensity of the magnetic field in 1832. Previously, only angles and relative intensities were measured at observatories using magnetised needles. Modern observatories use fluxgate theodolites to measure vector direction. The development of Gauss' method to measure the magnitude of the field encouraged the establishment of permanent ground-based magnetic observatories to continuously measure declination, inclination and strength.

1.3 Field Modelling

Gauss also developed the mathematical basis for modelling and analysing the magnetic field based on few measurements. Until the mid-20th century, only measurements from ground-based observatories and occasional land and marine magnetic surveys have been available. Such a sparse dataset poses problems for determining the expected field value at any particular point at or above the surface of the Earth, through interpolation for example. It is possible, however, to develop a robust field model from the available data using the method developed by Gauss, known as Spherical Harmonic representation (e.g. Parkinson, 1983).

If one assumes that the magnetic field (B) is measured in a source-free region (i.e. no electical currents), then the field can be treated as the gradient of a continuous potential field V, with values defined at any point at radius (r), co-latitude (θ) and longitude (ϕ), in spherical polar coordinates with the origin at the centre of the Earth.

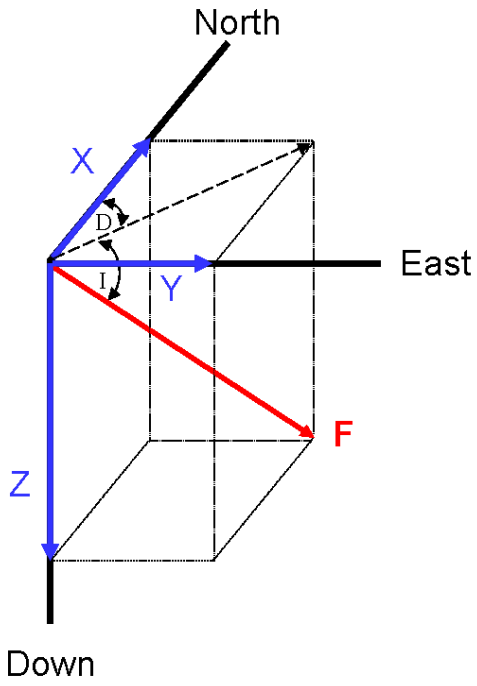

Figure 1.4: North-East-Down (or XYZ) reference frame for magnetic vector measurement. D is the declination angle and I is the inclination angle. See text for further explanation.

The solution $V(r, \theta, \phi)$ can be derived through the summation of a converging series of terms:

$$V(r,\theta,\phi) = a\sum_{l=1}^{\infty}\sum_{m=0}^{l}\left[\left(\frac{a}{r}\right)^{l+1}A_l^m + \left(\frac{r}{a}\right)^{l}B_l^m\right]Y_l^m(\theta,\phi) \tag{1.1}$$

where A_l^m and B_l^m are sets of constants. The term Y_l^m belongs to a class of functions called *spherical surface harmonics*, with l being the degree and m being the order of the function. The term a is radius of the Earth. We are interested only in the internal part of the field, and so focus on the constants contained in A_{lm} term (B_{lm} models the part of the field with sources external to radius r). The spherical harmonics are composed of associated Legendre polynomials $P_l^m(\theta)$ which are quasi-sinusoidal orthogonal functions on the surface of a sphere, dependent on θ and terms with sinusoidal variation in ϕ. Figure 1.5 shows four examples of the surfaces generated by altering the degree (l) and order (m). The constants of A_l^m can be resolved into $\cos(g_l^m)$ and $\sin(h_l^m)$ $m\phi$. The final solution for the description of the field is:

$$V(r,\theta,\phi) = a\sum_{l=1}^{L_{max}}\sum_{m=0}^{l}\left(\frac{a}{r}\right)^{l+1}[g_l^m\cos m\phi + h_l^m\sin m\phi]P_l^m(\cos\theta) \tag{1.2}$$

where g_l^m and h_l^m are called the Gauss coefficients. As the number of coefficients cannot, in reality, be infinite, the solution is truncated at a cutoff degree L_{max}. Traditionally, when using Gauss coefficients the associated Legendre polynomials are Schmidt semi-normalised:

$$\int_{\phi=0}^{2\pi}\int_{\theta=0}^{\pi}\left(P_l^m(\cos\theta)\right)^2\sin\theta d\theta d\phi = \frac{4\pi}{2l+1} \tag{1.3}$$

As the magnetic field (B), is modelled as a divergence-free field ($B = -\nabla V$), the X, Y and Z vector components of the field are computed using the following formulae:

$$X = \frac{1}{r}\frac{\partial V}{\partial\theta}; \quad Y = -\frac{1}{r}\frac{1}{\sin\theta}\frac{\partial V}{\partial\phi}; \quad Z = \frac{\partial V}{\partial r}; \tag{1.4}$$

Field models of the large-scale field (i.e. features larger 1500km) are produced by taking measurements of the magnetic field from across the globe and performing a least-

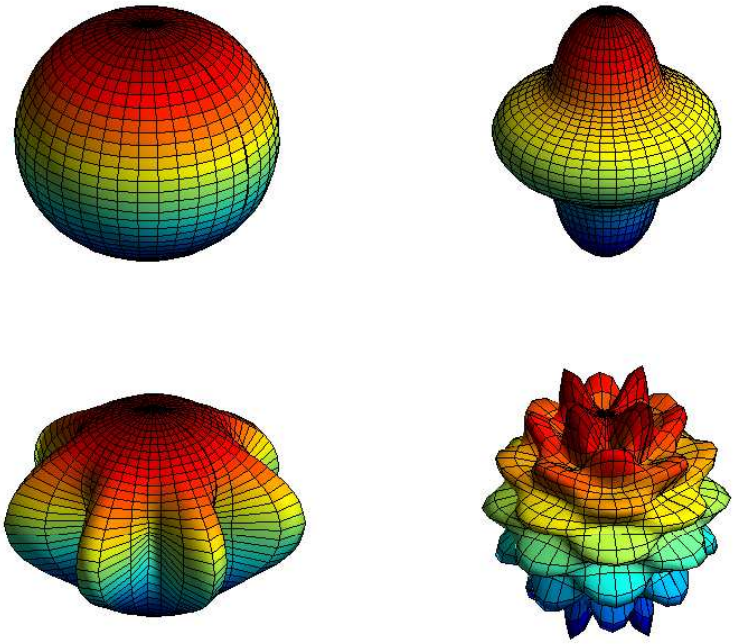

Figure 1.5: Example of spherical harmonic functions from $Y_l^m(\cos\theta)$. Top left: Y_1^0; Top right: Y_4^0; Bottom left: Y_7^7; Bottom right: Y_{14}^4.

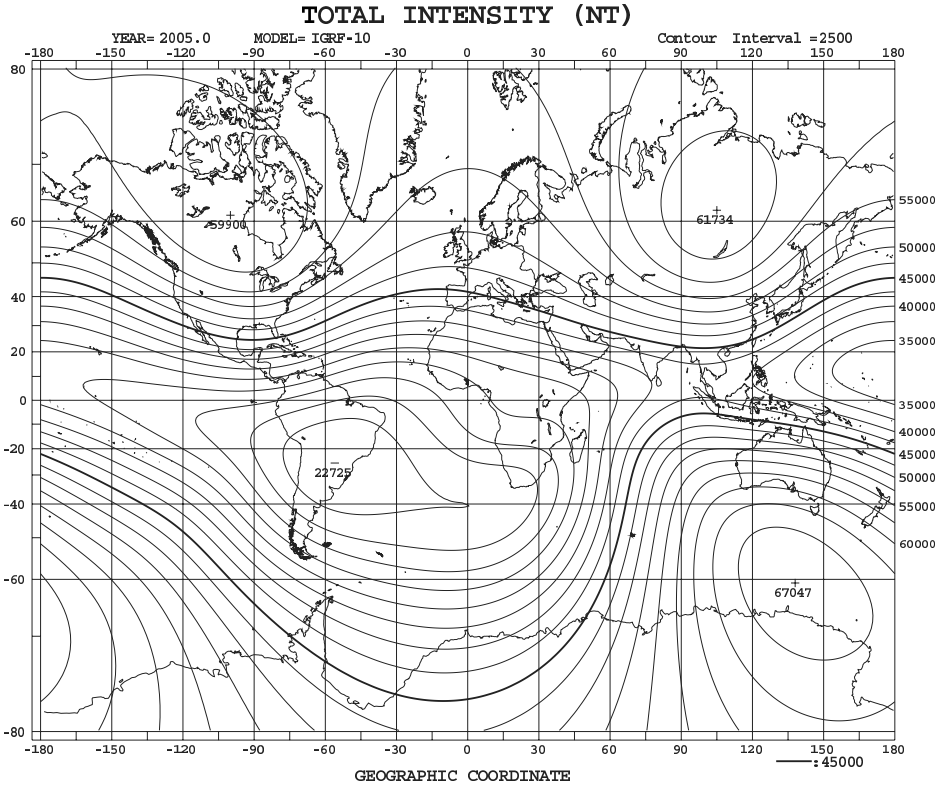

Figure 1.6: IGRF10 model of the geomagnetic field intensity at the Earth's surface upto degree and order 13.

squares inversion to solve for the Gauss coefficients (g_l^m, h_l^m), typically up to degree and order $(l = m =)$ 14. Every five years a reference model of the field, termed the International Geomagnetic Reference Field (IGRF), is updated and released, usually as part of an international effort (e.g. Macmillan & Quinn, 2000; Macmillan et al., 2003; Lesur et al., 2005). Until the release of the 10th IGRF model in 2005, the geomagnetic field has been based primarily on data from ground-based observatories with some input from satellite measurements for the 1965, 1980 to 2000 models (Gubbins & Herrero-Bervera, 2007, see Cain, p828; Purucker, p273; Macmillan, p411). The current IGRF model extends to degree and order 13. The largest coefficient is, unsurprisingly, the axial dipole which at 2005.0 had a modelled value of g_1^0 =-29,682nT. Figure 1.6 shows an example of a model of the field strength (total intensity) for 2005.0.

1.4 Secular Variation

Variations in the strength and direction of the magnetic field occur on a range of timescales from milliseconds to millions of years. The rapid variations (milliseconds to days) are related to the influence of the sun on the main field. There are a number of causes of rapid fluctuations, e.g., from ionospheric currents driven by solar heating (e.g. Thomson, 2000) to coronal mass ejections which trigger geomagnetic storms (e.g. Campbell, 2003). It is the change of the geomagnetic field on yearly to decadal timescales that is generally referred to as *secular variation* (SV). The annual SV at a given point (e.g. a magnetic observatory) for *month(t)* is the difference between the average field in *month(t-6)* and *month(t+6)* for the North (X), East (Y) and Downward (Z) components.

$$SV_{month}(t) = Field_{month}(t+6) - Field_{month}(t-6) \tag{1.5}$$

This approach removes both the stationary (crustal field) components of the signal and the annual variation (see next Section), without any direct filtering or averaging, giving the first derivative of the vector components ($\dot{X}$, $\dot{Y}$ and $\dot{Z}$) of the field.

The first investigations into secular variation were initiated by the observation of a change in declination over time. The declination of the field was accurately measured in London in 1580. When it was re-measured some 54 years later (in 1634) by Gellibrand it had changed by over 7° (Parkinson, 1983). This instigated the detailed continuous measurement of the field and a survey of the magnetic field of the Atlantic Ocean, leading Halley in 1692 to hypothesise that the change in declination of the field could be explained by westward drift of the whole field. He speculated the causes of this westward drift to be a fluid layer deep in the Earth's interior (Halley, 1692; Bloxham & Jackson, 1991). The composition of the Earth and its inner layering was finally resolved by the large scale deployment of seismic networks in the early 20th century, which confirmed the geomagnetic evidence for a liquid outer core (Oldham, 1906), with the existence of the solid inner core being inferred later by Lehmann (1936).

Several workers have produced temporally-varying models of the field at the core-mantle boundary using cubic B-splines to parameterise temporal change. These models are built with data from recent as well as historical sources such as marine navigation logs (Jonkers, 2000). Bloxham et al. (1989) inferred the field back to 1695 AD Further work by Jackson et al. (2000) pushed back the earliest field model to the late sixteenth century, again using archive marine navigational logs. From these data sources, several models of the field evolution over the past several hundred years have been developed (see Figure 1.7). GUFM1 is one such time-dependent model of the main field from 1590–1990 AD (Jackson et al., 2000). Use of paleomagnetic data from archeological sites, lake sediments and other sources has allowed Korte & Constable (2006) to deduce broad changes in the dipole strength and direction for the past 7000 years. The CALS7K.2 model, in common with the GUFM1 model, has poorer accuracy in the earlier parts of the model as the number and quality of data decline, although it does incorporate more reliable measurements in the later era. These models are regularised (smoothed) to best fit the data. Note that these models are also iterative as they make use of directional data.

Alfvén (1942) demonstrated that in the idealised situation of a moving fluid with perfect conductivity, magnetic field lines become entrained and effectively frozen into the fluid. Thus, they move (advect) with the flow of the fluid. If it were possible to individually label each field line, then the path traced out by the lines would allow the flow to be uniquely known (Backus, 1968). This so-called '*frozen flux*' theory was adapted to trace fluid flow in the Earth's core by Roberts & Scott (1965). Their arguments showed that the theoretical assumptions of Alfvén could be used in the context of the geomagnetic field. However, Kahle et al. (1967) produced a set of flow models derived from SV in which unrealistic velocities were found. Chapters 2 and 3 will discuss in greater detail the implementation of this approach, including the shortcomings and approximations.

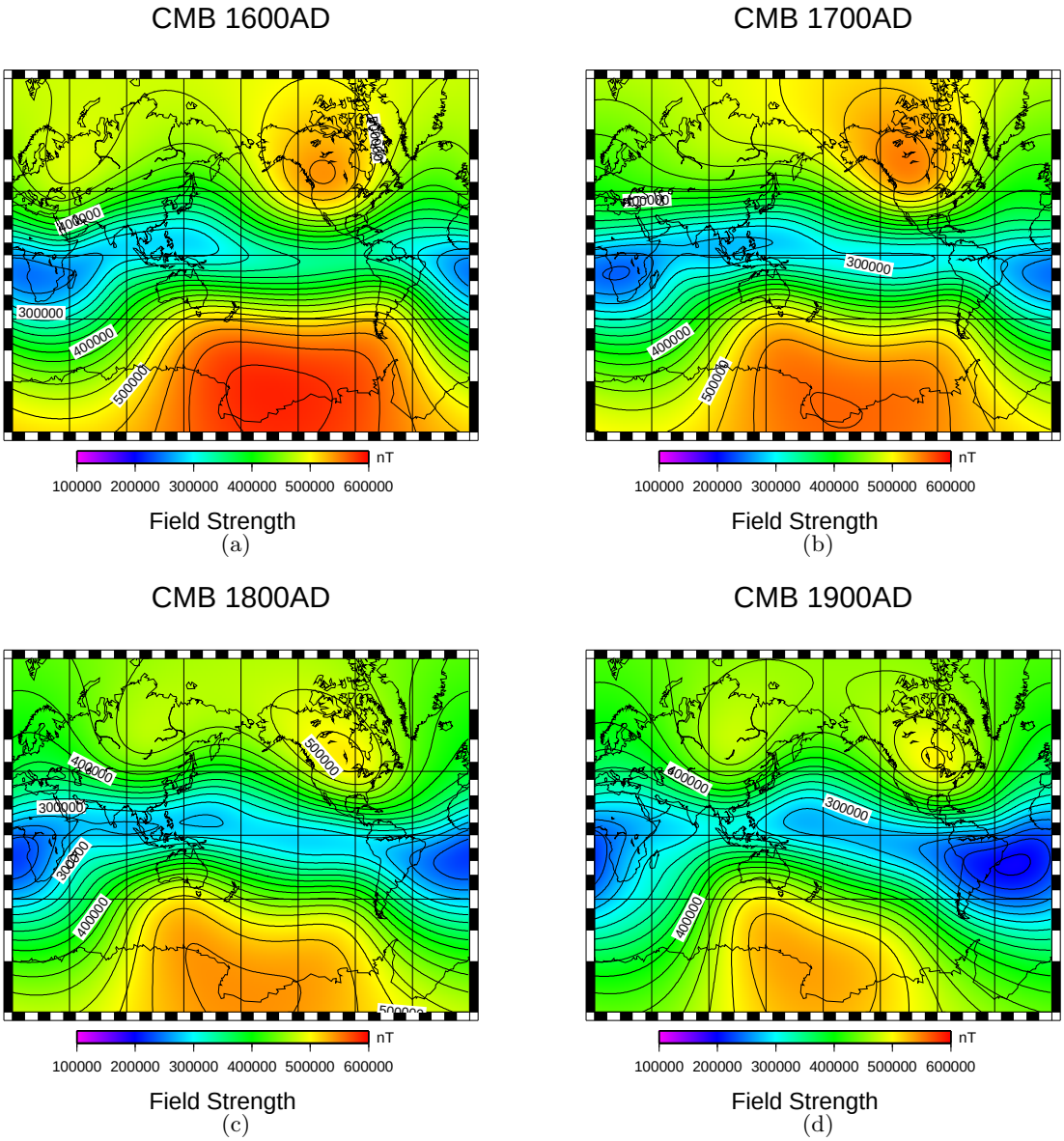

Figure 1.7: The time evolution of the total strength (F) of the Geomagnetic Field model GUFM1 at the Core-Mantle Boundary. Note the field strength before 1840 is unknown. GUFM1 extrapolates the average change in field strength from 1840–1990 back in time to 1590. (Maps drawn in Mercator projection with continents shown for reference only.)

1.5 Other Measurable Fields

The spatial and temporal variation of the geomagnetic field is complex - with contributions from internal sources both from deep within the planet and from the magnetised near-surface crustal rocks. The geomagnetic field as measured on the surface of the Earth is composed of several parts:

- the main field as generated in the core of the planet. Range: ± 50,000nT (e.g. Macmillan & Maus, 2005)
- crustal magnetisation from remanent and induced magnetisation of near surface rocks - Range: ± 1000nT (e.g. Sabaka et al., 2004)
- external fields and induced fields from variations in the magnetosphere – solar and interplanetary field. Range: ± 1000nT (e.g. Sabaka et al., 2004)
- induced fields from the ionosphere e.g. due to electrical currents generated by thermal heating of the atmosphere. Range ± 100nT (e.g. Olsen, 1997)
- induced fields from ocean circulation e.g. due to electrical currents generated by conductive fluid moving through the main field. Range: ± 10nT (e.g. Tyler et al., 2003).

Each contribution to the measured field also varies with time. A brief description of each field now follows:

Crustal Field

The remanent crustal field evolves but very slowly, for example through thermal and chemical remagnetisation (spatially changes are very rapidly though). In stable cratonic regions this process may be on the order of millions of years. The crustal field changes relatively more rapidly close to active mid-ocean ridge spreading centres as new crust is formed and in the crust of orogenic regions due to metamorphic processes. Secular variation of the main field alters the *induced* field of the crust allowing a distinction to be made between the remanent magnetism and the magnetism induced by the main

field. This can be achieved using aeromagnetic and marine magnetic data (Jackson, 2007). High spatial resolution global maps of the crustal field have recently become available (Korhonen et al., 2007) and are being continuously updated with newly-released national magnetic surveys.

External Fields

The Earth's magnetic field extends into space and interacts with the solar and interplanetary magnetic field. The Sun emits a continuous stream of charged particles (solar wind) which carry the heliospheric magnetic field. As the solar wind impinges on the Earth's magnetic field, the pressure compresses the field on the sun side of the planet and extends it into an elgonated tail on the night side. This interaction creates an extremely complex set of electrical currents and secondary magnetic fields. In particular, a large system of currents encircle the planet, causing a measurable disturbance on the ground (Campbell, 2003). The ring, partial ring and field-aligned current systems generate magnetic fields of varying intensity. These fields vary in strength daily and seasonally as the Earth rotates every 24 hours and orbits the sun once per year, and as the sun completes its 11 year magnetic activity cycle. However, during a solar storm event (e.g. from a coronal mass ejection), large magnetic fields are generated (particularly in the polar regions) occasionally giving rise to large deflections of the declination (up to 5° in Scotland) for several hours (see Figure 1.8).

Ionospheric Field

The thin atmosphere of the Earth extends up to 150km into space. The highest regions, known as the ionosphere, contain electrically charged particles which are thermally heated by the sun on the day side of the planet, causing motion of the air. As the particles move, electrical currents are generated (see Figure 1.9 (b)) generating a magnetic field, referred to as the ionospheric field. It is most intense within ±30° of the geomagnetic equator in the hours before and after local noon, decaying through

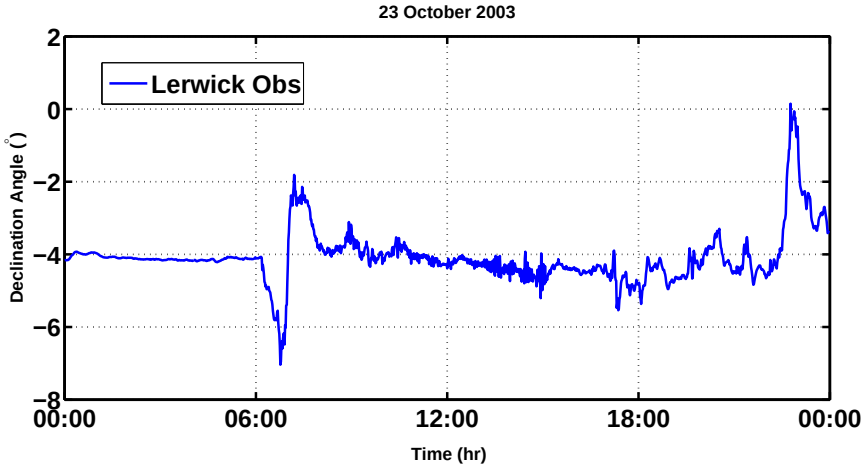

Figure 1.8: Record of the change of Declination angle at Lerwick, Shetland during the October 2003 geomagnetic storm. Data from the World Data Centre for Geomagnetism website (http://www.wdc.bgs.ac.uk/catalog/master.html).

the remainder of the day. Two sets of hemispherical current systems exist, with current flowing at a fixed point in one direction at the start of the day but reversing as the current system passes overhead. The concentration of eastward flowing current is called the equatorial electrojet. The Moon can also influence the air in this region and produces a detectable tidal signal in observatory measurements (Campbell, 2003). During solar storms, the polar regions of the ionosphere experience increased auroral activity (from charged solar particles entering along field lines) creating additional magnetic fields. At high latitudes, this auroral electrojet becomes particularly active during magnetic storm periods.

Induced Oceanic Field

A small induced field is created by the flow of seawater through the oceans. As the slightly conductive fluid passes through the Earth's magnetic field, a current is induced, which in turn generates a small secondary magnetic field. This signal is readily modelled and has been globally detected. Tyler et al. (2003) clearly detect the 12.4 hour period of the M2 lunar tide from satellite magnetic data over oceanic regions.

Thus, broadly speaking, the measurable field at the Earth has timescales which vary from seconds to millions of years. In this study, I am interested in the short term decadal

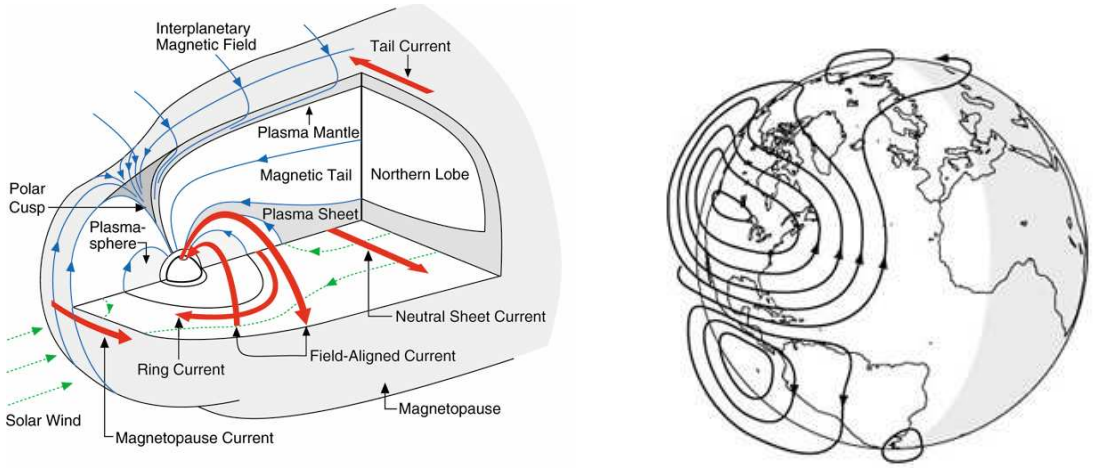

(a) Magnetospheric Currents

(b) Ionospheric Currents

Figure 1.9: (a) Schematic 3D illustration of the magnetic environment surrounding the Earth, from Russell (1999) and Campbell (2003); (b) Ionospheric currents generated on the dayside of the planet (sunlight from the left-hand side), from the USGS website (www.geomag.usgs.gov).

variation of the main field. From this regard, all other variations are to be removed, filtered and damped to correctly identify the secular variation of the internal field only.

1.6 Recent Developments

In the past decade, since the launch in 1999 of the Ørsted satellite mission, high accuracy global magnetic vector and scalar satellite data have become available to the geomagnetic community. In response to this near-deluge of data (compared to previous relatively sparse array of ground-based observatories, with some Magsat and POGO data), new methods of selecting, processing and analysing the data have been developed and tested. Historically, Gauss' method of least-squares fit of spherical harmonic coefficients to the observed data has proven adequate to model and separate the effects of the competing phenomena that generate magnetic fields measured on or above the Earth's surface. The advantage of Gauss' approach is that relatively few measurements are required to determine an acceptable model. Using larg numbers of correlated data will not continue to improve the model, due to measurement noise and uncertainty. Hence, to utilise the torrent of information available, other methods of treating the

data to produce more accurate field models must be considered.

With more accurate models of the Earth's main field and, more importantly for the purpose of the thesis, models of the change in the field, it becomes possible to explore more precisely the mechanisms and dynamics responsible for the secular variation. The benefits of better understanding SV range from improved prediction of the SV itself to probing the flow regime of the core, potentially extending our knowledge of core formation and processes. This could lead to breakthroughs in areas from planetary formation and evolution of the internal field.

1.7 Thesis Structure

The main aims of this research are:

- to understand the effects of differing flow regimes and assumptions in the formulation of core flow models
- to test and develop methods for utilising the large magnetic vector datasets available to improve magnetic field models
- to accurately forecast magnetic field change in the short term using core flow models derived from the improved SV models.

Completing these research tasks would produce a framework in which future data measurements could be directly used to improve field and flow models. In Chapter 2, the background and overview of the research area is given to orientate the reader, explaining the mathematical methods and examples. Chapter 3 builds on the methods of Chapter 2 and algorithmic approach used, exploring the effects of data uncertainty and the viable solution space of any particular flow regime. Chapter 4 discusses the 'Virtual Observatory' method of analysing vector magnetic field data and illustrates a number of new results concerning potential influences from fields outwith the region of interest. Chapter 5 examines simple advection of the magnetic field coefficients by flow models. Chapter 6 introduces and explains a technique called Ensemble Kalman Filter,

a method adapted from weather forecasting models. This is used as a novel approach for modelling and forecasting of the field and secular variation. I show the results of this approach compared to standard methods. Chapter 7 discusses the implications of this work for magnetic field research and gives suggestions for future work. Finally, Chapter 8 concludes with a summary of the main achievements.

Chapter 2

Background

If the core flow can be satisfactorily determined from secular variation, it can potentially be used to advect the magnetic field forward in time to produce a forecast. These are the two main aims of this study. First, I investigate the use of novel mathematical techniques in determining the flow regime at the core-mantle boundary. With such knowledge, it may be possible to answer questions on the processes in the planetary interior. Secondly, the project develops methods to forecast the variation of the main field forward in time which may have research and industrial applications.

This chapter focuses upon examining the physical aspects of the main field, core flows and their interaction with surrounding systems (e.g. the mantle and inner core). A mathematical description of the method for deriving flow models is given, along with a description of a new technique for inversion of SV datasets.

2.1 The Outer Core

The magnetic field of the Earth is often portrayed as a simple dipolar bar magnet located at the centre of the earth offset at an angle to the geographic poles. To the casual observer its manifestation appears to be a nearly steady, stable field. Thus, for most purposes, the simple dipole approximation suffices. Deeper study of the magnetic field of the Earth reveals it to be highly dynamic and variable in both time and space.

It is known that the Earth has had an active magnetic field for over 3.2Ga (McEl-

hinny & Senanayake, 1980; Biggin et al., 2008). From the available palaeomagnetic evidence and lunar rock samples, it appears that the main field formed early in the planet's evolution. However, the detailed evolution of the magnetic field (and its relation to the outer core and mantle) over the history of the Earth remains an active area of research, combining the efforts of a number of disciplines, including geochemistry, seismology and numerical modelling (e.g. Butler et al., 2005).

Since its formation the Earth has evolved into a layered, radially differentiated body. The planet initially formed a rocky silicate and oxide mantle while the heavier immiscible siderophile elements sank to the centre under the influence of gravity. Release of gravitational energy, in combination with the early decay of radiogenic nuclides (e.g. Al^{26}) is likely to have generated sufficient heat to keep the core entirely liquid, despite the enormous pressures. It is calculated that such conditions are sufficient to have initiated convection in the entire core (Labrosse et al., 1997), triggering the self-sustaining geodynamo. Convection and conduction are the primary cooling mechanisms for heat loss from the core to the overlying mantle and outer space (Lister & Buffett, 1998).

The persistence of the field means that it must be continually regenerated. It is estimated that Ohmic losses through heat would dissipate the field after approximately 10^4 years (e.g. Bloxham & Jackson, 1991). There are a number of mechanisms through which the field can be regenerated; for example, the so-called $\alpha\omega$-effect dynamo whereby fluid motions related to the rotation of the planet can amplify and sustain a magnetic field (Parker, 1955; Merrill et al., 1996; Love, 1999; Buffett, 2000). In the simplest case, shown in Figure 2.1, a poloidal magnetic field (a) diffuses through a convecting body of fluid (i.e. the core) and (b) is twisted by toroidal motion of fluid (parallel to the boundary surface). This motion forms toroidal magnetic field loops within the core. This process is called the ω effect. If this were the only process in the core the poloidal field would be reduced to zero, unless a further process was in operation. The core must have poloidal flow (upwelling/downwelling) to create new poloidal field loops (c), which coalese to reinforce the large-scale poloidal field. This process is called the α

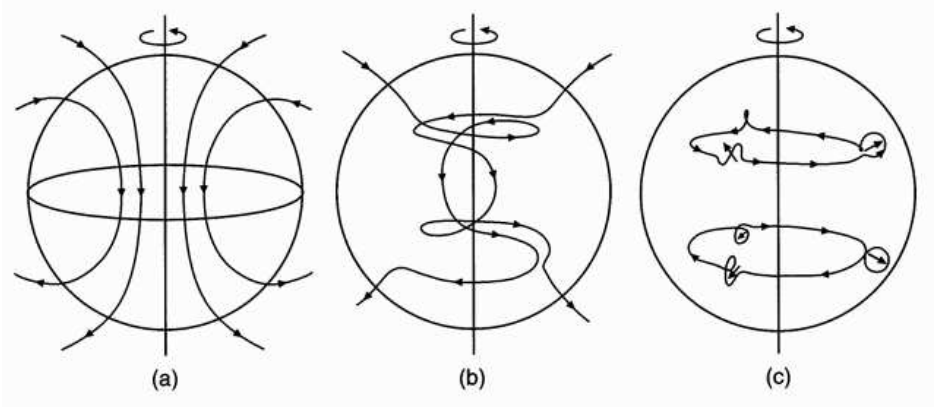

Figure 2.1: Idealised $\alpha\omega$ dynamo, from Russell (1999). See text for details.

effect. There are other types of dynamo model which have been proposed such as the α^2 and the $\alpha^2\omega$ model; for example, Love & Gubbins (1996) demonstrated a self-sustaining dynamo model with only poloidal flow.

Structure of Core Flow

Debate continues about the nature of the flow in the core: Whaler (1980) examined if there was evidence for whole outer core convection, while Gubbins et al. (1982) and Gubbins (2007) argue for a stably stratified layer at the top; or perhaps both types of behaviour occur (Lister & Buffett, 1998; Loper, 2007). The reason for such conflicting views is that the geophysical evidence for each case is still ambiguous. Support for any one particular theory based upon paleomagnetic evidence is also not particularly strong. It may be the case that different flow regimes have operated at different times in the planet's history.

Turbulence (chaotic flow, vortices and eddies on all spatial scales) must occur within part of the core, particularly close to the inner core boundary. Loper (2007) illustrates a model, shown in Figure 2.2, in which plumes of less dense material rise from the inner core boundary and become mixed in a large zone in the middle. (Note the 'stable' region below the core-mantle boundary.) The fluid flow within a plume is controlled by the Coriolis (rotation) and Lorentz (magnetic) forces, resulting in pancake-shaped elongate structures. Eltayeb (1999) studied the stability of these structures, to ascertain

the required parameters of the fluid in which they formed, and their contribution to dynamo action. He concluded that their modelled motion would be too slow to be significant factors in the geodynamo or secular variation. Ryan & Sarson (2007), however, have proposed that such turbulent plumes and chaotic flow do influence the timing of reversals and excursions and find that their modelled turbulent regime reproduces a statistically similar to the lognormal distribution of observed reversals and excursions they claim to observe in the paleomagnetic record. This is in contrast to the modelled Poisson distributions of other researchers such as Constable (2000).

The balance between the Coriolis and the Lorentz force in the core is still unknown, due to the uncertain strength of the toroidal magnetic field. An approximate balance between the forces seems to be the growing consensus, as this gives a toroidal field four times stronger than the poloidal field, consistent with self-sustaining dynamo models (Merrill et al., 1996). If a weak-field model is used, where the Coriolis dominates, the fluid motion is dominated by the rotation of the Earth. The flow becomes confined to columns parallel to the (rotational) z-axis, a consequence of the Proudman-Taylor theorem (Proudman, 1916; Taylor, 1917). This type of convection structure is known as Busse rolls after Busse (1975). A strong objection to this regime is that the calculated toroidal magnetic field has approximately the same strength as the poloidal field. However, if the Lorentz force is dominant, the Busse rolls are unable to form correctly, altering the strength of the dynamo.

Assuming that convection does indeed occur, it is generally agreed that thermally-driven convection is only a minor part of the mechanism for overturning of the liquid in the outer core. Far more efficient is compositionally-driven convection. It is suggested that the core composition consists of perhaps 90% iron, with sulphur, nickel, cobalt and lighter elements (e.g. H, O and C) being suggested as other candidate materials (Tschauner et al., 1999). When the liquid iron freezes to the solid inner core, heat is released from the latent heat of crystallisation; however, light elements are also freed from entrainment within the iron (Sumita & Bergman, 2007). These lighter 'volatiles' rise buoyantly to the top of the outer core, contributing to the convection regime. This is

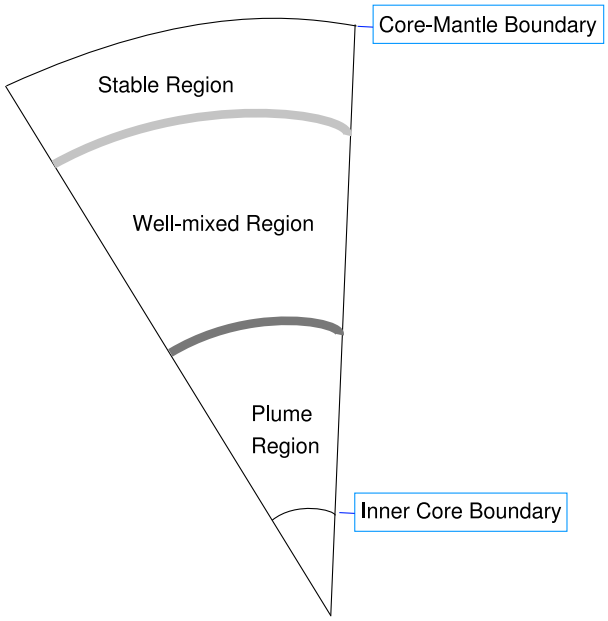

Figure 2.2: Notional Cross section of the outer core showing regions of flow, after Loper (2007).

thought to be the primary driver of the core magnetic field, the so-called gravitationally powered dynamo (Lister & Buffett, 1998; Buffett, 2000).

2.2 The Inner Core

The influence of the inner core in controlling and modifying the behaviour of the magnetic field is controversial. Christensen & Tilgner (2004) argue from experimental simulations that the power requirements of the geodynamo are lower than the calculated heat output of the core, thus allowing the early magnetic field to run on heat derived from radiogenic decay of potassium. The eventual initiation of freezing of the core would have drastically changed the flow regime (initially, as an obstruction blocking complete convection). The timing of the solid inner core formation is still under debate. Labrosse et al. (2001) estimates range from over 2.5Ga to 1.0 ± 0.5Ga depending on the inclusion of radiogenic isotopes in the initial core composition. The growth of the inner core strongly controls the level of compositional convection and additional heat from crystallisation being input into the outer core with Gubbins et al. (2003, 2004)

arguing the formation could have been as early as 3.5Ga.

The inner core has a radius of $\sim$ 1200km. If its extent is projected to the surface of the core-mantle boundary the cylinder containing the spherical inner core would impinge at a latitude of $\pm 68^{\circ}$. Within the regions above and below the inner core, the outer core flow in the so-called tangent cylinder is affected by its presence. The Busse rolls do not occur inside the cylinder, but may be tangent to the inner core outwith the cylinder circumscribing it. Bloxham & Gubbins (1985, 1986) point out that this phenomena may explain the presence of stationary foci of four radial component magnetic field features, found to be equatorially symmetric with opposite sign and at the latitude that the tangent cylinder intersects with the core-mantle boundary (see Figure 2.3). The computer simulations of dynamos from Glatzmaier & Roberts (1995b) also reveal intriguing behaviour of the magnetic field during reversals caused by the presence of an inner core. They found that the diffusion time of the magnetic field out of the inner core was much longer than the time between reversal attempts. Thus, their modelled inner core acted as a buffer against field reversals. Gubbins (1999) also proposes the idea that the diffusion of the magnetic field from the inner core is 10 times slower than in the outer core. This is one of the arguments used in Biggin et al. (2008) to justify the existence of the inner core at 2.8Ga, as there are no observed reversals in the period 2.82–2.45Ga. However, as the model simulations of Glatzmaier & Roberts (1995b) inevitably involve a large number of assumptions, a puzzle remains about the exact influence of the inner core on the magnetic field, which has yet to be resolved.

Other simulations have attempted to model and explain features due to the inner core. For example, Sreenivasan & Jones (2005) model a possible vortex within the tangent cylinder, while Guo et al. (2004) investigated the induced flow in the outer core from inner core (super)rotation. Stanley et al. (2007) have also attempted to understand how the inner core directly imposes constraints upon the field.

Finally, Stevenson (2008) argues that the core is much hotter (by $>1000^{\circ}$K) than it should be, if the heat were generated by gravitational collapse and radioactivity alone. This 'superheat', as he terms it, may be a remnant of the impact from the Moon-forming

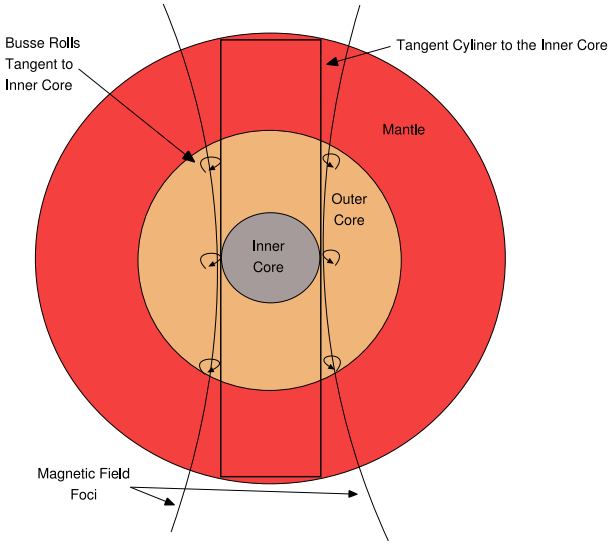

Figure 2.3: Schematic longitudinal cross section of the Earth showing the tangent cylinder, Busse rolls and magnetic foci.

planetessimal and could unexplain features of the layer lying just above the core-mantle boundary, known as D″ (c.f. van der Hilst et al., 2005). In contrast, the core of Mars cooled more rapidly, ceasing convection strong enough to generate a field early in its history (Stevenson, 2001), its magnetised crust retaining a record of the early dynamo (Whaler & Purucker, 2005). In Stevenson's (2001) view, the Earth's magnetic field represents a secondary cooling mechanism, linked to the presence of plate tectonics as the primary one. He concludes that because of the protection offered by the magnetic field (for example in the form of shielding from the solar wind and cosmic radiation), life on Earth is innately connected to the formation, composition and convection of the core.

2.3 Modelling Secular Variation

It was Halley (1692) who first offered evidence of a westward drift in the structure of the magnetic field in the North Atlantic, though he is better remembered in popular culture for his other numerous achievements (see Figure 2.4). Bullard et al. (1950) proposed the first modern theory of main field SV, consistent with dynamo understanding of the

Figure 2.4: Plaque erected in Westminster Abbey to Halley, commemorating the return of the comet named after him. Note the reference to 'geophysicist' (lower right).

time. Hide (1966) offered an alternative mechanism in terms of magnetohydrodynamic waves propagating about the outer core. However, the idea of wholesale global westward drift is simplistic; indeed parts of the field in the Pacific move eastwards (see Figure 2 in Hulot et al. (2002)). The slow decadal change of the Earth's geomagnetic (main) field is interpreted as indicative of motion of liquid iron in the upper parts of the outer-core. By assuming that the magnetic field lines of the main field are essentially 'frozen' into liquid at the top of the outer core, it is possible to deduce a flow model causing the observed field change at the surface of the Earth (Roberts & Scott, 1965). I outline the mathematical basis for modelling the field and SV, before examining how to use SV to model large-scale flow along the outer core-mantle boundary.

The change of the magnetic field over time is described by the so-called magnetic induction equation, which relates secular variation to fluid flow and magnetic diffusion

of the field in the core:

$$\frac{\partial \mathbf{B}}{\partial t} = \nabla \times (\mathbf{u} \times \mathbf{B}) + \eta \nabla^2 \mathbf{B} \tag{2.1}$$

where $\mathbf{B}$ is the magnetic field, $\mathbf{u}$ is the velocity of the fluid and $\eta = 1/(\mu_0 \sigma)$ is the magnetic diffusivity, defined by the constant μ_0 (permeability of free space) and the electrical conductivity (σ) of the core fluid. As the core-mantle boundary is a material one, there is no radial fluid flow across it. The induction equation can be reduced to

$$\dot{B}_r = -\nabla_H \cdot (\mathbf{u}_H B_r) + \frac{\eta}{r} \nabla^2 (r B_r) \tag{2.2}$$

where B_r is the radial part of the poloidal field, $\mathbf{u}_H$ are the flow components in the (θ, ϕ) directions on the surface of the boundary and ∇_H is the horizontal part of the divergence. From this point, one can simplify the relationship further by making some assumptions. If one assumed the conductivity of the core fluid to be extremely high (or infinite) then there would be no diffusion of the magnetic field. This is unrealistic, obviously, as the total integrated field strength would never change. However, at large horizontal spatial scales ($L > 1000$km) with a reasonable flow velocity of $u = 5 \times 10^{-4}$ m/s and a diffusion rate of $\eta \sim 1$ m^2/s, a ratio known as the Reynolds magnetic number:

$$R_m = \frac{uL}{\eta} \tag{2.3}$$

This formula is derived from 2.2 and suggests that advection dominates diffusion as $R_m > 500$ at short timescales (< 10 years, say) (Holme, 2007). However, deciding the length scale or even the flow velocity becomes a somewhat circular argument. At some sufficiently small length scale, diffusion does become important. However, for the length scales used in this study, it is sufficiently small to ignore.

Neglecting diffusion leads to the so-called 'frozen-flux' induction equation:

$$\dot{B}_r + \nabla_H \cdot (\mathbf{u}_H B_r) = 0 \tag{2.4}$$

The solution to this equation for $\mathbf{u}$ is ambiguous because there are two unknowns

(the flow in the (θ, ϕ) directions) for one equation. Additional assumptions must be made to constrain and reduce the non-uniqueness of the solution. However, there are numerous problems with such assumptions; indeed, much of the flow remains 'hidden' or ambiguous due to the innate inability to individually label field lines and the inherent non-uniqueness of the flow (Backus, 1968). A lack of observational data and knowledge of the exact conditions in the core (e.g. precise knowledge of $\dot{B}_r$ and B_r is not possible), lead to a range of plausible flow regimes being possible.

As an example of non-uniqueness, consider flow within a planet with a simple axial dipole magnetic field coincident with the rotation axis of the planet. If the flow within the planet is geostrophic, any SV and thus flow is invisible to the observer – measurement of the field at a single point would reveal no change in the strength or direction of the field. Thus, the problem is non-unique, as *any* flow (with velocity $u = 0 \rightarrow \infty$) is a solution to the problem.

Nonetheless, as Holme (2007) points out, Equation 2.4 provides a starting point – by measuring the observable radial field B_r and the secular variation $\dot{B}_r$, it is possible to model the flow $\mathbf{u}$, in some manner. I will next explain the method used to determine $\mathbf{u}$, given B_r and $\dot{B}_r$.

2.4 Core Flow Modelling

The strength and direction of the field has in the past been measured at the surface of the planet at a limited number of fixed observatories unevenly distributed across the globe. From these observations, models of the magnetic field and secular variation can be derived using spherical harmonic analysiss.

Typically, geophysical problems can be modelled in a number of ways. The use of the *forward* model requires the input of 'best-guess' parameters into a mathematical formulation of the physical manifestion, with the outcome being, hopefully, a solution that is within the bounds of error of the observations. (This is analogous to taking the ingredients for a cake and devising a recipe that results in a cake similar to the 'observed' cake). A series of sensitivity tests are undertaken to test which parameters

are most important in constraining the forward model.

The *inverse* model seeks to use the observed data in conjunction with a mathematical description of the physical manifestation in order to constrain each of the input parameters. (This is analogous to guessing the ingredients of a cake from an understanding of a basic recipe and a 'taste' test). The inverse model seeks a set of parameters that minimise the residual difference between the model calculated from the parameter solution and the observed data. In certain circumstances, when the number of data points and the number of model parameters are equal and the problem is well-behaved, it is possible to solve exactly for a set of parameters. However, in general, noise in the measurement of the observed data or a lack of (or too many) observational data give rise to a non-existant solution.

The formulation of a solution to the problem of determining the flow on the surface of the core-mantle boundary requires a deep understanding of the inverse problem. A full exploration of inverse theory can fill several volumes (e.g. Parker, 1994; Gubbins, 2004). However, common to most inverse problems is the requirement of assumptions to constrain the boundaries of the problem. In geomagnetism, the mantle and the atmosphere of the Earth are generally assumed to be electrically insulating and hence free of currents. The conductivity of the mantle is estimated in the range 10^{-4} S m^{-1} to 10 S m^{-1}, increasing with depth (Gubbins & Herrero-Bervera, 2007, see Katsura, page 684). Conductivity in the outer core is estimated as $\sim 5 \times 10^5$ S m^{-1}, a difference of over five orders of magnitude (Gubbins & Herrero-Bervera, 2007, see Price, page 98). In this simplified approximation, the measured field is modelled as being curl-free ($\nabla \times \mathbf{B} = 0$) and the field can be derived from the gradient of the scalar potential V, where $\mathbf{B} = -\nabla V$, where $\nabla^2 V = 0$, representing a harmonic field which satisfies Laplace's equation.

By assuming the observed field is due to internal sources only, it can be modelled as part of a spherical harmonic expansion, defined as a function of position on the globe. The potential V, due to internal sources (see Section 1.3), can be described as a spherical harmonic function in Equation 1.2.

Whaler & Gubbins (1981) pointed out that using spherical harmonic analysis of the magnetic field could be regarded as a linear inverse problem. However, as posed, the problem is one of an infinite sum. Due to only a finite number of data measurements on the Earth's surface being available, some simplifications must be made. Commonly, the series is truncated at some arbitrary level (e.g $L_{max} = 10$ for IGRF models prior to 2000).

Measurements of the components of the magnetic field at an observatory can be used to estimate the values of g_l^m and h_l^m, which gives the Gauss coefficients for a particular model at one time epoch at the Earth's surface. Continuation of the coefficients downwards from the surface of the Earth to the core-mantle boundary requires changing the radius at which the field is measured (at $r = a$), the Earth's surface, to ($r = c$), the core mantle boundary. This preferentially amplifies the power in the higher harmonics, thus increasing the complexity of the field and the noise level (Bloxham, 1988). The overall strength of the field at the core-mantle boundary rises by about an order of magnitude higher than at the surface.

2.4.1 Representation of flow inversion

The most convenient way to express the inverse problem of deriving a core flow model from observed SV data is through the use of a spectral spherical harmonic representation for the main field, SV, and the coefficient parameters of the flow (e.g. Roberts & Scott, 1965; Whaler, 2007). As the horizontal velocity averages to zero over the core-mantle boundary and the radial component across the boundary vanishes, the horizontal velocity vector $\mathbf{u}_H$ can be expressed in terms of the poloidal and toroidal scalars, S and T, which can be expanded in spherical harmonics, in a spherical polar coordinate system (r, θ, ϕ):

$$\mathbf{u}_H = \nabla \times (T\mathbf{r}) + \nabla_h(rS) \tag{2.5}$$

where

$$T(\theta,\phi) = \sum_{l,m} t_l^m Y_l^m(\theta,\phi)$$
$$S(\theta,\phi) = \sum_{l,m} s_l^m Y_l^m(\theta,\phi) \tag{2.6}$$

The coefficients $\{t_l^m, s_l^m\}$, stored in a vector $\mathbf{m}$, are the flow model coefficients which we seek to solve for. $Y_l^m(\theta,\phi)$ is a Schmidt quasi-normalised real spherical harmonic; l and m are the degree and order, respectively. Spherical harmonic SV coefficients can be related to flow coefficients by Equation 2.4 which can be recast as:

$$\dot{\mathbf{g}} = \mathbf{H}\mathbf{m}, \tag{2.7}$$

where $\mathbf{H}$ is the combined Elsasser ($\mathbf{E}$) and Gaunt ($\mathbf{G}$) matrix (e.g. Roberts & Scott, 1965; Whaler, 1986). The elements of $\mathbf{E}$ and $\mathbf{G}$, which involve integrals of triple products of spherical harmonics and their spatial derivatives and the main field coefficients ($\mathbf{g}$) can be expressed in closed form (e.g. Bullard & Gellman, 1954; Wigner, 1959; Whaler, 1986). Having calculated the $\mathbf{E}$ and $\mathbf{G}$ matrices, the problem can be written as (Bloxham et al., 1989):

$$\dot{\mathbf{g}} = (\mathbf{E} : \mathbf{G}) \begin{pmatrix} \mathbf{t} \\ \dots \\ \mathbf{s} \end{pmatrix}$$

with $\mathbf{m}$ being the toroidal ($\mathbf{t}$) and poloidal ($\mathbf{s}$) coefficients. The vector $\dot{\mathbf{g}}$ can be derived directly from the secular variation components of observations on the surface of the Earth, with $\mathbf{d} = \mathbf{Y}\dot{\mathbf{g}}$. The elements of the data vector, $\mathbf{d}$, are the components of the measured secular variation (e.g. $\dot{X}$, $\dot{Y}$ and $\dot{Z}$, where $X = -B_\theta$, $Y = B_\phi$ and $Z = -B_r$ denote the North, East and vertically downwards components respectively) expressed in spherical polar coordinates. $\mathbf{Y}$ has elements which are multiples of spherical harmonics and the θ and ϕ derivatives. Thus, including the observational error ($\mathbf{e}$), the linear

inverse problem becomes:

$$\mathbf{d} = \mathbf{Y}\dot{\mathbf{g}} + \mathbf{e} = \mathbf{YHm} + \mathbf{e} = \mathbf{Am} + \mathbf{e} \tag{2.8}$$

Rearranging Equation 2.8 gives the error (or residuals) between the observations and the data predicted by the model parameters.

$$\mathbf{e} = \mathbf{d} - \mathbf{Am} \tag{2.9}$$

This solution assumes equal uncorrelated errors in the data, but the equation can be further generalised to include weighting of the different observations by their errors. Introducing a data covariance matrix (denoted $\mathbf{C}_e$), where the off-diagonal elements indicate correlations, would be useful. However, though it is understood that errors in the measurements can be correlated, these errors are also often poorly known or characterised (Gubbins, 2004). To determine a solution, we seek the minimum of a norm of the error vector (where N is the number of data):

$$L_n = \|\mathbf{e}\|_n = \Big(\sum_{i=1}^{N} |e_i|^n \Big)^{1/n} \tag{2.10}$$

For $n = 1$, this is called the L_1 (or Laplacian) norm, while for $n = 2$, this is the standard L_2 least-squares formulation. Minimising the L_2 norm leads to the least squares solution called $\hat{\mathbf{m}}$ (i.e. the L_2 norm performs best when the errors are Gaussian-distributed):

$$\hat{\mathbf{m}} = (\mathbf{A}^T \mathbf{C}_e^{-1} \mathbf{A})^{-1} \mathbf{A}^T \mathbf{C}_e^{-1} \mathbf{d} \tag{2.11}$$

This is the so-called *unregularised* solution for $\hat{\mathbf{m}}$.

2.4.2 Reducing non-uniqueness of Flow Models

Kahle et al. (1967) first implemented a computational solution for a core flow model from SV. They employed a least-squares matrix solution to invert a spherical harmonic model of the global field and SV. Though they found that error-free simulations could

recover flow exactly, they were unable to correctly estimate the error in the spherical harmonic models of B_r and $\dot{B}_r$. The flow models they recovered showed unrealistically large flows. Prior to this, Roberts & Scott (1965) had noticed an ambiguity in the frozen-flux solution and Backus (1968) formalised the result. By re-writing Equation 2.4, it can be seen that the flow is sensitive to both the northward and eastward component, both of which need to be determined from one equation:

$$\dot{B}_r + B_r \nabla_H \cdot \mathbf{u} + \mathbf{u} \cdot \nabla_H B_r = 0 \tag{2.12}$$

Backus (1968) showed that the flow is only fully constrained when it is perpendicular to closed contours of the field where $B_r = 0$ (known as the 'null-flux' curves). Otherwise, only part of the flow is deducible. In the extreme case, flow parallel to null-flux curves is undetectable. Figure 2.5 illustrates the principle. Thus, in mathematical terms, there exists a large null-space, into which viable but unrealistic flow vectors can be projected.

To reduce the ambiguity, at least one additional equation is required, though this will not necessarily provide a unique solution. Strategies aimed at reducing the ambiguity of the core flow solutions have been investigated for several decades. Some strategies impose a framework on the type of flow that is allowed, while others appeal to physical or mathematical constraints. I will outline some of the more common strategies below.

To incorporate additional constraints into the solution for $\hat{\mathbf{m}}$, Gubbins (1983) and Shure et al. (1985) pioneered the application of stochastic inversion in geomagnetic studies. Due to the under–parameterisation of the problem, incorporating additional constraints into the solution is justified. These are imposed through the so-called regularisation matrix to give the stochastic form of the solution. This modifies (2.11) by the inclusion of a regularisation term to give:

$$\hat{\mathbf{m}} = (\mathbf{A}^T \mathbf{C}_e^{-1} \mathbf{A} + \lambda \mathbf{D})^{-1} \mathbf{A}^T \mathbf{C}_e^{-1} \mathbf{d} \tag{2.13}$$

$\mathbf{D}$ is the regularisation matrix which can be used to incorporate an *a priori* constraint, such as imposing a 'smoothness' on the flow. Including $\mathbf{D}$ into the formulation is thus

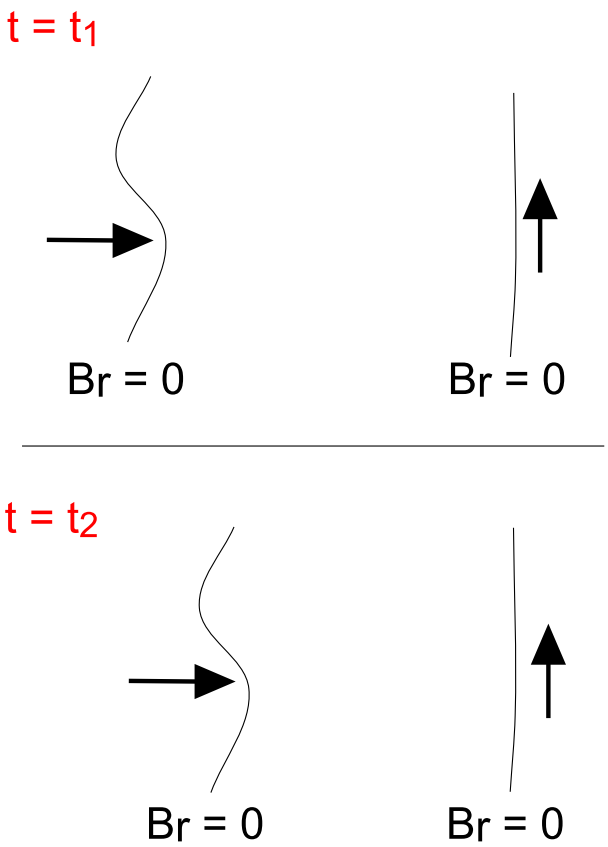

Figure 2.5: Schematic explanation of the flow ambiguity. Flow perpendicular to the $B_r = 0$ contour is fully resolved (lefthand images) while flow parallel to the $B_r = 0$ contour is invisible (righthand image).

equivalent to minimising a linear combination of the error vector and an initially defined solution norm. The variable λ acts as a Lagrange damping parameter (also known as a Lagrange multiplier in optimisation theory) to control the importance attached to the data versus the imposition of an *a priori* constraint. Regularisation also ensures numerical stability of the inversion and convergence of the expansion in Equation 2.6 when the spherical harmonic series is truncated. For example, smoothing the field, by imposing a constraint on the spatial complexity (e.g. Whaler & Gubbins, 1981), helps to alleviate the issue of noise amplification in high degree coefficients, through downward continuation of the field from the surface to the core-mantle boundary. Another example constraint is to apply a measurement of a norm to damp the complexity of the solution (Gubbins & Bloxham, 1985).

In further refinements to the theories of Backus, over the intervening decades researchers have imposed other constraints on the non-uniqueness of the flow. By making assumptions on the type of flow producing the secular variation, it has been possible to produce maps of the flow beneath the core-mantle boundary. Conditions of purely toroidal flow (Whaler, 1980), tangentially geostrophic flow (Hills, 1979; Le Mouël, 1984), helical flow (Amit & Olson, 2004) and steady flow in time (Gubbins, 1982; Voorhies & Backus, 1985) have been invoked to remove some of the uncertainties. Within these regimes, a flow model responsible for the observed secular varation can be constructed. Other types of flow modelling have been undertaken to investigate if external features of the system (such as relative mantle-core rotation) have an effect (Holme & Whaler, 2001).

Unconstrained flows

Flows allowing both toroidal and poloidal coefficients without additional conditions are known as unconstrained flows. The flow model is solved directly from Equation 2.13 by imposing a constraint in $\mathbf{D}$ which smoothes the flow. The small scale flow is damped by penalising higher-degree flow coefficients through the use of a norm. An example of a commonly employed norm is the so-called 'strong' norm of Bloxham

(1988), which minimises the complexity of the flow by strongly downweighting higher-degree coefficients:

$$\begin{aligned}\mathbf{m}^T\mathbf{D}\mathbf{m} &= \oint_{CMB}\left[\left(\nabla_h^2 u_\theta\right)^2 + \left(\nabla_h^2 u_\phi\right)^2\right] dS \\ &= 4\pi\sum_l \frac{l(l+1)^3}{2l+1}\sum_{m=0}^{l}(t_l^m)^2 + (s_l^m)^2 \end{aligned} \tag{2.14}$$

The level of smoothing is controlled by the size of the λ parameter in Equation 2.13. The larger it becomes, the more important the constraint becomes and so the solution is more heavily damped. Figure 2.6(a) shows an example of an unconstrained flow from ground-based observatory data for the epoch 1990.0.

Toroidal-only flows

Toroidal-only flows, where the radial motion of the fluid is set to zero (i.e. no upwelling or downwelling as $u_r = 0$) arises from the proposition that a stable boundary layer exists at the core-mantle boundary, constraining the vertical gradient of the flow. This constraint simplifies Equation 2.12 (Braginsky & Le Mouël, 1993; Gubbins, 2007). Using the condition $\nabla_H \cdot \mathbf{u}_h = 0$ requires that the poloidal flow coefficients are zero. This halves the number of equations of condition in $\mathbf{A}$, requiring just the Elsasser matrix to solve for the toroidal coefficients. Equation 2.7 simplifies to:

$$\dot{\mathbf{g}} = \mathbf{E}\mathbf{t}, \tag{2.15}$$

where $\mathbf{E}$ is the Elsasser matrix and $\mathbf{t}$ is the vector of toroidal coefficients. Figure 2.6(b) shows an example of toroidal-only flow from ground-based observatory data for the epoch 1990.0.

Imposing a toroidal-only flow extends the component of the flow that can be uniquely determined. In an unconstrained flow, Backus showed only the component moving perpendicular to the null-flux curve could be correctly determined. With a

toroidal-only flow, the flow perpendicular to all contours of B_r can be constrained. Whaler (1980) tested if observed data fitted the theory of toroidal-only flow, by testing if $\dot{B}_r = 0$ at local extrema of the field. The study supported the hypothesis, within observational error. However, Whaler (1986) showed that using poloidal and toroidal flow components produced a slightly statistically better fit to the flow. As there are more free parameters available to fit SV, this is not surprising. I examine some of the issues associated with different flows fitting SV in Chapter 3.

Steady flows

Flow model non-uniqueness can be removed by assuming a steady flow over a period of time. First attempted by Gubbins (1982) using a toroidal flow for computational convenience, Voorhies & Backus (1985) showed that the solution of a steady flow is unique. Steady flow models are currently calculated by combining the normal equations for each SV epoch into one large system of equations of condition and solving for a single set of flow coefficients, with an appropriate level of damping to produce a 'reasonable' flow solution. These flows appear to capture the gross large scale aspects of SV but cannot explain short-term features, such as geomagnetic jerks (Courtillot & Le Mouël, 1984; Macmillan, 1996; Wardinski et al., 2008). Figure 2.6(c) shows an example of steady flow from ground-based observatory data for the epoch 1990.0.

Tangentially geostrophic flows

As noted in Section 2.1 (page 28), there is still uncertainty as to the balance between the Lorentz and Coriolis forces in the core. If a balance at the top of the core exists between the pressure gradient, Coriolis force and bouyancy, then this produces geostrophic flow behaviour, where flow is constrained not to cross the equator.

Independently proposed by Hills (1979) and Le Mouël (1984), tangential geostrophy is derived by constricting the allowable flows patterns. It reduces the non-uniqueness of the flow by imposing the following condition on the radial flow, $\nabla_H \cdot (\mathbf{u} \cos\theta) = 0$,

where θ is the co-latitude. Substitution into the induction equation gives:

$$\dot{B}_r + \cos\theta \mathbf{u} \cdot \nabla_H \ (B_r / \cos\theta) = 0 \tag{2.16}$$

Bloxham & Jackson (1991) show that ignoring the Lorentz force in a full treatment of the Navier-Stokes equation of the magnetohydrodynamic solution can be justified, confirming the validity of the geostrophic flow assumption. The non-uniqueness in flow models with a geostrophic constraint is less severe than toroidal-only flow models but does still contain patches where flow is ambiguous. In the geostrophic case, flow is only undetermined along contours of $B_r / \cos\theta$, which is typically 40% of the core surface (e.g. Pais et al., 2004). The imposition of a geostrophic flow can be achieved by damping the solution via the **D** matrix in the inversion (Jackson, 1997; Holme, 1998). Figure 2.6(d) shows an example of tangentially geostrophic flow from ground-based observatory data for the epoch 1990.0. Recently, Pais & Jault (2008) have proposed a constraint of quasi-geostrophic large-scale flow in the outer core.

Other flows conditions

Alternative flow constraints have been suggested. Both Davis & Whaler (1996) and Holme & Whaler (2001) examined a steady flow in a drifting frame of rotation, essentially adding one additional free parameter to the solution. This produced good results, allowing the solution to match the observed SV. Amit & Olson (2004) proposed solutions based upon constraining the helicity of the flow. This follows from the requirement of helical flow to generate the α effect in the geodynamo. This constraint links the flow to the radial vorticity, where $\zeta = \nabla \times \mathbf{u}$, using the condition:

$$\nabla_H \cdot \mathbf{u} = \mp k_0 \zeta \tag{2.17}$$

and flow components are calculated using $\nabla_H^2 S = \mp k_0 \, T$. k_0 is a constant to be chosen (based on magnetic observations). The sign is negative in the Northern hemisphere and positive in the Southern hemisphere. Combined with tangential geostrophy, Amit &

Olson (2004) prove that the flow is uniquely constrained everywhere. Amit & Olson (2004) used a numerical (as opposed to an analytical) solution to implement their flow constraints. Horncastle (2008) has recently implemented the technique in terms of a spectral analytical solution.

(a) Unconstrained Flow

(b) Toroidal-only Flow

(c) Steady Flow

(d) Geostrophic Flow

Figure 2.6: (a) Unconstrained (Toroidal and Poloidal) Flow for 1990, (b) Toroidal-only Flow for 1990, (c) Steady Flow for 1980-1990 and (d) Geostrophic flow for 1990.

Comparison of Constraints

From Figure 2.6 illustrates that although the constraints have different physical meanings and interpretations, all produce similiar answers. Models with similiar flow patterns are obtained despite the initial conditions or *a priori* assumptions, suggesting that the flows are governed by the damping and the data rather than the imposed contraints. All of these constraints assume that the 'frozen flux' hypothesis is correct. Even this approximation is only valid for a short time period, however. Doubts have been raised about the timescales over which the frozen flux hypothesis is valid, with Bloxham & Gubbins (1986) and Bloxham (1988) arguing that the conditions for the approximation are invalidated (i.e. the diffusion term becomes significant at large scales) after just an 11.5 year period. Love (1999) suggests that a simple inspection of the equations governing the flow in the light of dynamo kinematics shows the assumption is uncertain at best and incorrect at the worst. However, Holme & Olsen (2006) suggest that it may be impossible to test for frozen flux on short timescales.

Rau et al. (2000) inverted SV data generated from dynamo models to test how well flow inversion recovered the actual velocities and patterns. Their work suggested purely toroidal and geostrophic flows gave better correlation between the actual and recovered flow than the unconstrained (i.e. combined toroidal-poloidal) flows. Whaler & Holme (2007) characterised the uncertainties at the extrema points of B_r and compared the results from inversion to those expected from the induction equation, finding that the use of 'frozen-flux' is still valid for core flow modelling when uncertainties are taken into account. Despite the known shortcomings of the approximation, research still continues into the use of the geomagnetic main field to deduce flow maps, as it represents a practical and pragmatic approach.

The mathematical methods for treating SV data and creating 'smooth' flow models have been developed over the past few decades (Whaler & Gubbins, 1981; Bloxham, 1987; Walker & Jackson, 2000). The models have typically assumed that Gaussian noise is present in the measurements of the field and that the inversion methods for obtaining the flow models should use least-squares two-norm method (e.g. Bloxham et al., 1989).

However, growing empirical evidence (Walker & Jackson, 2000) indicates that the noise is more characteristic of a Laplacian (or double exponential) distribution. This has led in the case of Walker & Jackson (2000) to the introduction of one-norm inversions, to reduce the errors associated with fitting a field model to the observed data and to avoid arbitrary data rejection methods. Whaler et al. (2002) have adapted this method for flow modelling. I now present the method below.

2.4.3 One-Norm Iterative Inversion

Walker & Jackson (2000) provide the motivation to calculate the model by an iterative one-norm minimisation method instead of the standard two-norm method. In particular, they offer empirical evidence that the distribution of residuals from a historical magnetic dataset comprising vector, scalar and directional data is well-described by a Laplacian probability distribution. Note that Walker & Jackson (2000) modelled the magnetic field, not the flow, with data being for the main field rather than the SV observations. The formulation of the one-norm solution follows the method set out in their paper. In essence, the residual errors from the previous iteration are used to modify an additional diagonal matrix $\mathbf{R}$, whose elements are $R_{ii} = \sqrt{2}/|e_i|$, where e_i is the residual of the ith datum at the kth iteration. $\mathbf{R}$ is calculated at each iteration, hence the data are iteratively re-weighted, reducing the influence of outliers. The iterative one-norm solution can be written as:

$$\hat{\mathbf{m}}_{k+1} = (\mathbf{A}^T \mathbf{C}_e^{-1^T} \mathbf{R} \mathbf{C}_e^{-1} \mathbf{A} + \lambda \mathbf{D})^{-1} (\mathbf{A}^T \mathbf{C}_e^{-1^T} \mathbf{R} \mathbf{C}_e^{-1}\ \mathbf{d}) \tag{2.18}$$

The starting point for the iterative solution can be taken as $\mathbf{R} = \mathbf{I}$, the identity matrix. In that case, Equation 2.18 is equivalent to Equation 2.13 i.e. the two-norm solution. Figure 2.7 gives a summary of the algorithm, inputs and outputs. The solution typically converges within 10–15 iterations (see Chapter 3).

As an example of the improvement between the Two-Norm and the One-Norm models, a set of SV measurements from ground-based observatories for 1990.0 (from Wardinski & Holme (2006)) were inverted using both algorithms. The flow models cal-

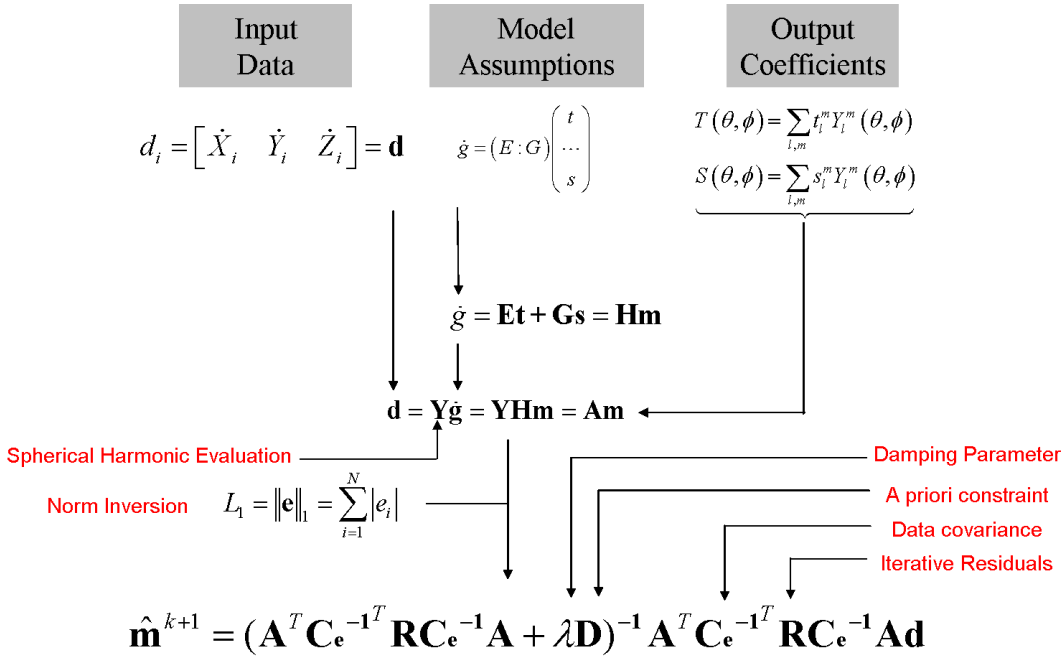

Figure 2.7: Summary of the One-Norm Iterative Algorithm.

culated by each method are shown in Figure 2.8(a) and (c). The residuals are calculated using the forward modelling of flow coefficients $\mathbf{R} = \mathbf{d} - \mathbf{A}\hat{\mathbf{m}}$ and plotted in histogram form. As can be seen, though the flow models are only slightly different, the histograms reveal that there has been a strong improvement in the fit of the models to the input SV data. Plotted on the histograms are the calculated fit to the data for a Gaussian and the Laplacian distribution. In the case of the Two-Norm histogram, Figure 2.8(b), the Laplacian (blue) curve has a better fit to the data distribution than the Gaussian (green) curve. The histogram of the residuals for the one-norm flow model 2.8(d) shows a strong peak about zero, indicating that the flow model better matches the *input* SV data. Again, the Laplacian curve better fits the distibution of the data than the Gaussian. The histogram also has fewer outlier points. From this evidence, one can state that the use of iterative one-norm method improves the fit of the model to the data compared to the two-norm, justifying the use of the Laplacian approach. Further exploration of the implementation and improvements based on the one-norm iterative algorithm will be shown in Chapter 3.

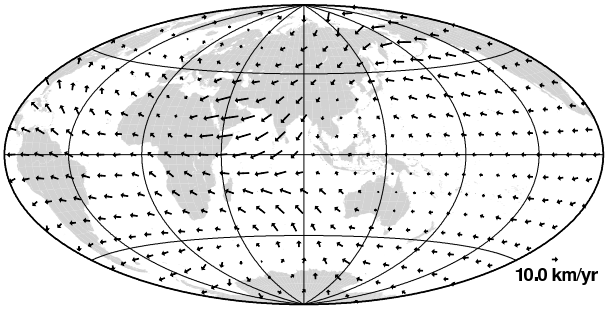

(a) Two-Norm Flow Model

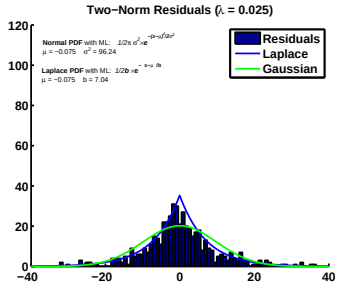

(b) Histogram of Residuals

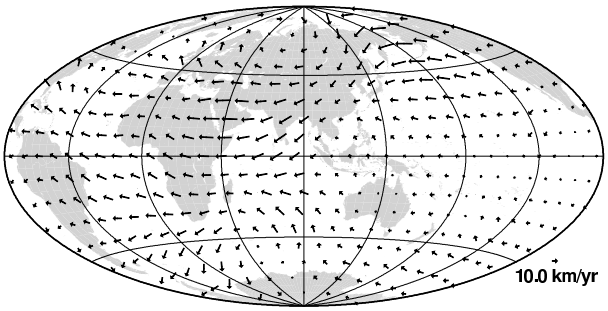

(c) One-Norm Flow Model

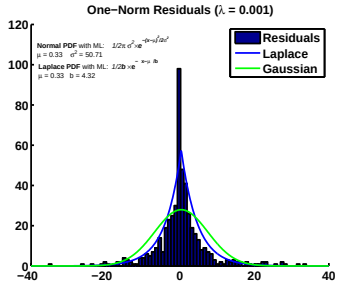

(d) Histogram of Residuals

Figure 2.8: (a) Unconstrained (Toroidal and Poloidal) Two-Norm Flow for 1990, (b) Histogram of Residuals, (c) Unconstrained One-Norm Flow for 1990 and (d) Histogram of Residuals. The damping parameter λ (shown in the title of each histogram) is adjusted to match the complexity (solution norm) of each model.

2.5 Core Flow Models and Length of Day

The length of day, defined by one full rotation of the Earth about its axis, is not fixed. Measurements show the period of the Earth's rotation is slowing by about 1.4ms/100yr, due to tidal drag from the Sun and the Moon (Stephenson & Morrison, 1990). Other factors affecting the rotation period are ocean circulation and atmospheric motion. When these factors are modelled and removed from the recorded length of day ($\triangle$LOD), there remains several milliseconds of change which is unaccounted over timescales of several decades. It was suspected that the excess angular momentum is due to exchange between the core and the mantle. Angular exchange could arise by three separate mechanisms *(a)* gravitational inhomogeneity, *(b)* topographic interaction on the CMB with the flow or *(c)* magnetic interaction with conductive lower mantle. Figure 2.9 illustrates the three potential mechanisms.

The core flow may impinge upon topography causing exchange of momentum. However, there is currently no conclusive evidence (seismic or modelled) for large ($>$ 5km) topographic features at the core-mantle boundary (Asari et al., 2006; Buffett & Christensen, 2007). A second mechanism might involve gravitational interaction between the inner core and large mass inhomogeneities in the mantle. Deformation of the inner core may be involved, though this is still uncertain (Dumberry, 2007). Finally, conductive material, for example, post-perovskite (Oganov & Ono, 2004) or subducted crust (Dobson & Brodholt, 2005) within the mantle at the core-mantle boundary may couple to the magnetic field causing exchange of momentum (e.g. Holme, 1998, 2000; Dumberry & Mound, 2008).

Jault et al. (1988) demonstrated that the core surface flows could be related to the change in the length of day through a simple formulation of two toroidal flow coefficients if the flow is tangentially geostrophic. This provided an independent way to verify the interaction of the core and mantle in the exchange of angular momentum to explain the decadal change in the length of day. They showed that the flow could be simplified

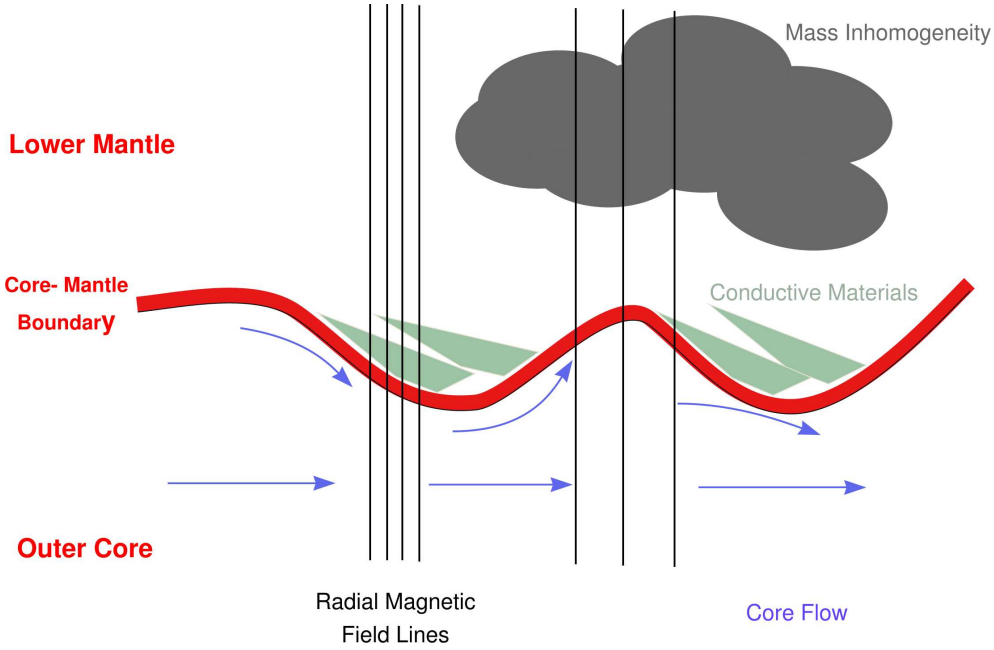

Figure 2.9: Schematic representation of the three types of possible core-mantle interaction for angular momentum exchange (topographical, gravitational and electromagnetic).

to calculate the exchange of core angular momentum ($\triangle\sigma_c$) by the folllowing formula:

$$\triangle\sigma_c = \frac{8\pi c\rho}{15}\left(\delta t_1^0 + \frac{12}{7}\delta t_3^0\right) \tag{2.19}$$

where c is the radius of the core, ρ is the mean density of the core and δt_1^0 and δt_3^0 are the toroidal flow coefficients measured in km/yr. The Jault et al. (1988) formula applies to tangentially geostrophic flows. Jackson (1997) provided further evidence from flows models over the period 1840–1990 that the decadal change in the length of day matched the change in the toroial components of the flow. Other studies have also used $\triangle$LOD to estimate the correlation of their modelled flows to the independent measure of angular exchange (Pais & Hulot, 2000; Holme & Whaler, 2001; Amit & Olson, 2006). Though the process of interaction between the core and the mantle remains to be correctly quantified, it appears to show that toroidal core flows can be independently verified, proving they represent some component of the large scale flow along the core-mantle boundary.

A major obstacle in the course of geomagnetic research has been the lack of high-resolution global data coverage. Many of the ambiguities are, hopefully, resolvable when sufficient data density becomes available. Better understanding of the global secular variation should allow improved core flow models to be developed. This can help identification and investigation of the problems discussed in the previous sections.

2.6 Entering the Satellite Era

Prior to the 1960's, study of the Earth's magnetic field had been confined to ground-based observatories and intermittant marine and land surveys. From the initial concerted efforts to continuously record the magnetic field in the 1830's, over 200 permanent observatories across the globe have been established, including over 100 observatories actively contributing to the INTERMAGNET project (Kerridge, 2001; Gubbins & Herrero-Bervera, 2007, see Rasson, pg 715). The project aims to create a worldwide network of digital magnetic observatories, with a set of defined standards and protocols for recording and disseminating the observed data.

Ground-based observatories provide high-quality time-series at a fixed point. Periodically, magnetic 'repeat' station surveys are undertaken, siting and re-occupying a larger network of points in a particular country or area. There is a large geographical bias in the global location of the observatories. In particular, a large number of observatories are sited in the northern hemisphere and Europe (over 40 permanent observatories), while the southern hemisphere and the Pacific regions have a paucity of observatories. The uneven coverage constrains the resolution for the main field and secular variation. One solution, discussed by Holme & Jackson (1997) was to deploy a set of ocean-bottom observatories, at optimal locations, which would minimise the large gaps and inherent spatial resolution of the ground-based observatory dataset.

Studying the global large-scale structure (>5000km) and evolution of the main field is incomplete using only the ground-based observatory dataset. Small scale crustal features (<100km, say) can be mapped in detail using aero-magnetic or ship-borne surveying equipment. However, the features of the intermediate scales prove more difficult

to quantify with either types of data. It is desirable to have a dataset which has high spatial and temporal resolution, to study phenomena related to length scales from both global and crustal sources of the Earth's field.

The advent of space-borne platforms for the study of the extra-terrestrial environment made such a proposition feasible. Sputnik 3 first collected scalar magnetic data in 1958, but as the tape-recorder on the satellite failed on launch, only data local to the receiver station were collected. A number of NASA satellite missions – collectively named the Polar Orbit Geophysical Observatory (POGO) – were launched in the period between 1962–1967. POGO-2, -4 and -6 of the satellites series carried scalar magnetometers and were placed into low-earth orbits (LEO) with altitudes varying from 400 - 1500km. Although these missions successfully characterised the large-scale scalar magnitude features of the Earth's main field, the measurements could not be used to uniquely resolve the vector components of the field (Backus, 1970). POGO-2 measurements were used to construct the first International Geomagnetic Reference Field (IGRF) for 1965 (Cain & Cain, 1971; Gubbins & Herrero-Bervera, 2007, Cain, pg 828). It must be noted that only recently has Lowes (2007) fully justified the assumption previously implied, that measurement of the magnetic field in the ionosphere using current instrument technology does not induce a bias.

In 1979, a dedicated magnetic observatory mission called MAGSAT was launched into a fixed dawn-dusk low earth sun-synchronous orbit (Langel & Hinze, 1998). It carried both a scalar and a vector magnetometer, becoming the first mission to include such an instrument. MAGSAT provided approximately six months of continuous data before orbital decay. In that period, detailed high resolution data for the main and crustal field were obtained. As the data covered a short period of time, it was still difficult to show the precise secular variation or secular acceleration that had occured during the mission (Langel & Estes, 1985). However, MAGSAT allowed extremely good models of the magnetic main field to be developed, giving confidence that the field at the core-mantle boundary could be adequately modelled and that ground based observatories could be used to accurately deduce the global field (Langel & Estes,

1982; Shure et al., 1985). It also provided an excellent dataset for comparison with future missions.

In the 1990's, several satellite missions were proposed to examine the main and crustal magnetic field in more detail. The first mission to be launched, in 1999, was developed and operated by the Danish Meteorological Institute in collaboration with a number of other Danish institutes (Neubert et al., 2001). Named in honour of the famous Danish physicist and chemist Hans Christian Ørsted (1777-1851), the satellite was inserted into an drifting polar LEO with an average altitude of approximately 800km. It carries a scalar and vector magnetometer on an 8m boom, to isolate the instruments from magnetic noise generated by the electronics within the chassis. The orientation of the vector measurements is calculated using a star camera fixed to the boom to estimate its pointing direction. Designed to operate for 14 months, the mission returned high quality vector data for many years until 2005. As of mid-2008 only the scalar magnetometer is producing reliable information (N. Olsen, pers. comm.). Hulot et al. (2002) derived a field model from the satellite data to produce a high resolution comparison between the field model from 1980 derived from MAGSAT measurements and the Ørsted measurements.

The CHAMP satellite, a collaborative effort between the GFZ Postdam and the DLR (German National Space Agency), was launched in 2000. It is a multi-purpose mission designed to study both the gravitational, electric and magnetic fields, with both a scalar and vector magnetometer on an extended boom (Reigber et al., 2002; Lühr et al., 2002). CHAMP was inserted into a lower orbit than Ørsted (average altitude is approximately 400km). With two star cameras, the orientation of the vector measurements are better constrained than those of Ørsted. The lower orbit allows finer resolution of small scale crustal features. The satellite orbit has been slowly decaying over time and is currently scheduled to de-orbit in late-2009. As the orbit decays, the satellite's lower altitude will improve the ability to resolve smaller crustal scales.

The CHAMP satellite samples the field at 1Hz, giving over 86,000 measurements and completing over 14 orbits per day. The satellite drifts approximately 2.5 hours in

local time each month. The GFZ make available several Level-2 magnetic data products, which have been correctly orientated into the North-East-Down reference frame (Figure 1.4). Several main field models have been derived from these data including GRIMM (Lesur et al., 2008b), POMME (Maus et al., 2005a, 2006) and CHAOS (Olsen et al., 2006b), while the data have been incorporated in the most recent IGRF (Macmillan & Maus, 2005) and Comprehensive Models (Sabaka et al., 2004). As a longer time-series of data become available, the estimate of secular variation and secular acceleration has improved (Olsen & Mandea, 2007, 2008; Lesur et al., 2008b). The CHAMP data have also been used to produce models of the crustal field (Maus et al., 2007) and ocean M2 lunar tides (Tyler et al., 2003).

The 'Decade of Geopotential' Research (1999-2009) which was inaugurated with the launch of Ørsted has been an international effort to provide continuous monitoring of the magnetic (and gravity) field of the near-Earth. The next generation of low earth orbiting magnetic satellites (known as Swarm) should launch in 2010. Knowledge of the crustal field in particular should improve through the use of the innovative three satellite cluster, by measuring both the field and the gradient of the field (Olsen et al., 2006a, 2007).

2.7 Magnetic Field Forecasting

As explained at start of the chapter, an aim of this project is to produce a method for forecasting the change in the shape and the strength of the main field for input to future versions of global models. Estimates of the starting error (i.e. the root-mean-square difference between the 'true' field and models such as CHAMP) suggest that all satellite era models lie within 10nT of the 'actual' field. Note, these estimates are based upon comparisons between differing field models themselves. Philosophically speaking, of course, none of the models are truly 'correct'. Establishing a baseline starting point for prediction is a logical requirement, but evaluation of the goodness of fit of any forecast (or hindcast) to a model will be dependent upon the model itself. In some sense, the problem becomes convoluted - how can the forecast be validated when the

correct start and end points are unknown?

Current forecasting practice is to use linear extrapolation of the change of the spherical harmonic coefficients from previous IGRF models forward in time. This approach tends to be quite in error by the end of the five year period for the validity of the IGRF model (see Figure 2.10). Maus et al. (2005b) suggests that models can be in error by over 100nT (root mean square difference). Much of the error is due to model misfit in the polar regions, particularly near the magnetic poles. By applying a physically-based approach to the forecasting of secular variation, it is hoped that a strong reduction can be achieved in the size of the misfit error. As already observed, core flow models are an example of a physical constraint on secular variation.

I seek to employ core flow models to generate forecasts for secular variation over a short (< 5 years) time span. Core flows generate secular variation by advection and, in this study, diffusion processes are ignored. Initial work by Maus et al. (2008) has examined several types of flow regime incorporating complex estimates of secular variation and acceleration for use in hindcasting. They concluded, paradoxically, that simple steady flows over time represented the best fit to the observed field. The reason for this conclusion was due to geomagnetic jerks - the so-far unexplained changes in secular acceleration of the flow (Courtillot & Le Mouël, 1984) - causing the flow acceleration to average to zero over several decades.

In summary, much new work has been initiated by the international effort through the Decade for Geopotential Research. The availablity of excellent satellite data and modern computing power have allowed the development of high quaility magnetic field models. I will exploit these new datasets to determine flow models for the core-mantle boundary. However, firstly I examine the assumptions and methods used to generate core flow models using ground-based observatory data, before proceeding to the modelling of the flow using satellite data.

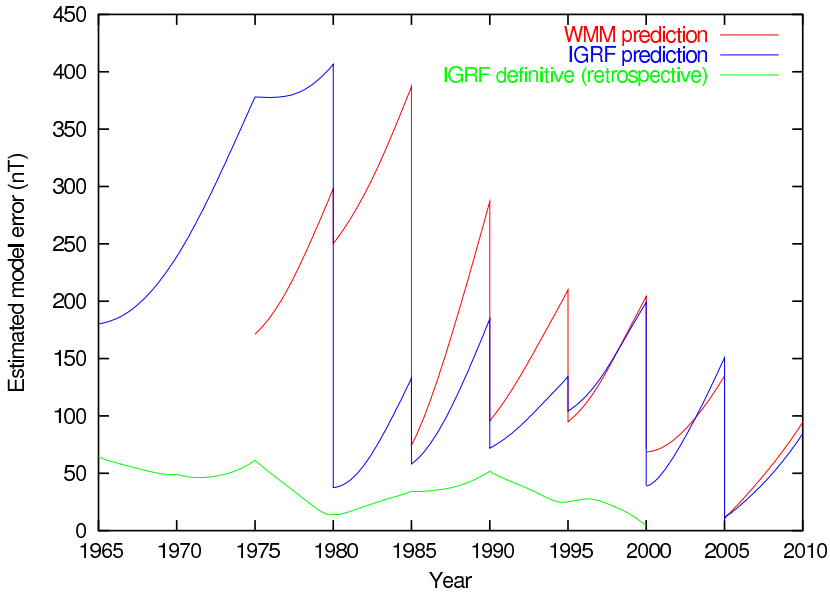

Figure 2.10: Estimate of the root-mean-square degree misfit of the models with IGRF10 model, from Maus et al. (2008).

Chapter 3

Core Flow Modelling Assumptions

3.1 Overview

Modelling of core flows at the core-mantle boundary from secular variation is a highly under-parameterised problem, which requires a range of both physical and mathematical assumptions and assertions. These typically include the frozen flux hypothesis and the imposition of specific flow regimes, outlined in Chapter 2. In this chapter, I explore the effects of several different assumptions and constraints on the inverted flow models and the fit of the flow models to the input data. This gives an insight into the best inversion techniques and constraints to use. It also highlights certain limitations on the fidelity of such flow inversions and illustrates that care must be exercised in the choice of modelling strategy adopted.

In Chapter 2 it was shown how flow can be calculated directly from the time derivatives of X, Y and Z components of ground-based observatories (rather than Gauss coefficients of the secular variation as commonly used in other studies). I adopt a Laplacian probability for the distribution of errors within the core flow solution, allowing the L_1 iterative one-norm minimisation method to be applied to the inverse formulation of the problem.

However, other considerations affect the solution, including *(a)* the assignment of observation errors through the data covariance matrix, *(b)* the *a priori* constraints placed upon the solution and *(c)* the type of flow regime assumed to be present in the core. This chapter examines the results of comparisons between combined and toroidal-only flows to model the observed SV, using the one-norm minimisation inversion technique, initially imposing a minimum global root-mean-square (RMS) flow velocity constraint. Poloidal-only flows were also examined, for completeness, throwing up a number of interesting results which I will elucidate upon below. Further, the competing effects of the various assumptions to control the final flow model are highlighted. These assumptions are investigated using four SV datasets to separate the effects of each set of assumptions.

Acknowledgements

This chapter is based upon some of the work for a paper published in *Physics of the Earth and Planetary Interiors* by myself and Kathy Whaler (Beggan & Whaler, 2008). Kathy was the original developer for much of the inversion code used (with some code from D. Gubbins, J. Bloxham, R. Holme and A. Jackson), though I have rewritten it all into MATLAB, streamlined and updated most of the FORTRAN programs and functions. Kathy has also given guidance on experiments to carry out and many suggestions on writing and improving the paper. Dave Gubbins' review prompted some additional work not shown in the original paper, now presented here. Richard Holme has pointed out an inconsistency in the use of covariance-corrected data (explained later) which warranted re-calculation and plotting of various datasets and flow models.

3.2 Examining Flow Constraints

As can be recalled from the previous chapter, flows allowing both toroidal and poloidal coefficients without additional conditions are known as unconstrained flows. Imposing constraints removes some of the flow ambiguity. As noted, in contrast to most other

studies, SV from observatory data are directly inverted – rather than spherical harmonic model coefficients – to calculate flow model coefficients. This allows a more rigorous test of flow assumptions made and incorporation of realistic data uncertainties. The inversion method is quickly summarised before examining the datasets used in the study.

As discussed in Chapter 2, the iterative L_1 inversion algorithm can be written as:

$$\hat{\mathbf{m}}_{k+1} = (\mathbf{A}^T \mathbf{C}_e^{-1^T} \mathbf{R} \mathbf{C}_e^{-1} \mathbf{A} + \lambda \mathbf{D})^{-1} (\mathbf{A}^T \mathbf{C}_e^{-1^T} \mathbf{R} \mathbf{C}_e^{-1}\ \mathbf{d}) \tag{3.1}$$

where $\mathbf{m}$ are the desired flow model coefficients. (See Section 2.4.3 and Figure 2.7 for a summary of the notation, algorithm, inputs and outputs.) The starting point for the iterative solution is the two-norm solution obtained in a single step when $\mathbf{R} = \mathbf{I}$. Figure 2.7 gives a summary of the algorithm, inputs and outputs.

In this chapter, I examine two formulations of the *a priori* constraint matrix, $\mathbf{D}$. Both constraints minimise quadratic norms of the flow. Firstly, the 'strong norm' of Bloxham (1988) minimises a global measure of the flow complexity:

$$\begin{aligned} D_{BSN} &= \oint_{CMB} \left[\left(\nabla_h^2 u_\theta \right)^2 + \left(\nabla_h^2 u_\phi \right)^2 \right] dS = \\ &= 4\pi \sum_l \frac{l(l+1)^3}{2l+1} \sum_{m=0}^{l} (t_l^m)^2 + (s_l^m)^2 \end{aligned} \tag{3.2}$$

This 'norm' results in a smooth, large-scale flow by heavily damping (or penalising) the high degree coefficients, as the damping is proportional to l^3.

An alternative approach is to minimise the core-mantle boundary RMS SV ($\dot{B}_r^2$) coefficients. This is typically applied when undertaking regularised inversion for SV coefficients (Gubbins, 1983), but can also be used for flow modelling (Whaler, 1986). Let a be the Earth's radius, c the radius at core-mantle boundary and with $\{\dot{g}_l^m, \dot{h}_l^m\}$

as the Gauss coefficients of the SV of the main field, this norm can be defined as:

$$D_{SV} = \oint_{CMB} \dot{B}_r^2 d\Omega = 4\pi \sum_l \left(\frac{a}{c}\right)^{2l+4} \frac{(l+2)^2}{2l+1} \sum_{m=0}^{l} (\dot{g}_l^m + \dot{h}_l^m)^2 \tag{3.3}$$

Equation 3.2 takes the form of a diagonal matrix with elements $l(l+3)^3/(2l+1)$. Equation 3.3 must be combined with Equation 3.2 in order to produce viable solutions due to computational issues. (i.e. the matrix would be poorly conditioned otherwise).

3.3 Observatory Data

The annual SV (or yearly change) at an observatory for *month(t)* is the difference between the average field (generally calculated from the five quiestest days of the month) in *month(t-6)* and *month(t+6)* for the North (X), East (Y) and Downward (Z) components.

$$SV_{month}(t) = Field_{month}(t+6) - Field_{month}(t-6) \tag{3.4}$$

This approach removes both the crustal field component of the signal and the annual variation, without any direct filtering or averaging, giving the $\dot{X}$, $\dot{Y}$ and $\dot{Z}$ vector components of the field. For this chapter, four SV datasets were considered, all consisting of $\dot{X}$, $\dot{Y}$ and $\dot{Z}$ data.

1. The initial dataset, termed Dataset 1, was derived from annual means recorded at 172 ground-based observatories for the year 1990.0 (see Figure 3.1). The SV is estimated over 12 months from July 1989 to June 1990. This assumes that there is little or no secular acceleration relative to the size of the SV. Observation errors were nominally assumed fixed at 1 nT/yr for all stations and components. This dataset provides a baseline to test how a naïve error assignment affects flow inversion.

2. The second dataset, termed Dataset 2, consists of SV estimates from 176 observatories for 1990.0 (Ingo Wardinksi, pers comm). This dataset is used to explore how errors which are anisotropic (not equal in all directions) and inaccurate (but

perhaps 'close' to the true estimate in some manner) can affect the flow modelling solution. Observation errors in each direction are taken from estimates made by fitting a field model through a time series of data from 1980–2000 and calculating the covariance of misfit at each observatory to the model. This results in error estimates for three principal component directions at the observatory. However, the principal component directions are not neccesarily aligned to the X, Y and Z directions. Hence, the error estimates for this dataset are mostly arbitrary, though the $\dot{Y}$ direction often coincides with the least noisy component direction.

3. As ground-based observatories are unevenly geographically distributed, a third evenly globally distributed synthetic SV data set was created, consisting of 288 points on the globe separated by 15° intervals in latitude and longitude. Dataset 3 was generated from the IGRF10 spherical harmonic model for the epoch 1990.0. In a manner similar to Dataset 1, the associated observation errors for Dataset 3 were also fixed at a nominal 1 nT/yr. This dataset tests whether the inhomogeneous global distribution of ground-based observatories strongly affects the flow modelling results from SV inversion.

4. The final dataset, termed Dataset 4, consists of SV from 162 ground-based observatories (Wardinski, pers. comm. 2009) for 1990.0, but with a further correction applied to remove internal covariance within the data (Wardinski & Holme, 2006). The associated observation error for each component was estimated by fitting a field model through a time series of data from 1980–2000 and estimating the covariance of misfit to the model at each observatory. The eigenvalues and eigenvectors for each observatory were supplied along with the SV data in the X, Y and Z directions. The eigenvalues ($\mathfrak{d}_i$) and eigenvectors ($\mathfrak{b}_i$) are multiplied in a diadic manner to produce the 3×3 covariance matrix for each observatory (Holme & Bloxham, 1996):

$$\mathbf{C}_e = \sum_i \mathfrak{d}_i \mathfrak{b}_i \mathfrak{b}_i^T \tag{3.5}$$

The inverse of the covariance matrix is placed into a block diagonal matrix $\mathbf{C}_e^{-1}$.

This is then used in the inversion equation (3.1).

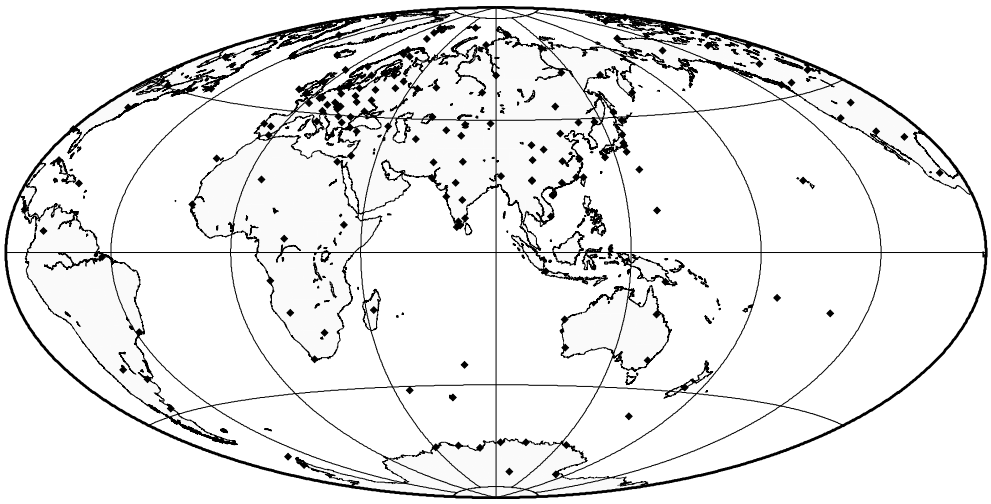

Figure 3.1: Locations (Diamonds) of the 176 observatories used in Dataset 2.

To perform the inversion, the GUFM1 field model (Jackson et al., 2000) provided the main field coefficients for the Gaunt and Elsasser (i.e. **H**) matrices. Calculating the toroidal- or poloidal-only parts of the flow requires omission of either the Elsasser or Gaunt matrix in the formulation of **H** and solving for the desired toroidal or poloidal coefficients respectively. The residual errors for the first iteration of the one-norm solution are obtained from an initial starting model calculated from a two-norm solution of the input data. The value of very small ($< 10^{-4}$) error residuals in the matrix **R** are set to 10^{-4} to prevent the formation of ill-conditioned matrices, as advocated by Walker & Jackson (2000). No other nonuniqueness constraints were imposed on the solution. Typically, 15 iterations ensure convergence of the solution. Models of the main field, SV and flow were calculated up to degree and order $l = 14$. Figure 3.2 shows examples of the convergence of the solution norm and RMS velocity.

3.4 Comparison of Flow Models

As discussed in Section 2.4.1, previous assumptions about the form of fluid motion on the surface of the core-mantle boundary have generally not invoked the case for poloidal-

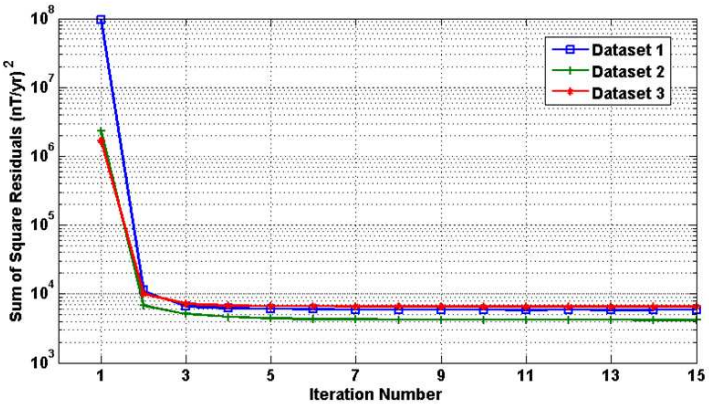

(a) Solution Norm

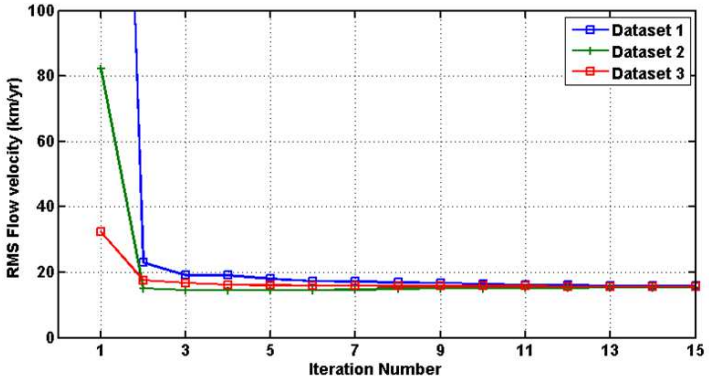

(b) RMS Veloicty Norm

Figure 3.2: Example iteration metrics for One-Norm algorithm showing convergence of (a) the Solution norm and (b) Root Mean Square velocity metrics for Datasets 1, 2 and 3. The models typically converge within 15 iterations.

only flow regimes. There are a number of strong arguments against such flows, including the assumed dominance of geostrophic flow (Bloxham & Jackson, 1991), the case for a stably stratified layer at the CMB which imposes toroidal-only flow (Whaler, 1980; Gubbins et al., 1982) and the breaking of the frozen flux assumption (Gubbins, 2007). However, it is recognised that although toroidal-only flows fit the data adequately, overall they do not fit well enough. A small poloidal component in the flow increases the number of degrees of freedom, but makes a statistically significant improvement to the data fit (Whaler, 1986).

Typically, the ratio of the energy of the toroidal to poloidal flow within a combined flow regime averages at approximately 0.85, under the model assumptions from Section 2.4.1 (also see Bloxham (1989)). An analysis of the individual contribution of each flow coefficient shows that, though most of the flow energy is in the toroidal coefficients, part of it is in the low degree and order coefficients of the poloidal flow, even though overall the total poloidal flow energy is relatively small.

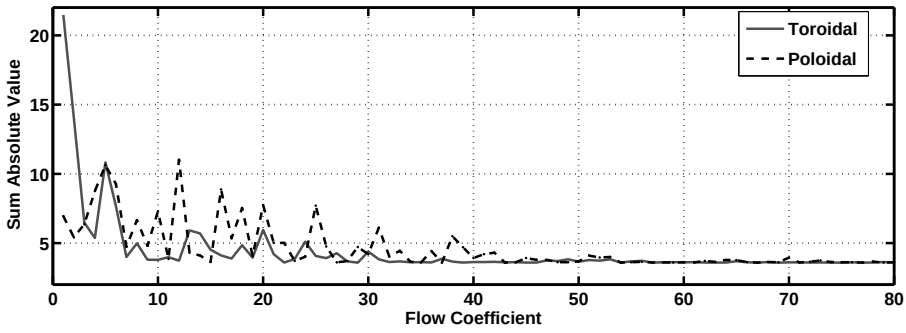

Figure 3.3: The sum of the absolute values (SAV) of the residual when each coefficient indicated is not included in the toroidal-poloidal flow solution from Dataset 3. When all 448 coefficients are present, the SAV is 3.59. Coefficients are ordered t_1^0, t_1^{1c}, t_1^{1s}, t_2^0, t_2^{1c}, etc.

Figure 3.3 shows the sum of the absolute values (SAV) of the residual errors from a one-norm solution in which an individual flow coefficient has been removed from the model vector and the resulting difference between the forward model predictions and the observed data calculated. Coefficients are ordered t_1^0, t_1^{1c}, t_1^{1s}, t_2^0, etc, with the superscripts c and s denoting coefficients multiplying $\cos m\phi$ and $\sin m\phi$ respectively

(See Table 3.1).

Flow Coefficient	Degree	Order	Flow Coefficient	Degree	Order
1	1	0	9	3	0
2	1	1s	10	3	1s
3	1	1c	11	3	1c
4	2	0	12	3	2s
5	2	1s	13	3	2c
6	2	1c	14	3	3s
7	2	2s	15	3	3c
8	2	2c	16	4	0

Table 3.1: Ordering of the first sixteen flow coefficients in Figure 3.3.

With all 448 flow coefficients present, for a particular solution norm the SAV is 3.59. A higher value thus indicates a worse fit to the data. It can be seen from Figure 3.3 that excluding individual coefficients lower than degree and order 7 has the largest effect on the solution, demonstrating that the flow has converged above degree and order 8. It also shows that some of the low degree and order poloidal terms contribute significantly to the data fit. For example, solutions without s_3^{1c} (poloidal coefficient 12) fit worse than solutions without t_2^0 (toroidal coefficient 4). This observation motivated the comparison of three different flow types (i.e. combined, toroidal- and poloidal-only).

Bloxham 'Strong' Norm Minimisation

I computed flow models for each of the four datasets, altering the value of λ to produce models with root-mean-square flow velocities of approximately 16 km/yr. Using the 'strong' norm, initially I compared the residual difference between the observed SV and the SV produced by the flow model ($e_i = d_i - A_{ij}m_j$). The relative 'fit' of the flow models to the observed data can be measured via the one-norm (L_1) and two-norm (L_2) measures of the error residuals defined (where i is the number of observations) as:

$$L_1 = \sum_{i=1}^{N} |e_i| \quad \text{and} \quad L_2 = \sqrt{\sum_{i=1}^{N} (e_i)^2} \tag{3.6}$$

The normalised misfit of the model to the data (called χ) is calculated by:

$$\chi = \sqrt{\frac{(\mathbf{d} - \mathbf{A}\hat{\mathbf{m}})\mathbf{C}_e^{-1}(\mathbf{d} - \mathbf{A}\hat{\mathbf{m}})}{N}} \tag{3.7}$$

where N is the total number of data (i.e. three times the number of observatories). Figure 3.4 illustrates models of the three different flow types calculated from Dataset 4. The accompanying histograms (in Figure 3.5) show the residual difference between the flow model prediction of the SV at each observatory and the actual data recorded. As can be seen, the histograms have a distinctly Laplacian distribution (rather than Gaussian, say).

The results from experiments where the *a priori* constraint is the minimisation of the 'strong' velocity norm (Equation 3.2) are summarised in Table 3.2. Note that the solution norm (also Equation 3.2) – controlled via the damping parameter λ – of *all* the models has been set to $1.4 \times 10^5 (\mathrm{km/yr})^2$. This corresponds to equalising the 'roughness' of the combined, toroidal- and poloidal-only flows for each dataset, making the three flow regimes directly comparable. This value of the solution norm was chosen to produce a flow solution with a 'reasonable' root-mean-square velocity of approximately 16 km/yr for the combined toroidal-poloidal model and a normalised misfit $\chi \approx 1$ for Datset 4. The 'fit' of the flow models to the observed data can be examined via the one-norm, two-norm measures of the error residuals and the normalised misfit.

The results from Datasets 2, 3 and 4 indicate that the combined toroidal-poloidal flow model has a far better fit to the observatory data than a toroidal-only or poloidal-only solution. Surprisingly, in Datasets 1 and 4, the poloidal-only flow model has a smaller one-norm value than the toroidal-only model. For Datasets 2 and 3, the toroidal-only flow model does fit the observations better than the poloidal-only model, but not by a large amount. However, the normalised data misfit for both Dataset 1 and 3 is very large. The combined toroidal-poloidal flow model produced from Dataset 4 has the lowest spread of residuals, thus giving the best overall fit. There is thus a relative improvement from the use of the Wardinski & Holme (2006) technique. In

all cases, the root-mean-square velocity of the toroidal-only flow models is slightly slower than the combined toroidal-poloidal flow models, while the poloidal-only flow is significantly slower at an average of about 7.2km/yr. Surprisingly, these slower flow speeds for poloidal-only models do produce an adequate fit to the input SV data.

The final column shows the root-mean-square SV calculated at the core-mantle boundary in units of 10^6 $(\mathrm{nT/yr})^2$. Magnetic field models such as IGRF10 (Macmillan & Maus, 2005) and CHAOS (Olsen et al., 2006b) predict values in the range $60-70\times10^6$ $(\mathrm{nT/yr})^2$. For comparison, the models from Table 3.2 behave in a similar manner, generating SV values between 50 and 209×10^6 $(\mathrm{nT/yr})^2$ for velocity norms of 1.4×10^5 $(\mathrm{km/yr})^2$. From inspection of Table 3.2, it appears that the toroidal-only flow and

Data	**Model**	**One-Norm**	**Two-Norm**	**Misfit**	**RMS Vel.**	**RMS SV**
1	TorPol	4110	$3.8\cdot10^5$	27.1	15.4	165
	Tor	6858	$4.5\cdot10^5$	29.6	12.2	97.8
	Pol	6405	$4.9\cdot10^5$	30.9	7.1	44.2
2	TorPol	364	734	1.18	16.06	176
	Tor	827	2935	2.36	13.9	125
	Pol	866	4725	2.99	8.2	56.9
3	TorPol	3213	$4\cdot10^4$	6.8	15.4	172
	Tor	9137	$1.9\cdot10^5$	14.4	11.9	86.3
	Pol	9871	$3.2\cdot10^5$	19.2	6.9	41.9
4	TorPol	520	1807	1.01	17.1	209
	Tor	1177	8968	2.46	12.2	100
	Pol	1159	10215	2.76	6.7	50.8

Table 3.2: Fit of flow models to observatory SV data using the *a priori* constraint to minimise the strong velocity norm. The solution norm of each model is $1.4\times10^5(\mathrm{km/yr})^2$. One-Norm, Two-Norm are in nT/yr. RMS Velocity is in units of km/yr. RMS CMB SV is in units of 10^6 $(\mathrm{nT/yr})^2$.

the poloidal-only flow maintain an equally good fit to the observatory data, based on the one-norm, two-norm and misfit measures. However, comparison of the histograms for Dataset 4 in Figure 3.5 *(b)* and *(c)* indicates that the poloidal-only flow model is actually more strongly peaked about zero than the toroidal flow model. On the other hand, the poloidal-only model has a larger spread of residual values leading to heavier tails than the toroidal-only flow model residuals. The flow patterns of the toroidal-only

flow model are broadly similar to the combined toroidal-poloidal model. The poloidal-only model has few visible similarities to the full combined model or the poloidal part of the combined flow. Analysis of the geographical distribution of the residuals for the combined flow reveals that the largest errors are from the fit to the $\dot{X}$ component of the observatory data, concentrated in the southern regions of Asia and Europe. Surprisingly, the error in the southern hemisphere for all four models is small. This can perhaps be explained by the relative paucity of data available in this region, where the flow can adjust more easily. The geographical distribution of the residuals in the $\dot{X}$, $\dot{Y}$ and $\dot{Z}$ components for Dataset 4 are shown in Figure 3.6.

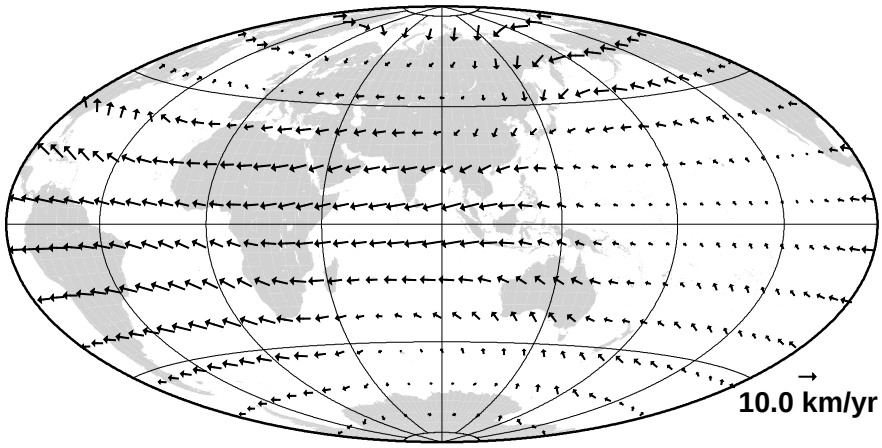

(a) Toroidal-Poloidal Flow Model

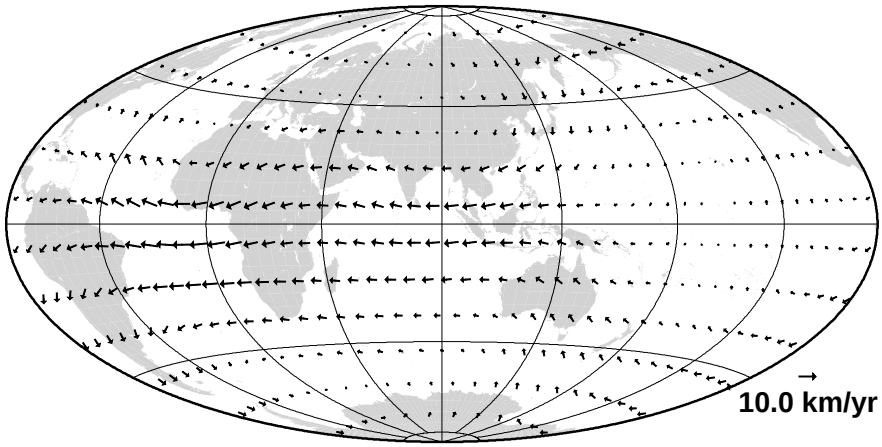

(b) Toroidal Flow Model

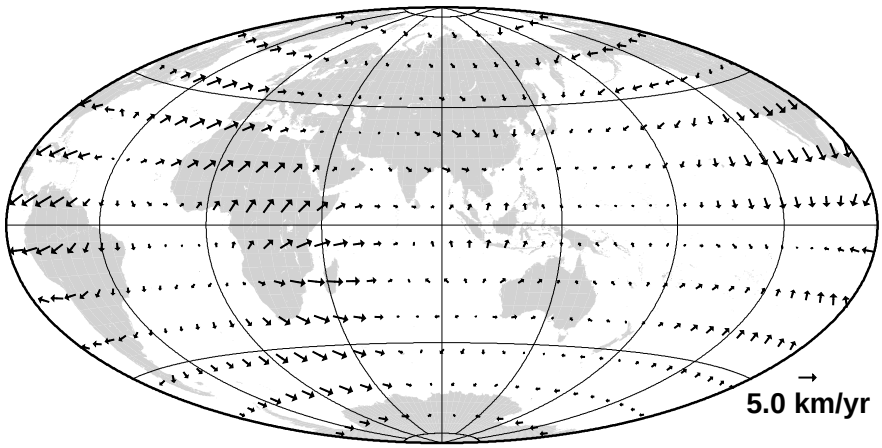

(c) Poloidal Flow Model

Figure 3.4: Core-mantle boundary flow models for Dataset 4 with the 'strong' velocity norm constraint applied. Continents shown for reference.

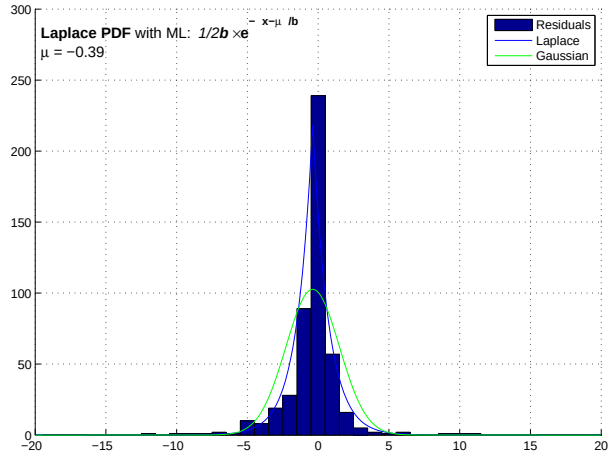

(a) Histogram of Flow Model Data Residuals

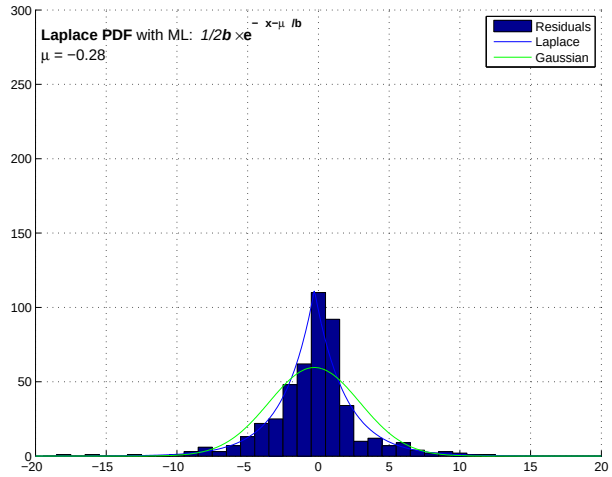

(b) Histogram of Flow Model Data Residuals

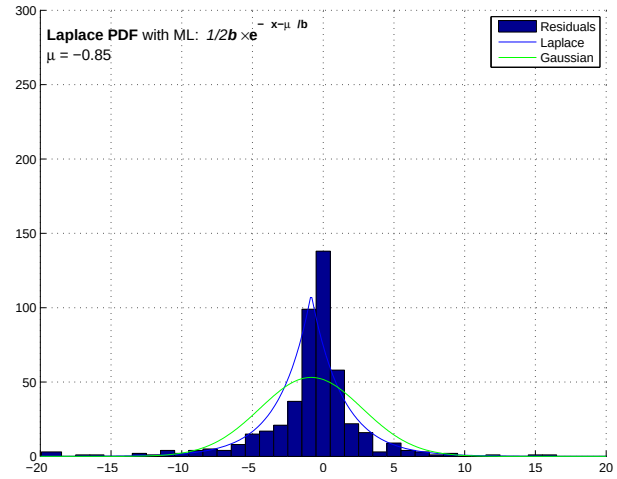

(c) Histogram of Flow Model Data Residuals

Figure 3.5: Histograms of residuals from the fit of core-mantle boundary flow models to observatory data for Dataset 4 with the 'strong' velocity norm constraint applied.

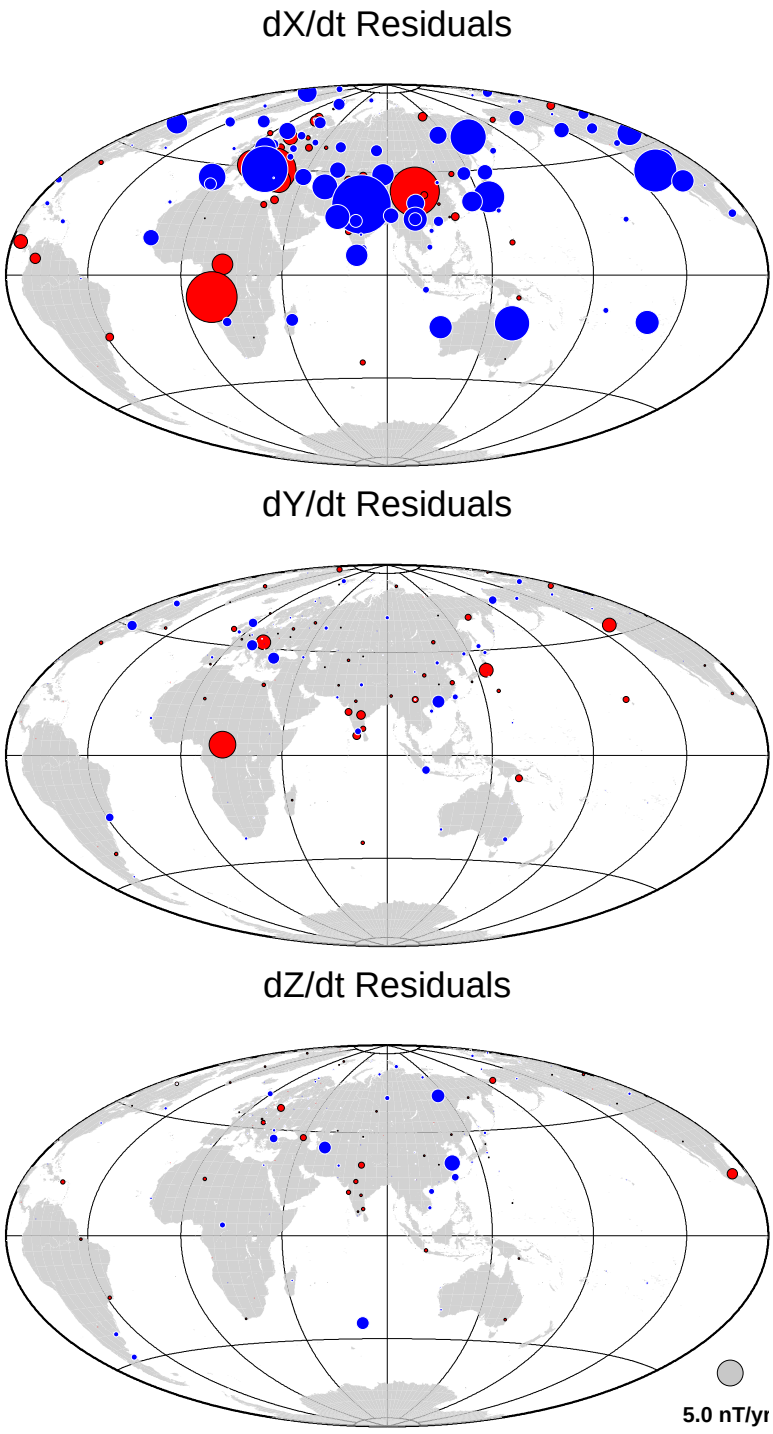

Figure 3.6: Residual distributions for Dataset 4 using the 'strong' velocity norm constraint. Colour indicates sign - red is positive, blue is negative. Circle indicates residual size. Continents shown for reference.

Secular Variation Norm Minimisation

The second set of experiments applied the *a priori* constraint of minimising the CMB RMS SV predicted by the model solutions. Due to numerical instability, minimisation using the norm from Equation 3.3 cannot be undertaken directly. Following Whaler (1986) I also added a flow constraint, but with a very small damping parameter, μ, typically two orders of magnitude smaller than the SV constraint damping parameter. This results in a slight change to the model (Equation 3.1):

$$\hat{\mathbf{m}}_{k+1} = (\mathbf{A}^T \mathbf{C}_e^{-1^T} \mathbf{R} \mathbf{C}_e^{-1} \mathbf{A} + \lambda \mathbf{D}_{SV} + \mu \mathbf{D}_s)^{-1} (\mathbf{A}^T \mathbf{C}_e^{-1^T} \mathbf{R} \mathbf{C}_e^{-1}\ \mathbf{d}) \tag{3.8}$$

The flow models from the three datasets were calculated in the same manner as previously, altering the values of μ and λ until the velocity norms are equal. Table 3.3 summarises the results. The velocity norm has been set to 7.4×10^6 (km/yr)^2 to achieve a RMS velocity of approximately 16 km/yr (for the combined toroidal-poloidal flow) and a normalised misfit of $\chi \approx 1$ for Dataset 4. The misfit and RMS velocity metrics of the solutions from the combined toroidal-poloidal flows are comparable to those in Table 3.2 where the one-norm and two-norm measures are approximately equal, but this requires a much larger solution norm. However, the toroidal-only and poloidal-only flows are significantly poorer than the solutions calculated with the strong velocity norm constraint. Furthermore, the flow patterns and residual distributions in Figures 3.7 and 3.8 reveal that the solutions are markedly different from those in Figure 3.4 3.5.

The results from increasing the damping via λ (and μ) to set the strong velocity norm equal to 1.4×10^5 (km/yr)^2 (i.e. comparable to the value in Table 3.2) are shown in Table 3.4. This produces extremely poorly fitting solutions when compared to both Tables 3.2 and 3.3. The flows generated using the strong velocity norm constraint converge around degree 8 (see Figure 3.9). In contrast, the flows generated from the RMS SV constraint have no significant power in any particularly dominant degree - their spectra are quite shallow (Figure 3.10).

The last column in Tables 3.3 and 3.4 gives the RMS SV generated on the CMB for each model. As can be seen in Table 3.3, combined toroidal-poloidal flows generate only slightly higher SV than in Table 3.2 for a similar RMS velocity. In contrast, the SV generated by toroidal and poloidal-only flows is minuscule. For the models in Table 3.4, the SV generated is orders of magnitude smaller. This is due to the extremely slow flow velocities, again reflecting the fact that the models are not vigorous enough to fit the data well, even though they are complex (as reflected by their strong velocity norm value).

Allowing the toroidal- or poloidal-only models in Tables 3.3 and 3.4 to become more realistic and complex (by reducing the damping parameters) generates SV values similar to Whaler (1986) and the standard magnetic field models. For the toroidal- and poloidal-only flows, the strong velocity norm rises to $\mathcal{O}(10^7)$, indicating the increased complexity of the flow. Thus, when using the SV norm (Equation 3.3), simple flows (as measured using the strong velocity norm) fit the data poorly, while very complex toroidal- or poloidal-only flows are needed to generate a realistic amount of CMB SV and give a better fit to observations.

Data	Model	One-Norm	Two-Norm	Misfit	RMS Vel.	RMS SV
1	Tor+Pol	3833	$3.7 \cdot 10^5$	26	18.0	324
	Tor	21931	$7.4 \cdot 10^5$	38	5.8	0.03
	Pol	21099	$6.9 \cdot 10^5$	26	6.1	0.05
2	Tor+Pol	319	625	1.1	18.6	300
	Tor	1689	13344	5.0	5.8	0.07
	Pol	1828	14780	5.3	6.6	0.01
3	Tor+Pol	2524	$4.4 \cdot 10^5$	7.1	17.9	175
	Tor	21931	$1.1 \cdot 10^6$	35	5.3	0.03
	Pol	21099	$1.1 \cdot 10^6$	34	5.8	0.05
4	Tor+Pol	542	2074	1.05	19.9	231
	Tor	1844	16415	5.1	6.1	0.14
	Pol	2033	19297	5.6	6.3	0.06

Table 3.3: Fit of flow models to observatory SV data using an *a priori* constraint to minimise the Root-Mean-Square Secular Variation over the CMB. The solution norm of each model is 7.4×10^6 $(\mathrm{km/yr})^2$. Other units as for Table 3.2.

Data	Model	One-Norm	Two-Norm	Misfit	RMS Vel.	RMS SV
1	Tor+Pol	8634	$5.7 \cdot 10^5$	33	3.0	0.79
	Tor	13641	$8.9 \cdot 10^5$	41	0.8	0.003
	Pol	13472	$8.8 \cdot 10^5$	41	0.8	0.006
2	Tor+Pol	1256	7997	3.9	2.6	0.76
	Tor	1944	16475	5.6	0.7	0.001
	Pol	1949	16510	5.6	0.8	0.001
3	Tor+Pol	17729	$7.5 \cdot 10^5$	33	2.3	0.22
	Tor	23975	$1.3 \cdot 10^6$	41	0.7	0.03
	Pol	23818	$1.3 \cdot 10^6$	41	0.8	0.05
4	Tor+Pol	1353	8652	3.2	3.3	1.6
	Tor	2012	18591	6.2	0.8	0.0004
	Pol	2019	18752	6.2	0.9	0.002

Table 3.4: Fit of flow models to observatory SV data using an *a priori* constraint to minimise the Root-Mean-Square Secular Variation over the CMB. The velocity norm has been matched to that of Table 3.2 ($1.4 \times 10^5 (km/yr)^2$). Units as in earlier tables.

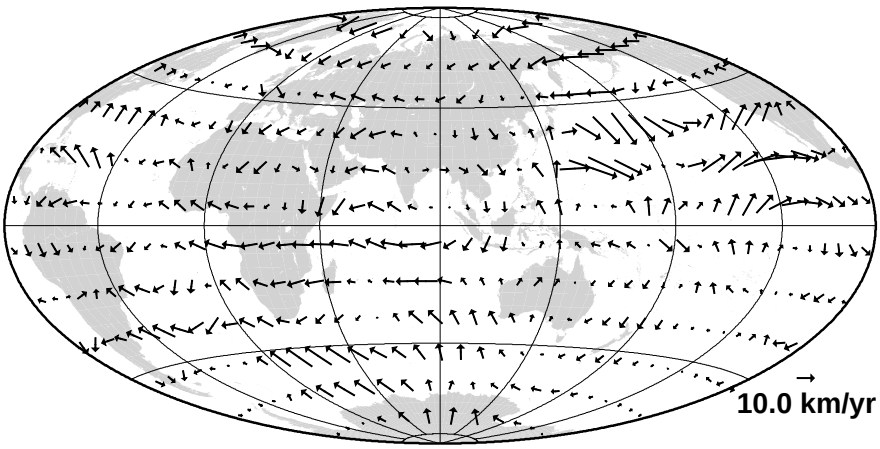

(a) Toroidal-Poloidal Flow Model

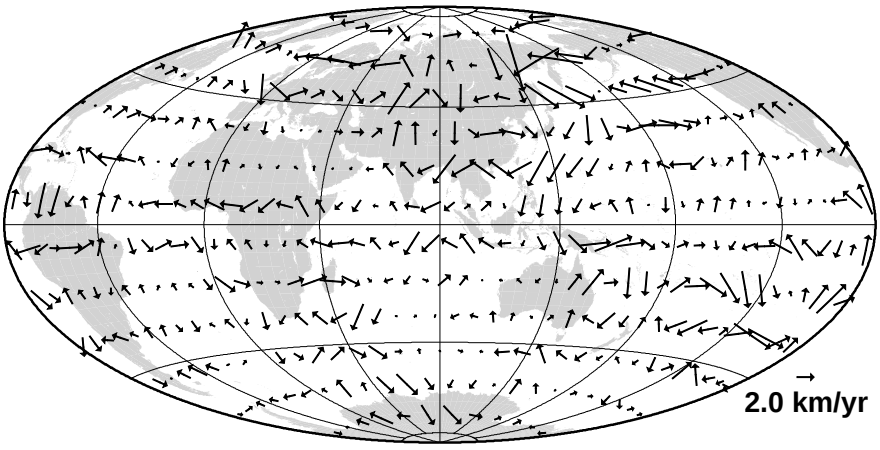

(b) Toroidal Flow Model

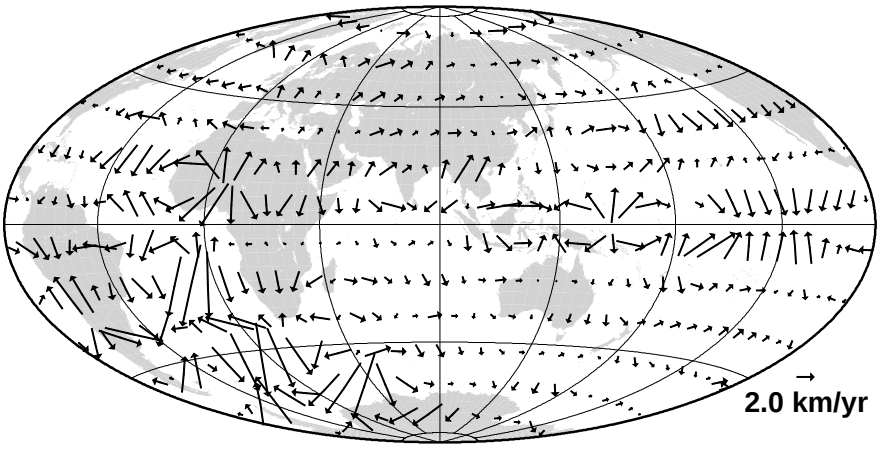

(c) Poloidal Flow Model

Figure 3.7: Flow Models for Dataset 4 using the *a priori* constraint of minimising the RMS SV predicted by the flow. Note the contrast with Figure 3.4.

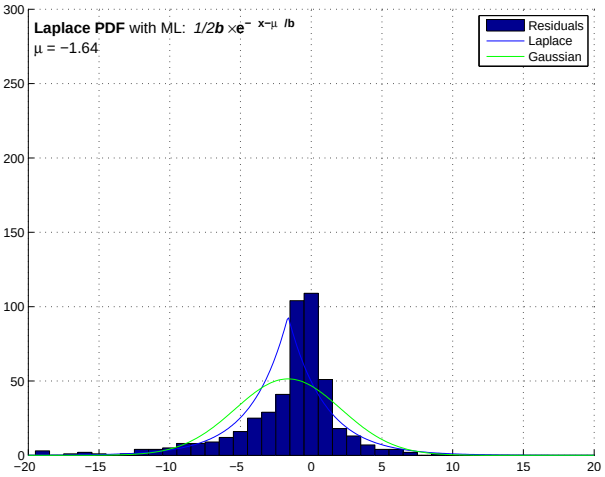

(a) Histogram of Flow Model Data Residuals

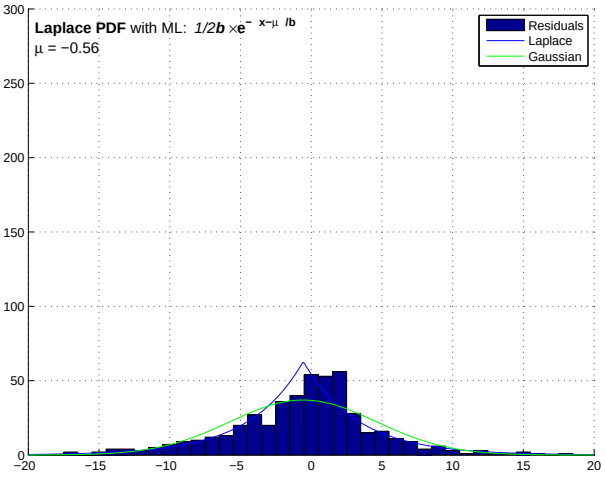

(b) Histogram of Flow Model Data Residuals

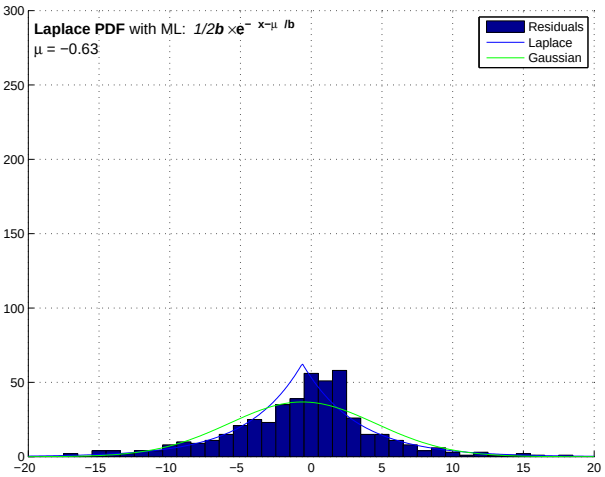

(c) Histogram of Flow Model Data Residuals

Figure 3.8: Histograms of the residuals fit to the observatory SV data for Dataset 4 using the *a priori* constraint of minimising the RMS SV predicted by the flow. Note the contrast with Figure 3.5.

3.5 Flow Spectra

An alternative way of examining the flows is to plot the power spectrum for each degree. The flow spectrum can be used to determine if the flows have converged or to identify what degree holds most power. The degree spectrum as defined by Lowes (1966) can be applied to the flow coefficients in the following form:

$$\oint \mathbf{v}^2 d\Omega = 4\pi \frac{l(l+1)}{2l+1} \sum_{m=0}^{l} ((\dot{t}_l^m)^2 + (\dot{s}_l^m)^2) \tag{3.9}$$

The truncation of both the flow and intermediate SV model occurs at degree $l_{max} = 14$. I have plotted out the spectra of the flows for each of the models from Table 3.2 in Figure 3.9, showing the individual power in the toroidal and the poloidal components of the combined toroidal-poloidal flow. Figures 3.10 and Figure 3.11 show the spectra from the flows in Tables 3.3 and 3.4, respectively. In the case of Figure 3.9 and Figure 3.10, only the toroidal-poloidal solutions converge, while the other solutions, which are obviously unacceptable, do not have significant power at any particular degree.

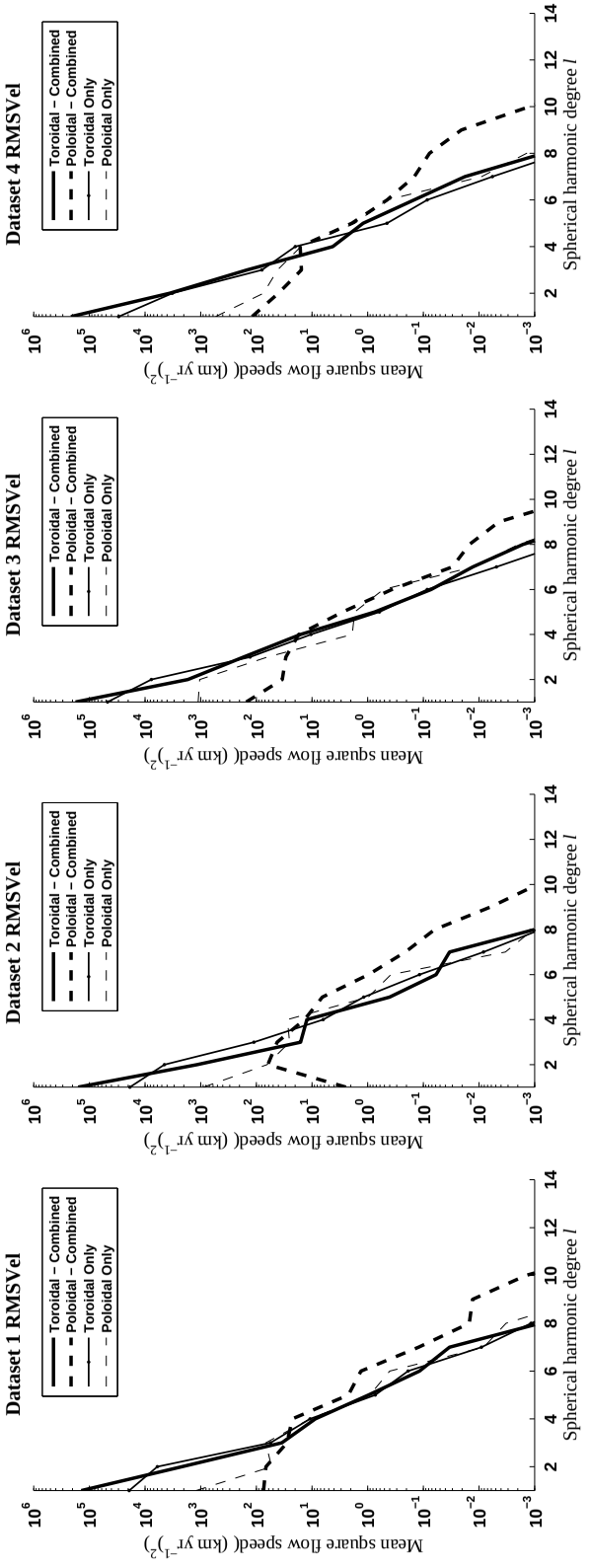

Figure 3.9: Flow spectra from the minimisation of the 'strong' velocity norm (c.f. Table 3.2).

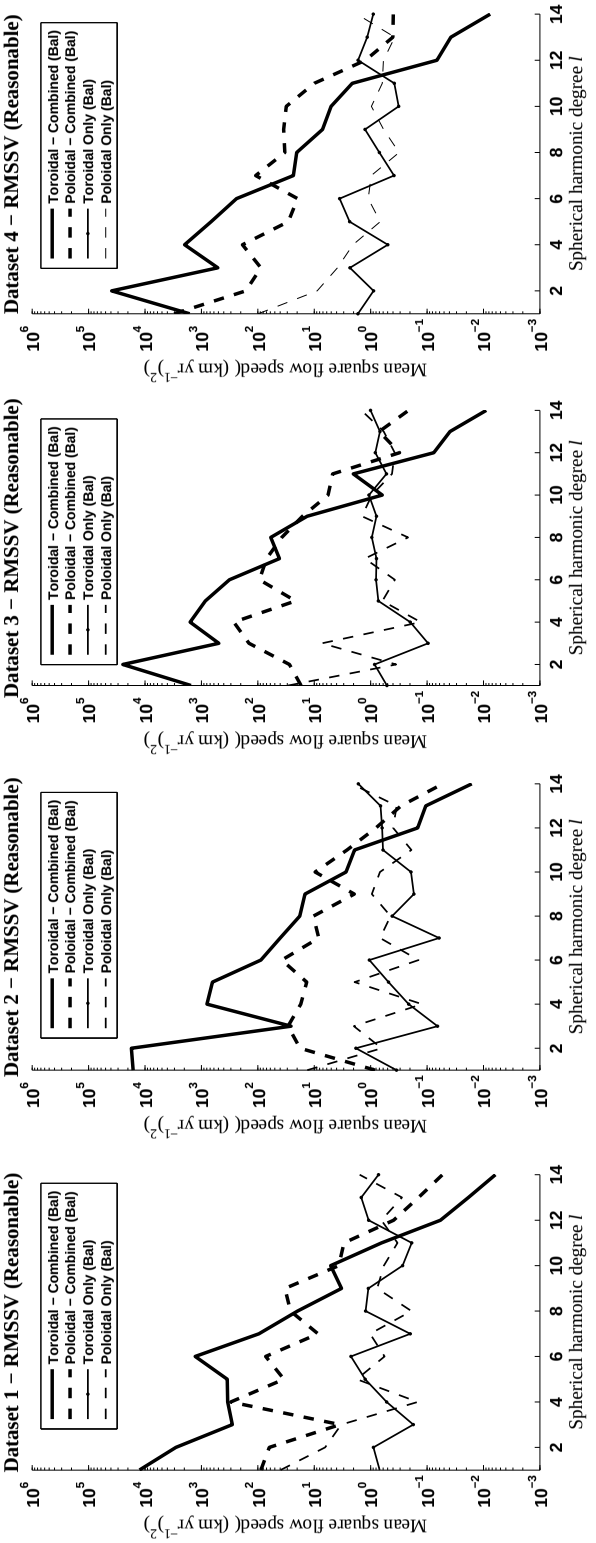

Figure 3.10: Flow spectra from the minimisation of the RMS SV norm with reasonable flow velocity (c.f. Table 3.3).

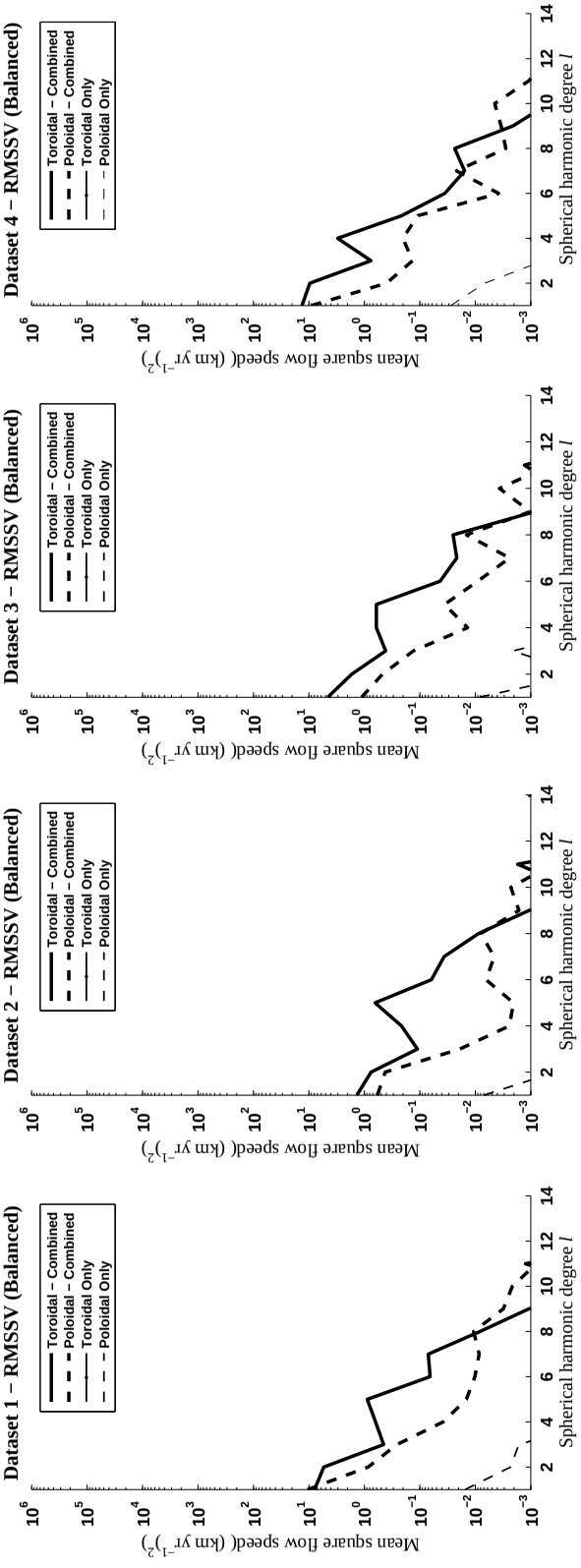

Figure 3.11: Flow spectra from the minimisation of the RMS SV norm with solution norm matched to that of the 'strong' velocity norm solutions (c.f. Table 3.4).

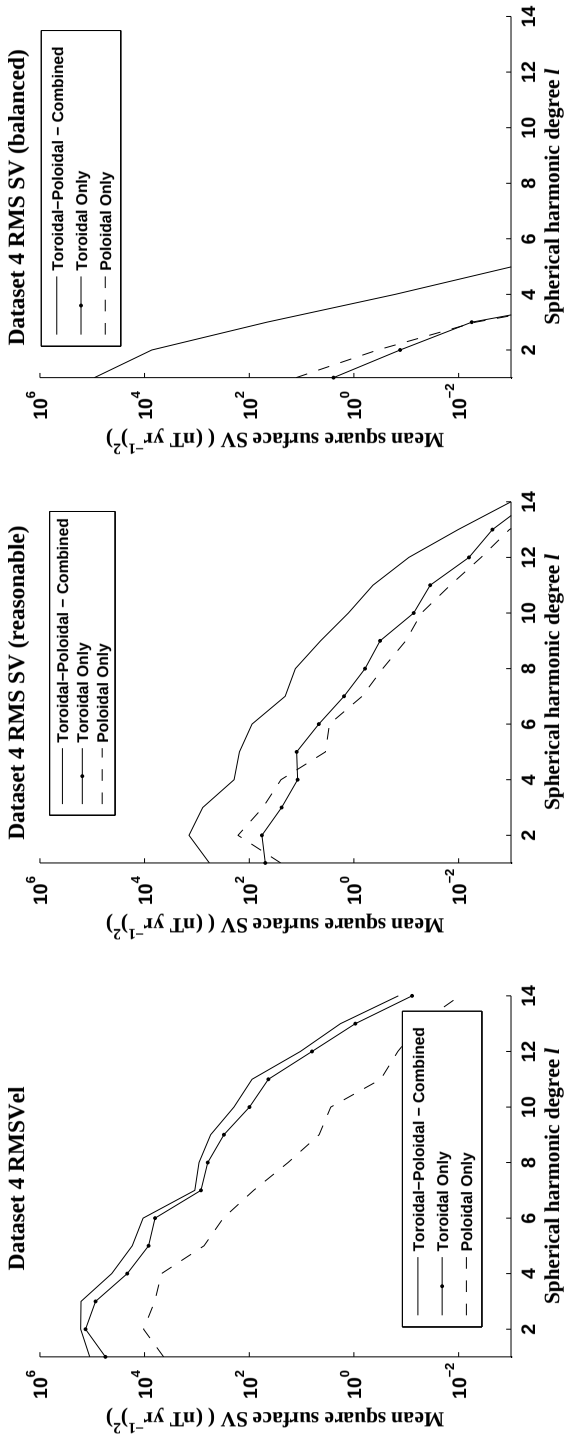

Figure 3.12: Spectra from the intermediate SV models.

The intermediate SV models (example shown for Dataset 4 – Figure 3.12) illustrate that each model converges before the maximum truncated degree and that there is little energy in the higher degrees. This suggests in the case of the RMS SV norm that the minimisation constraints placed upon the flow model are the primary reason for the poor fit to the data and the non-converging flow spectra.

3.6 Primary Controls on Flow Models

This study of flow behaviour differs from methods by most other workers through employing direct observations of the $\dot{X}$, $\dot{Y}$ and $\dot{Z}$ SV components in the inverse formulation, rather than a spherical harmonic model of the SV. This allows measurement of the residual errors and analysis of the geographical distribution of the fit. The use of the one-norm iterative minimisation method improves the fit of the flow model to the observations by iterative re-weighting of the residuals and repeating the inversion until the solution converges. The experiments focused on the three different datasets, using three separate flow regimes with two alternative *a priori* constraints.

There are a number of new results presented here. Firstly, the allocation of the error budget through the covariance matrix has a dramatic effect on the fit of the flow to the observations. Tables 3.2 and 3.3 indicate that Dataset 4 consistently achieves the flow with the best relative fit to the SV input data for the given assumptions and constraints. The observation errors in this dataset have been corrected for covariance between the X, Y and Z components, to limit the influence of contamination by external fields (Wardinski & Holme, 2006). Dataset 2 with similar errors (though without a correct covariance error matrix) achieves a consistently good relative fit to the data, though not quite as good as Dataset 4.

The observation errors for Datasets 1 and 3 have been set equal to 1nT/yr; a simple but physically unrealistic allocation. This is reflected in the relatively poor fit of the flow to the observations for these datasets. Assuming equal errors for each observatory component artificially constrains the inversion. In contrast, by indicating through the covariance matrix which data are poor, improved solutions can be calculated. For

variable errors, as in Dataset 4, the flow solution does not attempt to fit all directions equally e.g. the $\dot{Y}$ component is generally least noisy and, hence, has the smallest errors. Thus, Dataset 4 has the smallest misfit, while Dataset 2 has consistenly small misfit also.

Secondly, the choice of *a priori* minimisation constraint alters the resultant flow pattern significantly, despite an equivalently good fit. The minimisation using a *velocity* norm (Figure 3.4) produces flows showing patterns similar to those of other studies (e.g. Bloxham & Jackson (1991), Waddington et al. (1995), Holme & Olsen (2006)). However, the resulting flows calculated by minimising CMB root-mean-square *secular variation* are more complex (Figure 3.7) and admit only combined toroidal-poloidal solutions. They do not match the typical patterns found in other core flow studies. This suggests the constraint is overly restrictive in terms of the solutions that are allowed but might be useful for producing flows to predict SV. By contrast, the minimisation of the strong velocity norm allows a larger set of good solutions, supporting the proposition that it is a weaker constraint. Note that Dataset 3 consists of evenly geographically distributed 'stations', indicating that the conclusions drawn here are not a function of the particular distribution of observatories available.

Pais et al. (2004) explore the effects of imposing tangential geostrophy on flow inversions. They conclude, in a similar manner to this study, that flow solutions show a clear dependence on regularisation. They focused on a weak regularisation constraint, which allowed resolution of smaller length scales (as these are not as heavily damped). Indeed, in one model (with an additional geostrophic flow constraint), the poloidal coefficients of the flow dominate the energy spectrum (c.f. Figure 14(b), Pais et al. (2004)). In contrast, Rau et al. (2000) found that inversions using unconstrained (i.e. toroidal-poloidal) flow models tended to overestimate the poloidal energy in the flow, when compared to known flows generated by dynamo models. The correlation between the actual flow and the inversion was low (at +0.4). In most flows, the relative power of the poloidal flow was less then 10%.

Eymin & Hulot (2005) show that in regions with low local energy (defined by the

local value of $\mathbf{u}^2$) inversion of SV data is fraught with uncertainty due to interaction of flow structures with the main field. Interestingly, data inversion artifacts were very much larger than the uncertainty due to other processes. They calculate that in large regions — as much as 40% of the surface area — the inverted flow may be unreliable, as the local energy is equal to the average energy of the uncertainties.

The existence of seemingly viable and relatively well-fitting poloidal-only flow models is a surprising result, given that such flows are considered physically unfeasible in the current core dynamic regime. Love (1999) developed a dynamo model in which poloidal-only flow dominates at the core-mantle boundary. This particular dynamo model exhibits no SV at the surface, but does illustrate that such flows are theoretically possible. Breuer et al. (2004) explored the effects of varying Prandtl number (the ratio of kinematic viscosity to thermal diffusivity) on flow produced in a numerical three-dimensional Cartesian dynamo model. They found two distinct flow regimes existed when other parameters were fixed. A small ($\ll 1$) Prandtl number showed energy in the system was transported by strongly toroidal flow. However, a large Prandtl number resulted in a mainly poloidal flow regime (heat transport is dominated by plumes in these models). The models of Breuer et al. (2004) are more complex compared to those of Love (1999), but still show that realistic poloidal flows may occur under certain conditions. It is, however, Gubbins (2007) who most clearly shows that strong poloidal flows cannot exist as the resulting regime would expel large amounts of toroidal flux from the core, thus undermining the frozen-flux hypothesis, through diffusion.

Combining previous results with the findings from this study suggests that poloidal-only flows do not provide a good representation of the core-mantle boundary flow, despite the relatively good fit to the SV data. Additionally, this work shows that CMB SV values matching those in standard models can be achieved easily with velocity norm regularised solutions. SV norm regularised solutions produce complex flows for a comparable fit to the data, and only slightly smoother CMB SV. Hence, it is suggested that solutions minimising the SV norm are not to be recommended.

3.7 Summary

This chapter has examined the effects of some flow assumptions and constraints imposed upon inversions for core flow models directly from observed SV. Using three datasets of SV derived from ground-based observatories and a fourth consisting of synthetic SV on a global grid, core flow models were calculated. It was shown that observation errors affect the overall fit of the inverted flow model to the input data. Using a dataset for which variable observation errors have been calculated for each component by co-estimation, compared to models obtained assuming equal data errors, improved the overall fit of the flow model to the data.

The *a priori* constraints, normally imposed in a stochastic inverse solution, are shown to greatly influence the resultant flow regime. A constraint which minimises a velocity norm is shown to be weaker (i.e. permits a 'larger' model space) than a constraint that minimises the CMB RMS SV predicted by the flow. The weaker constraint allows solutions such as poloidal-only flow models to exist which are equally as valid as toroidal-only flow models, in some cases producing a better fit to the input data. The stronger constraint produces complex flow regimes, which do not match the simpler flow regimes from the weaker constraint or results from other studies. Therefore, it probably has little use beyond hypotheses testing frozen-flux and flow modelling assumptions. In the rest of the inversions used in this thesis, the 'strong' norm constraint is applied in conjunction with the L_1 norm minimisation.

Chapter 4

Biased Time-Varying Residuals of Core Flow Models from Satellite-Derived 'Virtual Observatories'

4.1 Overview

Standard magnetic field models of the internal field are generated by parameterising a small subset of measured data through a spherical harmonic representation and finding least squares values of the coefficients. This is true also of field models derived from satellite measurements (e.g., Hulot et al., 2002). Typically less than 0.1% of the data are used (e.g., Thomson & Lesur, 2007), chosen to be the 'quietest' or least noisy measurements. With large satellite vector datasets of the Earth's magnetic field having become available in recent years, and the increase in computational capacity, this chapter examines the use of a novel method from Mandea & Olsen (2006) to utilise more of the available satellite data than previously employed. This alternative approach is to create a set of 'Virtual Observatories' (VO) in space, mimicking the operation of fixed ground-based observatories. The flow models (and associated residuals) from inversion

of the VO SV data from this approach can then be examined in detail.

Section 4.2 of this chapter details the processing of satellite data to derive the VO, while Section 4.3 briefly summarises the assumptions and parameters used for the flow inversion. In Section 4.4 I examine the patterns seen in the residuals between the SV produced by the flow model and the observed SV. Section 4.5 assesses the evidence for potential causes and explanations for these residual patterns while Section 4.6 suggests methods for ameliorating the effects in the SV and core flow models produced[1].

Acknowledgements

This chapter is based, in part, upon a paper submitted to Geophysical Journal International, co-authored by myself, Kathy Whaler and Susan Macmillan. I performed all the work in the chapter, with Kathy and Susan giving advice throughout to suggest experiments or explanations for the observed phenomena. Susan provided the Dst index and F10.7 data. Nils Olsen provided initial MATLAB code for the Virtual Observatory method and the decomposition of the VO datasets into internal, toroidal and external parts. This was corrected and modified by myself during the course of the research. The CM4 parameterisation code (in MATLAB) is courtesy of Terry Sabaka, from the Comprehensive Model website[2]. The CHAMP and Ørsted data were provided by Alan Thomson at the British Geological Survey, who processed the data into a format suitable for my analysis. CHAMP data (Level 2) are available from GFZ Potsdam.

4.2 Virtual Observatories

Ground-based observatories provide a high-quality temporal record of the magnetic field at a single point on the surface of the Earth. Observations are taken typically at 1-second intervals, and made available in the form of minute, hourly, daily and monthly means. However, only a limited number of observatories are in simultaneous operation at any one time. The observatories are also unevenly distributed across the planet, with

[1]Note that Appendix C lists the directories on the accompanying CD which contain images and animations of the flow models and flow model residuals of all the datasets described in this chapter.

[2]Available at http://core2.gsfc.nasa.gov/cm/; Last accessed 22-10-2008.

a large number concentrated in Europe and the Northern Hemisphere and a paucity in the Southern Hemisphere and Pacific Ocean region (see for example Figure 3.1). Thus SV, as determined by ground observatories, is rather poorly constrained over large regions of the Earth.

Data from satellite missions (e.g. Magsat, Ørsted, CHAMP, SAC-C) have the advantage of sampling the magnetic field across almost the entire globe. However, depending on the orbital configuration, the revisit period for any particular point may be several days to months. This gives a poor temporal record for any specific region and hence comparison directly to ground-based observatory records is difficult. As the satellites are in low Earth orbit, they are continuously decelerated by the tenuous upper atmosphere, causing their orbit to slowly decay. Figure 4.1 (a) illustrates the average altitude of the CHAMP satellite since its launch in 2000. As the satellite approaches closer to the Earth, the measured data shows an apparent increase in field strength over time. Figure 4.1 (b) shows the range of values of the three vector components X, Y and Z from mid-2001 to late-2005 at the satellite altitude over Niemegk in Germany. There is a clear increasing trend with time, as the satellite altitude decreases. The slight eccentricity of the satellite causes the daily variation in intensity. Thus, attempting to directly deduce the magnetic field strength change, in a manner similar to ground-based observatories, from the raw vector data is complicated by the orbital dynamics of the satellite.

Previous studies have overcome this issue by parameterising the field using a spherical harmonic representation and least-squares solving for a set of coefficients which best fit a subset of the measured data (Hulot et al., 2002; Holme & Olsen, 2006). This approach generates a set of spherical harmonic coefficients representing both the field and the SV, though these field models are created from a very small selection of quiet-time data (Thomson & Lesur, 2007). The CHAOS field model of Olsen et al. (2006b) contains a larger subset of slightly noisier quiet time data (Kp index $\leq$ 2o) of satellite data from CHAMP, Ørsted and SAC-C. However, this still represents a vast under-utilisation of the available data.

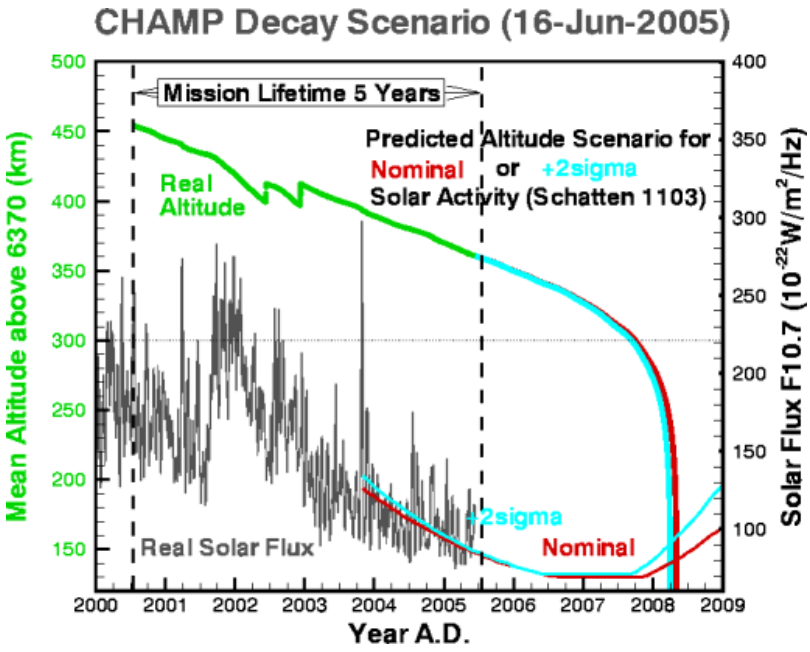

(a) CHAMP Orbital Decay

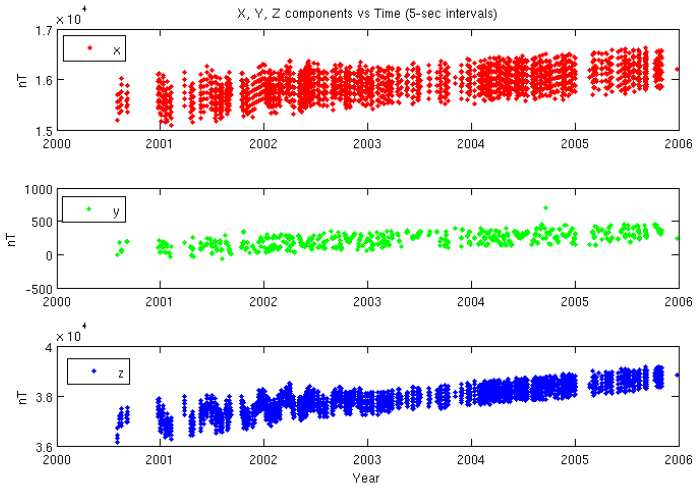

(b) Apparent Field Intensity Increase

Figure 4.1: (a) Altitude change of the CHAMP Satellite over time (from the **GFZ Potsdam** website) showing the recorded altitude decrease over time. The nominal and 2σ curves refer to the expected and extreme altitude scenarios as modelled from the future forecast changes in solar flux (F10.7 curve). (b) Apparent increase in magnetic field strength over time at satellite altitude over Niemegk, due to the satellite decreasing in altitude.

4.2.1 VO Method

Mandea & Olsen (2006) suggested another method for treating the large volumes of data generated during the satellite missions. By binning and averaging all available satellite vector data within a certain distance of a selected point into monthly time periods, they were able to match well the change in the magnetic field as recorded at ground observatories. As this approach attempts to mirror the method used for deriving monthly mean values for ground-based observatories, they refer to these points above the surface of the planet as 'virtual observatories'. A strong implicit assumption is that short-term external field effects will have a zero mean value over the period of a month.

To calculate the mean monthly field at a VO, the data must be reduced to a common height (due to the slightly elliptical and slowly decaying orbit of the satellite). Mandea & Olsen (2006) chose to bin data from a particular month within a cylinder of radius 400km about the chosen latitude and longitude of the VO position. A main field model is subtracted from observed vector satellite data ($\mathbf{B}$):

$$\Delta\mathbf{B} = \mathbf{B}^{Satellite} - \mathbf{B}^{MainField} \tag{4.1}$$

to produce a set of residual measurements $\Delta\mathbf{B}$. It is assumed that the residual field can be represented as a Laplacian potential field $\Delta\mathbf{B} = -\nabla V$, which varies linearly in local x, y and z Cartesian coordinates, with the origin in the centre of the cylinder at 400km altitude. This allows V to be calculated using 8 independent parameters:

$$\begin{aligned} V &= v_x x + v_y y + v_z z \\ &\quad + v_{xx}x^2 + v_{yy}y^2 - (v_{xx} + v_{yy})z^2 \\ &\quad + v_{xy}xy + v_{xz}xz + v_{yz}yz \end{aligned} \tag{4.2}$$

These parameters $(v_x, v_y, \ldots, v_{yz})$ are estimated using a Huber Robust Least-Squares method. The mean residuals to the main field at the virtual observatory are $\Delta\mathbf{B} = -(v_x, v_y, v_z)$. The main field model is added back to the residuals to produce values

of the X, Y and Z components of the field for a selected month. This procedure is repeated for all the available months in the dataset at all VO locations. Figure 4.2 illustrates the orbital track of the CHAMP satellite for a single day, marked in blue. The CHAMP satellite completes approximately 15 orbits per day. A VO position is marked with a red diamond. Measurements with 400km radius of the VO are marked in green. In the figure, the data have been rotated to a Earth centred, Earth frame (ECEF) i.e. Cartesian coordinate system.

The SV (or yearly change) at a given observatory for *month(t)* is then calculated as the difference between the average field in *month(t-6)* and *month(t+6)* for the North (X), East (Y) and Downward (Z) components.

$$SV_{month}(t) = Field_{month}(t+6) - Field_{month}(t-6) \tag{4.3}$$

As previously noted, this approach removes both the stationary crustal field component of the signal and the annual variation, without any direct filtering or averaging, giving the $\dot{X}$, $\dot{Y}$ and $\dot{Z}$ vector components of the field.

In their study, Mandea & Olsen (2006) found a strong correlation (for the period 2001.5-2005.5) between the SV observed at the Niemegk Observatory and the corresponding point at a height 400km above Niemegk in the $\dot{X}$ and $\dot{Z}$ components (though no strong correlation was present in the $\dot{Y}$ component). Comparison of the SV at Niemegk and 21 other observatories to their respective 'virtual observatory' values gave a mean correlation of $|\rho| = 0.65, 0.21, 0.73$ for the $\dot{X}$, $\dot{Y}$ and $\dot{Z}$ components, respectively. Figure 4.3 shows a comparison between the SV recorded at the Niemegk ground observatory and the SV calculated at a VO placed at an altitude of 400km, using a cylinder of 400km radius about the point($\theta = 37.928°, \phi = 12.675°$). The correlation at Niemegk is $|\rho| = 0.66$, 0.17, 0.54. It is thought the reason for the poor correlation in $\dot{Y}$ component due to its sensitivity to ionospheric currents.

Initially, for this study, corrected and calibrated CHAMP vector data were acquired from GFZ Postdam (Level 2, Release v50) for the time period from May 2001 to December 2005 (56 months). Magnetic field series for 648 virtual observatories

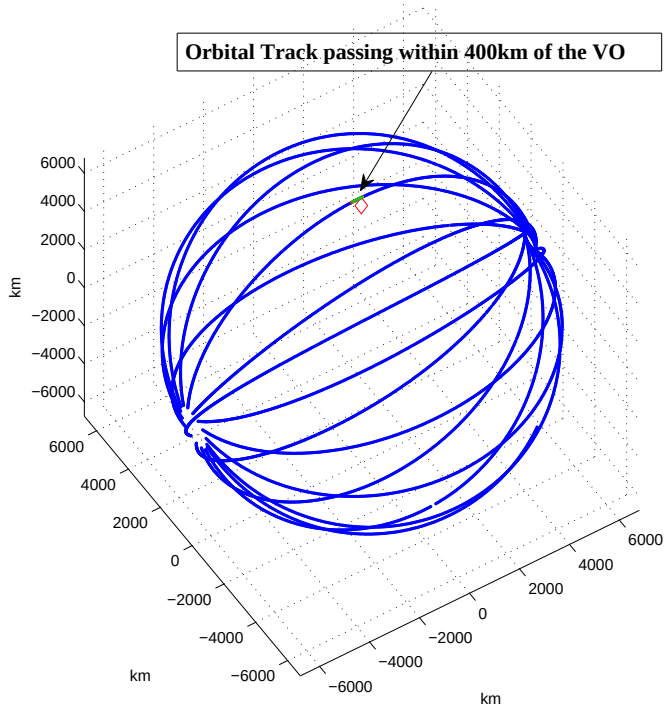

(a) VO data binning

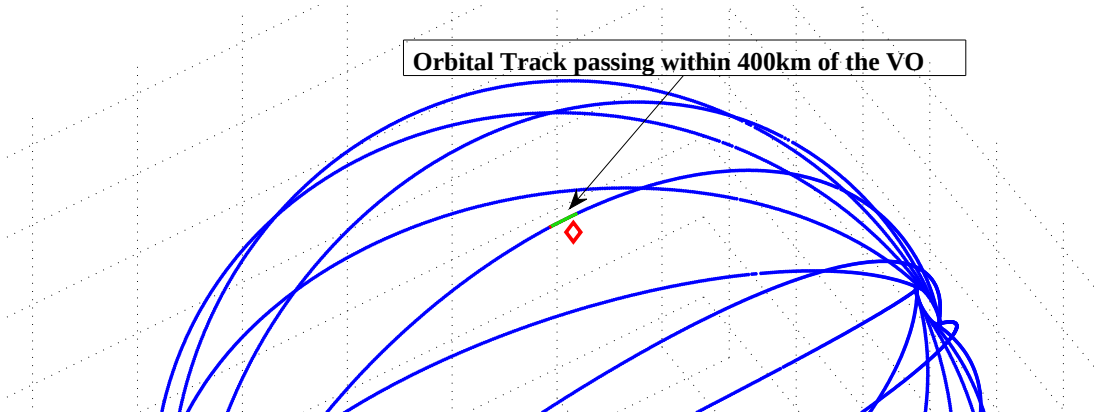

(b) Magnified Region of the VO

Figure 4.2: Example orbital traces from one day of CHAMP data (blue). VO position shown as a red diamond. Green points are data within 400km radius of the VO. In the figure, the data have been transformed into a Earth centred, Earth frame (ECEF) or Cartesian coordinate system from a spherical coordinate frame.

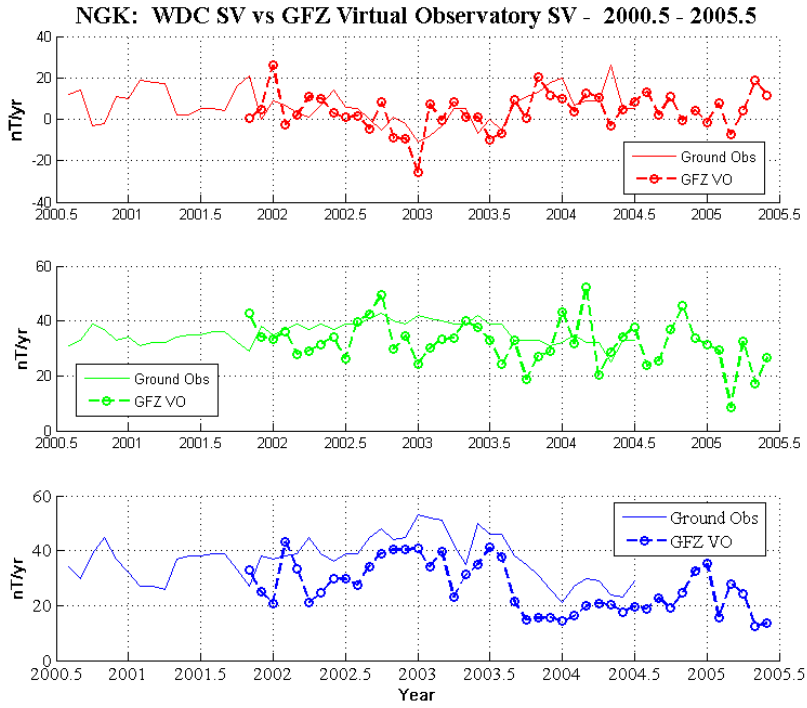

Figure 4.3: Comparison between the SV recorded at Niemegk (Germany) and the calculated SV from a VO $[\theta = 37.928°, \phi = 12.675°]$ at a height of 400km above the ground station in the $\dot{X}$ (red), $\dot{Y}$ (green) and $\dot{Z}$ (blue).

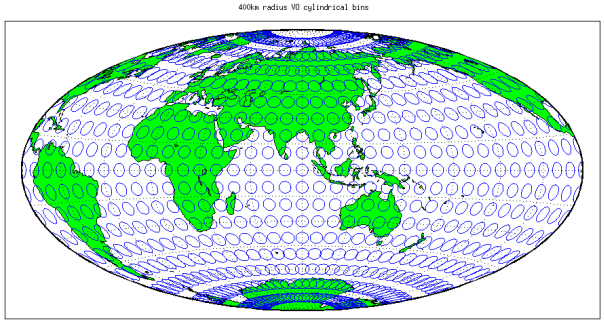

(a) Equal Latitude/Longitude Grid

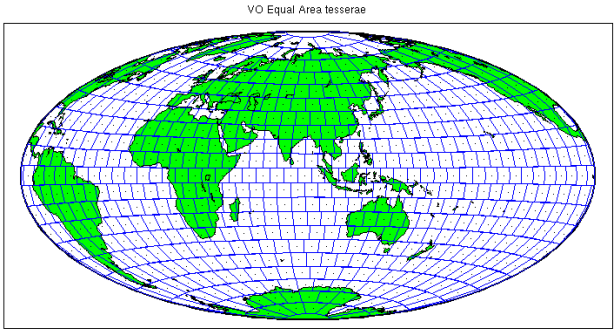

(b) Equal Area Tesserae

Figure 4.4: (a) VO grid of 648 400km radius cylinders spaced equally in latitude and longitude ($\theta = 5°, 15°, \ldots, 175°$; $\phi = -180°, -170°, \ldots, 170°$). (b) VO grid of 648 equal area tesserae.

were calculated on two separate grids: (1) a regular grid of colatitude and longitude ($\theta = 5°, 15°, \ldots, 175°$; $\phi = -180°, -170°, \ldots, 170°$) mimicking the grid point arrangement of Mandea & Olsen (2006) and (2) an equal area global grid of 648 tesserae (Leopardi, 2006). At higher latitudes on the grid of equal latitude and longitude, data included in the VO cylinders are binned into more than one VO, as the areas overlap. At lower latitudes, there are gaps between the cylinders, meaning some data are unused. Using a grid of adjacent non-overlapping equal-area tesserae uses each measured datum just once in the calculation of the VO grid. Figure 4.4 illustrates the difference between the two types of grid.

The CHAMP satellite samples the field at a frequency of 1Hz, giving over 86,000

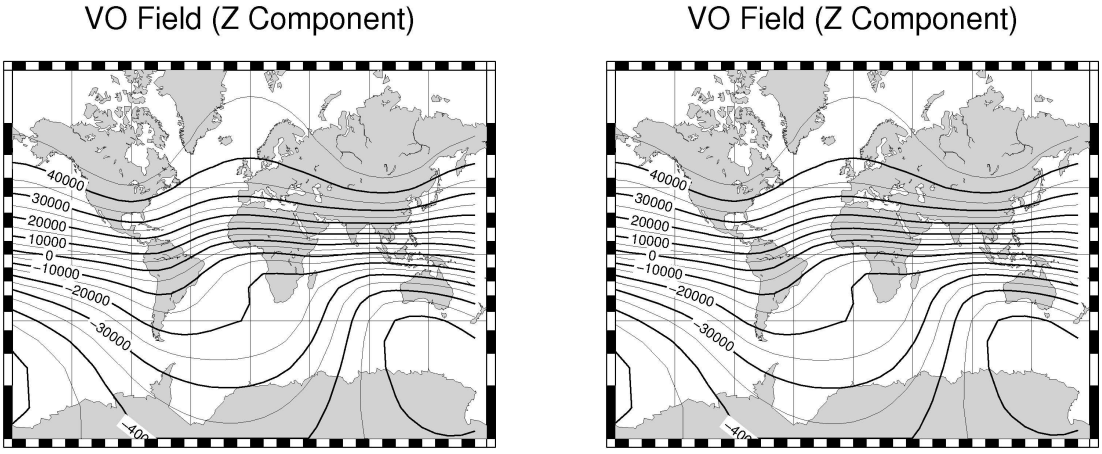

(a) May 2001 (b) May 2002

Figure 4.5: Unsmoothed VO field models derived from using all available CHAMP data: (a) May 2001 and (b) May 2002.

points per day on average. The CHAOS model (Olsen, 2006) was used in Equation (4.1) as the main field model to compute the magnetic residuals. Figure 4.5 illustrates the VO Z component of the magnetic field model for May 2001 and May 2002. Figure 4.6 illustrates the SV of the Z component for November 2001 i.e. the change in the field between May 2001 and 2002. Note the contours are unsmoothed in these figures.

4.3 Flow Modelling

The assumptions and methods for generating flow models have been explored in Chapters 2 and 3. For these flow models the CHAOS field model provides the main field coefficients for the Gaunt and Elsasser matrices ($\mathbf{B}$ in Equation (2.7)). The standard deviation of the residual misfit from the Huber Robust Least Square estimate of data fit to the VO field in $month(t-6)$ and $month(t+6)$ is used to form the data covariance matrix. The residual errors for the first iteration of the one-norm solution are obtained from an initial starting model calculated by a two-norm solution (Equation (2.13)) from the input data. The final solution of the one-norm iterative algorithm typically converges within 35-40 iterations. Figure 4.7 shows an example of convergence for one of the flow models. The flow coefficients are solved up to degree and order $l = 14$. Again

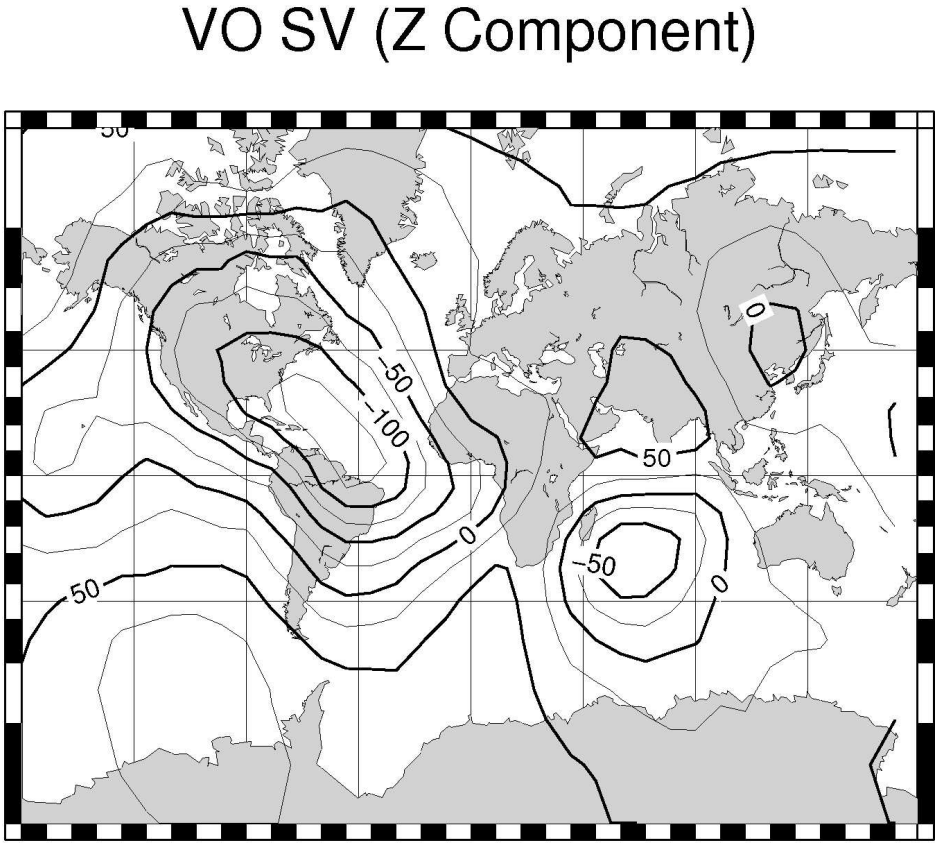

Figure 4.6: SV model for November 2001 derived from a VO model using all available CHAMP data.

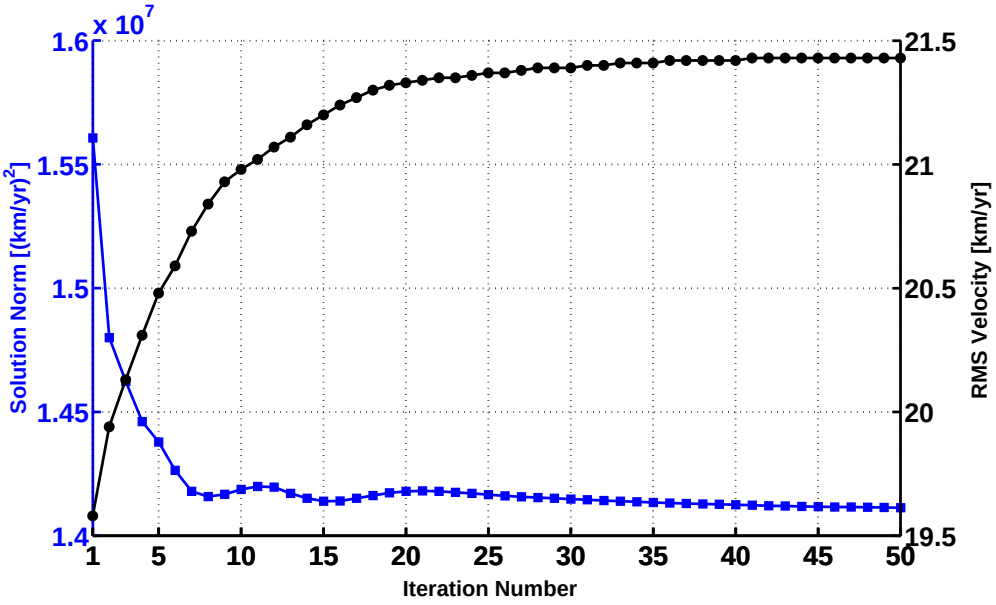

Figure 4.7: Convergence of the solution norm and root-mean-square velocity for SV model of March 2005, using the L_1 iterative algorithm.

the value of very small ($< 10^{-4}$) error residuals in the matrix $\mathbf{R}$ are set to 10^{-4} to prevent the formation of ill-conditioned matrices (Walker & Jackson, 2000). The damping parameter (λ) was set to 10^{-3} for all solutions. This produces solutions with different complexities (solution norm) but does not greatly affect the comparison between flow models. Note that there is no temporal smoothing of the flow.

The resulting flow model is forward modelled to produce the predicted SV at each VO. The residual at the ith VO is $(d_i - \sum_j A_{ij}\hat{m}_j)$. Plotting the histogram of the residuals reveals how well fit the predicted SV generated by the flow model is to the input SV from the VO.

4.4 Biased Residuals

Following the example of Mandea & Olsen (2006) and Olsen & Mandea (2007), initially we exploited all the available CHAMP vector data from *all* local times over each month (for 56 months) to generate the global set of VO on a grid of equally spaced latitude and longitude. Each cylindrical VO 'bin' contained a large number (250 to 10000) of points, depending on the data availability per month and generally increasing as a

function of latitude (due to the polar orbit). From an SV dataset calculated using Equation (4.3), we inverted for a flow model for each month. In general, histograms of the residuals have a Laplacian distribution. The global distribution of residuals was expected to show a random pattern of positive and negative errors, but surprisingly, revealed biases, patterns and correlations between the $\dot{X}$, $\dot{Y}$ and $\dot{Z}$ components. Note that no temporal structure or temporal damping constraints were imposed. Moreover, the distribution of the residuals in each component reveals complex spatial patterns, with strong temporal variation. Appendix C lists the directories on the accompanying CD which contain images and animations of the flow models and residuals. This chapter shows only selective, illustrative snapshots of the flows and residuals.

It was observed that the pattern of modelled core flow changes significantly each month of the dataset. Figure 4.8 shows three examples of the instantaneous flow and associated residual histogram and Figure 4.9 shows the geographic distribution of the residuals for three separate months: November 2001, February 2003 and March 2005. In Figure 4.8 (a, c, e) the core flow models derived from the SV show large differences in flow patterns, and are evidently influenced by a rapidly temporally-changing signal in addition to the internal SV signal. The typical southern Indian ocean gyre is present in all models; however, differences occur in the northern hemisphere and under western Eurasia. These month-to-month changes in flow are too large to be physically realistic.

The histograms of the residual fit of the SV generated by the flow model to the input data are shown in Figure 4.8 (b, d, f). An unbiased dataset and flow inversion would be expected to produce an approximately zero-mean distribution of residuals. However, February 2003 has a significant negative skew with, arguably, a bimodal distribution (i.e. second peak at -6 nT/yr). March 2005 has the smallest skew of the three histograms, but has a non-zero mean, suggesting that some bias exists.

The geographical distribution of the residuals in the $\dot{X}$, $\dot{Y}$ and $\dot{Z}$ components are shown in Figure 4.9. Examination of the distribution in each component of the SV suggests that the $\dot{X}$ component is consistently the noisiest, whilst the $\dot{Z}$ component tends to have the smallest residuals. The residuals in the $\dot{X}$ component tend to be strongly

biased – either positive or negative, while the $\dot{Y}$ and $\dot{Z}$ components have residuals with the opposite sign to $\dot{X}$ (i.e. inversely correlated.) In general, the component biases balance to generate the approximately zero-mean Laplacian distribution histogram. For some months, hemispherical biases are evident, and often longitudinal 'bands' or 'stripes' of larger (or alternating sign) residuals occur (e.g. the $\dot{Y}$ components of Figure 4.9 (a) and (b)). If viewed as a time-series, the longitudinal stripes can be seen to 'drift' or rotate consistently westward by approximately 30°/month, matching the satellite orbital drift.

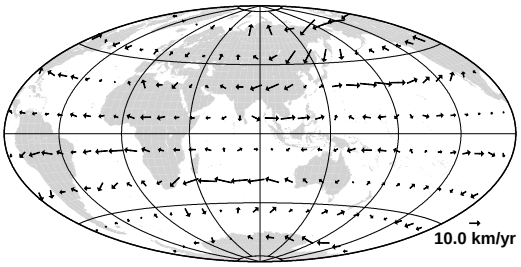

(a)

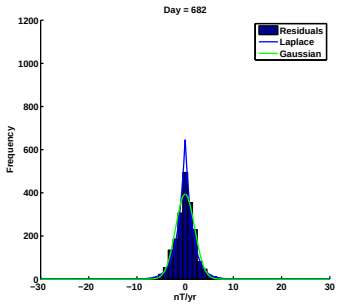

(b) November 2001

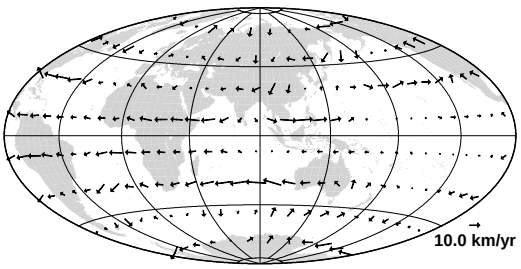

(c)

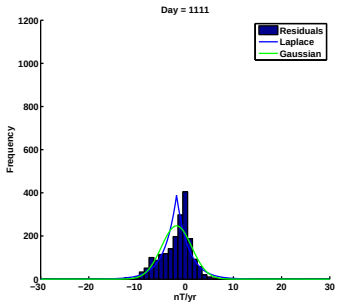

(d) February 2003

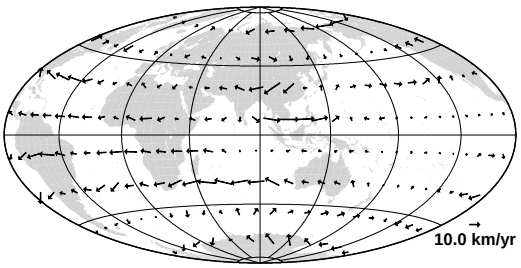

(e)

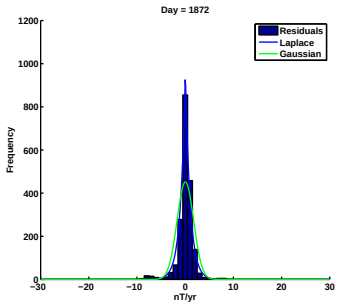

(f) March 2005

Figure 4.8: Core-mantle boundary flow models (a, c, e) and histograms (b, d, f) of residuals of each flow model to the SV generated from Virtual Observatory grid of equal latitude and longitude spacing for *all* available vector measurements. In (b, d, f), the Laplacian and Gaussian fits to the data are shown in the blue and green curves respectively. Continents shown for reference. (a)-(b) November 2001; (c)-(d) Febraury 2003; (e)-(f) March 2005.

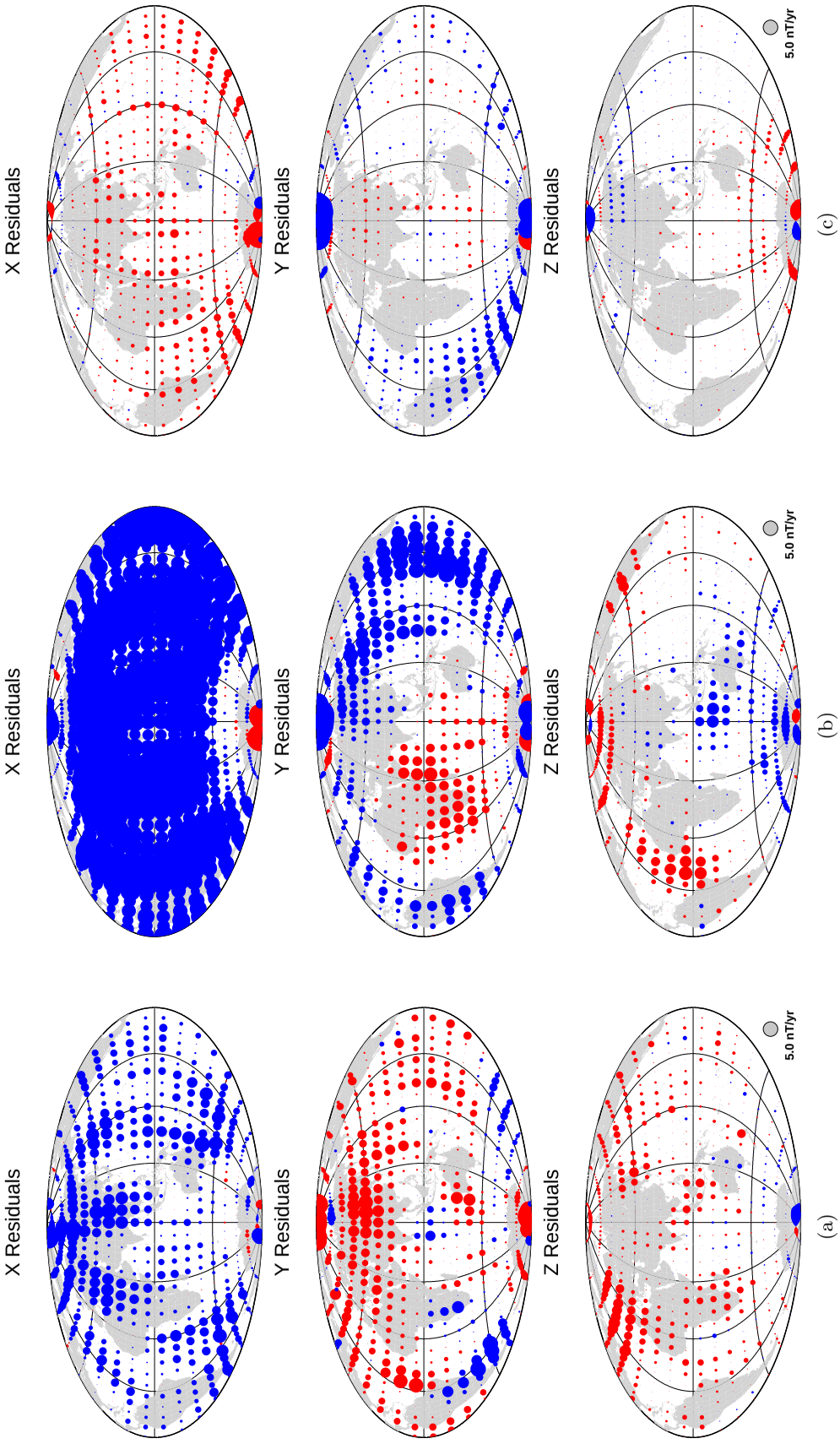

Figure 4.9: Geographic distribution of the residual fit of each flow model to the SV generated from Virtual Observatory grid of equal latitude and longitude spacing for *all* available vector measurements. Circle size indicates residual size, with reference circle shown in bottom right. Positive residuals in red, negative residuals in blue. (a) November 2001; (b) Febraury 2003; (c) March 2005.

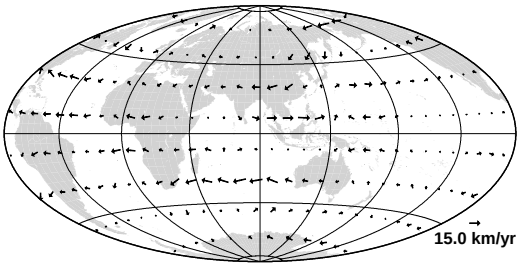

(a)

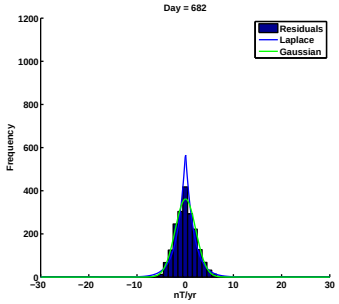

(b) November 2001

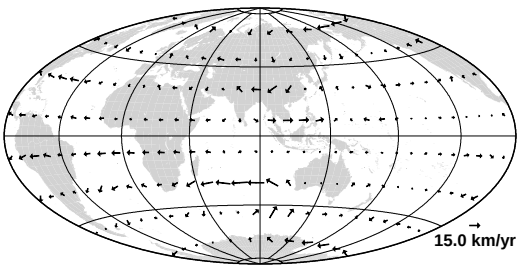

(c)

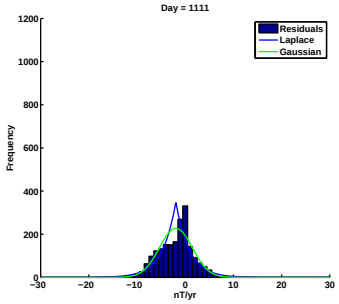

(d) February 2003

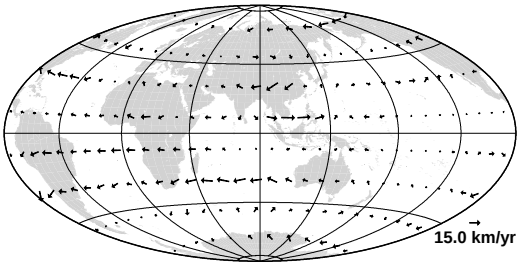

(e)

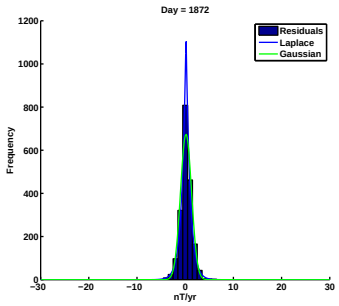

(f) March 2005

Figure 4.10: Core-mantle boundary flow models (a, c, e) and histograms (b, d, f) of the residual fit of each flow model to the SV generated from Virtual Observatory data grid of equal area tessera for *all* available vector measurements. In (b, d, f), the Laplacian and Gaussian fits to the data are shown in the blue and green curves respectively. (a)-(b) November 2001; (c)-(d) Febraury 2003; (e)-(f) March 2005.

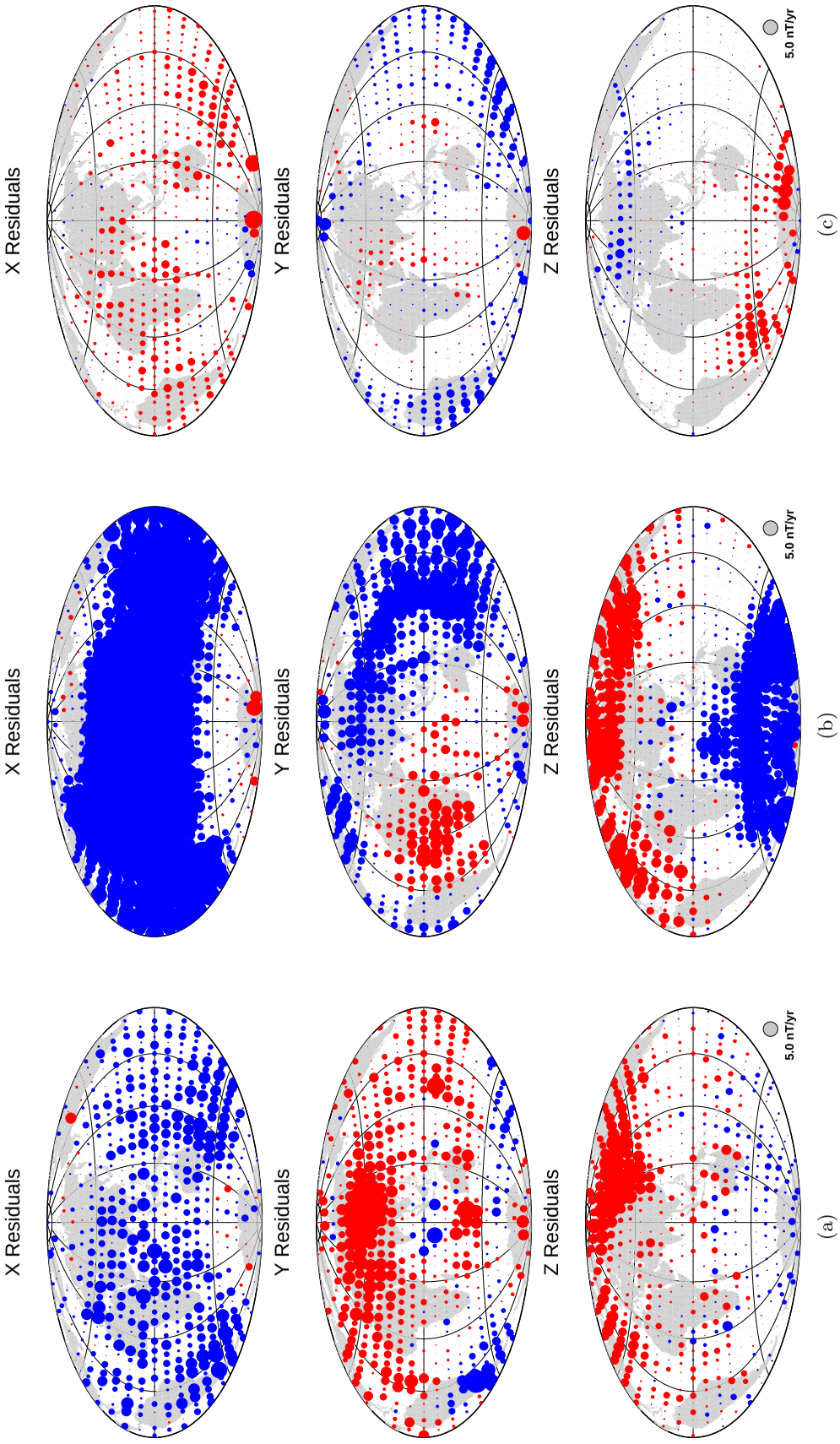

Figure 4.11: Geographic distribution of the residual fit of each flow model to the SV generated from Virtual Observatory data grid of equal area tessera for *all* available vector measurements. Circle size indicates residual size, with reference circle shown in bottom right. Positive residuals in red, negative residuals in blue. (a) November 2001; (b) Febraury 2003; (c) March 2005.

Figure 4.10 shows examples of flow models from VO calculated using a grid of equal area tesserae. The flow models in Figure 4.10 (a, c, e) are similar to Figure 4.8 indicating that the SV data from both gridding approaches are broadly equivalent. The fit of the flow models to the data is slightly poorer in these examples (compare the histograms (b, d, f) in Figures 4.8 and 4.10). The residual distribution in Figure 4.11 shows that the $\dot{X}$ component is still the noisiest. The $\dot{X}$ residuals in Figure 4.11(b) reveal that the bias is strongest in mid-latitudes, with opposite signed residuals in either hemisphere of the $\dot{Z}$ component. The sectorial banding seen in the residual distributions for the equal latitude and longitude VO grid (e.g. Figure 4.9(b) $\dot{X}$) is less apparent. The polar regions appear less noisy (except in the $\dot{Z}$ component), presumably due to fewer points in these regions.

4.5 Analysis

It is worth emphasising that, in this chapter, core flow modelling is being employed as a method both to study the consistency of the internal SV deduced from satellite data and the inverted flow models, with the main aim being to understand and remove undesired effects. An analysis of the patterns in the residuals may allow correction strategies to be developed.

Previous studies employing direct inversion of SV data from ground based observatories have not reported strong geographically biased vector components. For example no biases are seen in the ground observatory residual data of Chapter 3, so it is of interest to attempt to identify potential influences for the component biases and patterns seen, particularly the deviation from the implicit assumption of zero-mean noise. I wished to investigate if the residual bias results primarily from external or internal fields relative to the satellite, orbital drift or other effects. To investigate these effects, other datasets were produced – for example, by employing data selection criteria.

A second set of main field VO for the period May 2001 – December 2005 were calculated using local *night-side only* satellite data. The CHAMP vector data were winnowed to remove measurements outwith the local time window of 20.00–06.00hrs

Dataset	Characteristics	Grid type
Dataset 1	All CHAMP data	Equal Area
	All CHAMP data plus CM4 correction	Equal LL
Dataset 2	Night-side only CHAMP data	Equal Area
	Night-side only CHAMP data plus CM4 correction	Equal LL
Dataset 3	Selected quiet-time CHAMP and Ørsted data	Equal LL
Dataset 4	Simulated CHAMP data using CHAOS	Equal LL Equal Area

Table 4.1: Description of datasets generated for the Chapter. Equal Area refers to the grid of equal area tessera. Equal LL refers to a grid equally spaced in latitude and longitude.

(polar summer daylight conditions were ignored). The number of data in each cylindrical 'bin' (or tessera) was smaller (again dependent on the data availability during the particular month and latitude). Each month, approximately 5% of the VO did not have enough data to calculate a solution, so were spatially interpolated to fill the grid. As before, the SV for each VO was calculated and inverted for flow models for each month. We shall refer to this as VO Dataset 2, with the previous VO model using data from *all* local times called Dataset 1. (Table 4.1 summarises the datasets used in this Chapter.)

Comparison of residual histograms from this dataset (Figure 4.12) to those from Dataset 1 indicates that the fit of the flow model to the SV data improves, illustrating that the night-side only dataset is less contaminated. Figure 4.12 shows three examples of the geographic residual patterns using the equally spaced latitude/longitude grid. The $\dot{X}$, $\dot{Y}$ and $\dot{Z}$ components are still strongly biased, with the longitudinal stripes particularly evident in Figure 4.12 (b). Note that overall the residuals for these flow models are smaller than those for Dataset 1 (e.g. compare Figure 4.9 (b) and 4.12 (b)).

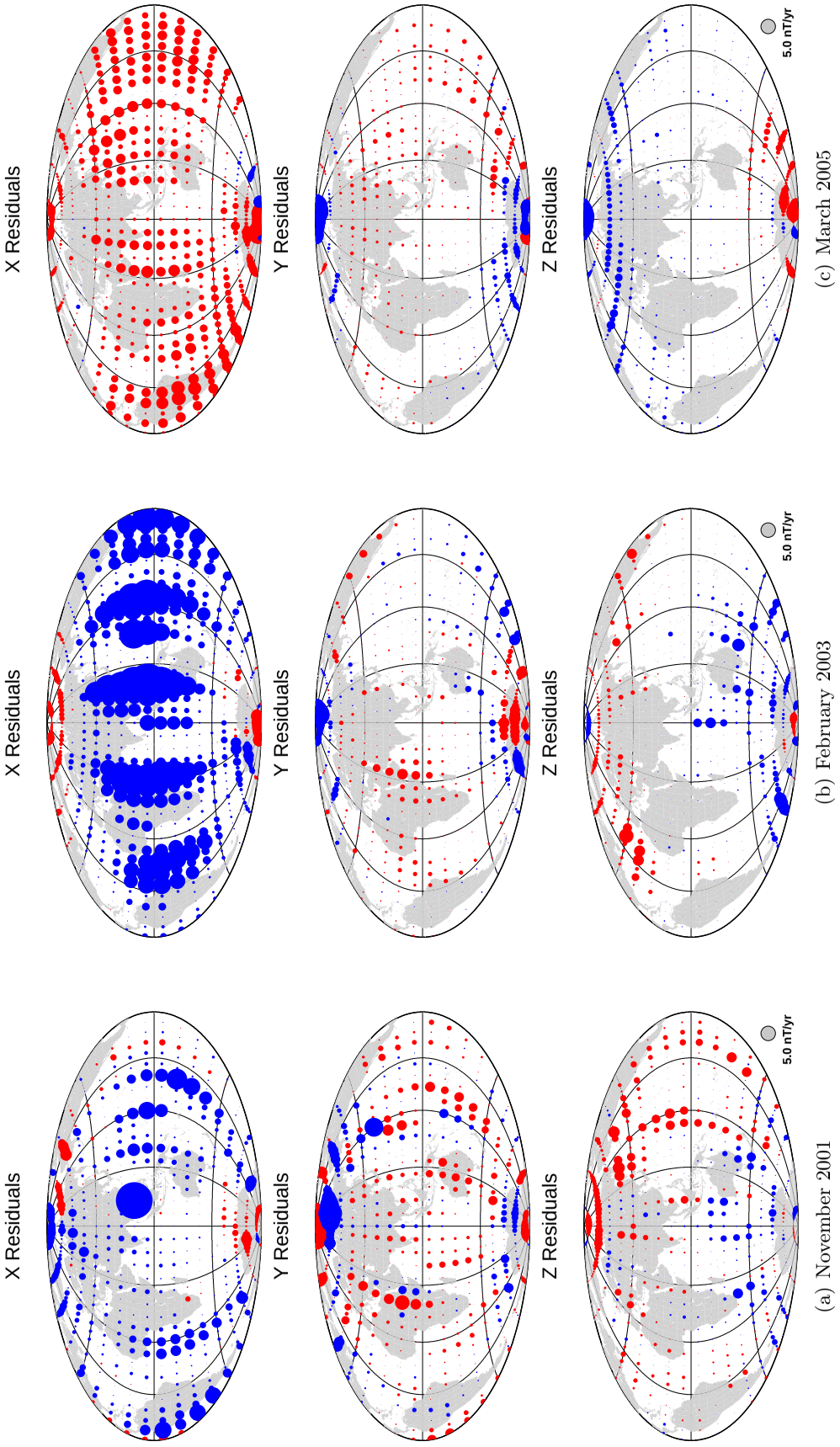

Figure 4.12: Geographic distribution of the residual fit of each flow model to the SV generated from Virtual Observatory grid of equal latitude and longitude spacing for *night-side only* vector measurements. Circle size indicates residual size, with reference circle shown in bottom right. Positive residuals in red, negative residuals in blue. (a) November 2001; (b) February 2003; (c) March 2005.

4.5.1 Influence of Fields External to Satellite Orbit

The previous results show that, though some unwanted effects within the data collected on the day side of the planet can be reduced or removed, the biases in each vector component still remain. To examine the effects of external field influence on the residual biases including the sectorial banding, a dataset of selected quiet-time data from Thomson & Lesur (2007) was used to generate a third VO dataset (referred to as Dataset 3). The selection consists of vector data from both the CHAMP and Ørsted satellites for the same time period (May 2001 – December 2005), though due to the rigorous noise criteria imposed, has very few data points (approximately 85000) compared to the previous CHAMP datasets. It was necessary to interpolate both spatially and temporally where lack of data prevented the calculation of an acceptable VO point. This is not ideal but is necessary to allow direct comparison to the other datasets. Figure 4.13 shows the VO data distribution for the flow models created for Dataset 3.

With such strong initial selection criteria, there should be little temporal correlation in the data. Comparisons show that the SV calculated from this dataset is reasonably consistent with the other two datasets. The SV was again inverted to produce instantaneous monthly flow models. Figure 4.14 shows examples of the resulting residual patterns from three months with the lowest level of interpolation. There is no obvious banding or strong bias in any of the components, suggesting that external field noise (mostly absent in this dataset) only affects the SV of VO generated using more relaxed data selection criteria (e.g. using all available data).

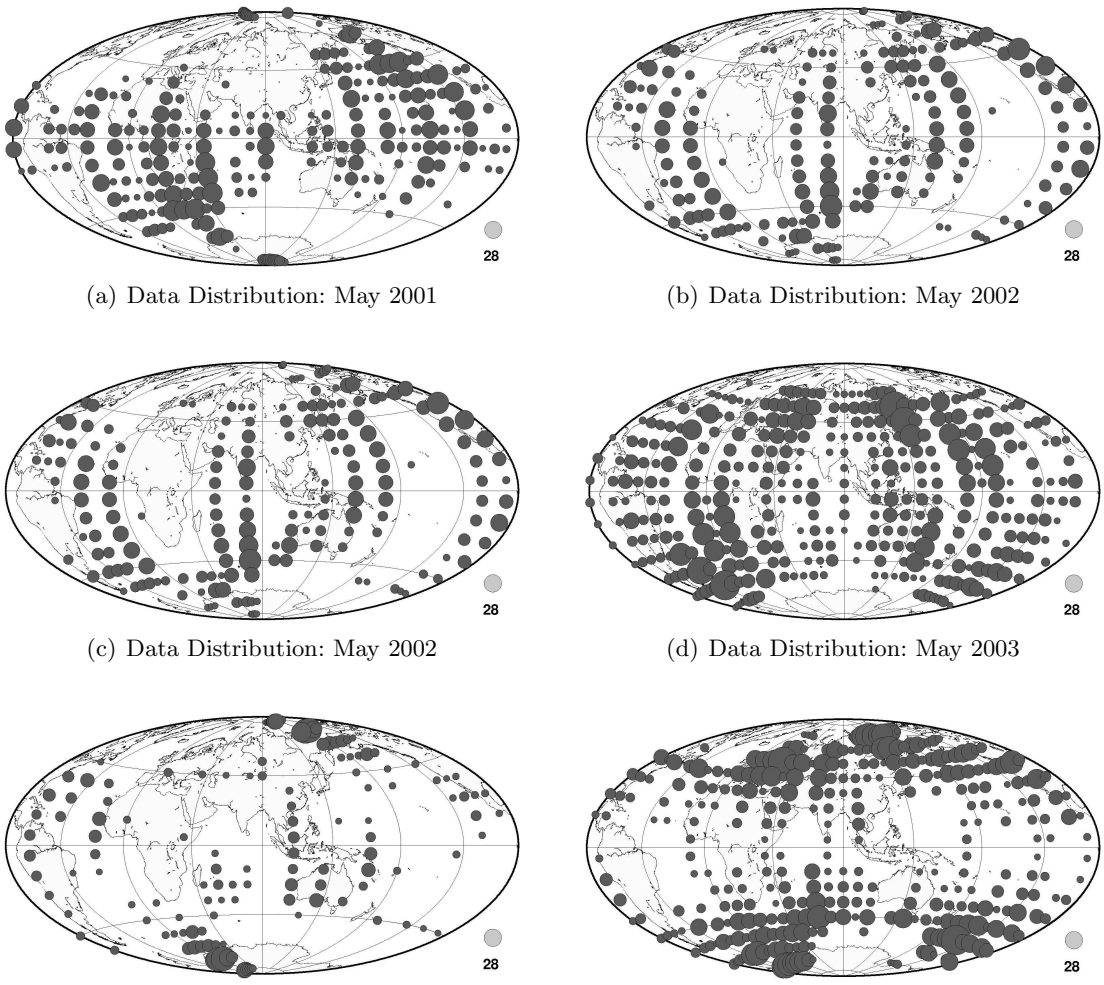

(a) Data Distribution: May 2001

(b) Data Distribution: May 2002

(c) Data Distribution: May 2002

(d) Data Distribution: May 2003

(e) Data Distribution: March 2003

(f) Data Distribution: March 2004

Figure 4.13: Geographic distribution of the VO datasets used to create the flow models for the *selected quiet-time* vector measurements (Dataset 3). Circles indicate number of measurements in each VO (at least eight data points are required to fulfil the criteria of Equation 4.2).

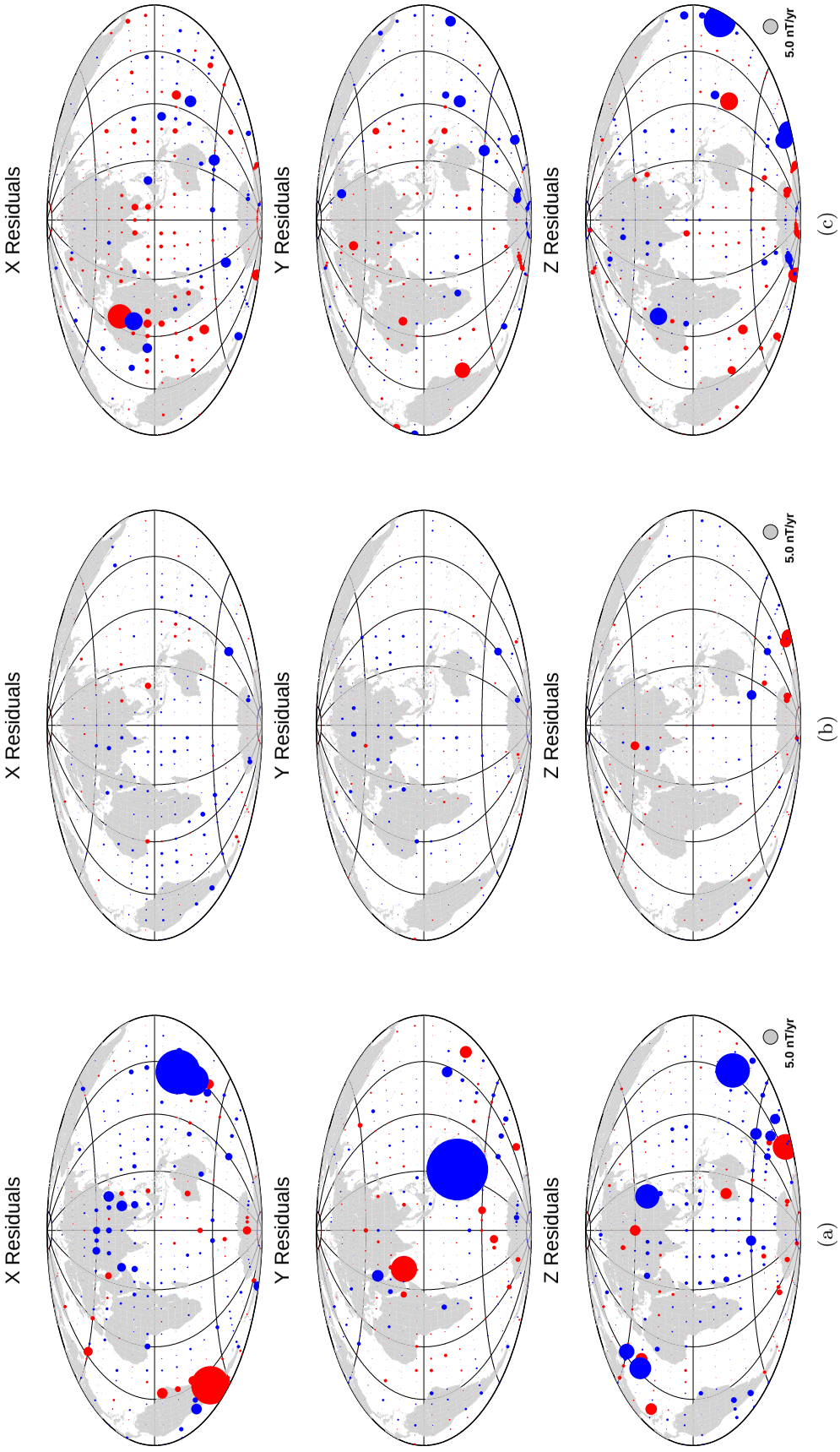

Figure 4.14: Geographic distribution of the residual fit of each flow model to the SV generated from Virtual Observatory grid of equal latitude and longitude spacing for *selected quiet-time* vector measurements (Dataset 3). Circle size indicates residual size, with reference circle shown in bottom right. Positive residuals in red, negative residuals in blue. Flow models are for month$_{(t+6)}$ in Figure 4.13. (a) November 2001; (b) November 2002; (c) September 2004.

External effects at satellite altitude come from a large number of phenomena including field aligned currents and ring currents. The Dst index measures magnetic disturbance from external fields, primarily due to ring current activity (Campbell, 2003). Comparison between a nominal average monthly Dst value for 2001–2005 and the mean residual bias in the $\dot{X}$ component of Dataset 1 revealed no obvious correlation. However, as the SV is calculated using data measured twelve months apart, the correct manner of comparison is to compute the difference between the mean monthly Dst values for $month(t-6)$ and $month(t+6)$. Figure 4.15 shows the annual difference in mean monthly Dst value plotted with the mean bias in the $\dot{X}$ component of Dataset 1 for both methods of gridding. (As the actual flow model residuals are approximately zero-mean, the $\dot{Y}$ and $\dot{Z}$ component residuals are generally inversely correlated to those of the $\dot{X}$ component). It is quite obvious that the change in Dst and mean biases are strongly correlated. The correlation coefficient is 0.67 for the equal area tesserae grid and 0.66 for the equally spaced latitude/longitude grid (both with a probability value of $\sim 10^{-7}$, indicating the correlation is significant at greater than the 99.9% level). The significant correlations between the change in Dst and the two residual mean biases suggest that the residuals contain external field signals.

The VO dataset created from selected quiet-time Ørsted and CHAMP measurements (Dataset 3) has been interpolated from a relatively small number of satellite data points both spatially and temporally. Hence, spatial correlation between measurements is not as strong (though some correlation will exist due to interpolation). The associated residual patterns, shown in Figure 4.14, do not have any of the features seen in those from Datasets 1 and 2. However, the correlation of the mean bias in $\dot{X}$ with the change in the Dst index is 0.49 (correlation is significant at greater than the 99.9% level), which suggests that there is still some influence from external fields.

4.5.2 Influence of Fields Internal to Satellite Orbit

Magnetic fields internal to the satellite orbit (in addition to the main and crustal field) can arise from ionospheric currents, auroral/equatorial electrojets and field-aligned cur-

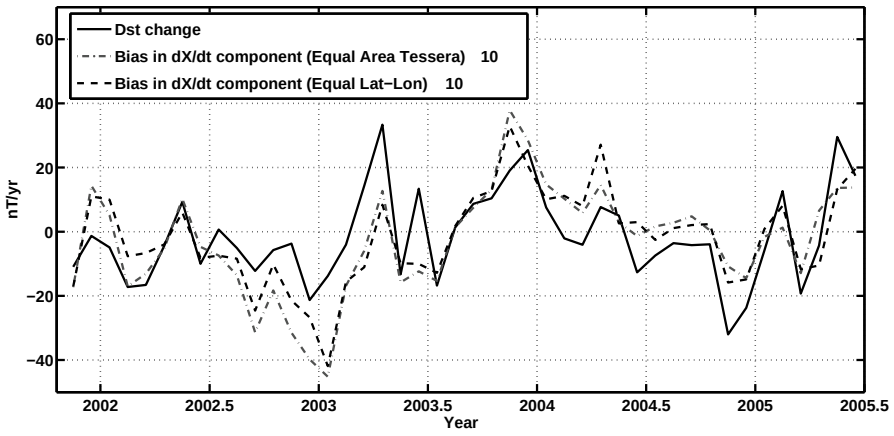

Figure 4.15: Twelve month difference of mean monthly Dst index versus the mean bias in the $\dot{X}$ component of Dataset 1 for the equal area tesserae VO grid and the equally-spaced latitude/longitude VO grid. (Note: The biases have been multiplied by 10 to better illustrate the correlation). The correlation is 0.67 and 0.66 respectively (both correlations are significant at greater than the 99.9% level).

rents, particularly on the sunlit-side of each orbit – increasing globally during solar-disturbed periods. Any such additional fields would break the assumption that the field was of internal origin (i.e. a Laplace potential field) in the region surrounding the satellite as measurements are taken.

The smaller residuals from Dataset 2 (derived from night-side only measurements) compared to Dataset 1 (derived from all local-time measurements) suggests that there is a strong influence from day-side fields (e.g. Figure 4.9 and Figure 4.12). Widening the window of local night-side measurements used in Dataset 2 from 20.00 – 06.00hrs to 18.00 – 08.00hrs slightly increased the magnitude of the residuals. This suggests that ionospheric currents and other day-side fields are not averaged to zero by the VO method and hence contribute to the biased residuals.

4.5.3 Influence from the VO method

The method by which each VO is generated through binning and fitting a local potential field to produce an average field measurement over a month is, in part, responsible for some of the residual patterns observed. The cylindrical bin size, in the latitude/longitude grid, is limited in radius (400km), so at higher latitudes data mea-

surements become common to several VO bins. The equal area tesserae grid does not have any overlapping regions and so removes these effects and uses all available observations. However, the fit of the flows using the equal area tessera method are, on average, slightly worse than those using the evenly-spaced latitude/longitude grid.

The satellite nadir local-time difference also has an effect on the VO data. As the CHAMP satellite drifts approximately 2.5 hours per month in local time, measurements taken at dawn-dusk configurations are subject to a different ionospheric magnetic field environment to those acquired during local noon-midnight configurations. The difference of the median local satellite time (at mid-latitudes) between $month(t+6)$ and $month(t-6)$ is approximately 3.5 hours. Satellite measurements taken at different local times are not sampling the same magnetic field conditions.

As a test of orbital configuration influence (for the sectorial banding pattern, in particular), a synthetic VO dataset (Dataset 4) was created using a simple satellite orbit simulator and the internal part of the CHAOS field model (Olsen et al., 2006b). Two years of synthetic satellite measurements and positions were simulated by combining the CHAOS model and the latitude, longitude and radius output from the satellite simulation. The data were binned into 400km cylinders on a regular grid of latitude and longitude to produce VO (similar to Figure 4.8) providing twelve months of SV values which were inverted for core flow models. A number of simple but unrealistic noise scenarios were tested using the simulation. Both biased (e.g. positive only) and unbiased random Gaussian noise was added to the CHAOS model in the polar regions and on the local dayside at low to mid latitudes, leaving other regions noise-free. Differing noise levels (up to 10nT) have little effect on the size of the residuals and the pattern seen but do produce rapidly varying flow patterns, similar to the changes in the flows seen in the other datasets. Figure 4.16 shows residual distributions for three consecutive months from the noise-free VO simulation. The residuals are seen to have persistent longitudinal banding features which drift westward when viewed as a time series. Residuals from a simulated VO dataset using a grid of equal area tessera show no latitudinal banding (Figure 4.17). This result demonstrates that the combination of binning method and

orbital drift is at least partly responsible for the sectorial banding of the residuals.

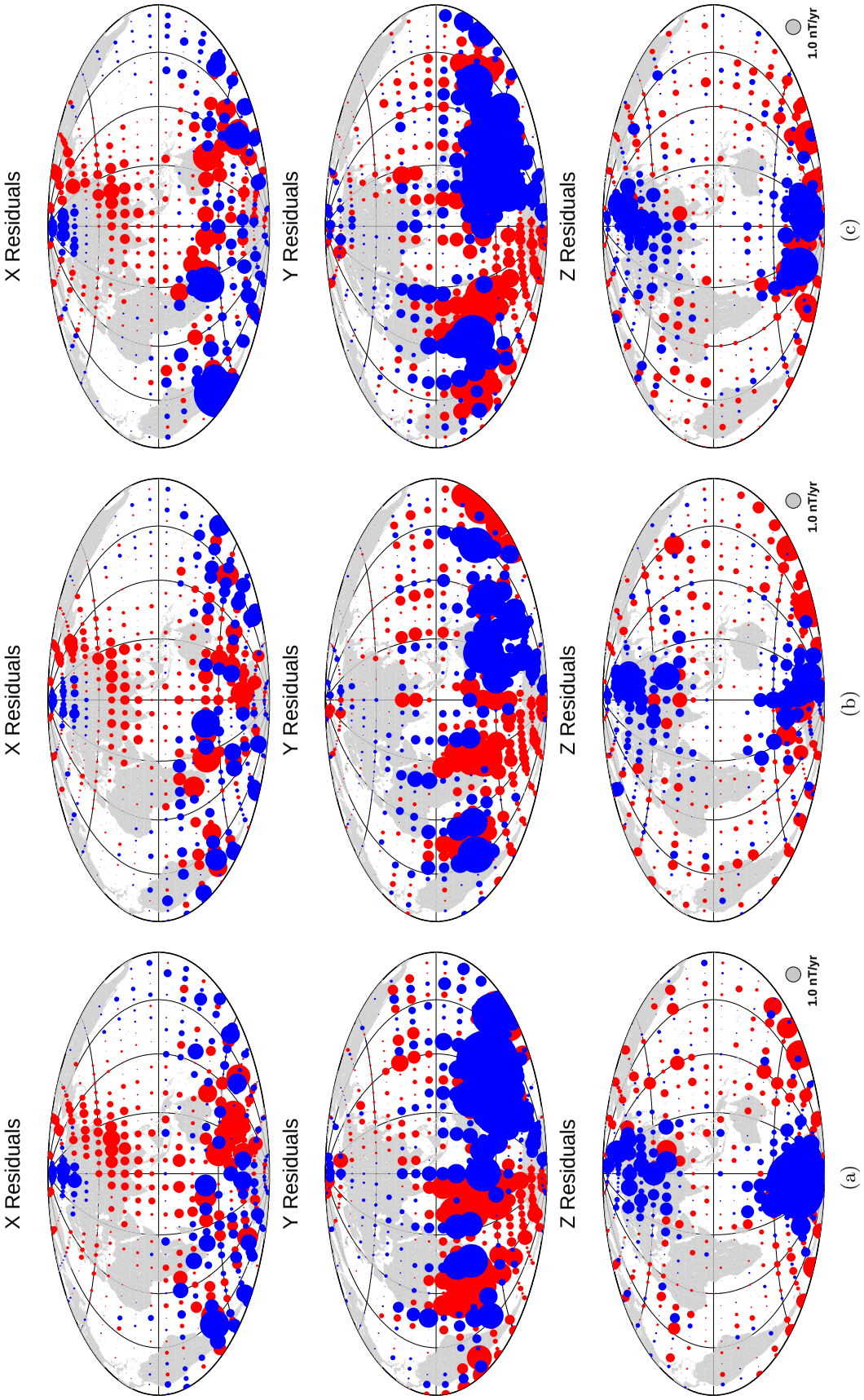

Figure 4.16: Geographic distribution of the residual fit of three flow models to SV data simulated from the CHAOS model and the CHAMP orbits generated from Virtual Observatory grid of *equal latitude and longitude*. Positive residuals in red, negative residuals in blue. (a) Month 1; (b) Month 2; (c) Month 3.

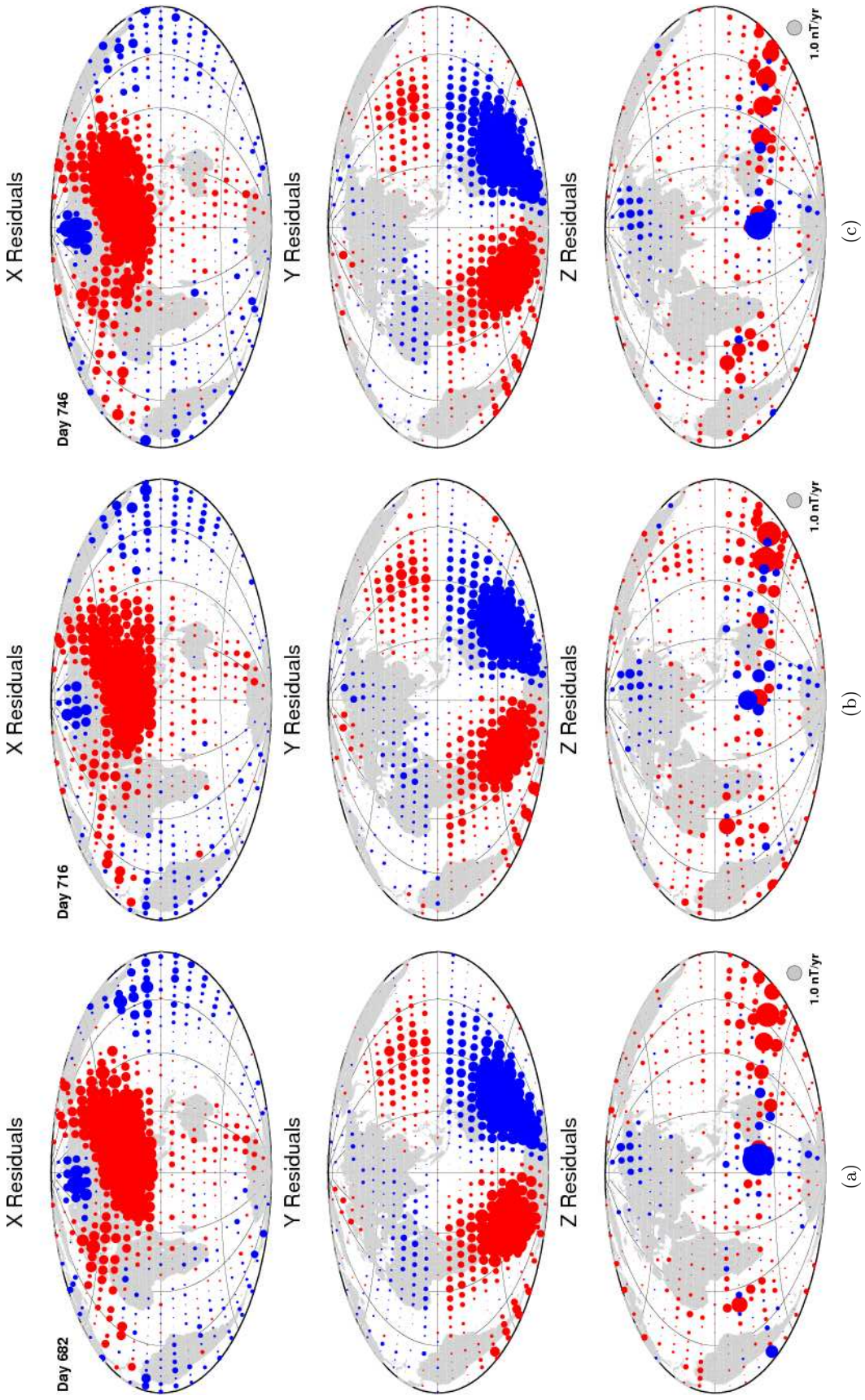

Figure 4.17: Geographic distribution of the residual fit of three flow models to SV data simulated from the CHAOS model and the CHAMP orbits generated from Virtual Observatory grid with *equal area* tessera. Positive residuals in red, negative residuals in blue. (a) Month 1; (b) Month 2; (c) Month 3.

4.6 Correction Strategies

Olsen & Mandea (2008) have indicated that rapidly changing flows occur within the core but note, in the Supplementary Information for their paper, that these variations may in part be due to unmodelled external (ionospheric and magnetospheric) sources. They also clearly demonstrate in a previous study (Olsen & Mandea, 2007, Figure 6) that the first differences of the external and toroidal field Gauss coefficients (e.g. dq_1^0/dt and dt_1^0/dt) are up to an order of magnitude larger than those for the coefficients for the internal SV. The results presented in the previous section strongly suggest that artefacts from external fields may affect their results.

The previous section presented tests of several causes for the biased residuals seen in Dataset 1 and Dataset 2, including effects from (a) fields external to the satellite orbit, (b) fields internal to the satellite orbit but external to the Earth, and (c) the orbital configuration of the satellite and the method of binning in preparation of the VO SV datasets. Here I further analyse the results of the tests, with the aim of removing or ameliorating the influence of these effects to produce datasets of purely internal SV which are temporally consistent and spatially un-biased. At the same time, I wish to ensure that there is minimal 'aliasing' of undesirable effects into the SV datasets. These could manifest as unrealistic secular acceleration within the flow models. Five strategies are tested, from individual data correction to model parameterisation, in an attempt to remove or reduce the impact of unwanted field contamination. The following corrections strategies are applied:

1. Removal of parameterised fields using the Comprehensive Model (CM4)
2. Spherical Harmonic decomposition of the SV into its internal, external and toroidal parts
3. Covariance Rotation of the SV data to reduce external contamination effects
4. Temporal smoothing of flow models using B-splines
5. Calculation of a steady flow model over the time period.

Each correction strategy is now described in detail.

4.6.1 Removal of fields using the Comprehensive Model

Modelling and removal of external, toroidal and induced magnetic fields at satellite altitude is complex. These magnetic fields have not been fully parameterised, nor can they be completely removed (Thomson & Lesur, 2007). However, models of the external and other contributory magnetic fields, derived from parameterised inversion of large datasets, can be used to correct measured satellite data.

I tested the influence of removing external and ionospheric field models from the CHAMP satellite data using the Comprehensive Model (CM4) of Sabaka et al. (2004). The nominal hourly Dst magnetic index and the monthly solar flux activity (called the F10.7 index) over 2001–2006 were used as input parameters (Sabaka et al., 2004). These indices are used to estimate the activity of the external and ionospheric magnetic fields. The sum of the primary and secondary magnetospheric, ionospheric and toroidal fields were subtracted from the individual CHAMP measurements before binning and calculating the VO field. The resulting residuals from inverting for flow models showed mixed results compared to those from Dataset 1 (see residuals in Figure 4.20), but the use of corrected data did not, on average, produce a better fit than Dataset 2 (based on the sum of the absolute values of the residuals). However, the CM4 correction does reduce the correlation between the residual bias and the annual Dst difference (i.e. change in Dst index). Table 4.2 shows the correlations between the annual Dst difference and the two VO dataset residuals with two binning methods. This approach has the largest decorrelation effect on Dataset 2, where selected 'night-side' only data are used, suggesting that the CM4 model performs better on the night-side of the planet perhaps due to the less complex field environment (see residuals in Figure 4.21).

However, correcting Dataset 2 using CM4 does not improve the overall fit of the flow to the data, as the size of the residuals remain approximately equal (for an equivalent solution norm). Figure 4.18 shows the sum of the absolute values of the residuals from month to month (using the equal latitude/longitude binning method). Dataset

	Dataset 1 (Equal LL)	Dataset 1 (Equal Area)	Dataset 2 (Equal LL)	Dataset 2 (Equal Area)
No correction	0.66	0.67	0.63	0.67
CM4 correction	0.41	0.42	0.10	0.16

Table 4.2: Correlation between the mean bias of the $\dot{X}$ component of the residuals for each Dataset and the annual Dst difference.

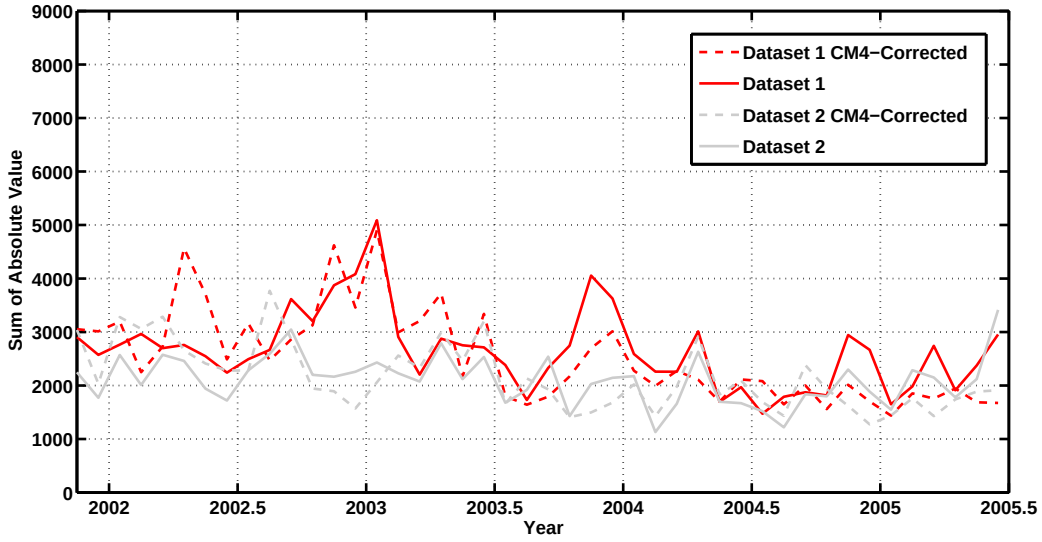

Figure 4.18: Comparison of the sum of absolute value of the residuals for Datasets 1 and 2 (grid of equal latitude/longitude) with and without data correction using CM4. Note the solution norms are approximately similar.

2 without CM4 correction provides the best overall fit to the data, though for some months (particularly towards the end of the data set), the CM4 corrected datasets are better. Individual comparison of the flow models between the CM4 corrected and uncorrected datasets show strong similarities. It would appear that CM4 removes much of the external part of the field and prevents most of it being aliased into the flow models, but introduces other unwanted signals, which reduces the effectiveness of the attempted correction. A similar result is encountered when using the grid of equal area tessera (shown in Figure 4.19).

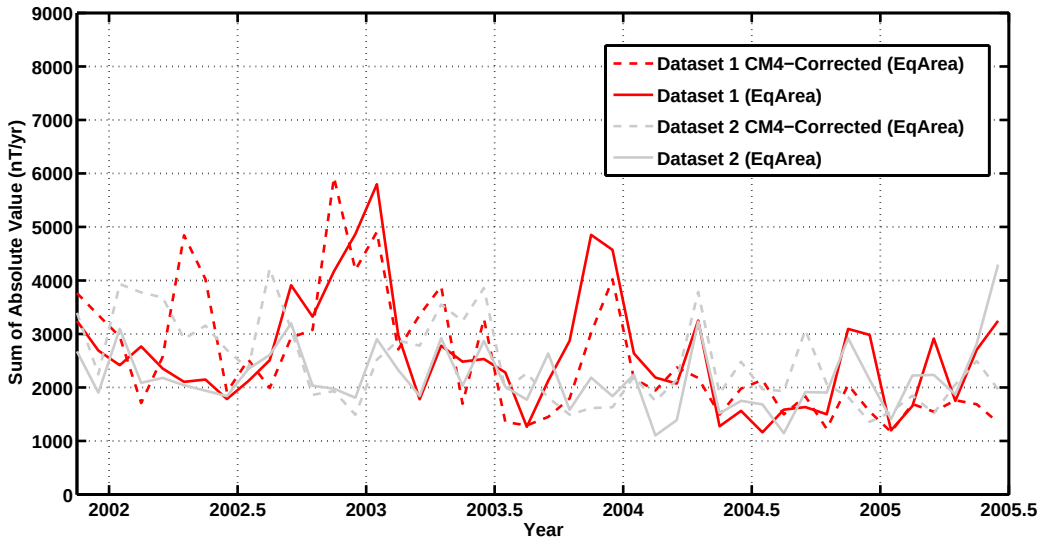

Figure 4.19: Comparison of the sum of absolute value of the residuals for Datasets 1 and 2 (grid of equal area tessera) with and without data correction using CM4. Note the solution norms are approximately similar.

(a) November 2001 (b) February 2003 (c) March 2005

Figure 4.20: Geographic distribution of the residual fit of each flow model to the SV generated from Virtual Observatory grid of equal latitude and longitude spacing for *all data with CM4 correction* vector measurements. Circle size indicates residual size, with reference circle shown in bottom right. Positive residuals in red, negative residuals in blue. (a) November 2001; (b) February 2003; (c) March 2005.

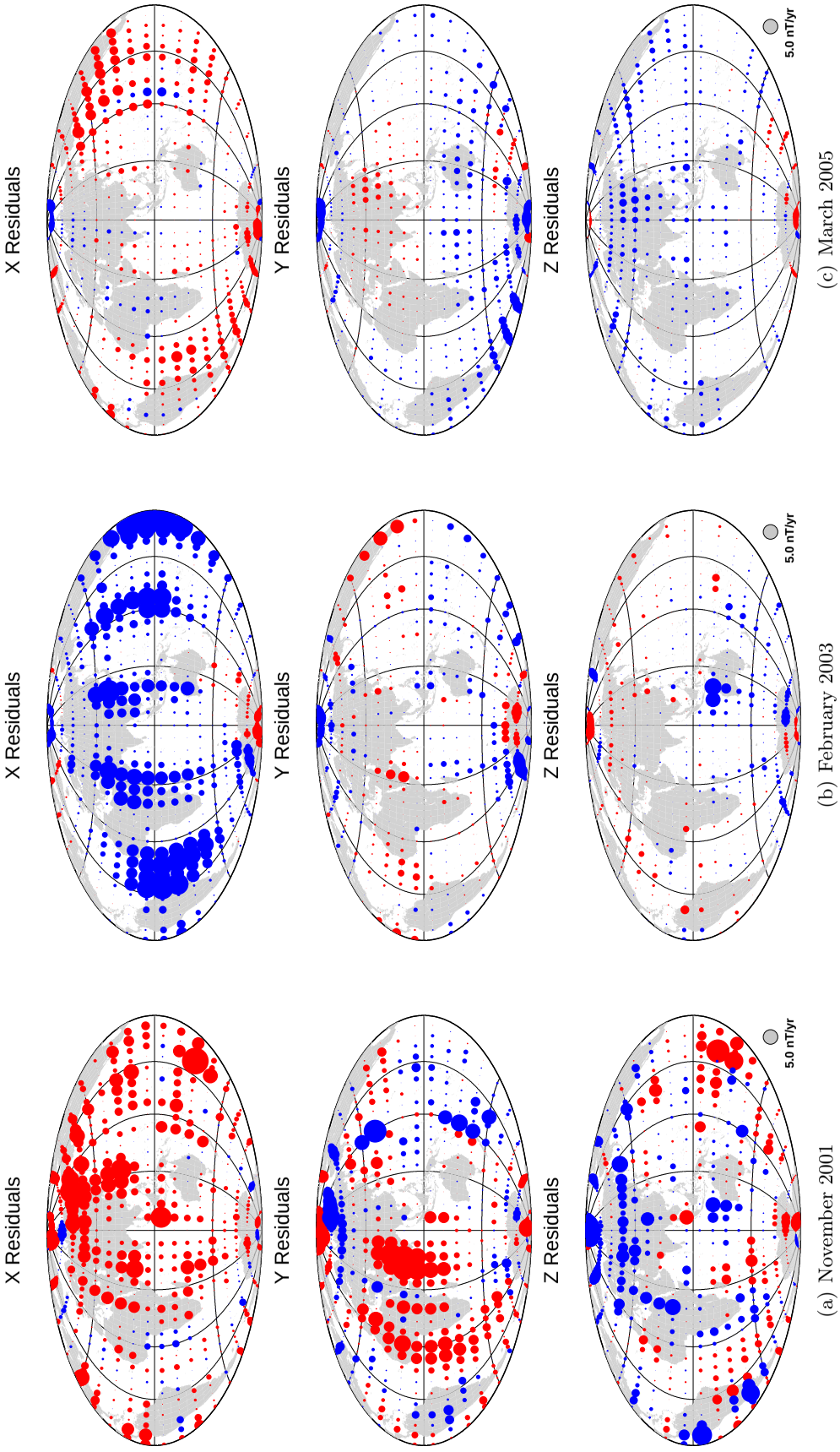

(a) November 2001 (b) February 2003 (c) March 2005

Figure 4.21: Geographic distribution of the residual fit of each flow model to the SV generated from Virtual Observatory grid of equal latitude and longitude spacing for *night-side only with CM4 correction* vector measurements. Circle size indicates residual size, with reference circle shown in bottom right. Positive residuals in red, negative residuals in blue. (a) November 2001; (b) February 2003; (c) March 2005.

4.6.2 Spherical Harmonic Analysis of the VO datasets

Rather than correcting the data individually, it might be possible to undertake a global correction of the VO field models. By applying spherical harmonic analysis to a VO field model, it is possible to separate the internal, external and toroidal field components (Olsen, 1997). The individual components of the field (internal, external and toriodal) can be examined to understand how each distinct part contributes to the SV. The separation into the three components is a least-squares fit and so is not exact. However, the residual difference between the summation of the internal, external and toriodal components and the input VO field models is very small (generally < 1nT) without any obvious patterns or bias.

For each dataset, the monthly VO fields were resolved (or decomposed) into internal, external and toroidal parts using the method of Olsen (1997). Each part (or component) of the field is resampled back to a VO grid of equal latitude and longitude and the annual SV calculated for the $\dot{X}$, $\dot{Y}$ and $\dot{Z}$ vector components. Each of the internal, external and toroidal field components are treated as if they were internal SV and inverted for instantaneous flow. The models of the flow generated by inverting internal SV (Figure 4.22), external SV (Figure 4.23) or toroidal SV (Figure 4.24) all show rapid temporal variation.

(a) Residual Distribution: November 2001

(b) Residual Distribution: February 2003

(c) Residual Distribution: March 2005

Figure 4.22: Core-mantle boundary flow models: geographic distribution of the residual fit of each flow model to the **Internal** SV generated from Virtual Observatory grid of equal latitude and longitude spacing for *all* available vector measurements. Circle size indicates residual size, with reference circle shown in bottom right. Positive residuals in red, negative residuals in blue. Continents shown for reference.

(a) Residual Distribution: November 2001

(b) Residual Distribution: February 2003

(c) Residual Distribution: March 2005

Figure 4.23: Core-mantle boundary flow models: geographic distribution of the residual fit of each flow model to the **External** SV generated from Virtual Observatory grid of equal latitude and longitude spacing for *all* available vector measurements. Circle size indicates residual size, with reference circle shown in bottom right. Positive residuals in red, negative residuals in blue.

(a) Residual Distribution: November 2001

(b) Residual Distribution: February 2003

(c) Residual Distribution: March 2005

Figure 4.24: Core-mantle boundary flow models: geographic distribution of the residual fit of each flow model to the **Toroidal** SV generated from Virtual Observatory grid of equal latitude and longitude spacing for *all* available vector measurements. Circle size indicates residual size, with reference circle shown in bottom right. Positive residuals in red, negative residuals in blue.

Dataset	Internal	External	Toroidal
Dataset 1: No correction	*0.12*	0.64	*0.02*
Dataset 1: CM4 correction	*-0.11*	0.38	*-0.01*
Dataset 2: No correction	*0.01*	0.61	*0.12*
Dataset 2: CM4 correction	*0.04*	*0.05*	*0.23*

Table 4.3: Correlation between the mean bias of the $\dot{X}$ component of the residuals for the Internal, External and Toriodal parts of Datasets 1 & 2 and the annual Dst difference. Values *in italics* indicate the correlation is not significant.

The residual biases from the flow models inverted from the external component of the field were the most strongly correlated to the annual Dst difference. The geographic distribution of the residuals from the external component are similar to those observed in Datasets 1 and 2, see Figure 4.23 (g–i).

Examination of the residuals from flow models of the internal SV show they are more randomly distributed than those from Datasets 1 and 2 (i.e. no patterns or $\dot{X}$, $\dot{Y}$ or $\dot{Z}$ component biases – see Figure 4.22 (g–i)), suggesting that the biases arise mostly from the external and toroidal parts of the field. However, there is still a rapidly time varying component in the internal flow models, suggesting that some unwanted signal still remains within the internal flow model. This supports the assertion of Olsen & Mandea (2008) that isolating the internal SV is difficult. Table 4.3 shows the correlation of the mean value of the $\dot{X}$ component of the internal, external and toroidal parts of the SV with the Dst index, showing that because of the high correlation the external part of the field has indeed removed much of the external signal, while the internal part is no longer correlated with the external field.

The residuals to the flow models of the toroidal part appear to be cleanest in the $\dot{X}$ and $\dot{Y}$ components, while the $\dot{Z}$ component is badly fit by the flow (Figure 4.24 (g–i)).

The flow models from the toroidal and external parts of the SV contain approximately 3.5% and 0.5% of the root-mean-square flow velocity compared to that of the internal SV model. Although the internal flow coefficients represent most of the power in terms of root-mean-square velocity, they are not necessarily the source of all the variability in the flow from month to month. The individual contributions of the in-

Dataset	Toroidal/Internal	External/Internal
Dataset 1: No correction	0.47	0.66
Dataset 1: CM4 correction	0.21	0.57
Dataset 2: No correction	0.40	0.23
Dataset 2: CM4 correction	0.28	0.41

Table 4.4: The mean ratio of the standard deviation of external and toroidal flow coefficients to the standard deviation of internal flow coefficients for the Equal Latitude/Longitude Datasets.

ternal, external and toroidal components to the variability of the flow were examined. Table 4.4 shows the mean ratio of the standard deviation of the external and toroidal flow coefficients to the standard deviation of the internal flow coefficients. It was found that the combined variance of the external and toroidal components was similar to the variance of the internal coefficients. This suggests that the variability in the flow models from month to month comes approximately equally from the internal and the combined external and toroidal parts of the SV.

In terms of the overall best fit to the flow models, Figure 4.25 shows the Sum of the Absolute Values (SAV) of the residuals for the internal flow models for Datasets 1 and 2. It reveals that, on average, Dataset 1 with CM4 correction has the lowest SAV, indicating that the flow models from the internal part of a internal/external/toroidal SH analysis of this dataset are best fit to the VO SV. This result is different to the conclusion of Section 4.6.1, where flows derived from the inversion of Dataset 2 best matches the input VO SV. A full comparison of all the methods is discussed later.

4.6.3 Covariance Rotation of the VO dataset

In the previous chapter (Chapter 3), three datasets of SV from ground-based observatories were employed to test the assumptions used for core flow modelling inversion. The first dataset consisted of the direct calculation of SV from first differences of the annual observatory means (in the X, Y and Z components). The second and third dataset of ground-based observatory SV, provided by I. Wardinski (pers. comm., 2009), had been partiall and fully processed to account for the covariance between the $\dot{X}$, $\dot{Y}$ and $\dot{Z}$ com-

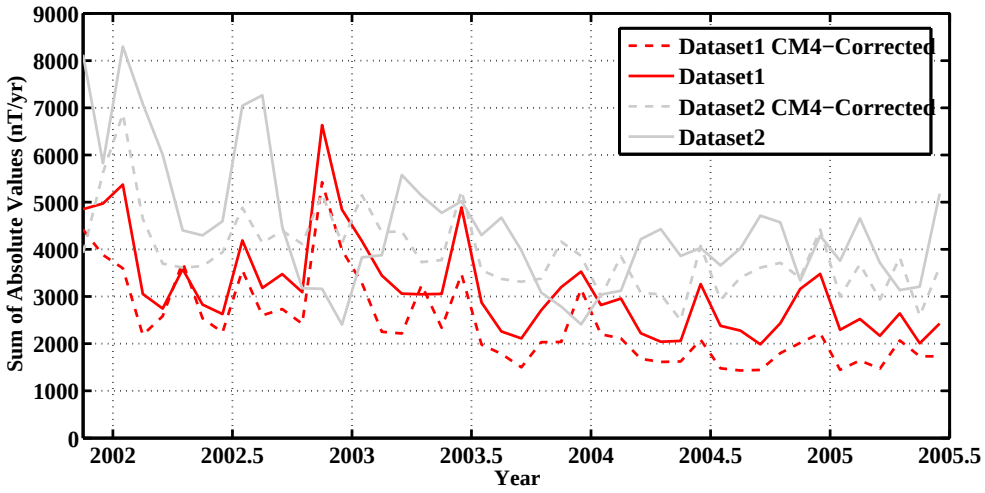

Figure 4.25: Sum of Absolute Values metric for internal parts of the SV from Datasets 1 and 2 with and without CM4 corrections applied.

ponents. The method of 'covariance rotation' (Wardinski & Holme, 2006) projects the $\dot{X}$, $\dot{Y}$ and $\dot{Z}$ components into a rotated coordinate axis, where directions are ordered (using the eigenvalues of the covariance matrix) from least to most noisy. This method reduces the noise in at least one of the directions.

Typically, $\dot{Y}$ is the least noisy direction, as the X and Z directions of the recorded magnetic field data are contaminated (at ground level) by external field noise. The advantage of this method is that the flow models from the covariance rotated dataset produce a better fit to the input SV (c.f. Table 3.2). Details of the method are found in Wardinski (2005) and Wardinski & Holme (2006). I implemented a Matlab version of the method in conjunction with Richard Holme (pers. comm., 2007).

To apply the covariance rotation to the VO datasets, the CHAOS field model is subtracted from the individual $\dot{X}$, $\dot{Y}$ and $\dot{Z}$ components for each virtual observatory, giving an individual time-series of field residuals. The covariance matrix of the $\dot{X}$, $\dot{Y}$ and $\dot{Z}$ residuals is calculated. The resulting individual covariance matrix for the observatory is then used to construct the full block diagonal covariance ($\mathbf{C}_e^{-1}$) for the inversion algorithm.

This method was applied to Datasets 1 and 2 (equal latitude/longitude grids) to

determine if the fit of the flow models to the VO SV improved (as was the case for the ground-based observatory datasets c.f. Chapter 3). For Dataset 1, the resulting flow models and residual distributions for the months of Nov. 2001, Feb. 2003 and March 2005 are shown in Figures 4.26 and 4.27. The flow models and distributions show rapid temporal variation. However, the distribution of the residuals have changed in comparison to Figure 4.9. The $\dot{Z}$ component has become far quieter while the $\dot{X}$ and $\dot{Y}$ components are noisier but no longer have strong longitudinal banding. The pattern in the $\dot{X}$ and $\dot{Y}$ residuals appears to be more constant over time. There is not a strong monthly variation in strength or sign of the residuals for any particular VO.

Analysis of Dataset 2 reveals (Figures 4.28 and 4.29) similar rapid flow variations and residual distributions. However, in ageement with the findings from Section 4.4, the fit of the flow models to the SV data is better - indicating the covariance rotation does improve the flow models by removing correlated external influences.

The covariance rotation was applied to Datasets 1 and 2 which had previously been corrected by subtraction of the fields parameterised by CM4 (see previous section 4.6.1). Figures 4.30 and 4.31 show the resulting residuals to the flow models. Interestingly, on average, Dataset 1 with CM4 correction has the lowest SAV, indicating that the flow models from this dataset are best fit to the VO SV. This is in contrast to the finding from the previous section (i.e. Dataset 2 is best fit).

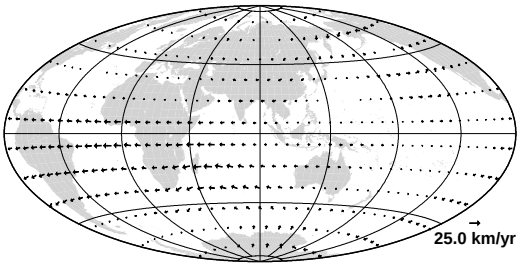

(a) Flow Model: November 2001

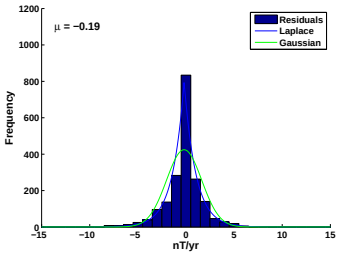

(b) Histogram of Flow Model Residuals: November 2001

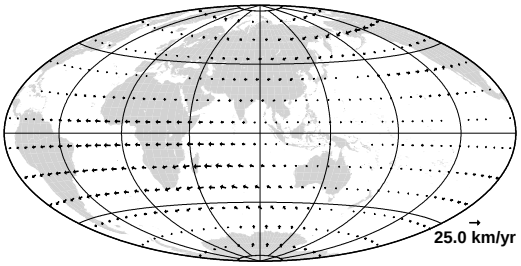

(c) Flow Model: February 2003

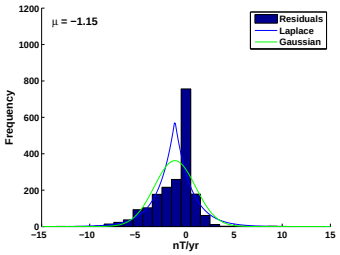

(d) Histogram of Flow Model Residuals: February 2003

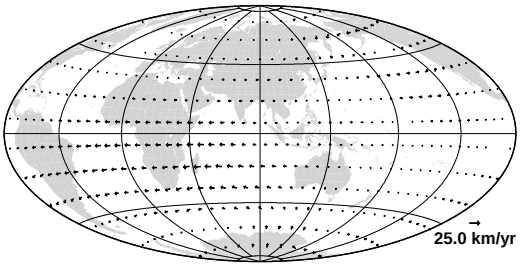

(e) Flow Model: March 2005

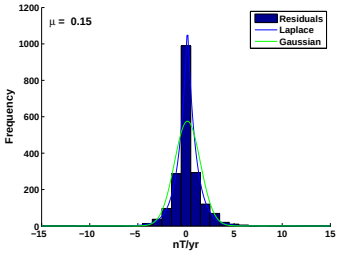

(f) Histogram of Flow Model Residuals: March 2005

Figure 4.26: Core-mantle boundary flow models (a, c, e) and histograms (b, d, f) of the residual fit of each flow model to the SV generated from Virtual Observatory data grid of equal latitude-longitude for *all* available vector measurements with a covariance rotation applied to the SV data. In (b, d, f), the Laplacian and Gaussian fits to the data are shown in the blue and green curves respectively. Continents shown for reference.

(a) Residual Distribution: November 2001

(b) Residual Distribution: February 2003

(c) Residual Distribution: March 2005

Figure 4.27: Geographic distribution of the residual fit of each flow model to the SV generated from Virtual Observatory data grid of equal latitude-longitude for *all* available vector measurements with a covariance rotation applied to the SV data. Circle size indicates residual size, with reference circle shown in bottom right. Positive residuals in red, negative residuals in blue. Continents shown for reference.

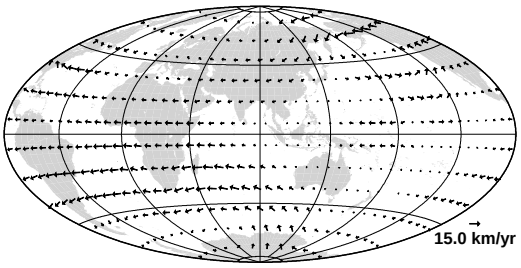

(a) Flow Model: November 2001

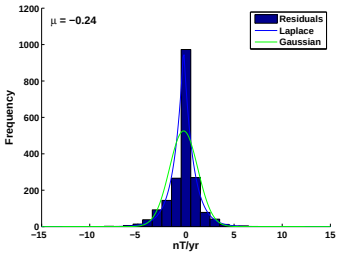

(b) Histogram of Flow Model Residuals: November 2001

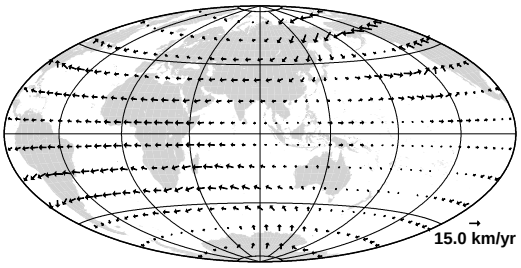

(c) Flow Model: February 2003

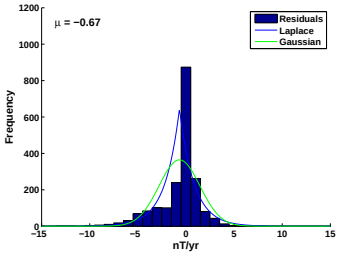

(d) Histogram of Flow Model Residuals: February 2003

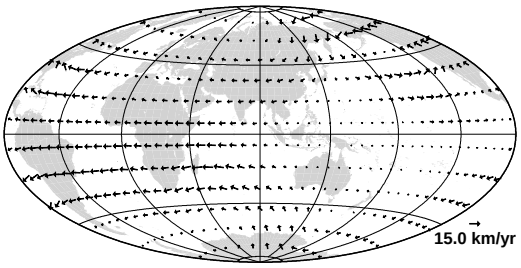

(e) Flow Model: March 2005

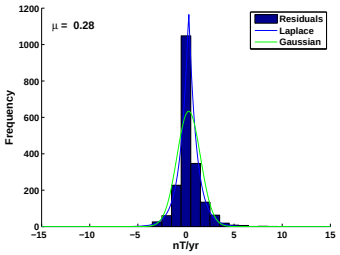

(f) Histogram of Flow Model Residuals: March 2005

Figure 4.28: Core-mantle boundary flow models (a, c, e) and histograms (b, d, f) of the residual fit of each flow model to the SV generated from Virtual Observatory data grid of equal latitude-longitude for *night-side only* available vector measurements with a covariance rotation applied to the SV data. In (b, d, f), the Laplacian and Gaussian fits to the data are shown in the blue and green curves respectively. Continents shown for reference.

(a) Residual Distribution: November 2001

(b) Residual Distribution: February 2003

(c) Residual Distribution: March 2005

Figure 4.29: Geographic distribution of the residual fit of each flow model to the SV generated from Virtual Observatory data grid of equal latitude-longitude for *night-side only* available vector measurements with a covariance rotation applied to the SV data. Circle size indicates residual size, with reference circle shown in bottom right. Positive residuals in red, negative residuals in blue.

(a) Residual Distribution: November 2001

(b) Residual Distribution: February 2003

(c) Residual Distribution: March 2005

Figure 4.30: Geographic distribution of the residual fit of each flow model to the SV generated from Virtual Observatory data grid of equal latitude-longitude for *all* available vector measurements with a correction from CM4 plus a covariance rotation applied to the SV data. Circle size indicates residual size, with reference circle shown in bottom right. Positive residuals in red, negative residuals in blue.

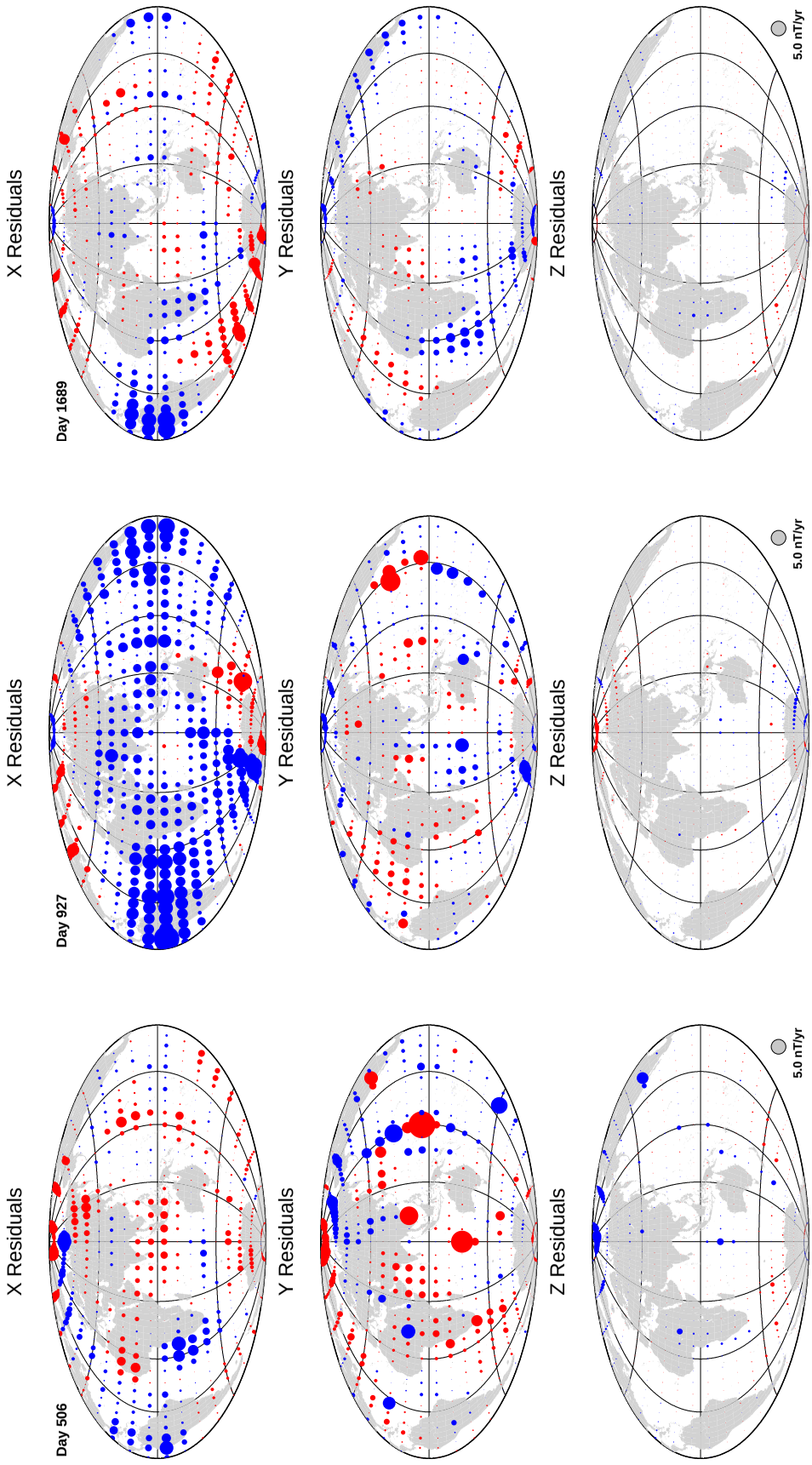

(a) Residual Distribution: November 2001 (b) Residual Distribution: February 2003 (c) Residual Distribution: March 2005

Figure 4.31: Geographic distribution of the residual fit of each flow model to the SV generated from Virtual Observatory data grid of equal latitude-longitude for *night-side only* available vector measurements with a correction from CM4 plus a covariance rotation applied to the SV data. Circle size indicates residual size, with reference circle shown in bottom right. Positive residuals in red, negative residuals in blue.

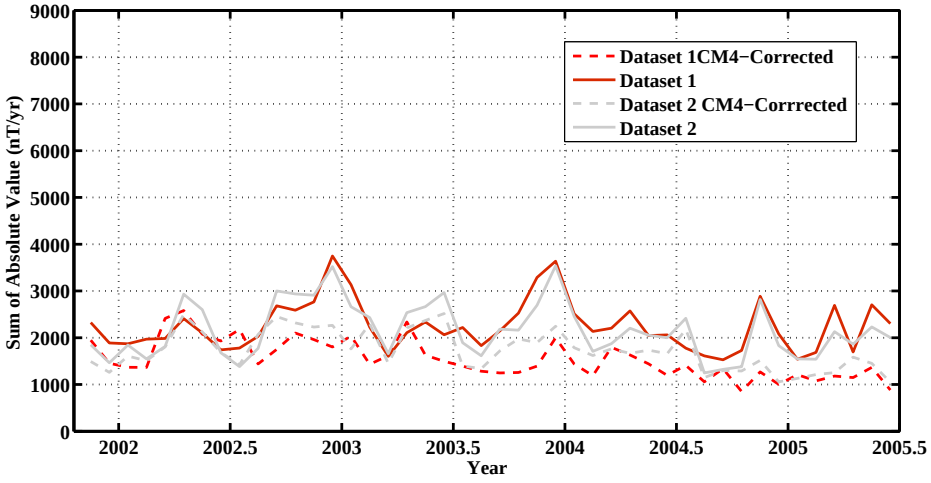

Figure 4.32: SAV metric for Covariance rotated Datasets 1 and 2.

To summarise the results from this section, Figure 4.32 shows the sum of the absolute value of the residuals for each month. It is of interest to note that the covariance rotation does strongly improve the fit of the flow to the data, particularly in conjunction with CM4. It is also worth noting that the variability of the SAV is much less with the covariance rotation applied (e.g. compare the variability in Figure 4.18 and Figure 4.32.) This suggests that the covariance correction is concentrating the noisy data into one direction, smoothing much of the month-to-month variance, as would be expected.

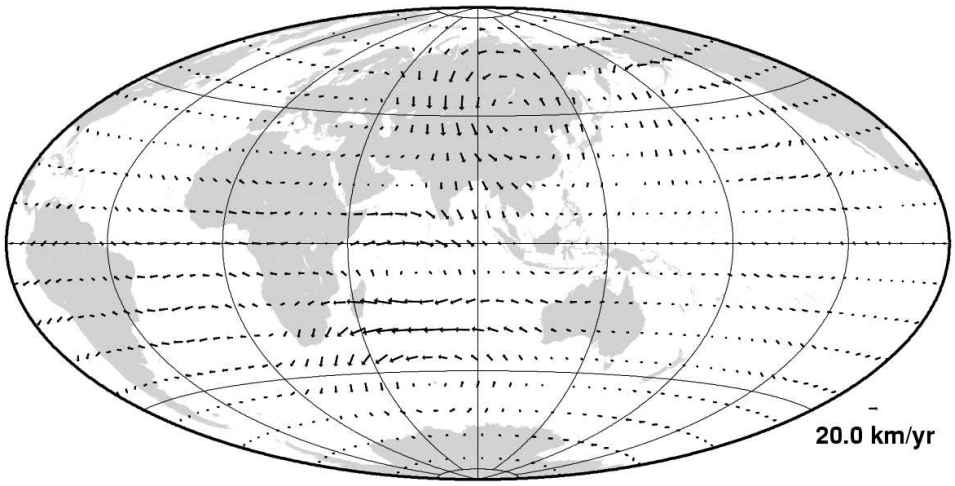

Figure 4.33: Steady Flow model from 2001–2005 for Dataset 1 (All CHAMP data) Equal Lat-Lon grid. Other steady flow models have similar flow patterns.

4.6.4 Smoothing using Steady Flow

An alternative approach to applying a correction to the satellite data is to attempt to smooth the flow models themselves, rather than treat the satellite data individually or globally. In particular, I attempted to (a) calculate steady flows over the specified period, averaging out the changing monthly flows and (b) fit a series of B-splines (de Boor, 2001) to the flow coefficients.

Steady flows calculated over the entire dataset period using Datasets 1 and 2 are very consistent, as indicated by their correlation coefficient, which can be expressed as:

$$\mathcal{C} = \frac{\sum_{l=1}^{l_{max}} \frac{l(l+1)}{2l+1} \sum_{m=0}^{l} \left(s_{l1}^{m} s_{l2}^{m} + t_{l1}^{m} t_{l2}^{m} \right)}{\sqrt{\sum_{l=1}^{l_{max}} \frac{l(l+1)}{2l+1} \sum_{m=0}^{l} \left({s_{l1}^{m}}^2 + {t_{l1}^{m}}^2 \right) \sum_{l=1}^{l_{max}} \frac{l(l+1)}{2l+1} \sum_{m=0}^{l} \left({s_{l2}^{m}}^2 + {t_{l2}^{m}}^2 \right)}} \tag{4.4}$$

where l is the degree, m is the order of the flow coefficients of the spherical harmonic expansion of the toroidal and poloidal scalars t and s; l_{max} is the maximum degree of the flow solution. Subscripts 1 & 2 denote coefficients from Dataset 1 and 2 respectively. Flow models that are similar have a correlation coefficient close to 1. Table 4.5 shows the correlation coefficients of the various steady flows generated by Datasets 1 and 2

	A	B	C	D
A: Dataset 1: No correction	1	0.91	0.97	0.92
B: Dataset 1: CM4 correction		1	0.91	0.91
C: Dataset 2: No correction			1	0.93
D: Dataset 2: CM4 correction				1

Table 4.5: Correlation matrix of steady flow coefficients for Datasets 1 and 2 generated from 44 months of SV data.

with and without CM4 correction. The values are remarkably consistent (for equivalent solution norms), suggesting that steady flows are removing the finer scale temporal features, producing a smoother flow solution. Note, the monthly residuals to the steady flows reveal features and patterns similar to those from Dataset 1, confirming that particular flow model assumptions are not directly related to or the cause of the residual patterns. Figure 4.33 shows the steady flow from 2001–2005 for Dataset 1 (using the equal latitude/longitude grid). There are two large gyres visible - one beneath Asia and the other in the Indian Ocean. All other steady flows show similar patterns of flow.

4.6.5 Smoothing using B-Splines

Cubic B-splines were fitted to the flow coefficients to examine temporal changes in the flow. Rather than assuming a simple steady flow or using the rapidly-varying flow models from each month, B-spline fits to the flow coefficients allow the flow to vary slowly over the period in question. By altering the tension within the spline via a damping parameter, the amount of SV and secular acceleration can be adjusted. This allows some secular acceleration to be parameterised through the B-splines, resulting in a more sophisticated explanation of the change than steady flow.

Following the approach of Wardinski (2005) and Olsen & Mandea (2008) splines were fit through the 44 monthly flow models using 10 knot points with a damping parameter of 100. These smooth the variations of the flow over time. Figure 4.34 shows a set of B-splines fitted through the first six flow coefficients from Dataset 2. An interesting comparison to make is the change in the misfit of the smoothed flow to the SV data. Inevitably, the fit of the smooth flows to the VO SV will decrease.

To calculate the misfit of the B-spline fitted flows, the residuals to the VO SV generated by the flows for each month were computed. Figure 4.36 shows the comparison of the Sum of Absolute Values of the residuals for each month. Figure 4.35 illustrates the spatial distribution of the residuals. Note the change in the legend (25nT/yr) compared to other residuals plots (5nT/yr). It is concluded that smoothing the flow leads to more slowly varying flow changes but increases the misfit to the SV data approximately ten-fold, in this case. Note the continued presence of the hemispherical and banded residual patterns.

An alternative method of smoothing, instead of smoothing flow coefficients using B-splines, would be to invert for both temporal and spatial smoothing of the flow similtaneously. This would certainly produce a smoother overall flow change, but would not fit the data as well as instantaneous flows. It would also act as more complex low pass filter, aliasing some of the unwanted field signals into the flow. It would be thus more difficult to identify the various contaminating contributions at that point.

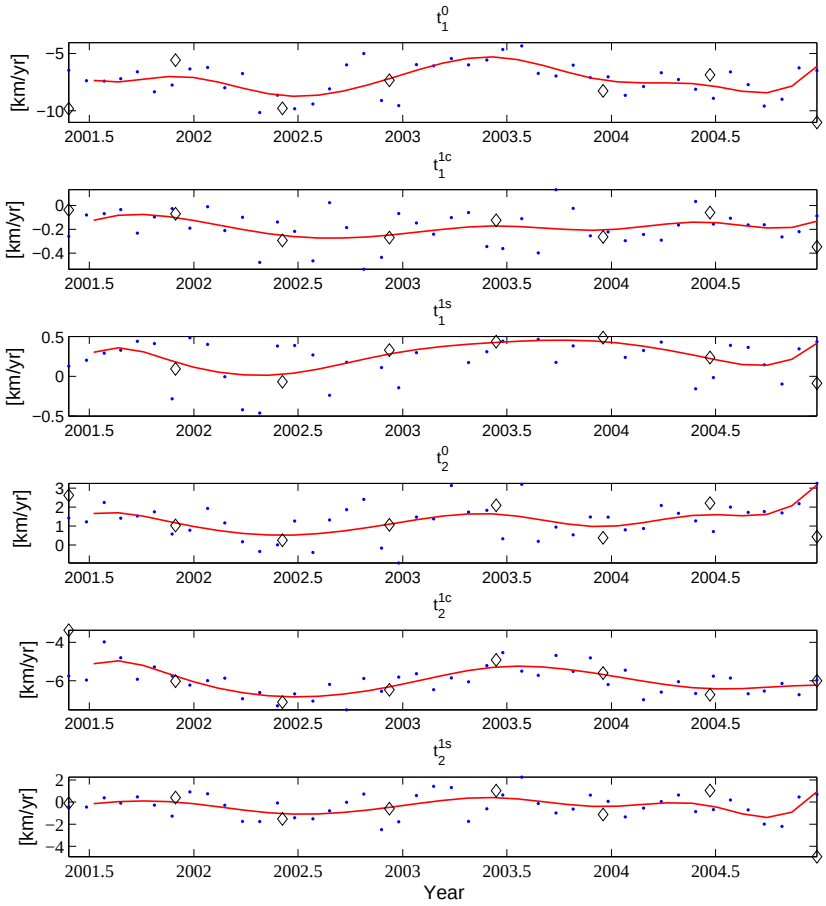

Figure 4.34: An example of B-Spline fits to the first five coefficients of the flow model from Dataset 2 Equal Latitude-Longitude VO model. Blue dots are the values of the flow coefficients each month; Black open diamonds are the knot control points and the solid red line is the B-spline fit through the flow coefficients.

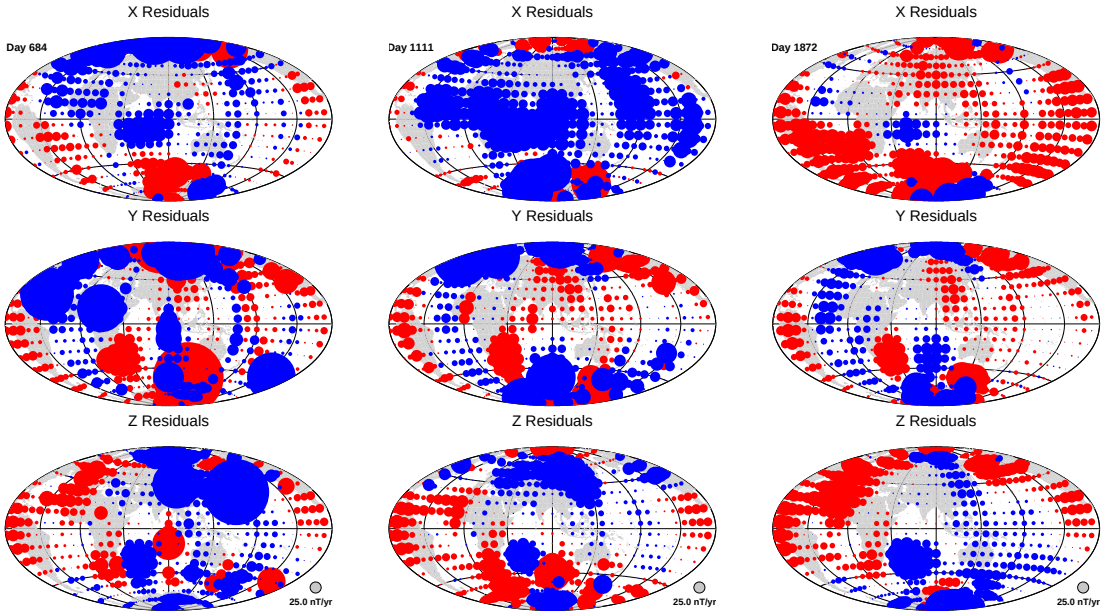

(a) November 2001 (b) February 2003 (c) March 2005

Figure 4.35: Geographic distribution of the residual fit from B-spline smoothed flow models to the SV generated from Virtual Observatory grid of equal latitude and longitude spacing for *night-side only* vector measurements. Circle size indicates residual size, with reference circle shown in bottom right (now 25nT). Positive residuals in red, negative residuals in blue. (a) November 2001; (b) February 2003; (c) March 2005.

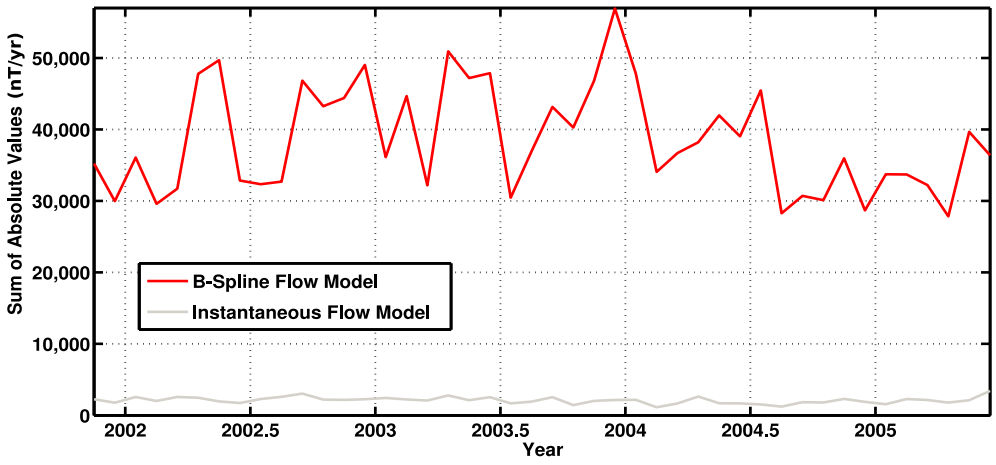

Figure 4.36: SAV metric for B-spline smoothed flows and Dataset 2.

4.7 Comparison of Datasets and Correction Strategies

In this section, I compare the fit of the flow models from Datasets 1 and 2 when different gridding methods and data corrections are applied. It should be noted that using a metric based upon flow model misfit is only one method of examining flow model fits. However, the comparisons of flow model fits are not exactly equivalent, as each SV dataset is slightly different. Nevertheless, in conjunction with the visual appraisal of the data given in this chapter, it is clear that the different corrections, processing and data selection produce markedly contrasting results from the initial starting CHAMP satellite dataset.

Figure 4.37 shows the sum of the absolute values of the residuals for each of the processes and corrections applied to the satellite data. (Note all these figures have been previously shown.) A number of conclusions can be drawn from examination of the graphs:

1. The residuals from Dataset 1 with and without CM4 correction always show most variability in the first half of the period (except in Figure 4.37(d)).

2. Without covariance rotation or SH analysis of the satellite data, Dataset 1 has the poorest fit while Dataset 2 fits best (Figure 4.37(a) and (b)).

3. With covariance rotation and SH analysis, Dataset 1 with CM4 correction fits best, particularly in the second half of the period (Figure 4.37(c) and (d)).

4. Overall, it appears that the covariance correction strategy has the strongest positive effect in removing contamination and improving the fit of the flow to the data.

Table 4.6 summarises the Mean SAV from each of the graphs in Figure 4.37. The best fit flow appears to be generated from Dataset 1 with CM4 correction and covariance rotation, i.e. by including corrections for known parameters and further filtering out correlated signals in the data.

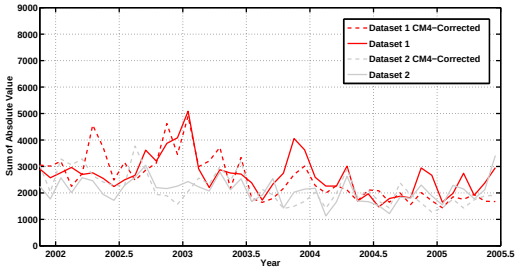

(a) SAV Metric: Equal LL Grid

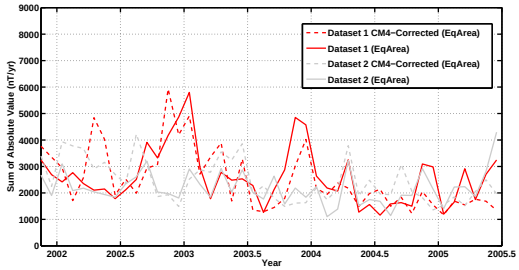

(b) SAV Metric: Equal Area Grid

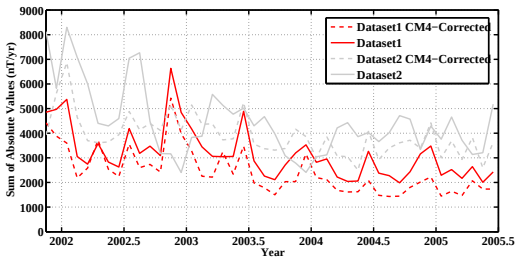

(c) SAV Metric: SH Internal

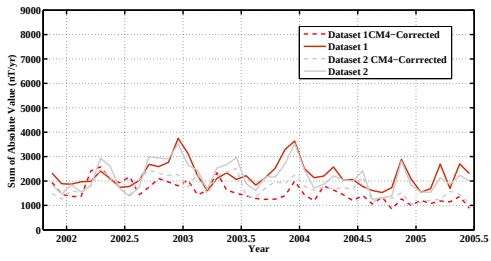

(d) SAV Metric: Covariance Rotated

Figure 4.37: Summary of the Sum of Absolute Value Metric for Datasets 1 and 2 using several correction techniques.

4.8 Summary

The results from this study strongly suggest that the assumption of Mandea & Olsen (2006) that the VO method produces zero mean, unbiased monthly field estimates is incorrect. The geographic distribution of the residuals to the flow models are strongly biased by external magnetic fields. When viewed in sequence, the flow models generated using all available CHAMP vector data (Dataset 1) show rapid variation in direction, strength and structure from month to month. The geographic distributions of the residuals are not random - they show continuous variation in component bias (from positive to negative), hemispherical bias, sectorial banding and the magnitude of residual biases.

There is a small improvement in the fit of the flows to the data when the night-side only vector data are used to create a VO dataset (Dataset 2). A similar improvement can be seen when each satellite datum is corrected using a CM4 model to remove unwanted external and internal (to the satellite) fields prior to binning. This points to magnetospheric, ionospheric and day-side current systems as significant sources of contamination. In contrast, the smaller, more randomly-distributed residuals from the

Dataset	Grid	CM4	Covariance	SH Internal	Mean SAV
Dataset 1	LL	Y	Y		**1544**
Dataset 2	LL	Y	Y		1734
Dataset 2	LL				2104
Dataset 2	LL	Y		Y	2156
Dataset 2	LL	Y			2160
Dataset 2	Area				2192
Dataset 1	LL	Y			2244
Dataset 1	LL	Y		Y	2432
Dataset 2	Area	Y			2459
Dataset 1	Area	Y			2504
Dataset 1	Area				2617
Dataset 1	LL				2654
Dataset 1	LL			Y	3158
Dataset 2	LL		Y		3757
Dataset 1	LL		Y		4269
Dataset 2	LL			Y	4467

Table 4.6: Summary of the mean SAV from Datasets 1 and 2 with varying gridding and corrections applied. Table is sorted in ascending order. The following headings are used: Grid is the type of gridding method *(a)* Equal Latitude/Longitude (LL) or *(b)* Equal Area Tessera (Area). CM4 denotes if the Dataset has been corrected by subtraction of parameterised fields generated by Comprehensive Model 4. Covariance denotes if the covariance rotation correction has been applied. SH Internal indicates the internal part of the SV as derived from Spherical Harmonic analysis of the VO field model was used.

selected quiet-time Ørsted-CHAMP data (Dataset 3) indicate that contamination of these data is much less, though still present. This points to signals external to the satellite orbit contaminating Datasets 1 and 2.

Another potential source of non-zero mean error is the method of generating the VO dataset. The CHAMP satellite precesses approximately 2.5 hours per month in local time. As the data used to generate the VO are not from all local times, but rather a small subset of day/night local times, this has the effect of *not* averaging out diurnal effects. For example, in a month where the local time is noon on the day side and midnight on the night side, a significant bias must be present due to currents internal to the satellite orbit. As noted in Equation (1.5), to calculate the annual SV for a particular month the VO value for six months prior is subtracted from the VO value six months ahead. The magnetic field environment will also be different for measurements collected 12 months apart, as the satellite nadir local times vary between 3 and 5 hours due to orbital drift. For example, a VO with a predominantly noon local time subtracted from a VO with predominantly morning local time will sense different ionospheric-related fields. A grid with equal latitude/longitude spacing, where bins overlap near the poles and have gaps between them at the low latitudes, rather than equal area tessera, was found to accentuate certain patterns, such as sectorial banding and predominance of large residuals at the polar regions. The results from a synthetic dataset support the conclusion that sectorial banding is related to the orbital drift and binning method.

Separation of the SV into its internal, external and toroidal components partitioned most of the influence from external sources into the external part of the SV, as expected. However, the flow models inverted from the internal component of the VO SV dataset still retained a rapidly varying signal, indicating that isolation of the purely internal field is difficult.

Steady flow models generated from the entire set of SV data of 44 months produce very consistent flow regimes, while B-spline fits to the flow coefficients can also smooth the variation from month to month, but result in a larger overall misfit to the data.

The most promising technique for the amelioration of the external field correlation

is the covariance correction technique. This produced the best relative fit of the flow model to the SV data and removed much, though not all, of the month to month variation. This approach appears to be the best method for treating VO data.

In conclusion, unwanted signals from a number of sources have been identified in the field models derived from employing the VO method. Some of the effects from these sources can be removed or ameliorated, through the selective use of data, external field modelling and alternative binning approaches. Using a grid of equal latitude/longitude with all available data (Dataset 1), applying a CM4 correction and removing correlations within the data, best isolates the internal SV and reduces the influence from other sources. However, it appears that the VO datasets are still influenced by unmodelled sources from fields other than the main field. These external influences appear to be responsible for the rapidly changing core flows.

This result has a number of implications for satellite modelling and geomagnetic research. It suggests that it is currently difficult to completely and correctly remove external field contamination from satellite measurements.

The next few chapters of the thesis focus on using these flows for model forecasting and data assimilation for the purposes of predicting secular variation into the future.

Chapter 5

Forecasting the change of the Main Field using Core Flow models

The pragmatic assumption of this thesis is that the large scale geomagnetic field is entrained into the fluid at the top of the core and is thus advected by the flow, allowing the effects of diffusion to be neglected. Previous workers have studied this assumption and surmised it to be valid over short time periods. In Chapter 4, I derived sets of flow models from different satellite data selection criteria. In this chapter I now apply these flow models to the task of matching and predicting the change in the magnetic field.

Initially, simple flow models will be tested against existing satellite models, in a manner similar to that of Maus et al. (2008). The magnetic field models GRIMM (Lesur et al., 2008b), POMME (Maus et al., 2006) and xCHAOS (Olsen & Mandea, 2008) are used as testbeds against which to judge the accuracy of the flow model predictions. To begin, a steady flow model is employed to examine how quickly the predicted magnetic field deviates from the field models. Secondly, the SV predicted by month-to-month flow models (calculated in Chapter 4) are compared to GRIMM, IGRF10, POMME and xCHAOS.

The magnetic field models are tested against ground observatory measurements to

deduce the fidelity to the data recorded at discrete points on the surface and to examine the crustal biases of the model.

5.1 Simple Flow Modelling

By representing the main magnetic field as a vector of Gauss coefficients, denoted here as $\mathbf{g}_l^m$ (with degree and order l and m, respectively), the annual change of the main magnetic field ($\dot{\mathbf{g}}_l^m$) can be trivially added to a starting model to produce a time series of evolving field models. Correctly deducing the coefficients of SV ($\dot{\mathbf{g}}_l^m$) is, of course, the problem to be solved.

Magnetic models such the 10^{th} International Geomagnetic Reference Field model (IGRF10) (Maus et al., 2005b) and the World Magnetic Model (WMM) (McLean et al., 2004) estimated the future SV until the release of the next model (five years) using linear fits to recorded SV change from observatories and satellite data. This approach does not invoke any particular physical arguments to support the assumption that the SV will continue linearly nor indeed that the estimated change ought to be linear. McLean et al. (2004) used a combination of linear prediction from observatory data and polynomial extrapolation from satellite data to predict SV. By contrast, I have estimated core flows from SV generated from satellite magnetic field models and used them to predict SV. This should hopefully allow an improved estimate of SV outwith the period of available data.

The U.S. Defense Mapping Agency requirement in MILW89500 1993 (document inactive since 1998) states that the value of the F total intensity of a main field model forecast should not be greater than 280nT RMS difference from the 'true' field at the end of its five year validity. This requirement has driven research into better methods of estimating the SV; in the past the predicted model has been outwith the desired maximum error. Currently, McLean et al. (2004) state their model error in the F component is no larger than 100nT. The first section of the chapter investigates how well simple flow models can match the actual change compared to three published magnetic field models.

To begin, a 'true' field model is required – the xCHAOS field model has been nominally chosen for this purpose. The Gauss coefficients for the xCHAOS model at the epoch 2001.45 (May 2001) are calculated (as provided by Olsen[1]) to provide a starting point. The annual SV calculated from flow model coefficients are added to the Gauss coefficients to produce the forecast of the magnetic field:

$$\mathbf{g}_l^m{}_{new} = \mathbf{g}_l^m{}_{old} + \mathbf{H}_{old} * [\mathbf{t}_l^m : \mathbf{s}_l^m] \tag{5.1}$$

where $\mathbf{H}$ is the Gaunt/Elsasser matrix for the epoch and $(\mathbf{t}_l^m, \mathbf{s}_l^m)$ are the toroidal and poloidal flow coefficients respectively. The matrix $\mathbf{H}$ is updated at each timestep using the predicted field coefficients $(\mathbf{g}_l^m{}_{new})$.

To measure the difference between the forecast field model and the actual field model (e.g. xCHAOS), the sum of the modified Mauersberger/Lowes spectrum is calculated (Maus et al., 2008):

$$dP = \sum_{l=1}^{l_{max}} \sum_{m=0}^{l} (l+1)[\mathbf{g}_l^m{}_{actual} - \mathbf{g}_l^m{}_{model}]^2 \tag{5.2}$$

The square-root of dP (i.e. $\sqrt{dP}$) is referred to as the Root-Mean-Square (RMS) difference or misfit between the model and the forecast.

I now compare the forecasting technique to a set of field models using the SV generated by a steady flow model over the period 2001.91 – 2005.5 and the SV generated from the time series of flow models from 2001.91 – 2007.5. The field models are derived up to degree and order 14.

5.1.1 Steady Flow Model

A steady flow model can be considered as the flow required to generated the average field change observed over a period of time, calculated by the accumulation of at least three instantaneous SV measurements (Voorhies & Backus, 1985). Figure 5.1 shows

[1] Available at `http://www.spacecenter.dk/files/magnetic-models/xCHAOS/`, accessed November 2008.

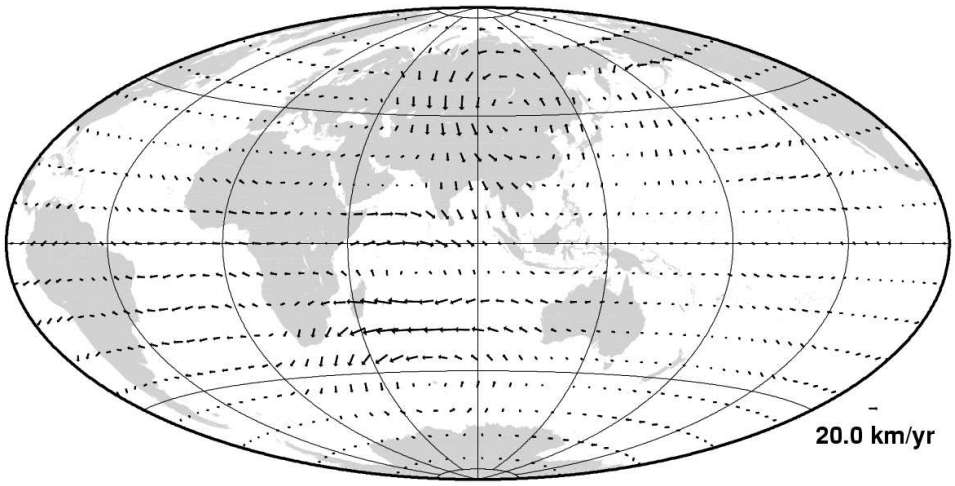

Figure 5.1: Steady Flow Model using All CHAMP data over the period 2001.91 – 2005.5.

the steady flow model generated using all available CHAMP data from 44 months from 2001.91 – 2005.5. In this case, the flow coefficients in Equation 5.1 are constant over time. As shown in Table 4.5 the steady flows generated by the different data selections (e.g. all CHAMP data, night-side only data) are very similar, so only one flow model needs to be examined in detail.

The monthly SV of the field is predicted by the steady flow from 2002.45 – 2008.45 and added to the Gauss coefficients of the previous month (i.e. Equation 5.1) to generate a time-series of predicted Gauss coefficients based on the steady flow model. The Gaunt/Elsasser matrix (**H**) is updated every month, as the SV from the flow model is calculated. For comparison, the SV generated by the xCHAOS model at 2001.5 is used as a simple, constant SV model. Also computed is the SV predicted from the Steady flow without updating the Gaunt/Elsasser matrix monthly. The xCHAOS model provides the initial Gauss coefficients for 2001.45.

Figure 5.2 shows the RMS difference between the forecast field model derived from the SV generated by the steady flow model and the GRIMM, xCHAOS and IGRF10 models. Figure 5.3 shows the RMS difference between the forecast field model and POMME3/POMME4/POMME4s field models. Table 5.1 summarises key properties of the field models.

Model	Data Source	Validity	SV/SA
GRIMM	Satellite + Ground Obs data	2001.5–2005.5	B-spline SA
xCHAOS	Satellite + Ground Obs data	1999.0–2007.0	B-spline SA
IGRF10	Satellite + Ground Obs data	2005.0–2010.0	Constant SV
POMME3	Satellite data only	2000.5–2005.5	Constant SA
POMME4	Satellite data only	2000.6–2007.5	Constant SA
POMME4s	Satellite data only	2000.6–2007.5	Variable SA

Table 5.1: Description of field models used in the chapter. SV: Secular Variation; SA: Secular Acceleration.

The following observations can be made about the fit of the steady flow model:

- The RMS difference between the GRIMM model is initially low (< 20 nT) between 2002.5 and 2006 but increases quickly after 2006 for the steady flow predictions (Figure 5.2(a)). The constant SV from the xCHAOS model does remarkably well in the 2004–2006 period. Updating the Gaunt/Elsasser matrix each month produces a better fitting field model than assuming **H** is constant. The xCHAOS model is constructed with similar data to the GRIMM model, explaining coincidence of the models during the 2004–2006 period.

- As the xCHAOS model is the starting point for the initiation of the steady flow model, only Figure 5.2 (b) is in total agreement (i.e. $\sqrt{dP} = 0$) at 2002.45. The total RMS difference between xCHAOS and the field derived from the steady flow model becomes larger than 40nT after approximately 5.5 years (at 2007.9, Figure 5.2(b)). Despite claiming to include secular acceleration within the Matlab code for generating field model values, the SV from the xCHAOS model is constant, exactly matching the evolution of the field model.

- The most recent part of IGRF10 model is valid from 2005.0 to 2010.0, with constant SV. The average values for the SV coefficients are smaller (more conservative) than the SV for the xCHAOS model. Hence, it appears that the xCHAOS model only matches the IGRF model at approximately 2006.5 and diverges afterwards (Figure 5.2 (c)). The predictions from the flow models produce a similar response though appear to best match the IGRF at 2005.5.

- Three POMME models are used for comparison with constant SV from the xCHAOS model and SV from the steady flow models. POMME3 and POMME4 include different estimates for SV and Secular Acceleration. POMME4s has an estimate for pre-2004.0 SA and post-2004.0 SA, to account for a geomagnetic jerk about that time. Analysis of Figure 5.3 suggests that the xCHAOS SV model best matches the POMME4s model. The steady flow model best matches the POMME3 model over the period and matches the POMME4 and POMME4s models equally well.

For each of the GRIMM, xCHAOS, IGRF10 and POMME models, the constant SV coefficients from xCHAOS produce the closest match. The SV values from the steady flow model when using a monthly updated Gaunt/Elsasser matrix perform better than using just constant SV from the steady flow.

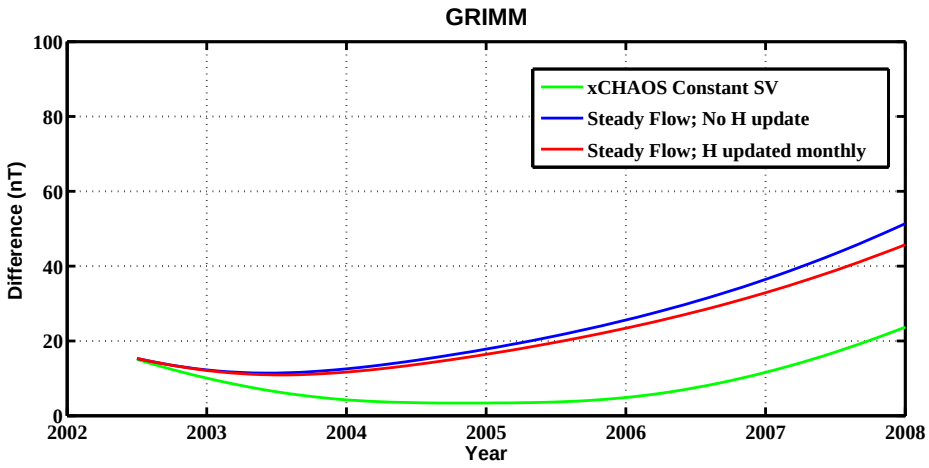

(a) GRIMM field model

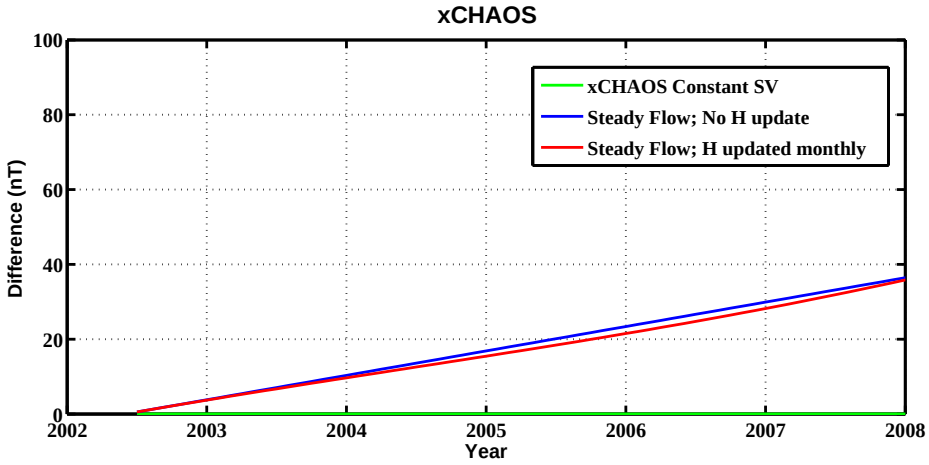

(b) xCHAOS field model

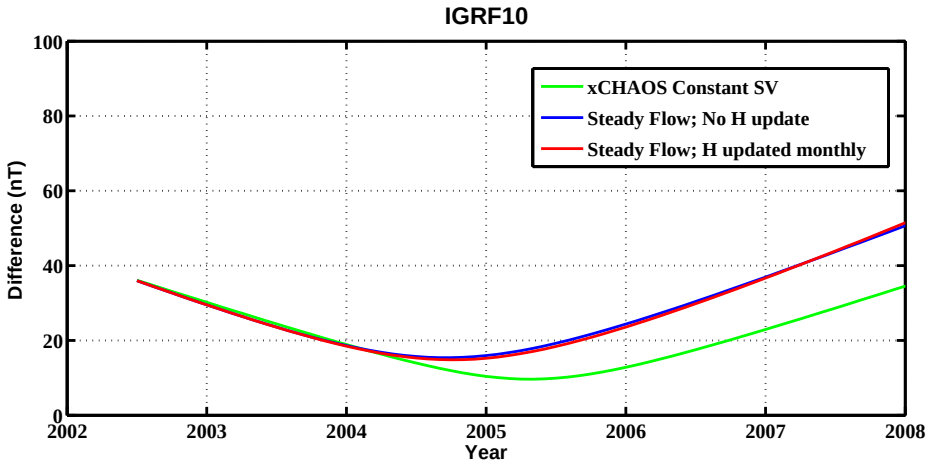

(c) IGRF10 field model

Figure 5.2: RMS difference (in nT) between a forecast field model derived from SV generated by a steady flow model and the (a) GRIMM, (b) xCHAOS and (c) IGRF10 field models.

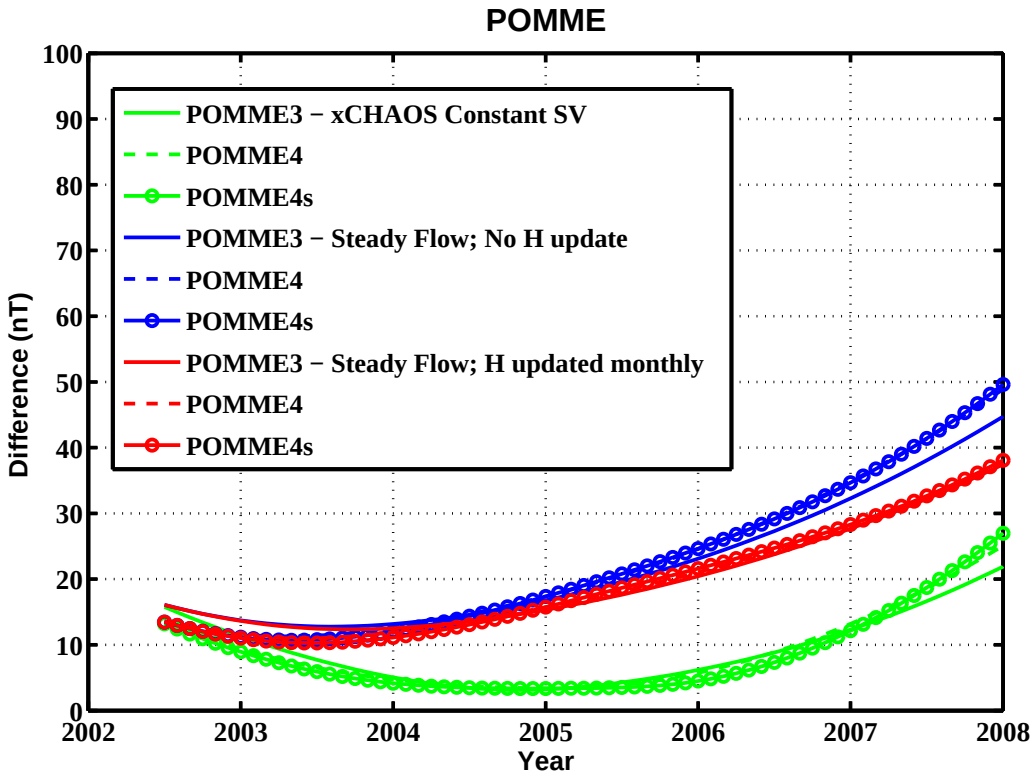

Figure 5.3: RMS difference (in nT) between a forecast field model derived from SV generated by a steady flow model and the POMME3, POMME4 and POMME4s field models.

5.1.2 Forecasting using Steady Flow models?

To test the ability of a steady flow to forecast field change within a period where no flow data is available, I created a steady flow model from SV data over the period 2001.91–2003.91. I then compared the SV predictions from the steady flow model for the period of 2004.0–2009.0, to the actual field, as modelled by the spline version of xCHAOS and GRIMM. The GRIMM spline model currently only extends to 2006.75. The forecast from the POMME4 were also included in the comparison. Figure 5.4 (a) shows the resulting forecast. The RMS difference for the xCHAOS model is just under 90nT. The GRIMM model follows the xCHAOS model closely until 2006.75. In Figure 5.4 (b), the forecast from a steady flow model generated using data from the period over 2001.91–2006 is shown. The RMS difference between the flow forecast model and the xCHAOS model at the end of 2008 is about 60nT. This illustrates that the longer steady flow model partially covering the forecast period does, unsurprisingly, improve the misfit.

5.1.3 Non-steady Flow Models

In Chapter 4 a series of month-to-month flow models was derived from different selections of satellite data. To calculate the predictions of these non-steady flows, the annual SV from the flow models for each month was calculated by placing the flow coefficients into Equation 5.1 and dividing the result by twelve. This produced a value for the monthly SV which was added to the starting field model Gauss coefficients (from the xCHAOS model). There are 68 flow models generating SV over the period 2002.45 – 2007.91.

As will be recalled, Dataset 1 was derived from the use of all available satellite data, while Dataset 2 was constructed from night-side only data. The predictions from the monthly flow models (computed using the grid of equal latitude and longitude) from both of these datasets were compared against the GRIMM, xCHAOS, IGRF and POMME field models. Figures 5.5 and 5.6 shows the resulting comparison of the prediction of flow from Dataset 1, while Figures 5.7 and 5.8 illustrates the prediction

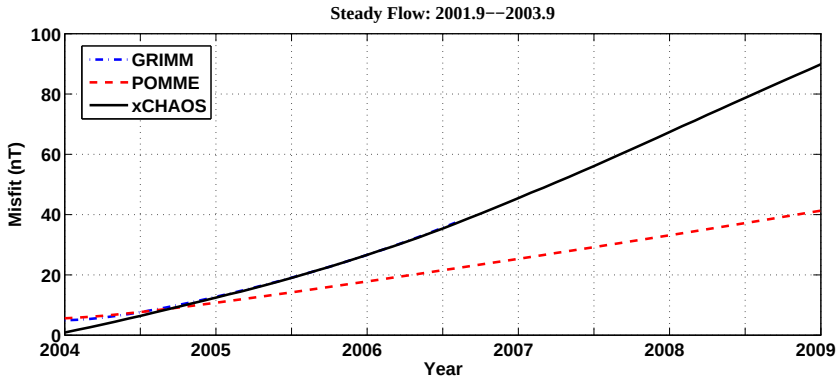

(a) Steady Flow: 2001.91–2003

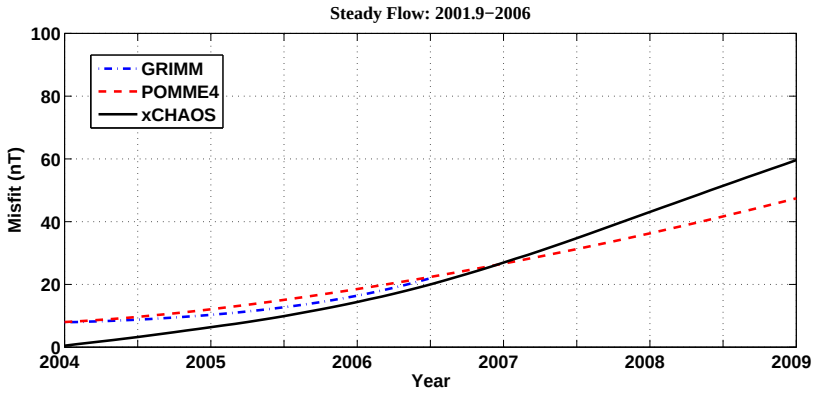

(b) Steady Flow:2001.91–2006

Figure 5.4: RMS difference (in nT) between a forecast field model derived from SV generated by (a) a steady flow model generated from VO data over the period 2001.91–2003 and (b) a steady flow model generated from VO data over the period 2001.91–2003.

of SV from Dataset 2.

The following observations can be made about the fit of the steady flow model:

- As the xCHAOS model is the initial starting model, only Figures 5.5 and 5.7 (b) have zero difference at the beginning of the period. By comparison to Figure 5.2 it can be clearly observed that the overall difference remains below 50nT for each of the models until end-2008. The GRIMM field model is not valid beyond 2005.5, so the more rapid divergence in 2008 is not realistic.

- The SV generated by the flow models in Figure 5.5 are slightly better fit to the field models than Figure 5.7, which seems to be a counter-intuitive result as Chapter 4 indicated Dataset 2 was less contaminated by external field noise. However, the difference is marginal. One possible explanation for this may be the inclusion of observatory data in the GRIMM and xCHAOS field models, which may impart some external induced field signal into the field models, thus better fitting Dataset 1. Another observation to be made is the slight rise in the difference up to 2004.25 followed by an improvement in each of the models to approximately 2005.5. It is not known why this occurs (though this may be related to the supposed 2004 jerk (Olsen & Mandea, 2008)).

- The non-steady flow models initially match the POMME3 model best but after 2006.75 the POMME4 and POMME4s models are better match by the flows, presumably as POMME3 is only valid until 2005.5.

One might now ask how the flow models with CM4 correction applied to the data predict the change of the field over time. In Figures 5.9 and 5.10, the RMS differences between the forecast field models are shown. The RMS difference appears to have visible inter-annual 'wiggles' and overall the fit is poorer than those of Datasets 1 and 2 without the CM4 correction applied. This suggests that the CM4 parameterisation may be over- or under-compensating for some particular seasonal or annual magnetic field effects. In any case, the prediction from the flows with CM4 correction are always poorer than those without.

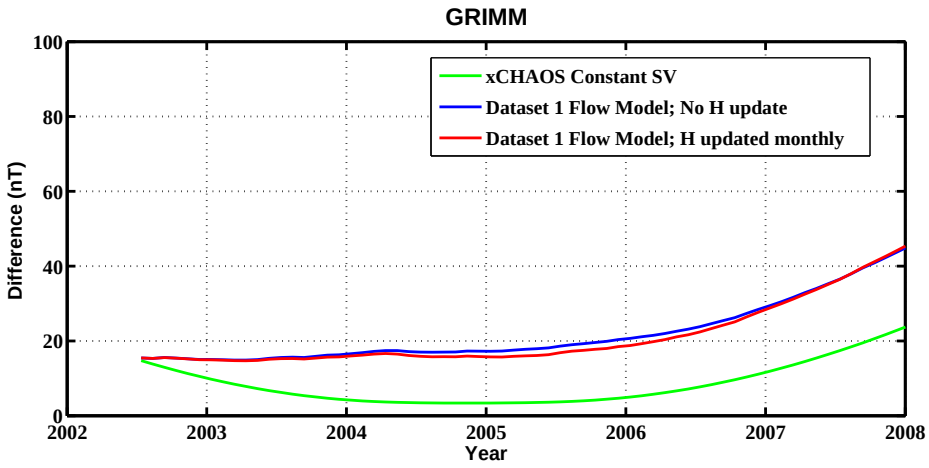

(a) GRIMM field model

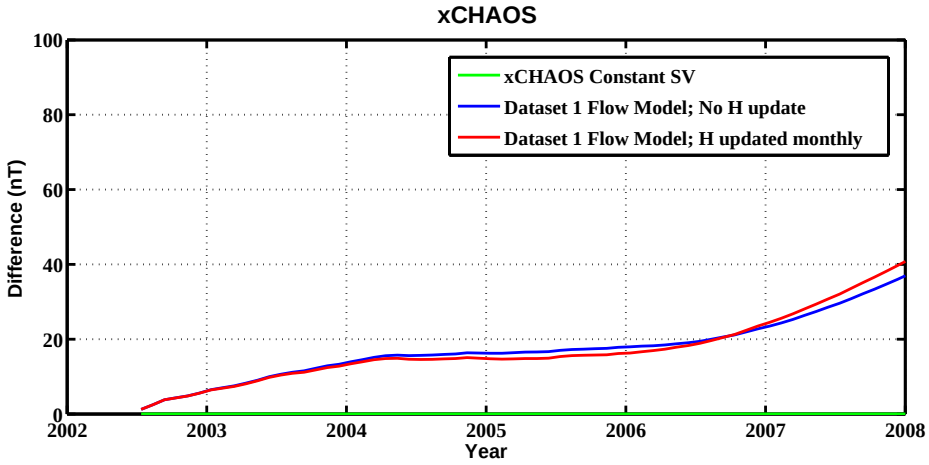

(b) xCHAOS field model

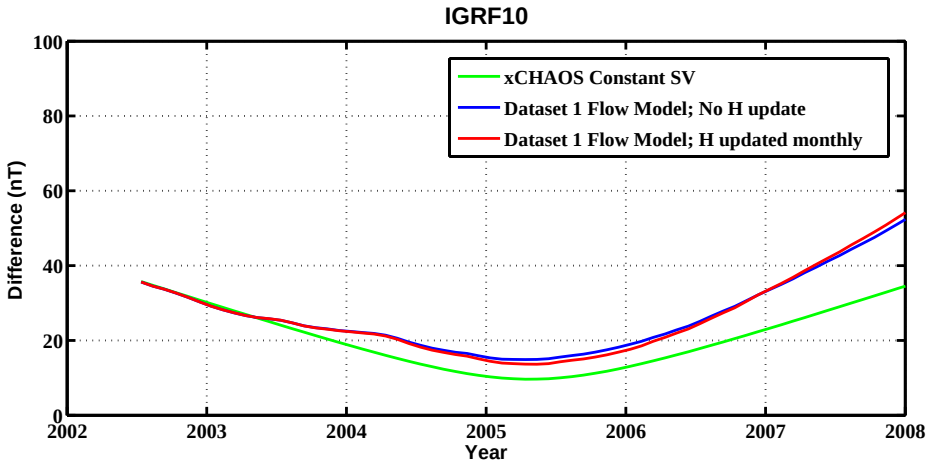

(c) IGRF10 field model

Figure 5.5: RMS difference (in nT) between a forecast field model derived from SV generated by non-steady flow models from Dataset 1 and the (a) GRIMM, (b) xCHAOS and (c) IGRF10 field models.

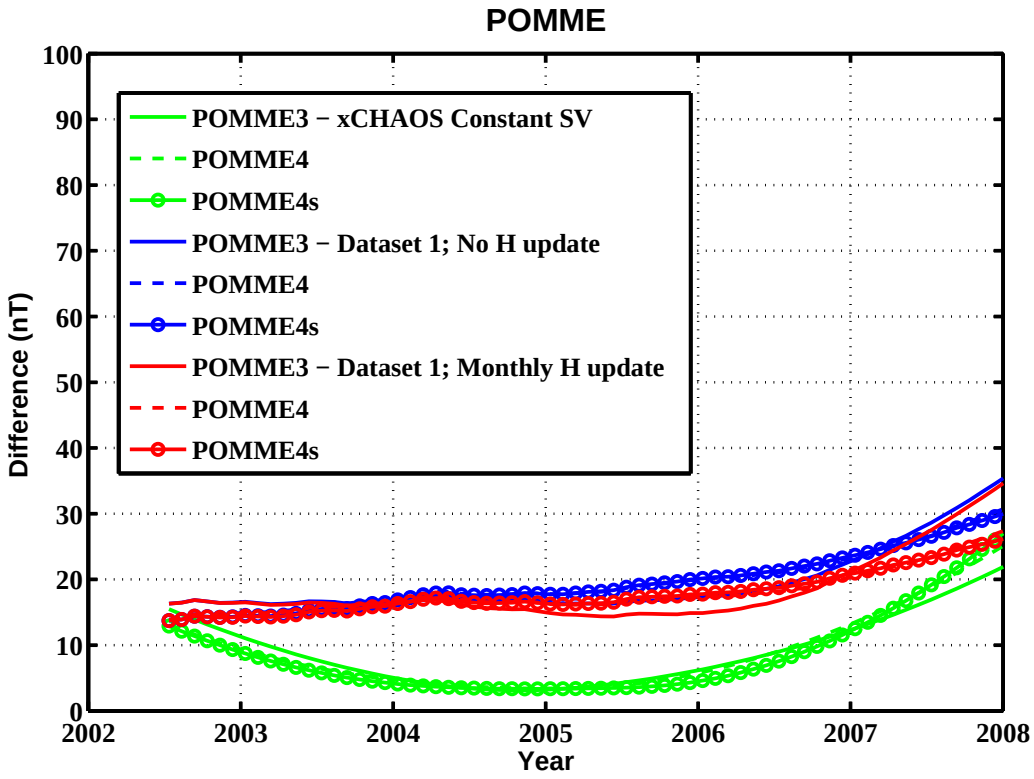

(a) POMME field model

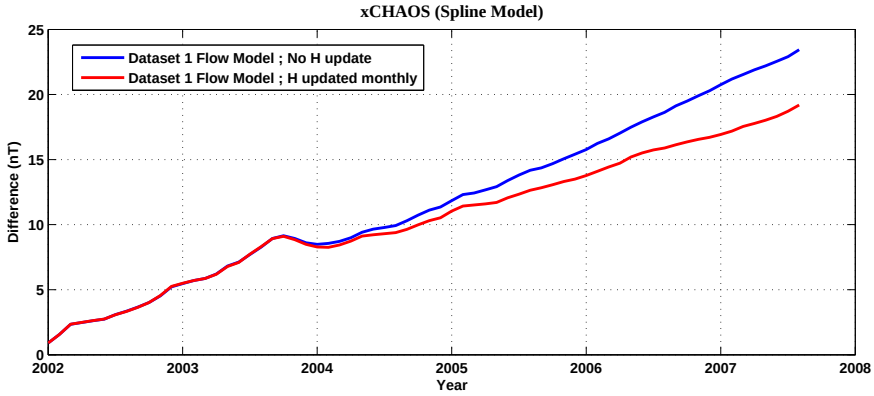

(b) xCHAOS (spline) field model

Figure 5.6: RMS difference (in nT) between a forecast field model derived from SV generated by non-steady flow models from Dataset 1 and (a) the POMME3, POMME4 and POMME4s field models, and (b) xCHAOS spline model.

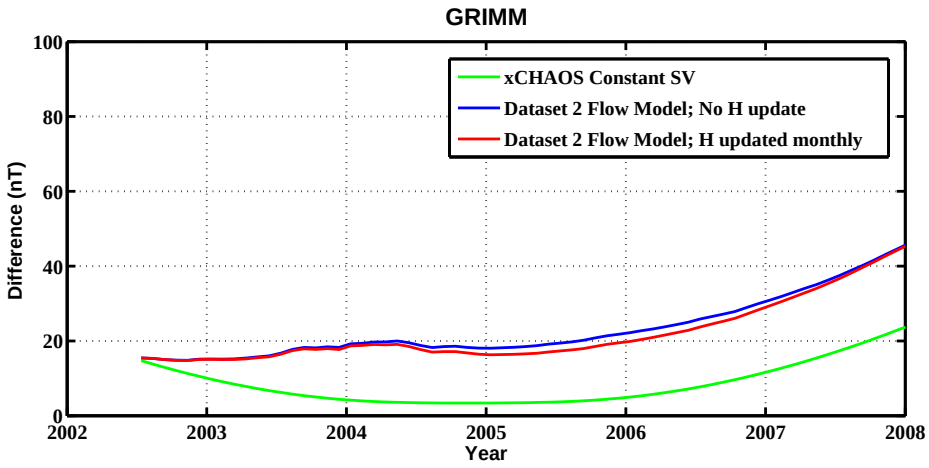

(a) GRIMM field model

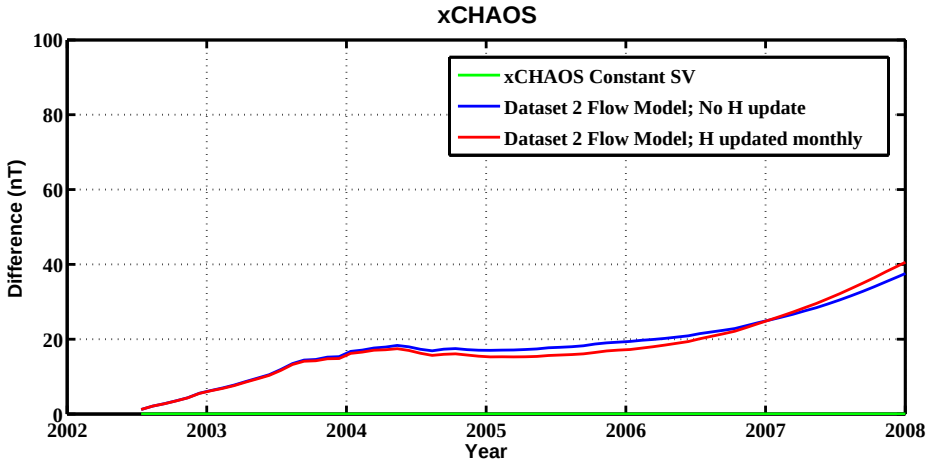

(b) xCHAOS field model

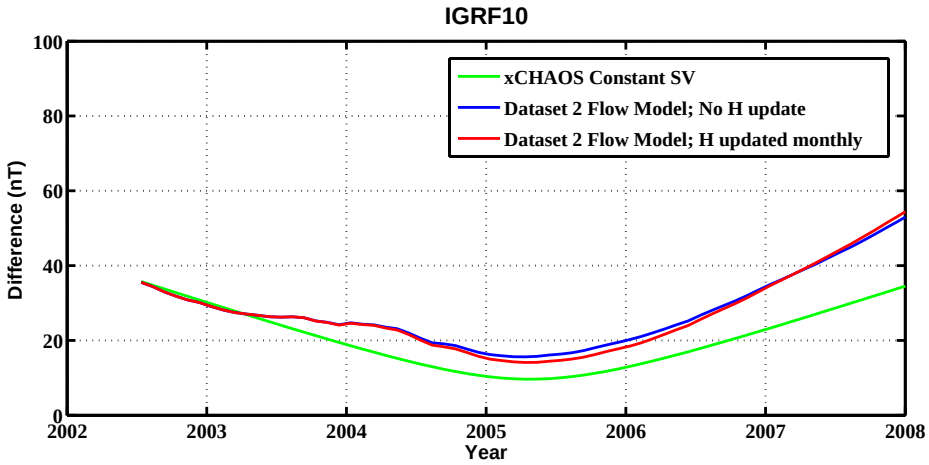

(c) IGRF10 field model

Figure 5.7: RMS difference (in nT) between a forecast field model derived from SV generated by a non-steady flow models from Dataset 2 and the (a) GRIMM, (b) xCHAOS and (c) IGRF10 field models.

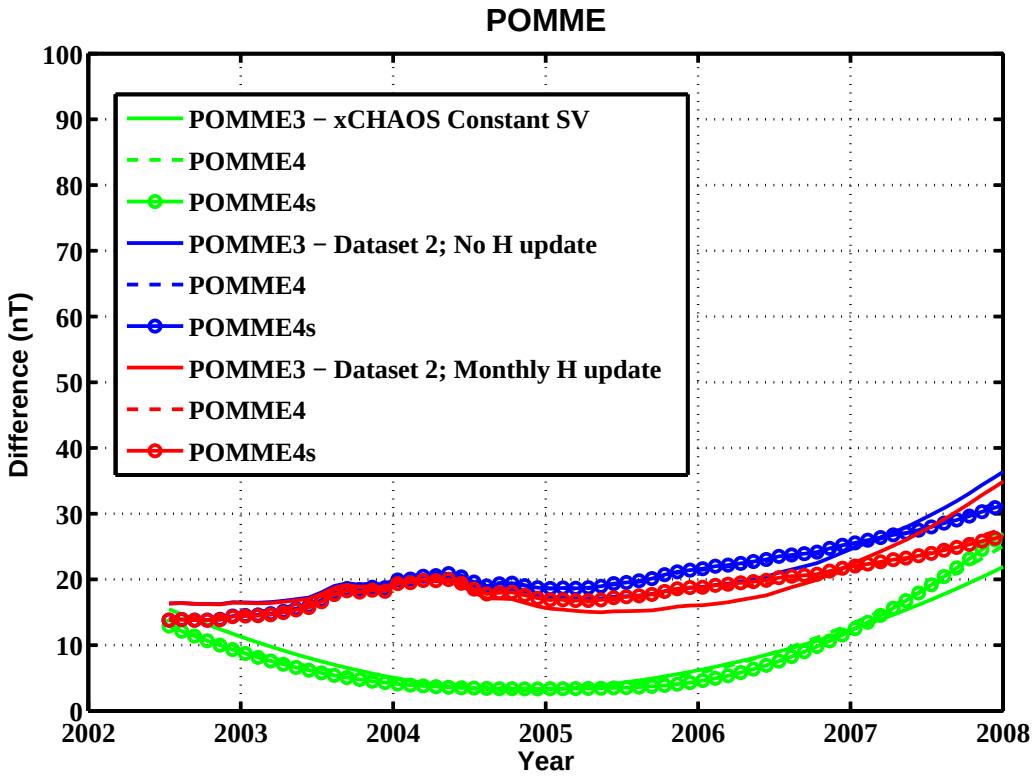

(a) POMME field model

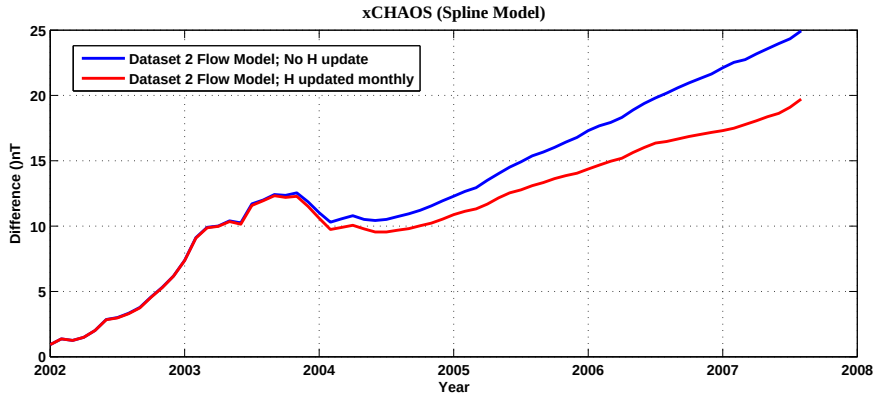

(b) xCHAOS (spline) field model

Figure 5.8: RMS difference (in nT) between a forecast field model derived from SV generated by non-steady flow models from Dataset 1 and (a) the POMME3, POMME4 and POMME4s field models, and (b) xCHAOS spline model.

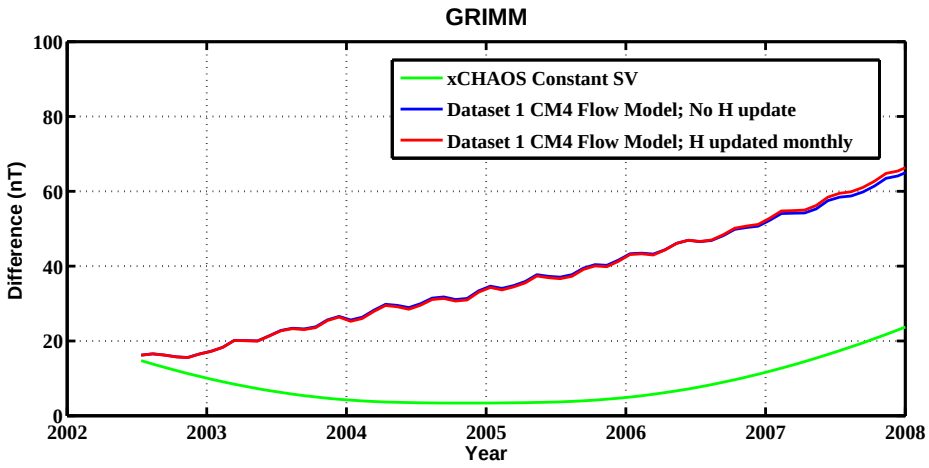

(a) GRIMM field model

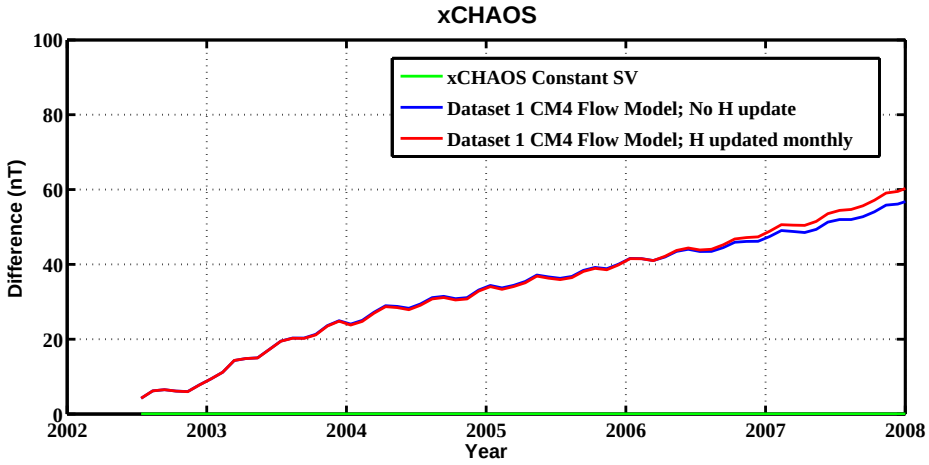

(b) xCHAOS field model

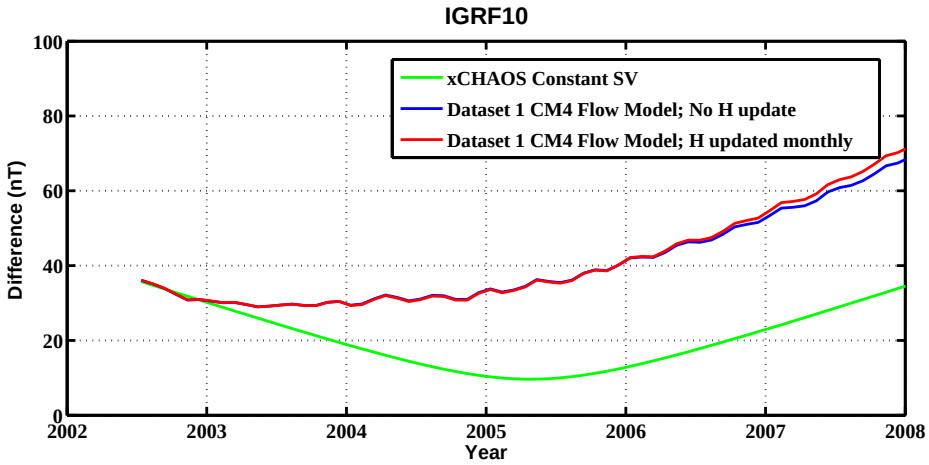

(c) IGRF10 field model

Figure 5.9: RMS difference (in nT) between a forecast field model derived from SV generated by a non-steady flow models from Dataset 1 with CM4 correction applied and the (a) GRIMM, (b) xCHAOS and (c) IGRF10 field models.

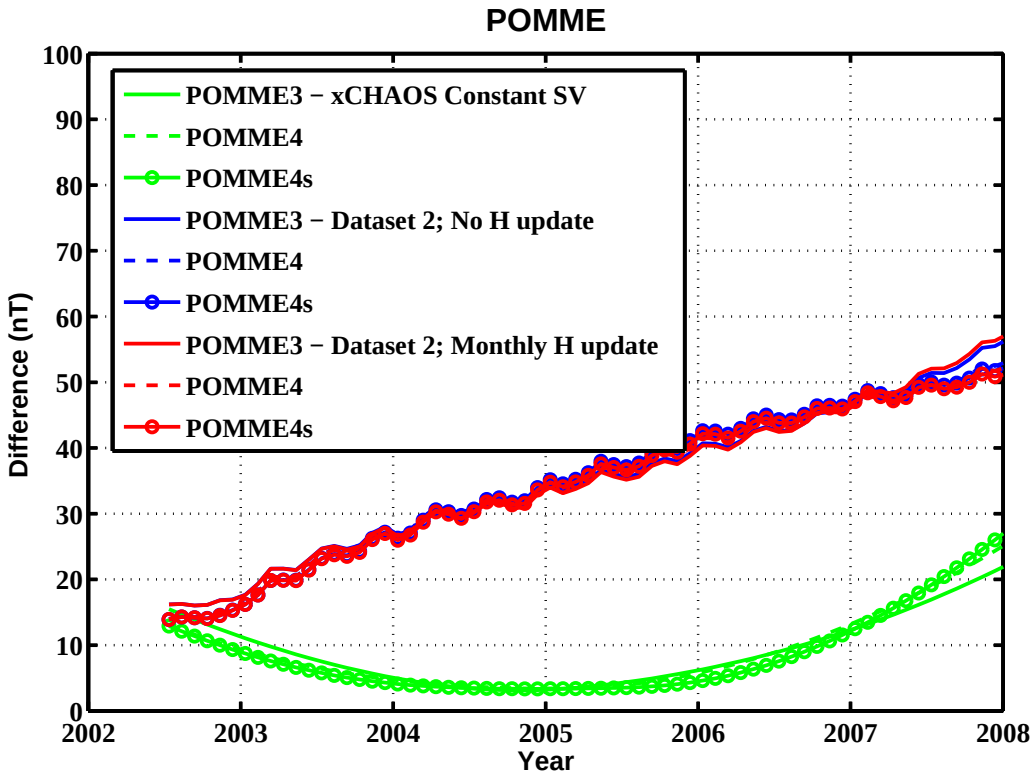

(a) POMME field model

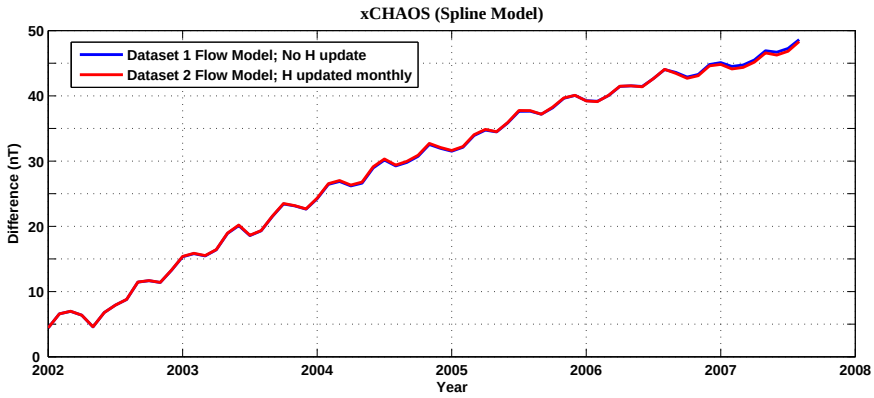

(b) xCHAOS (spline) field model

Figure 5.10: RMS difference (in nT) between a forecast field model derived from SV generated by non-steady flow models from Dataset 1 (with CM4 correction) and (a) the POMME3, POMME4 and POMME4s field models, and (b) xCHAOS spline model.

The assumption of simple advection of the magnetic field by core flow models appears to give reasonable field predictions. The results of forecasting SV in this manner provide an acceptable level of misfit to the main field after five years, even using a steady flow model. In the next chapter I apply the Ensemble Kalman filtering method to the problem to investigate if the total misfit of the prediction can be reduced by optimally incorporating measurements at discrete intervals.

5.2 Comparison of predictions from Flow Models to Ground Observatories

Having extensively tested the flow models and satellite data for contamination from external field and other factors, no evidence has been yet been presented as to the fidelity of the SV generated by the flow models compared to that of ground observatories. Ground observatories record the instantaneous magnetic field typically at a frequency of 1 Hz. Data values for the field components at ground level are available from the World Data Centre for Geomagnetism[2]. Monthly mean values for over 100 observatories were calculated for both the field and the annual SV using the average value from the measurements on the five International Quiet Days. These were used for comparison with the field and annual SV values as computed from the monthly flow models from the VO All CHAMP dataset.

As before, a starting model (using xCHAOS Gauss coefficients) was integrated forward in time by the addition of the SV from the flow models generated from Dataset 1 (see Figure 5.5). The monthly values of the X, Y and Z field and SV coefficients were compared to those from the ground observatories. Overall, the average correlation between the forecast field and the measured (observatory) field was 0.85, 0.95 and 0.86, in the X, Y and Z components, respectively. (Correlation is significant: $\rho < 10^{-7}$.) The SV of the monthly means are quite scattered, leading to a lower average correlation of 0.29, 0.47 and 0.22 for the $\dot{X}$, $\dot{Y}$ and $\dot{Z}$ components, respectively. Figures 5.11 – 5.16 show six typical examples of the fit of the predicted field model and the SV (red dashed line in the plots) to the measurements recorded at ground-based observatories (blue dots).

The values of the X, Y and Z components of the field as recorded at ground observatories are different to those values derived from satellite models due to the unmeasured small-scale (high degree) features of the field at the Earth's surface, assumed to be of lithospheric origin. This manifests as a roughly constant offset mainly due to attenua-

[2] http://www.wdc.bgs.ac.uk/
(Observatory monthly means from S.Macmillan, pers. comm., Nov. 2008)

tion of small scale anomalies at satellite altitudes. The difference between field model predictions and the actual value as measured at an observatory is referred to as the crustal anomaly or bias. This varies between field models, depending on the degree and order to which they are calculated. There are a few published tables of crustal bias, examples include Sabaka et al. (2000), Bloxham et al. (1989), and Volume 1 of Jacobs (1987). Other satellite models calculated to the same degree (e.g. GRIMM, xCHAOS) showed a similar crustal bias. A second independent method of estimating crustal bias comes from parameterisation of the field by attempting to fit a global field model to observatory data.

In Appendix A I have tabulated the crustal biases for the field model derived from the VO using All CHAMP data to degree and order $l = 14$. Table 5.2 compares a selection of crustal biases as calculated from the VO field model to the biases from the CM3 model (Sabaka et al., 2000). The computed biases are related to the degree of the spherical harmonic model. CM3 is calculated to degree 50 and so includes a significantly better estimate of the crustal field compared to the VO field models. The biases of the VO model and CM3 model generally agree on sign and magnitude of the bias in most components (e.g. for BEL and HON) but occasionally differ completely in several components (e.g. ABK and HER). Estimating crustal biases from satellite altitude is also subject to errors from upward attentuation of the field. Note that the observatory data can be quite scattered but on average the trends are consistent.

Overall, the SV from the flow models matches the change in the recorded field over the time period of available satellite data. In the next section, I investigate how well the field can be hindcast and compare the results with those of Maus et al. (2008).

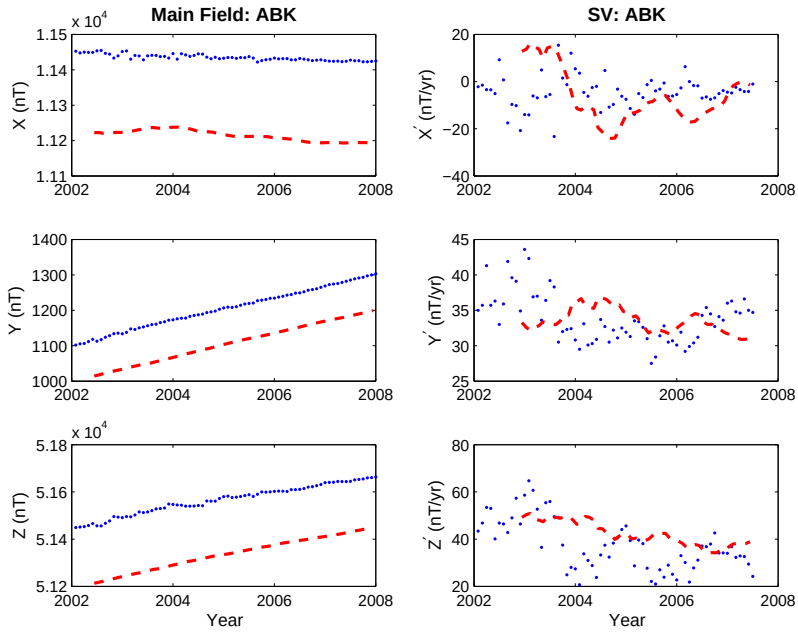

Figure 5.11: Comparison of monthly means from Abisko (Sweden) [blue dots] to the predicted field and SV [red dashed line] from the VO flow model from Dataset 1.

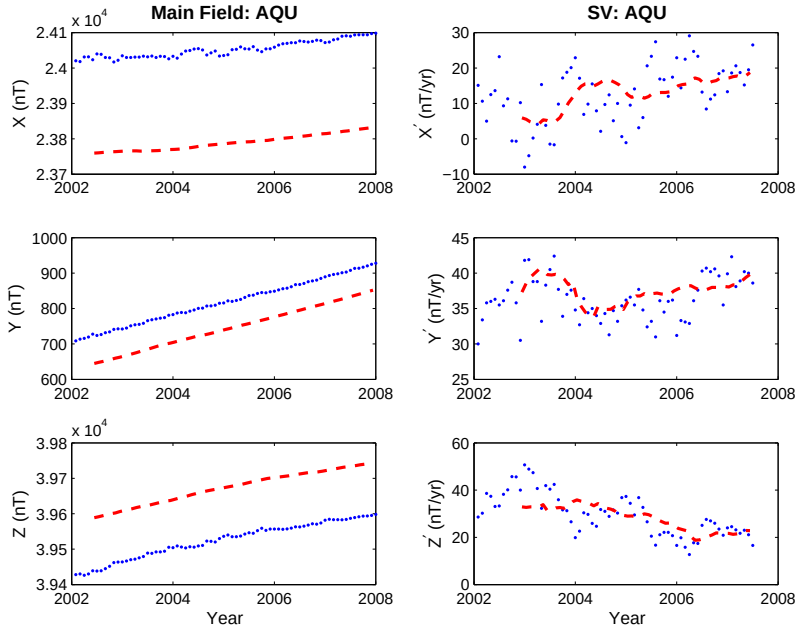

Figure 5.12: Comparison of monthly means from L'Aquila (Italy) [blue dots] to the predicted field and SV [red dashed line] from the VO flow model from Dataset 1.

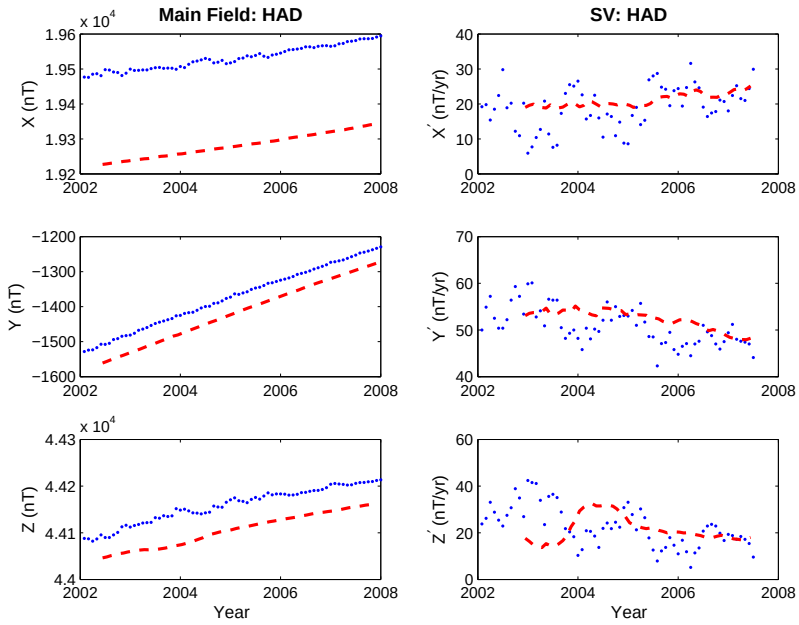

Figure 5.13: Comparison of monthly means from Hartland (UK) [blue dots] to the predicted field and SV [red dashed line] from the VO flow model from Dataset 1.

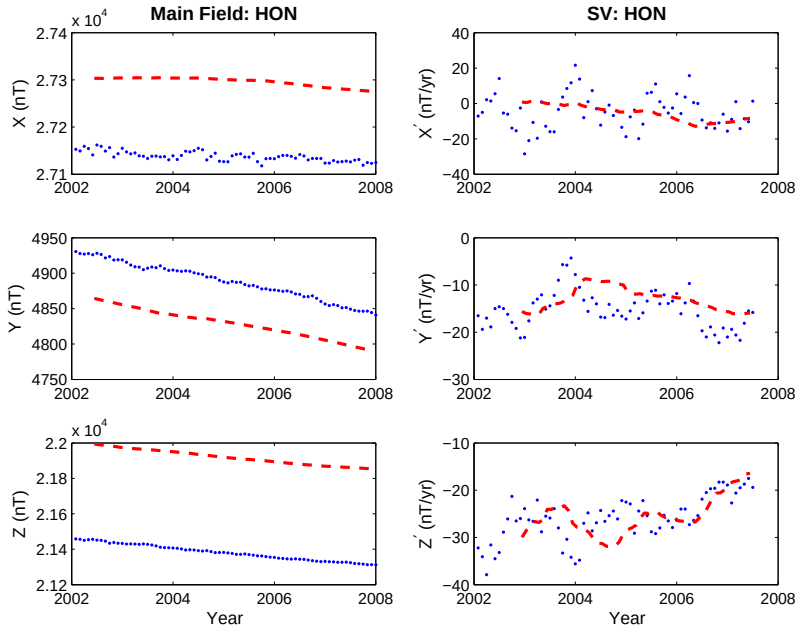

Figure 5.14: Comparison of monthly means from Honolulu (U.S.A.) [blue dots] to the predicted field and SV [red dashed line] from the VO flow model from Dataset 1.

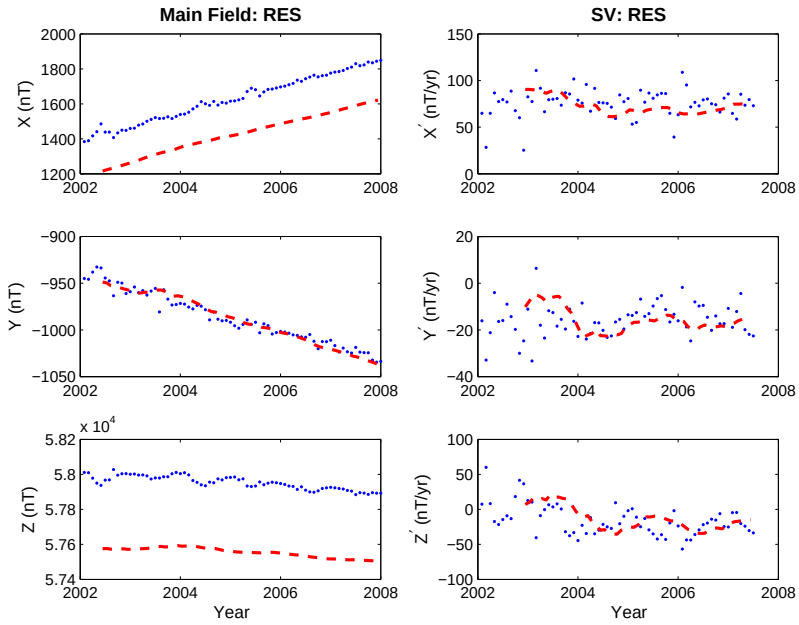

Figure 5.15: Comparison of monthly means from Resolute Bay (Canada) [blue dots] to the predicted field and SV [red dashed line] from the VO flow model from Dataset 1.

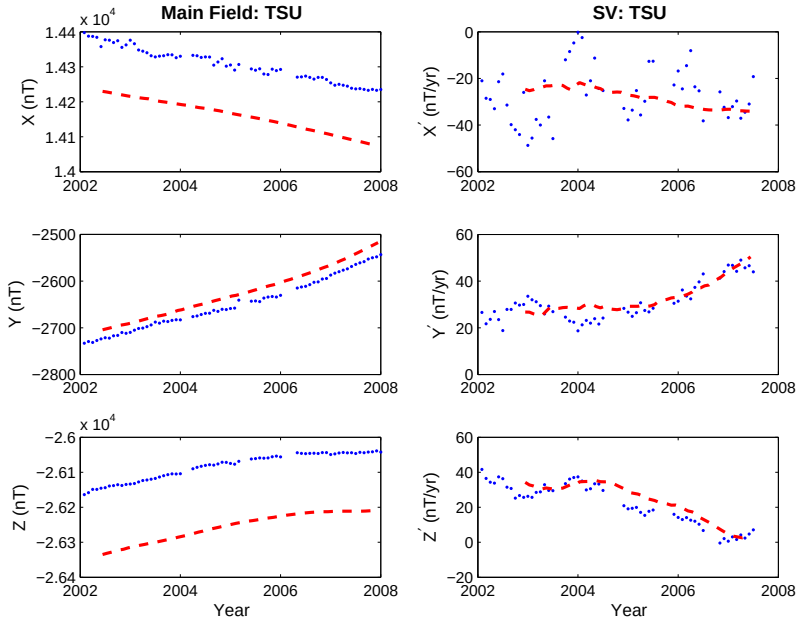

Figure 5.16: Comparison of monthly means from Tsumeb (Namibia) [blue dots] to the predicted field and SV [red dashed line] from the VO flow model from Dataset 1.

Obs Code	VO Crustal Bias			CM3 Crustal Bias		
	X	Y	Z	X	Y	Z
AAA	432	10	-301	150	-9	-259
AAE	584	-92	446	430	-265	-141
ABK	220	101	234	105	13	-95
AQU	264	76	-144	2	26	-29
BEL	388	173	328	90	61	279
ESK	293	-3	-4	-7	5	-25
GUA	38	76	-140	122	102	48
HAD	251	49	55	-30	12	13
HER	74	14	36	46	-39	-56
HON	-159	58	-540	-161	101	-323
KAK	187	28	-356	-2	36	-53
LER	134	198	163	-83	179	2
NGK	254	35	-65	-25	-2	-12
RES	211	0	397	-6	87	49
TUC	91	-329	-78	-70	105	90
VIC	339	4	-396	13	-20	-400

Table 5.2: Table of Crustal Bias in the X, Y and Z components of the field as recorded at selected ground observatories minus the values as modelled by CHAMP satellite VO and as derived from CM3 (Sabaka et al., 2000). Biases are in units of nT.

5.3 Hindcasting using Flow Models

A valid mechanism to investigate how a flow model may predict field change over longer periods of time is hindcasting i.e. reversing the time direction of the prediction. Maus et al. (2008) have shown that hindcast predictions from steady flow models produce the smallest deviation from the 'true' models over time. This assertion was tested using the methods from the previous sections. The study by Maus et al. (2008) was rather unsatisfactory, as it used an unusual method for inverting SV for flow and made little mention of how the flow contraints (toroidal, steady and tangentially geostrophic) were calculated. In this section, I wish to test the claim using my methods.

A steady flow derived from the period 2001.91 – 2005.5 was used to predict the average SV of the field over the period. This constant SV was used to propagate the field backwards in time at annual timesteps from 2002 to 1990. The CM4 model of the field, which is valid from 1960–2002, was used both as the starting model and for comparison to calculate RMS misfit (using Equation 5.2). In addition, the hindcast

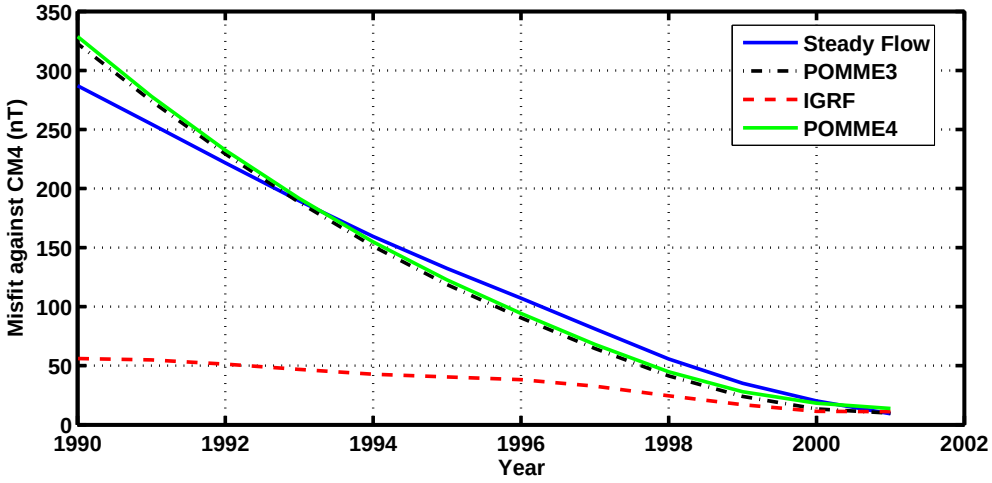

Figure 5.17: Comparison of hindcast main field change from a steady flow model and satellite field models to CM4 calculated using Equation 5.2.

field changes from the POMME3 and POMME4 satellite models were also calculated. Figure 5.17 shows the resulting evolution of the hindcast field models in comparison to the actual field as computed using CM4. The figure bears an excellent resemblance to Figure 8 of Maus et al. (2008) (see Figure 7.2), validating their methods and results. The relative difference between CM4 and IGRF10 over the period is shown by the red dashed line in Figure 5.17.

Figure 5.18 shows the comparison with the IGRF10 field model and the POMME3/4 and steady flow models. The interesting feature to note in both figures is that the steady flow model produces the smallest RMS difference between the models after 12 years. This supports the conclusions of Maus et al. (2008) that a steady flow (i.e. without secular acceleration) provides a best 'average' description of the field change over longer time periods. POMME3 and POMME4 better describe the detailed change during their periods of validity (2001–2006) and back in time until 1993 but become poorer beyond that point.

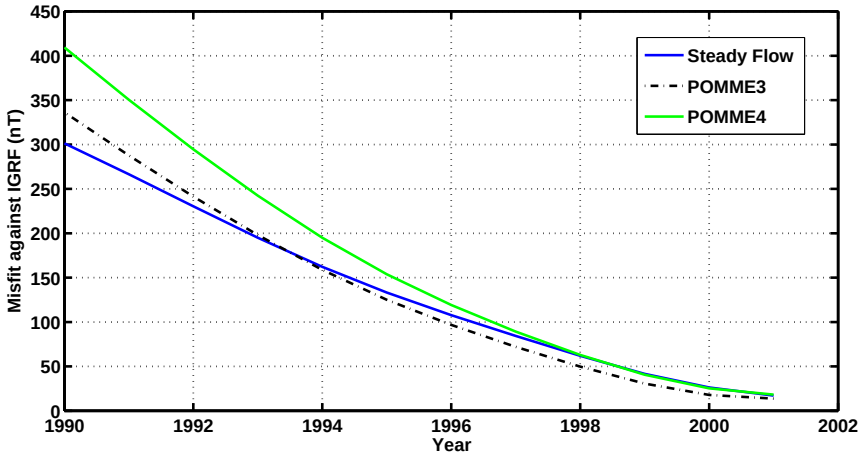

Figure 5.18: Comparison of predicted main field change from a steady flow model and satellite field models to IGRF10.

5.4 Forecasting the field in 2010–2015

As a final exercise, a field forecast for 2010-2015 was undertaken using a steady flow generated from VO SV from Dataset 2. The steady flow is constructed from 36 monthly instantaneous flow models from 2004.5 to 2007.5. This gives a steady flow after the last jerk in 2004.3 (Olsen & Mandea, 2007). Figure 5.19 shows the steady flow model for the period. The xCHAOS model was extrapolated to 2010 to act as a starting model for the forecast. The field was propagated forwards using the SV from the flow model. The comparison shown in Figure 5.20 is against the constant SV from the xCHAOS model. In Table 5.3 the first four Gauss coefficients of the forecast field are given for each year from 2010 to 2015.

As with any forecast, the exact starting point is not well defined, as the xCHAOS model is not valid beyond 2007.5. We shall also have to wait until 2015 to see how the forecast matches the 'true' field. From the previous sections in this chapter and the projection in Figure 5.20, it is suggested that the forecast will not be more than 80nT RMS different from the correct field.

Year	g_1^0	g_1^1	h_1^0	g_2^0
2010	-29508	-1619.7	4988	-2390.3
2011	-29494	-1603.5	4963.1	-2402.4
2012	-29480	-1587.1	4937.7	-2414.4
2013	-29466	-1570.7	4911.8	-2426.4
2014	-29452	-1554.3	4885.5	-2438.3
2015	-29438	-1537.8	4858.7	-2450.1

Table 5.3: Forecast of the first four Gauss coefficients from 2010–2015 based upon a starting field model from extrapolation of the xCHAOS field model.

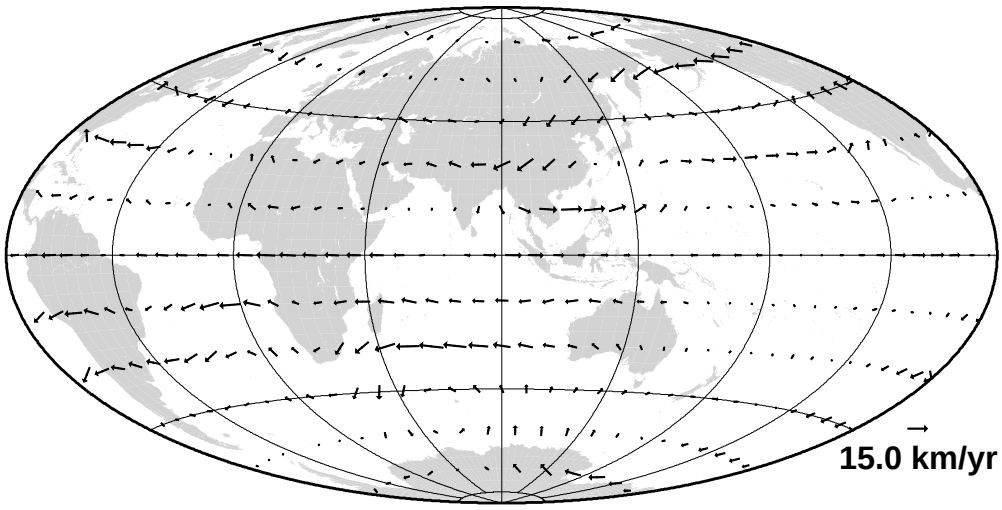

Figure 5.19: Calculated Steady Flow model from VO SV over the period 2004.5 to 2007.5.

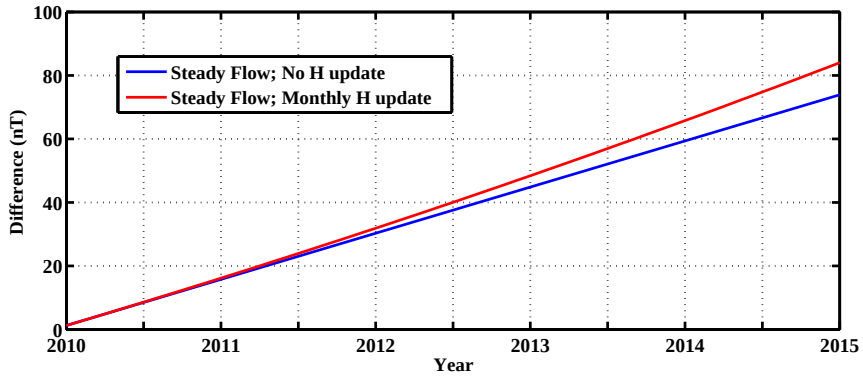

Figure 5.20: Comparison of predicted main field change from a steady flow model against the xCHAOS satellite field model for the period 2010–2015.

5.5 Summary

It has been shown that the field models POMME, GRIMM and xCHAOS are very similar, which is, of course, to be expected. However, slight differences exist between the SV of each model, altering the match between them and flow models. Overall, the field models perform better at predicting the SV over the 2002–2008 period than the steady flow or the non-steady flows from VO field models. However, the non-steady flows produce a uniform RMS mismatch (approximately 20nT) over much of the period, while the steady flow model only slowly diverges, being typically less than 40nT RMS difference by the end of 2008. The field models have been compared to observatory data and shown to match the observed changes with reasonable confidence.

Without access to magnetic field information in the future, one must choose how to predict the change based upon current knowledge. Hindcasting tests suggest that a steady flow can capture much of the gross change of the magnetic field for at least five years and perform better than a constant SV assumption in the longer term (10 years).

The forecasting and comparison to known field models shows that flows generated using all available satellite data (Dataset 1) are slightly better fit than flows using night-side only data (Dataset 2). The use of CM4 to correct satellite data before inversion for flow has introduced some seasonal and annual artefacts, seen as fluctuations in the misfit curves.

The results of this chapter are discussed in more detail in Chapter 7. In the next chapter I investigate methods of improving the forecast of the magnetic field and assimilation of data into the forecasting process using Kalman filtering.

Chapter 6

Forecasting and Data Assimilation using Ensemble Kalman Filtering

A major objective of this research has been to develop a methodology for forecasting the change in the Earth's magnetic main field. The science (though many say the 'art') of successful forecasting is most commonly associated with weather and climate. Over the past century, a vast body of knowledge and scientific understanding has been developed in the hope of producing methods for accurate short and long term forecasting of weather and climate. The science of weather forecasting has driven forward the adoption of a number of technologies (from supercomputers to satellite monitoring), the procurement of the global coverage of sensors required to capture the data and development of the vast resources to process the measurements and data in near real-time (Randall, 2000). It is from this branch of science that, I feel, geomagnetism can adopt methods for forecasting the behaviour of non-linear systems and assimilation of data into models. Indeed, some workers have started to apply it in geomagnetism (e.g. Fournier et al., 2007; Kuang et al., 2008).

6.1 Motivation

The motivation for the work in this chapter is distinct from the direct investigation of forecasting using core flows. Instead, this chapter investigates the situation when only partial, incomplete or inaccurate data is available for the magnetic field. This situation may arise in future if there are no satellite missions available for complete global coverage of the magnetic field. In this scenario, it may be useful, for example, to optimally assimilate data from core flow models derived from high accuracy field models with data from ground-based observatories. The Ensemble Kalman filter can be used in this case to optimally assimilate forecasts of the change in the magnetic field from a flow model with field models derived solely from observatories. The field coefficients can, hopefully, be more accurately modelled (in regions of sparse coverage for example).

The background history and motivation of the Kalman and the Ensemble Kalman filter is first described before discussion of the mathematical implementation. I give examples of one- and three-dimensional systems before investigating the use of the Ensemble Kalman filter for magnetic field forecasting.

6.2 Background

The Lagrangian principle of deterministic motion was commonly held to apply to complex systems until the beginning of the twentieth century. The idea that all systems could be predicted (and hence understood) in some clockwork fashion was shaken by the discovery (by Heisenberg, for example) of the bizarre behaviour of atomic and quantum systems (Gutzwiller, 1990). However, it was assumed that large-scale systems such as the climate could be predicted accurately, if the starting state and boundary conditions were known exactly.

The equations governing the climate system were initially developed in the late nineteenth century and thought to be limited only by the lack of global data coverage (Scorer, 1997). With the advent of research into dynamical and complex systems, it was

realised that extremely small errors in knowledge of the initial conditions would rapidly cause divergence between the non-linear equations modelling a system and the natural phenomenon under consideration. Lorenz (1963) published results from an extremely simplified atmospheric model. He used three non-linear equations to describe heating and wind advection. After discovering that relative differences of less than 0.1% between two model inputs gave completely opposite answers after only a relatively small number of iterations, Lorenz realised that dynamical systems were extremely sensitive to error. Further research over the past four decades has found that chaotic behaviour resides in all non-linear three-dimensional systems from climate (e.g. Hansen et al., 1997) to planetary orbits (e.g. Varadi et al., 1999). Moreover, it is now accepted that complex non-linear systems cannot be accurately forecast beyond a limited time-period.

The development of computational general circulation models (GCM) of the atmosphere began in the years after World War II (Edwards, 2000). With increasing computational power real-time forecasts could be made. Numerous mathematical techniques were developed to increase the accuracy and speed of computation. The rapid increase in measurements from satellite and global weather stations allowed the assimilation of data into the GCM, and the expansion of computing power allowed GCM to represent ever more sophisticated atmospheric states. However, with advances in data collection, the improving accuracy of numerical weather prediction models began to level off. For example, in 1999, a large winter storm developed in Europe which was not predicted by the weather forecasting models (Mackenzie, 2003). Analysis of the modelling revealed that the atmosphere was in a state in which it was extremely sensitive to input conditions (i.e. errors in the measurements).

Searching for a method to better represent the potential divergence of the system led to the introduction of Monte Carlo simulation methods into the forecasting models. The primary approach in modern forecasting is to use Ensemble Kalman Filtering to produce a collection of initial models, all slightly perturbed from the measured or expected starting point. The models are run forward in time and when a measurement is available, it is input into the system (in combination with the expected error of the

measurement). This approach allows the development of error bounds on the predictions and examination of the evolution of the model. In particular, it allows non-linear states to evolve - for example, in a system very sensitive to initial conditions, the divergence to two or more opposite end-members can be observed.

This powerful technique can potentially be applied to the problem of forecasting the non-linear SV of the Earth's magnetic field. Similar approaches have been reported in the recent literature. Fournier et al. (2007) describe a simple non-linear physical dynamo model in which they assimilate data while Kuang et al. (2008) worked on a complex numerical geodynamo model in which Kalman filtering is employed. In the next section I describe the attributes of the Kalman filter.

6.3 Kalman Filtering

Kalman (1960) developed the mathematical description for the optimal combination of data and model forecasts based upon the relative weight of the known errors of each. The applications of this filter are varied - from guidance of the Apollo missions (the original problem for Kalman) to modern control systems for robots (Dorf & Bishop, 2008). Consider the simple problem of optimally combining two measurements x_1 and x_2 with known variances σ_1^2 and σ_2^2. The minimum variance solution is given by:

$$\hat{x} = \frac{\sigma_2^2}{\sigma_1^2 + \sigma_2^2} x_1 + \frac{\sigma_1^2}{\sigma_1^2 + \sigma_2^2} x_2. \tag{6.1}$$

Within the Kalman Filter, x_1 represents the 'guess' from the forecast while x_2 is the physical measurement of the state (i.e. reality). In essence, the Kalman Filter optimally blends an imperfect representation of an actual process with a measurement of the process contaminated with error. The following pages explain the notation and concepts of the Kalman Filter before proceeding to the description of the Ensemble Kalman Filter.

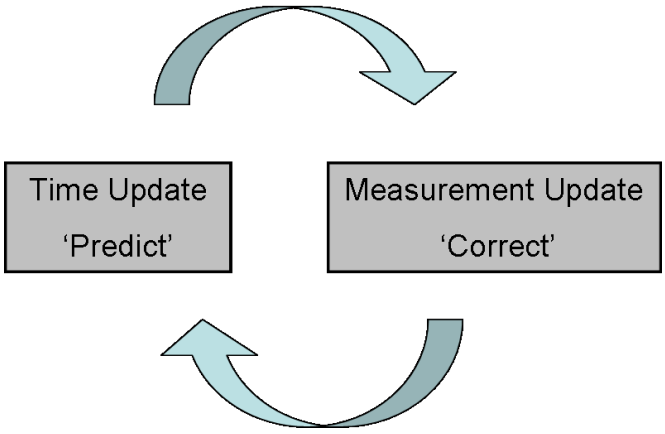

Figure 6.1: Flow Diagram for a discrete Kalman Filter.

6.3.1 Representation of State, Process and Noise

In a standard forecasting problem, the initial state is assumed approximately known and the process by which the state evolves over time is modelled by a set of equations which relate a prior state to the current state. Over time, the imperfect knowledge of the initial state or representation of the process for propagation of the state forward in time causes the modelled state, as computed, to diverge from the true state, as measured. Assimilation of a measurement is required to realign the state of the process with reality. Ideally, a measurement would be error-free and assimilated into the process as it is taken. However, for practical purposes, no measurement is error-free nor can it be used the instant it is taken. Hence, all measurements contain errors.

A Kalman Filter is implemented in two steps - forecast of the evolution of the model state and assimilation of a measurement. In computational terms, these steps are separate and known as the *predictor-corrector* sequence (Figure 6.1).

The formulation of the discrete Kalman Filter follows the arguments of Kalman (1960) and Welch & Bishop (2001). Let a vector, $\boldsymbol{x} \in \Re^n$, represent the state of a dynamic process governed by a linear stochastic equation. (The non-linear case will be discussed later.) At time k, the vector can be updated by the relation:

$$\boldsymbol{x}_k = \boldsymbol{A}\boldsymbol{x}_{k-1} + \boldsymbol{w}_k. \tag{6.2}$$

When a measurement $\boldsymbol{z} \in \Re^m$ is taken, it has the form:

$$\boldsymbol{z}_k = \boldsymbol{H}\boldsymbol{x}_k + \boldsymbol{v}_k. \tag{6.3}$$

The matrix $\boldsymbol{A} \in \Re^{n \times n}$ is the prediction equation relating the state at time k to that at time $k-1$, while the matrix $\boldsymbol{H} \in \Re^{m \times n}$ is the measurement matrix, relating the measurement vector to the state vector. These matrices may be time-dependent (i.e. change at each timestep k). The random variable vectors $\boldsymbol{w}_k$ and $\boldsymbol{v}_k$ represent process and measurement noise and are assumed i.i.d. (independent and identically distributed) and Normally-distributed:

$$p(w) \sim N(0, Q) \tag{6.4}$$

$$p(v) \sim N(0, R) \tag{6.5}$$

where the process noise has covariance $\boldsymbol{Q}$ and measurement noise has covariance $\boldsymbol{R}$. The process and measurement matrices may be constant or evolve over time. The noise covariances may also change with each time step, e.g. depending on the quality of the data available.

The goal of the Kalman filtering is to minimise the error between the true state vector, $\boldsymbol{x}^t$, and the estimated state vector, $\boldsymbol{x}^f$, before a measurement or the estimated state vector, $\boldsymbol{x}^a$, after a measurement has been assimilated. The *a priori* error before assimilation of a measurement can be expressed as $\boldsymbol{e}_k^f = \boldsymbol{x}^t - \boldsymbol{x}^f$ while the *a posteriori* error after measurement assimilation can be written as $\boldsymbol{e}_k^a = \boldsymbol{x}^t - \boldsymbol{x}^a$.

The *a priori* estimate of error covariance is:

$$\boldsymbol{P}_k^f = E[\boldsymbol{e}_k^f \boldsymbol{e}_k^{f^T}] \tag{6.6}$$

while the estimated error covariance of the measurement is $\boldsymbol{R}$, as given in Equation 6.5.

From Kalman (1960), the optimal blending of the forecast and measurement to

generate the assimilated state vector, $\boldsymbol{x}_k^a$, at time k is through the so-called Kalman gain matrix ($\boldsymbol{K}_k \in \Re^{n \times m}$):

$$\boldsymbol{x}_k^a = \boldsymbol{x}_k^f + \boldsymbol{K}_k(\boldsymbol{z}_k - \boldsymbol{H}\boldsymbol{x}_k^f) \tag{6.7}$$

where

$$\boldsymbol{K}_k = \boldsymbol{P}_k^f \boldsymbol{H}^T (\boldsymbol{H}\boldsymbol{P}_k^f \boldsymbol{H}^T + \boldsymbol{R})^{-1}. \tag{6.8}$$

Examination of Equations 6.7 and 6.8 reveals the important aspects of the filter:

- If the measurement $\boldsymbol{z}_k$ and model prediction $\boldsymbol{x}_k^f$ are equal, then the update has no effect.
- If the measurement covariance error ($\boldsymbol{R}$) is small, then the *innovation* [($\boldsymbol{z}_k - \boldsymbol{H}\boldsymbol{x}_k^f$)] is more heavily weighted in the update.
- Equally, if the model covariance error ($\boldsymbol{P}^f$) is small then the forecast state ($\boldsymbol{x}_k^f$) is more important.

To update the covariance of the model at each time step:

$$\mathbf{P}_k^f = \mathbf{A}\mathbf{P}_{k-1}^f \mathbf{A}^T + \mathbf{Q} \tag{6.9}$$

where $\mathbf{Q}$ is the covariance matrix for the model errors. When the Kalman gain matrix has been calculated, the covariance of the assimilated state vector is calculated as:

$$\mathbf{P}_k^a = (\mathbf{I} - \mathbf{K}_k\mathbf{H})\mathbf{P}_k^f. \tag{6.10}$$

The advantage of the Kalman filter is the measurements can be assimilated whenever they are available. When no data are available, the process is modelled by forecasting. Even relatively poor data can be used to constrain the forecast, as they are optimally included into the filter. The steps for predicting and correcting are given in the algorithm shown in Figure 6.2.

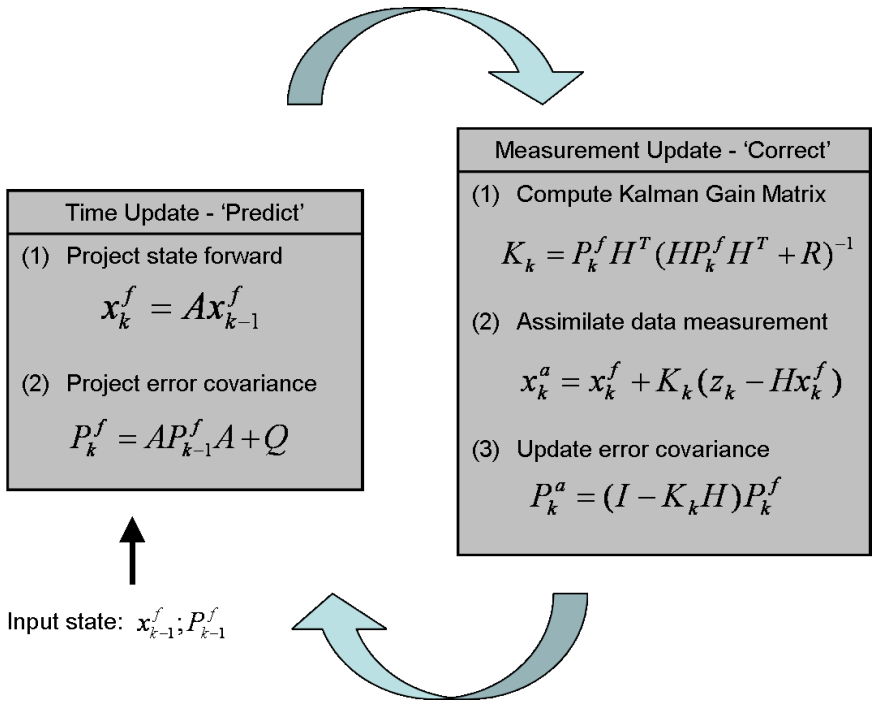

Figure 6.2: Algorithm for the discrete Kalman Filter.

6.3.2 Extended Kalman Filtering

The Kalman Filter, as described above, is for linear systems of equations under the primary assumption of Gaussian zero-mean noise in the model and the measurements. The filter can be extended to the non-linear domain, where most interesting geophysical problems lie. The Extended Kalman Filter (EKF) is computed by linearising the forward model about the current mean and variance. In this case, the prediction of the non-linear forward model is expressed as:

$$x_k = f(x_{k-1}, w_k) \tag{6.11}$$

using the partial derivatives of the process and measurement functions. Measurements are assumed to have the form:

$$z_k = h(x_k, v_k). \tag{6.12}$$

The EKF allows more complex processes to be modelled - such processes are no longer required to be Gaussian, for example. However, it is an *ad hoc* method for estimating the state of the system and has serious difficulties.

In practical use, EKF models have been shown to have very unstable behaviour. Evensen (1992) pointed out that discarding the higher order terms, in order to linearise the model, led to the unbounded growth of the covariance matrix. To control this growth, approximations are required, which lead to further error. Additionally, models using the Extended Kalman Filter not only require a huge computational overhead both for calculation of the partial derivatives and the linearisation but also for storage of the covariance matrices. In a weather forecasting model, memory space can quickly become exhausted if the covariance matrices are needed for each calculation (e.g. a standard GCM can have over 75 million cells). Clearly, a better solution was required. Evensen (1994) proposed the Ensemble Kalman Filter to overcome the unstable behaviour of the EKF and to approximate the behaviour of non-linear models using a massively less computationally expensive method.

6.4 Ensemble Kalman Filtering

In his classic paper, Evensen (1994) outlined the method of data assimilation using Monte Carlo methods as an alternative to the Extended Kalman Filter. The method uses a set (or ensemble) of perturbed models to carry information about the non-linearity of the process forward in time while still optimally assimilating data, hence giving rise to the name of Ensemble Kalman Filtering (EnKF). In this section, I outline the salient features of the method based on the work of Evensen. The details and proofs of the technique are more fully developed in Evensen (2004) and Evensen (2007).

6.4.1 Stochastic Dynamic Prediction

It must be recognised that any complex model attempting to predict and forecast the 'real world' will do so imperfectly. The initial conditions of state are only known to within a certain error and at worst will be a 'best guess'. The model will only

be replicating the behaviour at a certain scale and measurements will be sparse and contaminated with some form of error. Any forecast is difficult to validate, as the 'true' state of the system cannot be known. In a similar manner to under-parameterised inverse problems, there are an infinite number of forecasts which are close to the true state and are consistent with the measurements. The best that can be achieved is an approximation to the truth. I will now explain the concept and implementation of the Ensemble Kalman Filter.

Using the notation of Evensen (1994), let the state of the system at time k be represented by the vector $\psi(k) \in \Re^n$. This can be imagined as a point in n-dimensional phase space $\mathcal{D}$. The evolution of the vector can then be considered as tracing a path through phase space. If the initial state is thought of as the most likely state, the uncertainty could be represented by a randomly distributed discrete set (or ensemble) of other states, scattered about in $\mathcal{D}$, each with a particular probability of being correct. This can be thought of as a cloud of points in $\mathcal{D}$. With each time step and forward projection, the cloud of points evolves, changing position and shape (see Figure 6.3).

If there are N points in the cloud surrounding the initial estimate, then as N increases and becomes very large, the probability distribution can be thought of as becoming continuous. The probability density, ϕ, must satisfy:

$$\int \phi(\psi) d\psi = 1. \tag{6.13}$$

This forces the 'true' state of the system to lie within the domain. For this distribution of points, the first and second order moments can be defined as:

$$\mu_i = \overline{\psi_i} \tag{6.14}$$

$$P_{ij} = \overline{(\psi_i - \mu_i)(\psi_j - \mu_j)} \tag{6.15}$$

where μ_i is the mean and P_{ij} is the covariance. If the starting point of a model is set to be the mean of the ensemble $\mu(k = 0)$, it therefore coincides with the initial ensemble estimate $\psi(k = 0)$. The evolution of the ensemble allows the variance in the model to

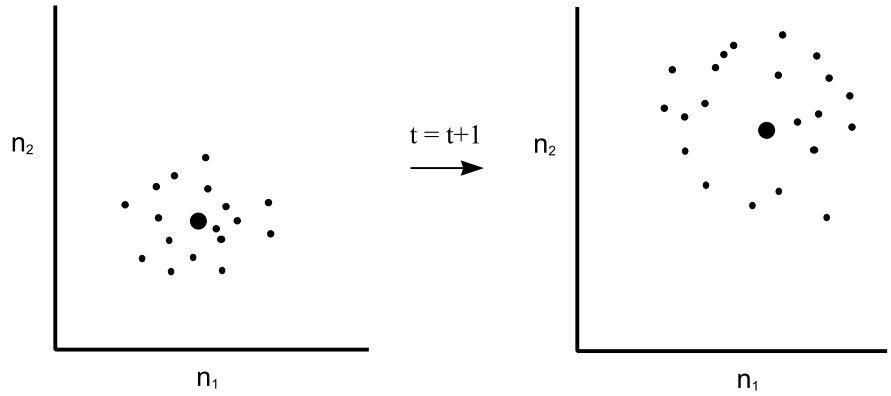

Figure 6.3: Time evolution (from time t to $t+1$) of an ensemble of states about a mean vector for $n = 2$ dimensions. The large dot in the centre represents the mean value of the ensemble.

be captured by the diffusion of the cloud of possible states. Under the assumption of Normally-distributed statistics, the further away from the mean value, the less likely the state is of being equal to the 'true' state. The initial state is defined as the central forecast, while the ensemble of other states is generated randomly using the initial variance of the initial state error. The model error of each is forced by the addition of a specific variance at each step, providing an increase in overall variance.

The ensemble moves in phase space by forward propagation through the equations governing the model evolution. As it evolves, the probability density distribution of the ensemble itself contains information about the non-linearity of the model equations. This information can be used in conjunction with the physical predictions of the state vector. Equation 6.13 implies the system is Hamiltonian (i.e. closed), where ensemble points are neither created nor destroyed over time. The cloud may deform and contort over time, but the total energy within the system must be conserved. This type of process is known as dynamic stochastic prediction (Evensen, 1994).

6.4.2 Approximating the Kalman Filter

A key assumption, so far, is that the ensemble of states behaves in an equivalent manner to a standard Kalman Filter. In the EnKF, the prediction step of the filter produces an ensemble of vectors ($\mathbf{x}_k^f$) which have a mean and covariance. Assimilating a measure-

ment ($\mathbf{z}_k$) produces an updated ensemble ($\mathbf{x}_k^a$) with a new (hopefully smaller) mean and covariance. However, does this method approximate a true Kalman filter? The EnKF can be shown to do so, as follows.

Consider a scalar example, at time k, where x_k^f is a model forecast with noise w_k^f and z_k is a measurement with some associated measurement noise v_k. The forecast, x_k^f, the assimilated estimate, x_k^a, and measurement, z_k, are related to the true state of the system, x_k^t, by:

$$x_k^f = x_k^t + w_k^f \tag{6.16}$$

$$x_k^a = x_k^t + w_k^a \tag{6.17}$$

$$z_k = x_k^t + v_k \tag{6.18}$$

with expectations (i.e. the mean of) $\overline{w}_k^f = \overline{w}_k^a = \overline{v}_k = 0$, given a large enough ensemble.

Using the result from Equation (6.7), the optimal combination of measurement and forecast is:

$$x_k^a = x_k^f + \frac{P_k^f}{P_k^f + R_k}(z_k - x_k^f) \tag{6.19}$$

where $P_k^f = \overline{(w_k^f)^2}$ and $R_k = \overline{(u_k)^2}$ are the error covariances. As shown in Evensen (1994), the updated error of the ensemble can be estimated as:

$$\begin{aligned} P^a &= \overline{(w^a)^2} = \overline{(x^a - x^t)^2} \\ &= \overline{\left(x^f + \frac{P^f}{P^f + R}(z - x^f) - (x^t)\right)^2} \\ &= \overline{\left(w^f + \frac{P^f}{P^f + R}(z - x^f)\right)^2} \\ &= \left(I - \frac{P^f}{P^f + R}\right) P^f + 2\frac{P^f}{P^f + R}\left(I - \frac{P^f}{P^f + R}\right)\overline{w^f u}. \end{aligned} \tag{6.20}$$

If the ensemble is large enough, the expectation is that $\overline{w^f u} = 0$ and so

$$P^a = \left(I - \frac{P^f}{P^f + R}\right) P^f \tag{6.21}$$

which is equal to the result from a standard Kalman Filter in Equation (6.10), assuming the measurement and forecast errors to be uncorrelated. This proves the ensemble Kalman Filter to be equivalent to the standard Kalman filter when a suitably large number of ensembles states are used. From the second line in Equation (6.20) it can be seen that P^a can be calculated directly from the ensemble – though as defined, the true state is required to be known. However, in practice, this can be approximated as the mean or the central forecast of the model.

6.4.3 Practical Implementation

It is essential that the model state and measurements are perturbed by a random matrix with zero-mean rows. In a practical implementation, this relies upon an efficient random number generator. This section examines the formulation of the method into a scheme for computational use.

An initial ensemble of state vectors can be defined from the perturbation of the input state vector $\mathbf{x}_k^f$. Assuming that the model error can be described by covariance $\mathbf{Q}$, then at time k, an ensemble of N members can be created by the addition of random vectors to the initial state:

$$\mathbf{x}_j = \mathbf{x} + \epsilon_j \tag{6.22}$$

The subscript j is the index into the ensemble from $1, \ldots, N$. The variable ϵ is a vector of randomly generated numbers. Each of the ensemble states is integrated forward in time using the model equations:

$$x_{j_k} = f(x_{j_{k-1}}) \tag{6.23}$$

The covariance matrices have to be estimated from the ensemble:

$$\boldsymbol{P}^f \simeq \boldsymbol{P}_e^f = \overline{(\boldsymbol{x}^f - \overline{\boldsymbol{x}}^f)(\boldsymbol{x}^f - \overline{\boldsymbol{x}}^f)^T} \tag{6.24}$$

$$\boldsymbol{P}^a \simeq \boldsymbol{P}_e^a = \overline{(\boldsymbol{x}^a - \overline{\boldsymbol{x}}^a)(\boldsymbol{x}^a - \overline{\boldsymbol{x}}^a)^T} \tag{6.25}$$

In a similar manner, assume a vector of measurements $\mathbf{z}$ with a known error covariance $\mathbf{R}$. An ensemble of measurements, with N members, is created by perturbing the vector:

$$\mathbf{z}_j = \mathbf{z} + \epsilon_j \tag{6.26}$$

where $j = 1, \ldots, N$. The expectation of the simulated measurements should be zero. The ensemble covariance is calculated as:

$$\mathbf{R}_e = \overline{\epsilon\epsilon^T} \tag{6.27}$$

which is an approximation but, of course, in a large enough ensemble, converges to $\mathbf{R}$. It can be argued that often the error associated with measurement is not well-defined, so this approximation introduces only slight additional uncertainty. The impact of the approximation of $\mathbf{R}$ is only in the Kalman gain matrix, whilst the approximation of other values - such as P_e^f - is larger as it appears twice in the predictor-corrector algorithm.

At each assimilation time step, the ensemble members are updated by Equation (6.7):

$$x_j^a = x_j^f + \mathbf{P}_e^f \mathbf{H}^T (\mathbf{H}\mathbf{P}_e^f \mathbf{H}^T + \mathbf{R}_e)^{-1} (z_j - \mathbf{H}x_j^f). \tag{6.28}$$

The ensemble mean $\mathbf{x}_k$, the variance of the ensemble and the distribution of the ensemble members can be used to characterise the process and to examine the 'spread' of the forecast models. (Note, again, $\mathbf{H}$ relates the measurement vector to the state vector).

6.4.4 Efficient Computational Implementation

The computational implementation of the EnKF for large-scale numerical models can be difficult. However, Evensen (2004) outlines an efficient scheme for the calculation of the assimilation.

Let the matrix $\boldsymbol{M}$ store the range of ensemble state vectors $x_j \in \Re^n$:

$$\boldsymbol{M} = (x_1, x_2, \ldots, x_N) \in \Re^{n \times N} \tag{6.29}$$

where N is the number of ensembles. The mean vector of the ensemble can be defined as $\overline{\boldsymbol{M}}$ and the perturbation matrix of the ensemble from the mean vector described as:

$$\boldsymbol{M'} = \boldsymbol{M} - \overline{\boldsymbol{M}} = \boldsymbol{M}(\boldsymbol{I} - \mathbf{1}_N) \tag{6.30}$$

where $\mathbf{1}_N \in \Re^{N \times N}$ is an $N \times N$ matrix where every element is equal to 1 and $\boldsymbol{I}$ is the identity matrix with dimension $N \times N$. The ensemble covariance matrix can be calculated as:

$$\boldsymbol{P}_e = \frac{\boldsymbol{M'}(\boldsymbol{M'})^T}{N-1} \tag{6.31}$$

Let the perturbation of a measurement vector $\boldsymbol{d} \in \Re^m$, (i.e. the random perturbation of the observation) be written as:

$$\boldsymbol{d}_j = \boldsymbol{d} + \epsilon_j, \qquad j = 1, \ldots, N, \tag{6.32}$$

and stored in the matrix

$$\boldsymbol{D} = (\boldsymbol{d}_1, \boldsymbol{d}_2, \ldots, \boldsymbol{d}_N) \tag{6.33}$$

where $\boldsymbol{D}$ is a matrix of dimension $m \times N$. The perturbations of the measurement create an ensemble of vectors with zero mean and variance equal to that of the measurement error. The measurement perturbations can be stored in a matrix Υ:

$$\Upsilon = (\epsilon_1, \ldots, \epsilon_N) \ \in \Re^{m \times N} \tag{6.34}$$

The measurement covariance matrix is thus calculated as:

$$\boldsymbol{R}_e = \frac{\Upsilon(\Upsilon)^T}{N-1} \tag{6.35}$$

Finally, the *innovation* can be calculated separately to reduce it to a single matrix:

$$\boldsymbol{D'} = \boldsymbol{D} - \boldsymbol{H}\boldsymbol{M} \tag{6.36}$$

From Equation (6.28) the expression for the Kalman filter assimilation step is:

$$\boldsymbol{M}^a = \boldsymbol{M} + \boldsymbol{P}_e\boldsymbol{H}(\boldsymbol{H}\boldsymbol{P}_e\boldsymbol{H}^T + \boldsymbol{R})^{-1}(\boldsymbol{D} - \boldsymbol{H}\boldsymbol{M}) \tag{6.37}$$

The above formulation of the Kalman filter assimilation step is thus implemented using Equations (6.30) – (6.36) as follows:

$$\boldsymbol{M}^a = \boldsymbol{M} + \boldsymbol{M'}\boldsymbol{M'}^T\boldsymbol{H}^T(\boldsymbol{H}\boldsymbol{M'}\boldsymbol{M'}^T\boldsymbol{H}^T + \Upsilon\Upsilon^T)^{-1}\boldsymbol{D'}. \tag{6.38}$$

This form of the expression can be easily encoded, but care must be taken as the central portion of the equation can be singular depending on the relative size of the model and measurement perturbations. Hence, the pseudo-inverse is required to guarantee a suitable inversion of the matrix. Evensen (2004) explores further the use of singular value decomposition and eigenvalue analysis to solve Equation (6.38) for large systems. However, in this study, the current form of Equation (6.38) is easily applied to the size of systems under consideration.

6.5 EnKF: One-Dimensional Example

In order to test the program, a simple example of the implementation is shown. Consider a $1D$ linear system with a model process adding time-correlated (red) noise at each step of the forecast to a variable - this is a so-called random walk model. In this example, the forward model is $f(x) = x$. However, model noise contaminates the forward integration, forcing the variance to grow. This can be implemented in a model by allowing random noise with a known variance:

$$x_k = x_{k-1} + \sigma q_k \tag{6.39}$$

where σ is the square root of the model variance and q_k is the time-correlated pseudo-random noise, defined by:

$$q_k = \alpha q_{k-1} + \sqrt{1 - \alpha^2} w_k \tag{6.40}$$

where $\alpha \in [0, 1)$ is the correlation of the noise and w_k is a vector of white noise values from a random distribution with mean equal to 0 and variance equal to 1. If $\alpha = 0$, there is no correlation (i.e. white noise). To impose a correlation length on the noise correlation, an extra time-dependent term can be added to Equation 6.39:

$$x_k = x_{k-1} + \sqrt{\triangle t}\rho\sigma q_k \tag{6.41}$$

where $\triangle t$ is the time step. The value of ρ depends on the rate at which the variance is allowed to grow. It can be solved for through the following identity:

$$\rho^2 = \frac{1}{\triangle t} \frac{(1-\alpha)^2}{n - 2\alpha - n\alpha + 2\alpha^{n+1}} \tag{6.42}$$

where n is the number of ensembles. Again, if $\alpha = 0$, the equation becomes $\rho^2 = \frac{1}{n\triangle t}$. To update the forecast, an occasional measurement corrupted by noise with known variance is taken and assimilated into the system. The variance of the measurement is smaller than that of the model, so this has the effect of resetting the ensemble and reducing the overall 'spread' of the model.

The model has the following parameters and has been implemented in the MATLAB programming environment:

- ensemble size = 100
- time step = 0.1
- the initial value = 2.0
- model error distribution from $N(0, 1.0)$
- measurement error distribution from $N(0, 0.5)$
- measurements occur every 2 timesteps
- $\alpha = 0.95$.

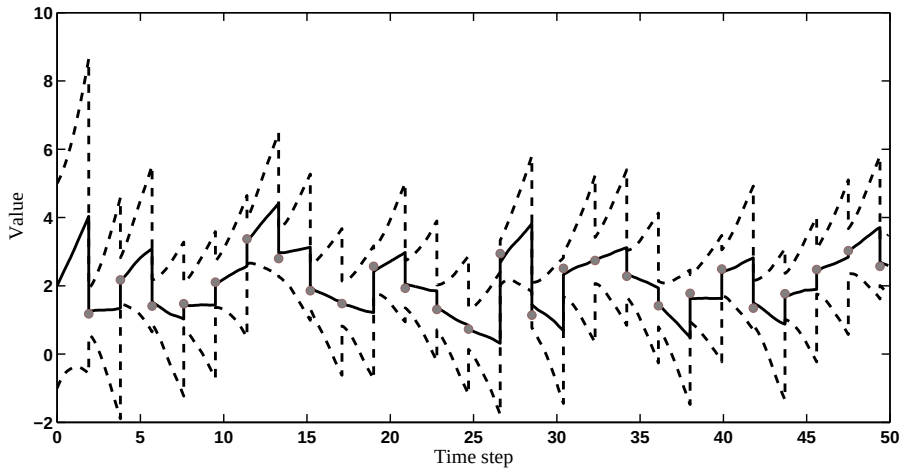

Figure 6.4: Time evolution of a scalar Ensemble Kalman Filter. The solid black line represents the mean value of the ensemble, dotted black lines show the ensemble standard deviations about the mean. Gray dots are measurements.

Figure 6.4 shows the results of a simulation for this model. At each forecast timestep, a small amount of red noise (from Equation 6.40) is added to the each of the previous ensemble members. When a measurement is taken, the mean and the covariance of the ensemble are updated using the measurement statistics. At each assimilation step, it can be seen that the mean of the ensemble approaches (though does not always equal) the measurement but the overall variance of the ensemble is reduced.

As an addition to the EnKF, Evensen & van Leeuwen (2000) developed a method for using prior ensemble information to smooth the model forecast retrospectively. This additional smoothing requires the summation of the previous ensembles from $j = 1, \ldots, l$ where l is the number of steps reached out of a total n_{steps}. The smoothing can be easily performed by storing a single vector calculation from each of the time steps. Figure 6.5 illustrates the effect of retrospective smoothing of the ensembles.

Uncorrelated noise

If the model noise of the system is assumed to be white (i.e. no time correlation) the directed nature of the 'walk' due to correlation disappears. Figure 6.6 shows a forecast simulation in the presence of white model noise. This model has the following

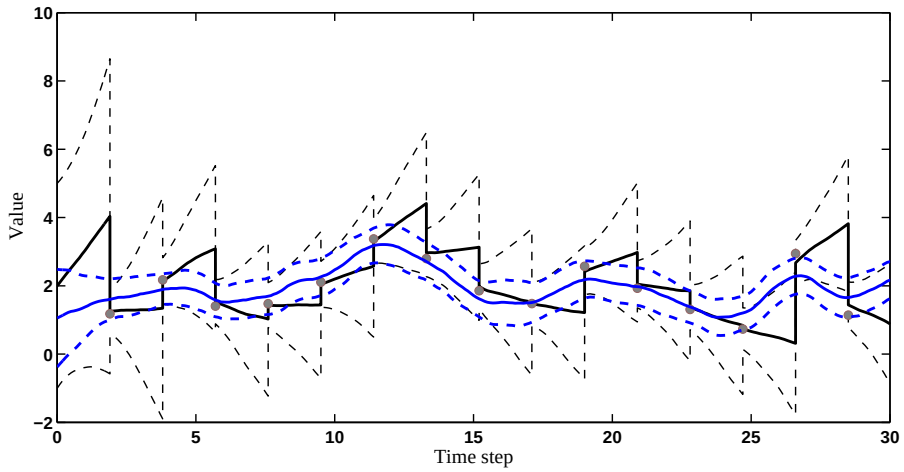

Figure 6.5: Time evolution of a scalar Ensemble Kalman Filter. The solid black line represents the mean value of the ensemble, dotted black lines show the ensemble standard deviations about the mean. Gray dots are measurements. In addition, the solid blue line represents a retrospectively smoothed forecast of the ensemble mean. The dotted blue lines show the smoothed standard deviations of the ensemble about the mean.

parameters:

- ensemble size = 100
- time step = 0.1
- the initial value = 2.0
- model error distribution from $N(0, 1.0)$
- measurement error distribution from $N(0, 0.5)$
- measurements occur every 2 timesteps
- $\alpha = 0.$

As can be seen in comparison to model in Figure 6.5, the forecast in Figure 6.6 is much noisier. This more 'wiggly' behaviour is to be expected and proves the ensemble sensitivity to noise.

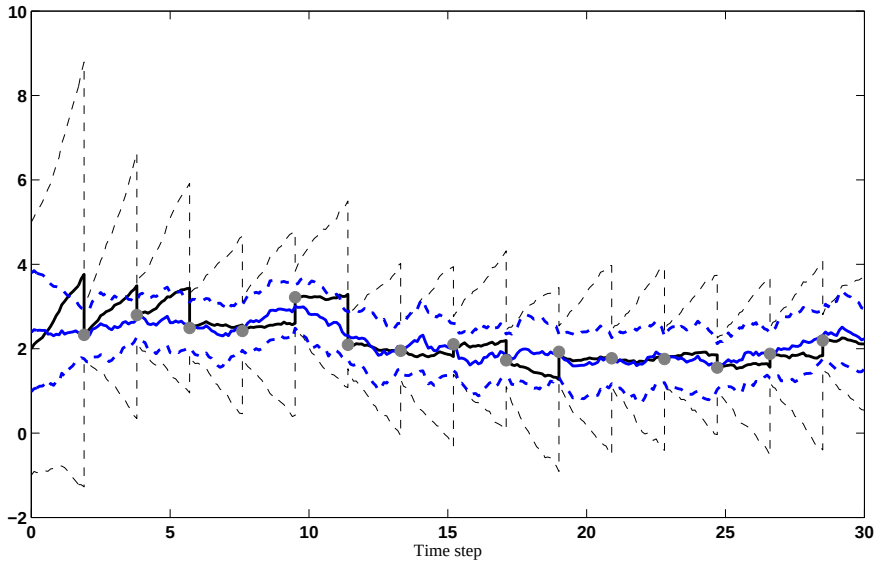

Figure 6.6: Time evolution of a scalar Ensemble Kalman Filter with white noise (no time-correlation, $\alpha = 0$). The solid black line represents the mean value of the ensemble, dotted black lines show the ensemble standard deviations about the mean. Gray dots are measurements. In addition, the solid blue line represents a retrospectively smoothed forecast of the ensemble mean. The dotted blue lines show the smoothed standard deviations of the ensemble about the mean. Compared to Figures 6.4 and 6.5, the model is much noisier.

6.5.1 EnKF: Three Dimensional Example

The one-dimensional EnKF can be extended to higher dimensions. Although it becomes more difficult to visualise high-dimension examples, coding the change is relatively simple. As an example, Figure 6.7 shows the evolution of the ensemble mean of a three-dimensional random walk model, similar in structure to the one-dimensional sample. In the figure, each line of blue dots represents the time-evolution from a measurement point. The model noise is correlated, hence the 'walk' (i.e direction of motion of the mean) always moves in a consistent direction, generally with a small amount of turning towards the end, as the correlation-length of the noise is set to be smaller than the inter-measurement time period. As the model is run for a time period of 50, there are 24 model forecast/assimilations visible. It is difficult to represent the evolution of the variance in a three dimensional model, but it can be envisaged as a cone of uncertainty about each mean.

The extension of the Ensemble Kalman Filter to higher dimensions can now be used in the modelling and forecast of the Earth's magnetic field, which can be viewed as an n-dimensional problem, where $n = l(l+2)$, l being the degree of the field model coefficients.

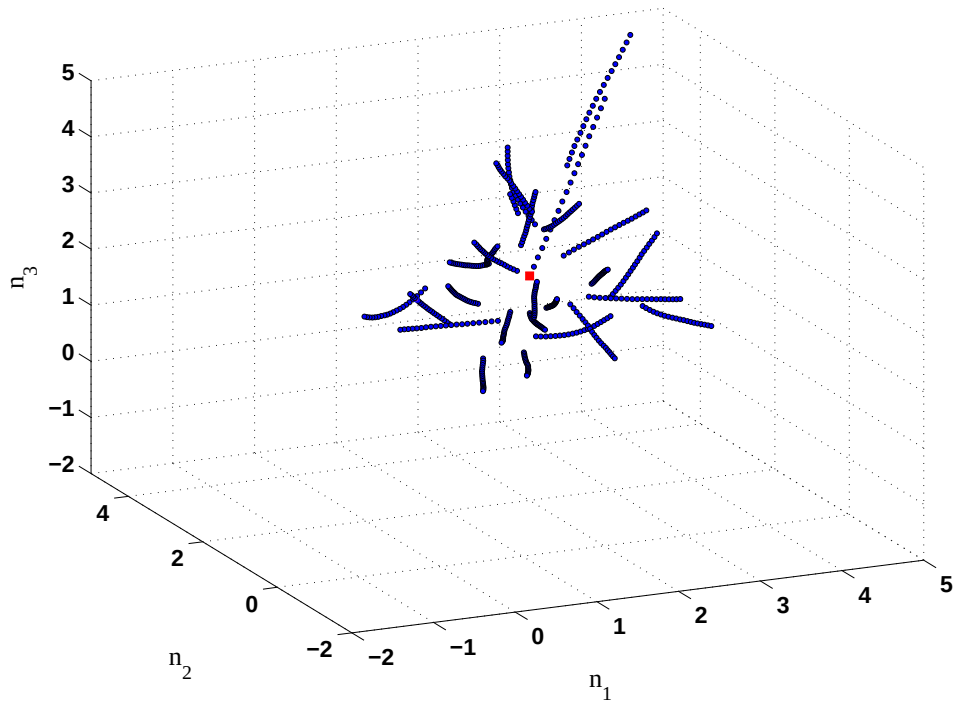

Figure 6.7: Time evolution of the mean of an Ensemble Kalman Filter. The solid black lines represent the mean value of the ensemble for a series of forecasts over time. The red square represents the true measurement value [2, 2, 2], with the variance of the measurement noise equal to 1.0.

6.6 Applying Ensemble Kalman Filtering to Forecasting

The previous sections explore the mathematical derivation and computational implementation of the Kalman and Ensemble Kalman Filter. A scalar example was presented to illustrate the principles of the technique. However, it is not clear how best to implement the EnKF for predicting field evolution. After some deliberation and experimentation it was decided to use the main field coefficients as the state vector, updated by SV estimates generated from core flow models. The main issue was how to allow the flow models control the evolution of the field and the ensemble in a meaningful and direct manner. I also considered what manner to capture the variability in the flow over time, how many ensemble members were needed produce statistically robust results and how best to visualise the resulting ensembles.

There are three stages required to implement the EnKF for this problem: (1) generation of the initial ensemble, (2) forecasting the change of the field by driving the field model with SV from core flow models and (3) assimilation of measurements from a 'true' field model. Each of these stages is explained in detail below.

Initiating the Ensemble

The method for initiating the ensemble is outlined in Figure 6.8. A perturbed set of Gauss coefficients whose mean value is equal to the initial state of the field is generated to produce the first ensemble. This is implemented as follows:

1. An initial state vector is set to be a vector of Gauss coefficients ($[\mathbf{g}_l^m]_1$) from a field model (e.g. xCHAOS) up to degree and order $l = 14$.

2. To generate the perturbation to the $\mathbf{g}_l^m$ coefficients, the standard deviation for each coefficient over the entire set of flow models is calculated (e.g. see Figure 4.34 for an example of the variability in each flow coefficient $[\mathbf{t}; \mathbf{s}]$).

3. A matrix of normally distributed random numbers $N(0, 1)$ with size $[l(l + 2) \times n_{ensembles}]$ is created, where $n_{ensembles}$ is the number of ensemble states (in this case, 1000 was found to be sufficient to gain almost exactly repeatable results).

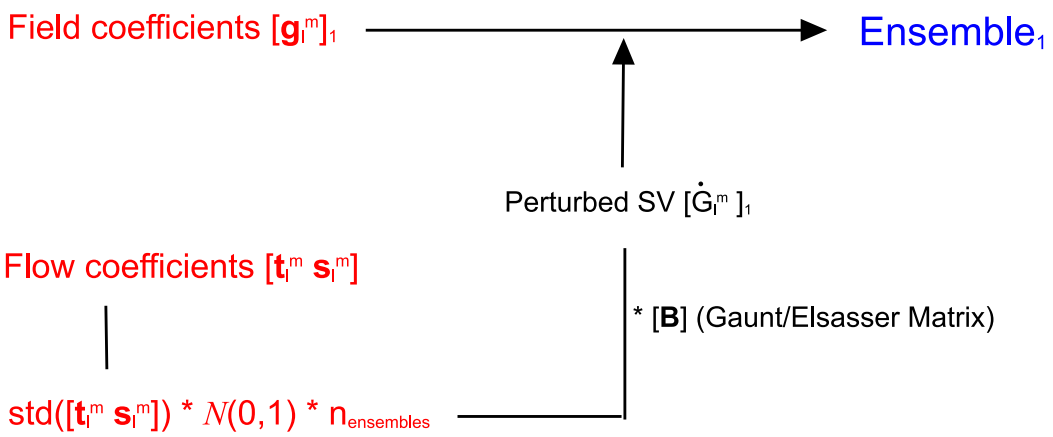

Figure 6.8: Algorithm for initiating the EnKF ensemble. See the text for details.

4. The matrix of random numbers is multiplied by the standard deviation of the flow coefficients to give a perturbed flow coefficient matrix.

5. The perturbed flow coefficient matrix is pre-multiplied by the Gaunt/Elsasser matrix to produce a perturbed matrix of SV $[\dot{\mathbf{G}}]$, correctly scaled to reflect the uncertainty in the flow models.

6. The perturbed SV matrix is then added to the initial state vector to produce an ensemble (Ensemble$_1$) of size $[l(l+2) \times n_{ensembles}]$.

Once the initial ensemble has been created, forecasting and assimilation can commence.

Driving the Ensemble Forecasts

The forecast (prediction) of the field is driven forwards by adding to each field coefficient its monthly SV from the flow model perturbed by a random matrix with zero mean and standard deviation controlled by that of the overall flow. In addition, at each timestep, model noise is added to simulate the variance of the ensemble, forcing it to grow at each forecast iteration. The model noise is controlled by the size of the time-step (Δt), the standard deviation of the SV from the previous iteration and the value of ρ, as calculated in Equation 6.42. Figure 6.9 illustrates the steps involved in the forecast step.

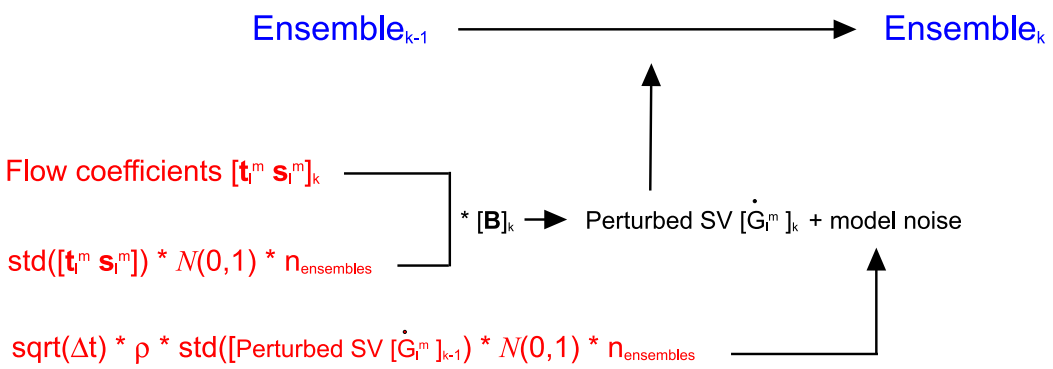

Figure 6.9: Algorithm for forecasting in the EnKF. See text for details.

1. The SV generated by the flow model for month$_k$ is calculated by multiplying it by the Gaunt/Elsasser Matrix (**H**).

2. The monthly SV is perturbed by the standard deviation of the flow converted into an equivalent SV.

3. Model noise is simulated by multiplication of a matrix of random zero-mean normally-distribution numbers (of size $[l(l+2) \times n_{ensembles}]$) with the square-root of the timestep ($\sqrt{\Delta t}$) and ρ.

4. The matrix of perturbed SV and model noise is added to the ensemble from the previous timestep (Ensemble$_{k-1}$) to produce the forecast for the current ensemble (Ensemble$_k$).

This process is repeated until a measurement becomes available for assimilation into the ensemble.

Assimilation of Measurements into the Ensemble

Over time, the model field will begin to diverge from the actual field. To improve the forecast, measured data can be input into the ensemble to update (correct) it. The measured data have associated errors. These are used to generate a perturbed matrix of measurements, whose mean is equal to the input data. This perturbed measurement is assimilated into the ensemble using the Kalman Filter algorithm, as outlined in Section

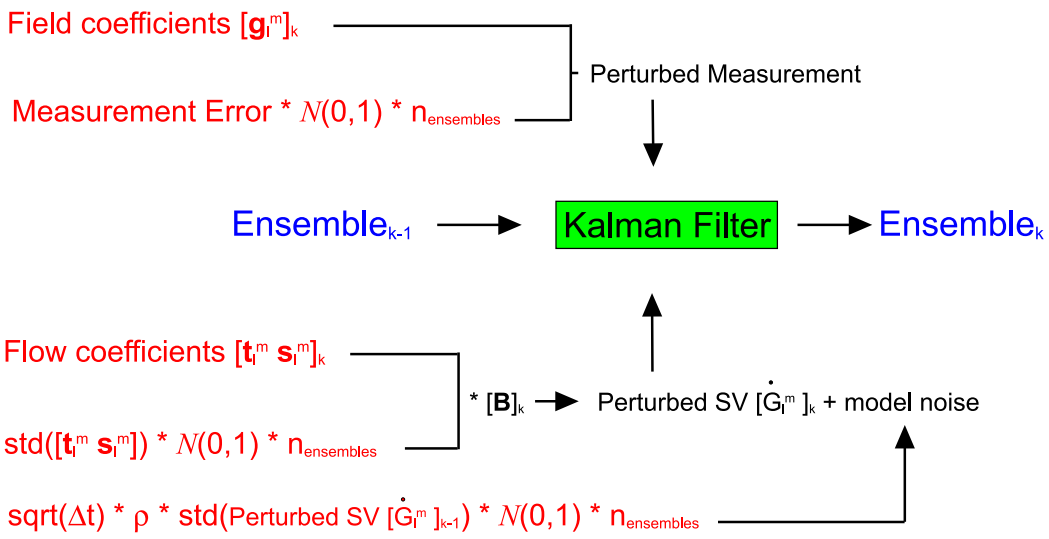

Figure 6.10: Algorithm for assimilating measurements into the EnKF. See the text for details.

6.4.3. The steps involved during the assimilation step of the algorithm are illustrated in Figure 6.10.

1. A measurement of the field is taken ($[\mathbf{g}_l^m]_k$) with a certain (known) 'Measurement Error' for each coefficient. A matrix of zero-mean Gaussian random numbers of size $[l(l+2) \times n_{ensembles}]$ is generated and scaled with the measurement error

2. The measurement is added to the matrix of scaled random numbers to produce a matrix of 'perturbed measurements' with mean equal to that of the measurement itself.

3. Using Equation (6.38) the measurement perturbation matrix and the perturbed SV are optimally assimilated into the ensemble at this timestep. Assimilation occurs typically once every 12 months.

The process and algorithm for computing field models using the EnKF method has been outlined above. Appendix B gives an example of MATLAB code used to implement Equation (6.38) for flow forecasting and data assimilation. In the next section I describe the details of implementing the method for steady and non-steady flows.

6.7 EnKF Combined with Flow Modelling Forecasts

To better understand the behaviour of the EnKF, it is worth noting that the primary controlling parameters are the errors of the model and the measurements (see Equation 6.8). These control the relative weightings assigned to forecast or the assimilated data and hence strongly influence the behaviour of the ensemble over time. Additionally, the correlation of the model noise can be controlled through the parameter α, though for this study, the model noise is assumed to be uncorrelated.

Deducing measurement or model errors for the Gauss and flow coefficients is a difficult task. Model errors of the steady flow, for example, are set to be the standard deviation of the flow coefficients divided by 10. If the model error is larger, then the ensemble becomes widely 'spread' after only a few forecasting steps. Conversely, making the model error small assumes that the flow models are correct and does not allow the ensemble to evolve with sufficient variation to capture possible non-linearities. Estimating reasonable error bounds on the measurements of the field is also awkward. If the error is set to be small, the measurement will reset the ensemble. If the error is too large, then the measurement will have little effect on the evolution of the ensemble. In the following examples, the measurement error is assumed to be one-tenth of the standard deviation of the SV from the flow models.

One point to note is that it is difficult to visualise how the forecast error diverges in a $\Re^{224}$ space (see for example Figures 6.5 and 6.7) . In the graphs shown in the next few pages, the evolution of the mean of an ensemble is shown. To illustrate how well other states within the ensemble might fit the 'true' Gauss coefficients of the field, states representing $\pm 1\sigma$ away from the ensemble mean are plotted. These are calculated by finding the mean and the standard deviation of each coefficient across the state vectors and constructing a mean vector (of size $\{224 \times 1\}$) and vectors with values $\pm 1\sigma$ from the mean. The purpose is to show graphically how 'spread out' the Gauss coefficients are within the ensemble. As random noise is added to the forecast at each timestep to enlarge the variance of the ensemble, it should be expected that the models $\pm 1\sigma$ away from the mean diverge over time.

6.7.1 EnKF using a Steady Flow Model

As shown in Section 5.1.1, the steady flow model initially diverges from the main field models slowly before accelerating at the end of the time period. Assimilating actual field measurements would be expected to improve the fit of the predicted field to the 'true' field. The steady flow model consists of a single set of coefficients, thus preventing a good estimate of the associated error. The model error was thus set, arbitrarily, to be one-tenth of the value of each flow coefficient. The measurement error was set to be one-tenth of standard deviation of the SV generated by the flow model. The timestep (Δt) was set to be $1/12^{th}$ of a year.

The results of the forecast and data assimilation for the GRIMM, xCHAOS and POMME field models are shown in Figure 6.11. Each ensemble was initiated using the respective field model. A measurement (i.e. Gauss coefficients from the field model) was assimilated every twelve months. (These are seen as jumps in the curves.)

The black line represents the mean Gauss coefficients of the ensemble, while the red dashed lines are Gauss coefficients calculated by subtracting or adding the values one standard deviation away from the mean ensemble model. In Figure 6.11 (a), the mean ensemble (black line) fits to within 10nT of the GRIMM model until 2005.75. Interestingly, in this example, the ensemble model $+1\sigma$ away from the mean actually fits the 'true' model better than the mean ensemble model, while the -1σ model is worse. Another note-worthy point is that certain measurement assimilations have no effect or cause the fit to become slightly worse (e.g. 2004.5 and 2005.5). This is due to the mean misfit being small ($\sim$ 5nT) and so the measurement assimilation does not affect the mean but does reduce the 'spread' of the ensemble (hence the $\pm 1\sigma$ models become equivalent to the mean). At the end of the period, the forecast begins to rapidly diverge from the GRIMM field model, but as stated earlier, the GRIMM model is not valid beyond 2005.5.

The forecasts for the xCHAOS and POMME models in Figure 6.11 (b) and (c) behave in a similar manner to the GRIMM model, though do not diverge as rapidly toward the end of the period. Overall, the forecast model best fits the POMME model.

With a steady flow model and annual data assimilations, the RMS difference between the forecast model and the 'true' field can be maintained at less than 10nT.

6.7.2 EnKF using Non-steady Flow Models

Using a series of non-steady flow models should give a better estimate of the likely variation of the flows from month-to-month, allowing some sort of quantification of the model errors. As shown in Section 5.1.3, non-steady flows provided a better fit to the field models than steady flow. The following sub-sections examine the comparison of forecasts from three different VO datasets using the EnKF method.

6.7.3 Dataset 1

For Dataset 1 (from Section 4.4), the size of the model error is determined from the variability of the flow coefficients about the mean flow over 68 months of data. The SV from the monthly flow model is randomly perturbed to produce $n_{ensembles}$ of possible SV models. The standard deviation of the SV models is calculated from the standard deviation of the flow coefficients, forward modelled to produce equivalent SV. The model noise is generated from a matrix of zero-mean Gaussian numbers multiplied by the standard deviation of the perturbed SV and scaled by $\sqrt{\Delta t}$ and ρ. Figure 6.12 shows the results of an ensemble forecast and assimilation experiment, over the period 2002.5 – 2008.0.

In Figure 6.12 (a), the mean of the ensemble fits the GRIMM field model better than the models from $\pm 1\sigma$ away from the mean, suggesting that it is a good representation of the 'true' field model. The associated red dashed lines of $\pm 1\sigma$ rapidly diverge from the GRIMM field model, as the forecast error is larger than that imposed in the ensemble in Section 5.1.3. At each assimilation, the forecast error variance (the $\pm 1\sigma$ curves) does converge toward the mean, suggesting that the error of the measurement is much smaller than that of the forecast model. The $+1\sigma$ forecast model does occasionally provide an almost exact fit to the GRIMM model (e.g. at 2004.5).

The xCHAOS and POMME models (Figure 6.12 (b) and (c)) behave in a similar

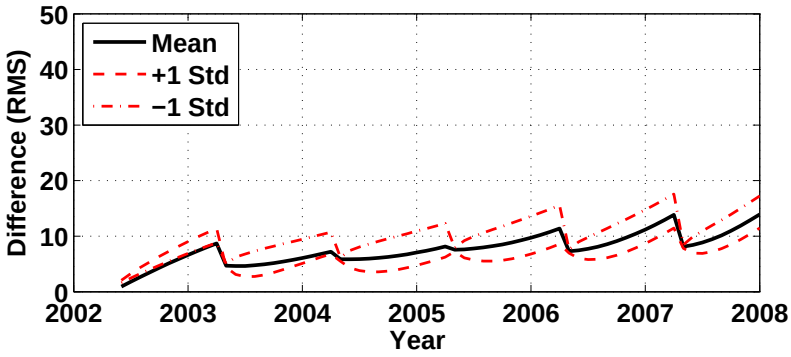

(a) GRIMM field model

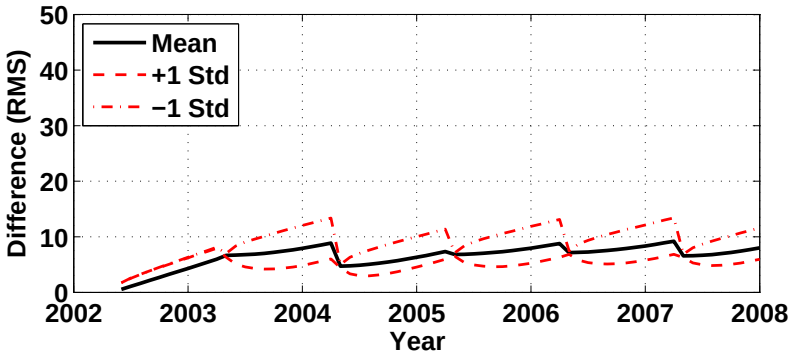

(b) xCHAOS field model

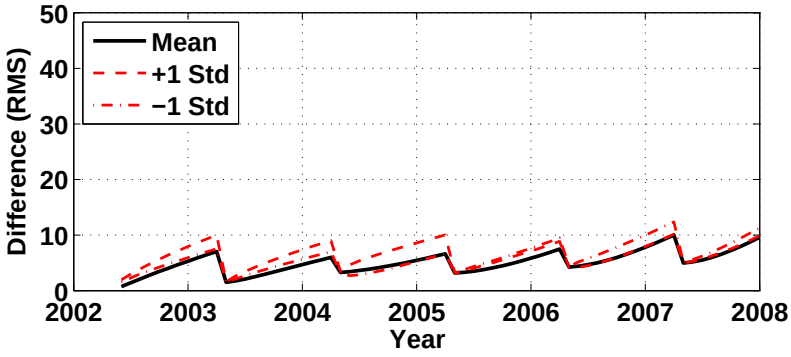

(c) POMME field model

Figure 6.11: RMS difference (in nT) between a EnKF field model derived from SV generated by a steady flow model from All CHAMP data and the (a) GRIMM, (b) xCHAOS and (c) POMME field models. See text for explanation. Note the y-axis scale is 0–50nT.

manner, though with slightly differing ensemble evolution, indicated by the unequal $\pm 1\sigma$ curves. Overall, the RMS difference between the forecast and field models remains within 20nT. Note that using a smaller model error would result in a much better fit to the field models.

6.7.4 Dataset 2

Figure 6.13 shows the comparison of the flow models from Dataset 2. The results are remarkably similar to those of Figure 6.12. Although Dataset 2 has been shown to be less contaminated by external field noise, flows derived from it predict the field models of GRIMM, xCHAOS and POMME slightly less well. The mean of the ensembles are only slightly larger on average than those from Dataset 1. In detail, the forecast model around 2004 is better fit, but the misfit is larger toward the start and the end of the models. In Figure 6.13, the $\pm 1\sigma$ curves show a larger divergence, on average, than those in Figure 6.12.

6.7.5 Dataset 1 with CM4 Correction

In Section 4.6.1 I investigated whether a parameterised field model such as the Comprehensive Model (CM4) could be used to remove external field contamination from each individual satellite datum based upon the estimated Dst and F10.7 indices, before calculation of the VO grids. It was shown in Chapter 4 that while CM4 correction did reduce correlation between the residual bias and the Dst index of the external field, other artefacts were introduced into the data (c.f. Table 4.2 and Figure 4.18), cancelling the benefits of external field removal. The forecasts from the flow models generated from Dataset 1 with CM4 correction applied are examined in this section.

In Figure 6.14, the comparison of the forecast with the field models shows the mean ensemble diverges much more rapidly than Dataset 1 and 2. The ensemble states at $\pm 1\sigma$ are also very much more in error than those in Figures 6.12 and 6.13. Of interest too are the semi-annual peaks and troughs in the mean ensemble curves. When Dataset 2 with CM4 correction applied was tested in the same manner, curves with similar peaks and

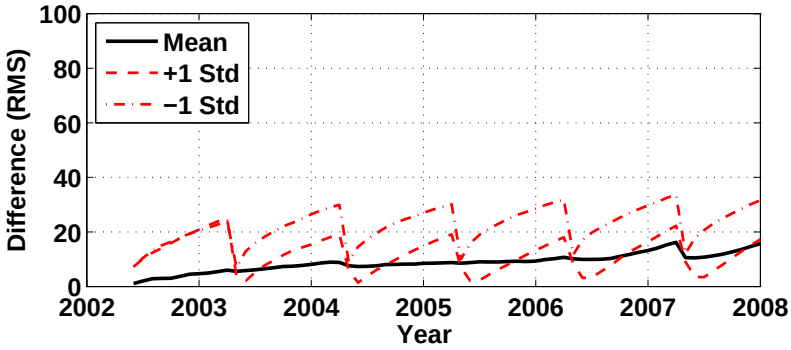

(a) GRIMM field model

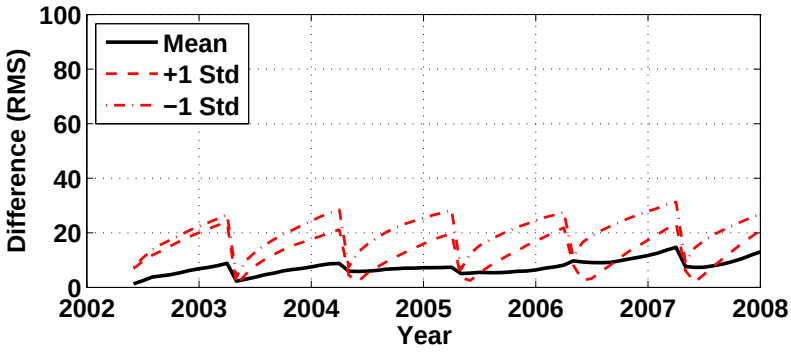

(b) xCHAOS field model

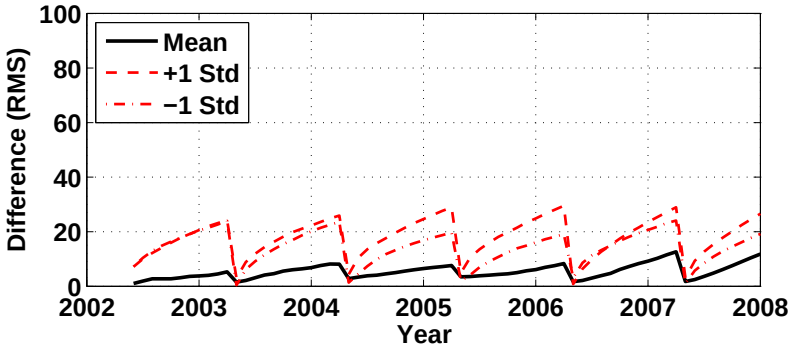

(c) POMME field model

Figure 6.12: RMS difference (in nT) between a EnKF field model derived from SV generated by flow models from Dataset 1 and the (a) GRIMM, (b) xCHAOS and (c) POMME field models. See text for explanation. Note the y-axis scale is 0–100 nT.

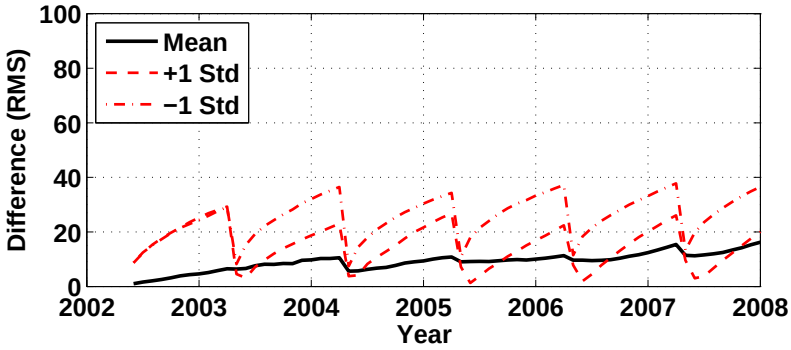

(a) GRIMM field model

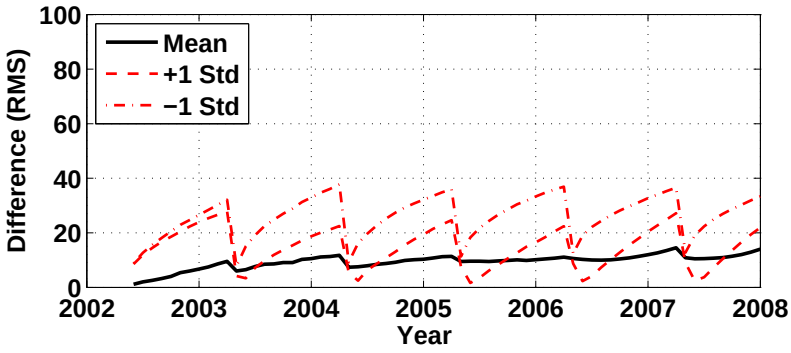

(b) xCHAOS field model

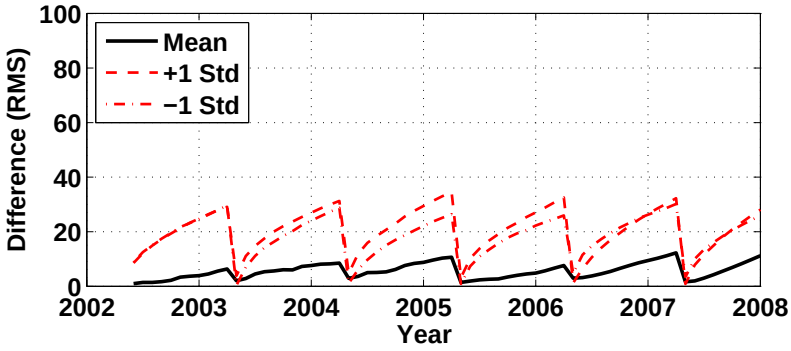

(c) POMME field model

Figure 6.13: RMS difference (in nT) between a EnKF field model derived from SV generated by flow models from Dataset 2 and the (a) GRIMM, (b) xCHAOS and (c) POMME field models. See text for explanation.

troughs were also observed. This, again, suggests that the CM4 correction has somehow introduced an additional inter-annual signal into the flow models. It is not known why CM4 behaves in this manner. Further research on this topic is suggested in Chapter 7.

Note that even with pessimistic errors applied to the SV from the flow coefficients (up to 10% of each coefficient), the ensemble does not 'spread' more than 30nT RMS difference in $\pm\sigma$ models away from the 'true' models during a single year. This places a bound on how rapidly the forecast could diverge. For comparison, Maus et al. (2008) estimate the RMS difference of IGRF and WMM models to be greater than 200nT prior to 2000 (i.e. the modern satellite era) and less than 100nT at the end-2010 (see Figure 2.10).

6.8 Summary

The standard Kalman Filter optimally blends data from a model forecast and a measurement based upon the assigned covariances (Kalman, 1960). The Ensemble Kalman Filter (Evensen, 1994) can be viewed as a Monte Carlo statistical simulation whereby the mean of the ensemble may be interpreted as a best-estimate for the forecast and distribution of the ensemble contains information about the variance of the model. The Ensemble Kalman Filter has been coded in MATLAB and developed for a multi-dimensional system, appropriate for use with magnetic field modelling. I have discussed the method of implementation for forecasting of the magnetic field using core flow models and the results of research into the evolution of the forecast field models and the error bounds that can be placed upon them.

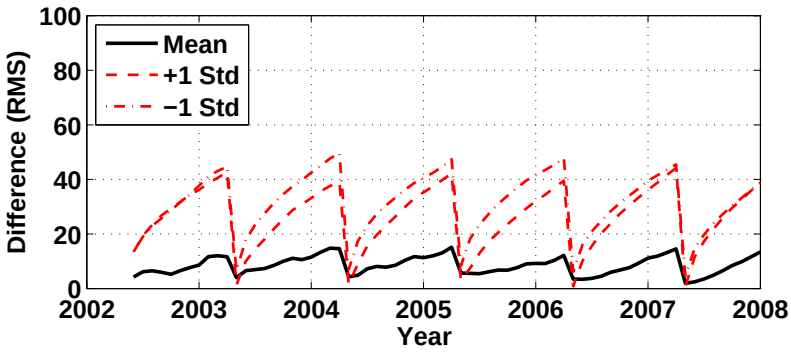

(a) GRIMM field model

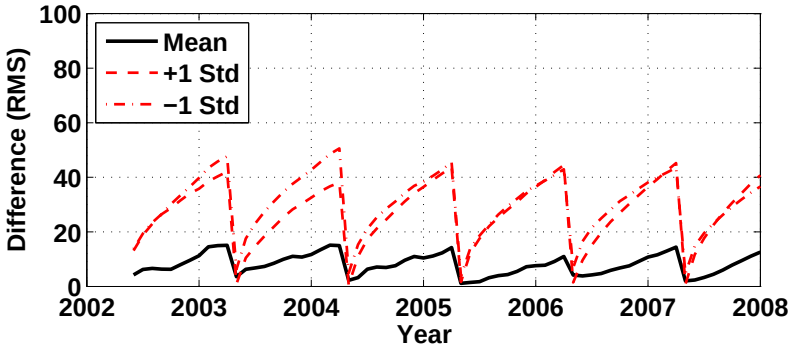

(b) xCHAOS field model

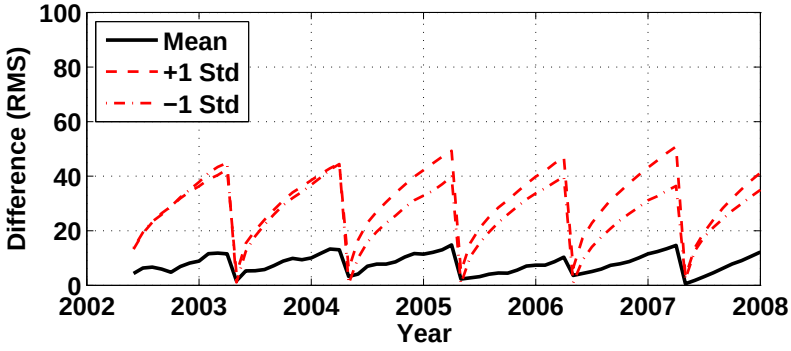

(c) POMME field model

Figure 6.14: RMS difference (in nT) between a EnKF field model derived from SV generated by flow models from Dataset 1 corrected using CM4 and the (a) GRIMM, (b) xCHAOS and (c) POMME field models. See text for explanation.

Chapter 7

Discussion

As the International Decade of Geopotential Research officially draws to a close in 2009, it is useful to review the developments and understanding that have arisen from the combined research efforts of the community. The major technological achievement for the geomagnetic community has been the launch and successful operation of the Ørsted and CHAMP satellites, returning vast amounts of vector magnetic field data for over seven years which will provide ample study material for many years. Substantial progress on the modelling and understanding of a number of geophysical phenomena, from outer core processes to the crustal magnetic field, has been made in the past decade through the use of satellite data.

This chapter discusses the results from a number of research papers within areas of core processes, flow modelling, satellite data measurements and geomagnetic field forecasting, released in the past few years. I attempt to put the results from this thesis into perspective within the overall research framework, exploring the implications and examining important conclusions while highlighting the contributions that this study has made to the field.

7.1 Core Processes

The processes and interactions of the outer core with the mantle and the inner core can be partially inferred from magnetic field studies in combination with results from seis-

mic, gravitational, nutation and physics-based dynamo modelling studies. Particularly interesting questions arise about the evolution of the heat budget of the core and its thermal history and the interaction between the magnetic field, mantle and the inner core.

Models of core flow can give some insight into the magnetohydrodynamic conditions within the core. Recent work in the area has attempted to use core flow models in combination with seismic data and modelling to infer processes responsible for inner core growth and the small-scale flow within the core. Since the suggestion from geodynamo models of the differential rate of inner core rotation compared to the mantle by Glatzmaier & Roberts (1996) and subsequent confirmation (Song & Richards, 1996), more detailed study of inner core properties has been attempted. Current seismic observations suggest that the top 100km of the inner core is strongly anisotropic (Wookey & Helffrich, 2008), both in the equatorial plane and the longitudinal plane (Irving et al., 2008) with the Eastern hemisphere being more isotropic then the Western hemisphere (Nui & Wen, 2001; Yu & Wen, 2006). The viscosity of the inner core is still poorly known (Dumberry, 2007) but work by Mound & Dumberry (2008) suggests that inner core differential rotation is only a temporary phenomenon. Their work suggests that the inner core should gravitationally lock to the mantle within a century, based on a reasonable estimate of inner core viscosity. This leaves the puzzling paradox of how super-rotation of the inner core may occur.

In a recent paper, Pais & Jault (2008) have proposed core flow models with the assumption of quasi-geostrophic flow in the interior of the outer core, extending to the inner core boundary (ICB). They infer a large circum-equatorial jet of fluid flow approximately 700km wide touching the CMB on the Atlantic hemisphere and the ICB on the Pacific side of the planet. This would account for the large SV observed in the Western hemisphere and the smaller observed SV in the Eastern hemisphere. The quasi-geostrophic flow models of Pais & Jault (2008) also produce the correct change of length of day, suggesting they are viable. Figure 7.1 illustrates diagramatically the position of the inferred cirum-equatorial jet and anisotropy of the outermost 100km of

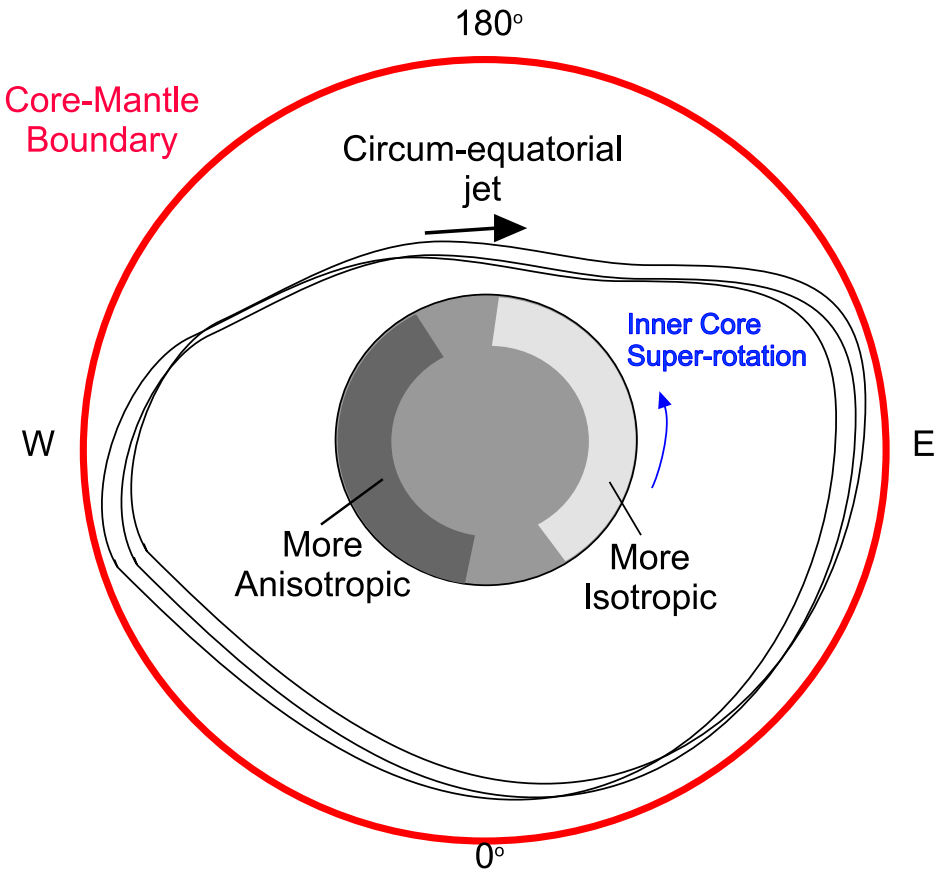

Figure 7.1: Simplified diagram of Inner Core Anisotropy and quasi-geostrophic core flow in equatorial cross-section viewed from the North. See text for details.

the inner core.

Based upon the work of Pais & Jault (2008), Aubert et al. (2008a) now offer an interesting explanation for inner core anisotropy and a mechanism for inner core rotation. They propose that mantle temperature variation expressed at the CMB induces textural heterogeneity on the inner core solidification front. In particular, this affects the core flow regime and the magnetic field, and interlinks the observed SV on the Earth's surface, the inner core growth history and the influence of the mantle upon the core. Based primarily upon numerical dynamo modelling, they show that the mantle seismic heterogeneity of the inner core (interpreted as temperature flux) can produce differential freezing rates at the ICB affecting the crystallisation mechanism, making it more sensitive to the flow regime of the local region. They also speculate that light element

release from freezing may induce the formation of locally different chemical conditions. This drives the flow and causes differential mass accumulation on the inner core, forcing relaxation of the ICB through gravitational torque and viscous re-adjustment. The surface relaxation initiates oscillations on a six and sixty year time scale (Dumberry, 2007) as the inner core is gravitationally attracted to mantle inhomogeneities. The theory thus accounts for many of the intriguing features of the core that are currently unexplained.

However, much of the work by Aubert et al. (2008a) is from dynamo model simulation with a large number of unknown parameters. Although dynamo models are approaching what appear to be realistic representation of conditions within the centre of the Earth, they are still in regimes many orders of magnitude from simulating the actual magnetohydrodynamic conditions of the core (Christensen & Wicht, 2007). It must also be recalled that inversion of the SV data for core flows is inherently dependent on the assumptions that are made. For example, it was shown in Section 3.4 that poloidal only core flow models may be mathematically feasible, but it is considered unlikely that such a flow regime exists (Gubbins, 2007). The work of Pais et al. (2004) and Eymin & Hulot (2005) also shows that small scale flow influences the large scale flows recoverable from inversion of SV, reiterating the conclusions of Rau et al. (2000) that inferring small scale flow features from SV is not possible. Although the suggestions of Aubert et al. (2008a) are intuitively appealing, better proof of such assertions is still required.

7.2 Field and Flow Modelling

Techniques for modelling core flows have advanced in the past decade, with increased computational capacity, allowing larger datasets to be processed. This thesis has, in particular, explored the improvements in fitting flow models to SV data using an L_1 minimisation norm with a large number of ground-based and satellite derived virtual observatories. This technique, originally applied by Walker & Jackson (2000) for field modelling, was implemented by Whaler et al. (2002) for core flow modelling and adapted

and expanded during the research for this thesis. Importantly, using an L_1 minimisation norm algorithm produces consistent improvements over the L_2 minimisation norm technique. This improvement of the fit of the flow model to the SV data by iterative re-weighting of the residuals was demonstrated in Chapter 3 and applied in Chapter 4 (shown for example in Figures 3.2 and 4.7).

It is now possible to compute ensembles of flows to examine the effects of small scale flows on large scale inversion. Gillet et al. (2008) have built a series of models to perform tests of frozen flux violation from time-dependent quasi-geostrophic flows using the CM4 model and xCHAOS models. These models match the observed SV well and provide evidence for a long-lived circum-equatorial jet corroborating the results of Pais & Jault (2008).

Lesur et al. (2008a) have taken a different approach, employing flow models as constraints to build main field, SV and SA models. They seek to minimise the flow and SV over time using the constraint:

$$\int_{t_0}^{t_1} \int_{\Omega} |\partial_t \boldsymbol{B}_r + \nabla_h \cdot (v_h \mathbf{B}_r)| \, d\Omega \, dt \tag{7.1}$$

This method does require extra parameterisation of the model, including additional damping parameters. However, there is a significant improvement in the ability to correctly model the secular variation and acceleration to higher degrees (up to $l = 8$). This represents a new approach to regularisation of the flow-induced SV.

Olsen & Mandea (2008) investigated whether core flows vary rapidly over short periods of time. They used the xCHAOS model to examine the SV over the period 1999-2008 and find several geomagnetic 'jerks': in 1999, 2003, 2007 (Mandea et al., 2008). The cause of 'jerks' is unexplained, but observations from satellite magnetic data make it clear that they do not occur globally simultaneously. Research by Pinheiro & Jackson (2008) indicates that mantle conductivity may be responsible for the time delay in different parts of the planet, preferentially filtering the 'impulse' by spherical harmonic degree.

In some cases, however, 'jerks' have been observed to occur only locally (e.g. in

2004 the abrupt change in SA was observed mainly below Asia and the Indian Ocean regions). Cannelli et al. (2007) modelled the likely deformation effect of the December 2004 Sumatran earthquake on the CMB and in Cannelli et al. (2008) tentatively suggest this may cause a sudden disruption on the CMB, enhancing local flow and giving rise to a 'jerk'. However, there is scant evidence for this hypothesis and it still leaves reasons for global 'jerks' unexplained. A recent paper by Ryan & Sarson (2007) on dynamo modelling linked geomagnetic reversals to turbulence within the core. Other dynamo simulations from Coe et al. (2008) show energy jumps between spherical harmonic degrees during field reversals as large scale flow breaks down. Could 'jerks' be indicative of turbulent conditions at the onset of a possible field reversal (Gubbins, 1999; Gubbins et al., 2006; Amit & Olson, 2008)?

Much of this work relies on the assumption that inversion for field and flow can reveal complex information. However, inevitably, inversion is a crude tool for these types of geophysical analysis. As Eymin & Hulot (2005) show and Chapter 3 demonstrates, analytical inversion is heavily reliant on the physical assertions imposed to constrain the flow models. Direct numerical dynamo modelling is unable to reproduce inferred core flows (though Kuang et al. (2008) claim to do so), leaving little choice but to continue with the current form of linear inversion.

7.3 Data Processing

The magnitude and spatial extent of the large scale rapid flow variation derived by Olsen & Mandea (2008) is still unclear, particularly as there is evidence for some external field contamination as shown in Chapter 4. From examination of the residuals to flow models from Virtual Observatories (Section 4.5.1), it is apparent that external field contamination is dominant when using all available CHAMP data are used. Other influences such as magnetic environment of the orbit (dawn/dusk vs. noon/midnight) are noticeable within the data but can be ameliorated (though not fully removed) through data selection or correction. However, when VO are created using relatively 'clean' data such as the selected quiet-time Ørsted and CHAMP dataset from Thomson

& Lesur (2007), a small external field presence was still discernible. The correlation coefficient of the residual biases with the change in Dst was 0.49, indicating external field effects are not easily removed even by stringent data selection.

One key assumption that has been proven incorrect by this research is that the VO method produces an 'average' value of the magnetic field for a single month at a single point. Although this method produces SV data with good correlation to SV recorded at ground-based observatories, particularly in the X and Z vector components they are perhaps still too noisy to be of direct use in core-field SV studies.

It has proven extremely useful to examine the residuals of the flow models to the SV data. If one considers the inversion process for flow model as a low-pass spatial filter, then the residuals can be regarded as higher degree aliasing of noise into the signal (i.e. the SV). This allows one to judge both the data and the process of VO creation, though unpicking the effects from noise and the effects from processing is more difficult.

The analysis leads us to a rather unsatisfactory position whereby vast quantities of magnetic field vector data have been measured over the past decade (somewhere in the region of 3×10^8 samples from CHAMP alone) in one of the quietest solar cycles on record (e.g. de Toma & White, 2004). However, only a tiny fraction of these data are used to create main field models, leaving an enormous resource to be mined in the future. Although global data availability is no longer an issue, methods to make the best possible use are still being developed.

Ideally, we would like to image the field and the change of the field to high degree to examine small-scale features, identify rapid variations correctly and confirm theories about the outer and inner core. It is unclear as to how best to isolate the internal field signal and remove the effects of external, ionospheric and other influences from within the satellite data. It is also unclear, I feel, how external field noise leaks or is aliased into temporal models of the internal field. For example, although Olsen & Mandea (2008) show core flows vary rapidly over short periods of time, no analysis has been carried out into the effectiveness of their external field removal, as even a relatively small residual can affect the modelled SV and in particular the SA. What are the implications of this,

for example, on the inferred field spectra at the CMB e.g. blue/red spectra (Holme & Olsen, 2006)? More work is required to improve the estimate of the internal field and to utilise the satellite data to their fullest potential. I would suggest that core flow residuals are used as one method to determine the effectiveness of any method attempting to isolate the internal magnetic field.

During this research, the CM4 model was extensively used to correct for known parameterised fields, both external and internal to the satellite altitude. This had limited success in fully removing unwanted contamination in the data. Further processing of the data after CM4 correction revealed a number of interesting additional effects had been enhanced or added to the data. In particular, forecasting using the CM4 corrected flows gave rise to inter-annual signals within the RMS difference curves (c.f. Figure 5.9). The other interesting feature to note in the the RMS difference curves of Dataset 1 and Dataset 2 flow models (c.f Figure 5.5 is the slight 'kink' at about 2004.3. which is approximately a year later than the 'jerk' announced by Olsen & Mandea (2007)). The forecast field match to the satellite field models improves slightly after this date, for a period of between 1–2 years. Is this related to the 'jerk' or is it actually a feature of the satellite models themselves (e.g. the balance point of the GRIMM model is 2003.5, for POMME4s it is 2004.0)?

7.4 Forecasting the Change of the Magnetic Field

The forecasting of magnetic field change has been attempted in many forms over the past 400 years since Halley's observation of tendency of the field to drift westward in the Atlantic hemisphere (Halley, 1692). However, the first 'official' efforts to produce forecasts related to the IGRF model (Cain & Cain, 1971). Magnetic models such as the 10^{th} International Geomagnetic Reference Field model (IGRF10) (Maus et al., 2005b) and the World Magnetic Model (WMM) (McLean et al., 2004) estimated the future SV until the release of the next model (five years) using linear fits to recorded SV change from observatories and polynomial extrapolation of satellite data. This approach does not invoke any particular physical arguments to support the assumption that the SV

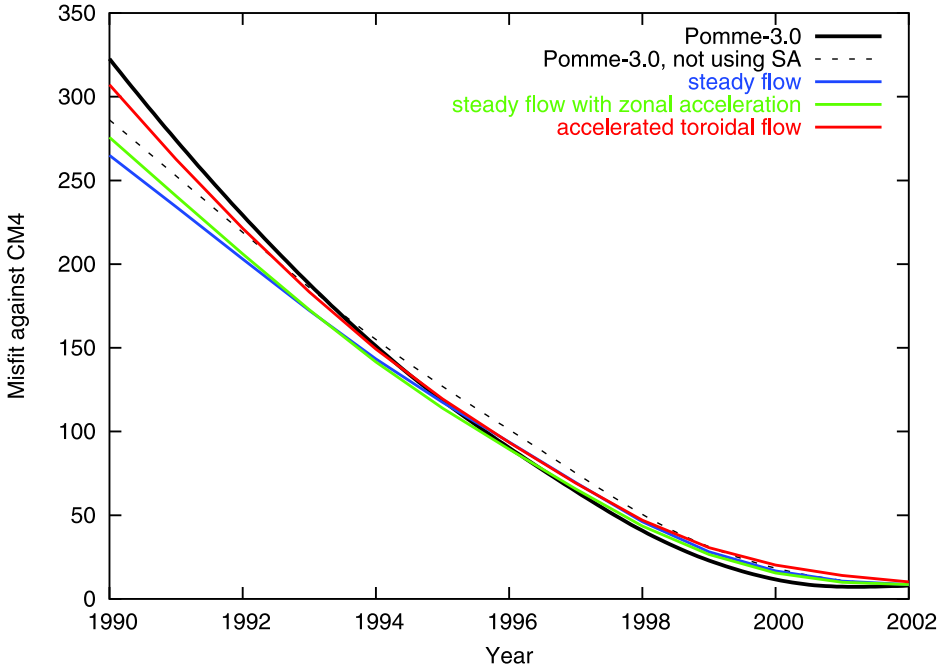

Figure 7.2: Comparison of hindcasting of the magnetic field with CM4, redrawn from Maus et al. (2008). See also Figure 5.17 in this thesis.

will continue linearly nor indeed that the estimated change ought to be linear.

Maus et al. (2008) produced a study of how well hindcasting of the magnetic field using core flow models reproduced the observed field over 13 years. In their investigation, they compared the prediction of the field back in time from the SV generated by a number of core flow modelling assumptions including steady flow, toroidal only and accelerated flows. They also compared the predictions of the POMME3 field model using constant SV and SA. The CM4 model was used as the baseline for the comparisons. Figure 7.2 shows their result of their hindcasts. The primary conclusion from the paper is that flow models do not appear to predict the actual field to less than 200nT RMS difference after ten years and rapidly diverge after that time period. It also concludes that a steady flow produces the best long-term average fit. This result was confirmed in Chapter 5, for example in Figure 5.17.

By comparison, work in this thesis has established that it is possible to improve upon the methods of Maus et al. (2008). Forecasting using steady and non-steady flow models shows that the field can be predicted to an acceptable level of RMS misfit. Figures 5.2 –

5.8 illustrate how well the flow models predict the field over a five year period. However, a linear flow model prediction does not directly improve on the assumption of constant SV. For the purposes of forecasting, an underlying assumption must still be made, e.g. steady flow produces best average fit. Introducing non-linear relationships through the updating of the Gaunt/Elsasser matrix or adding secular acceleration and higher order terms are required to produce more interesting evolution of the field. Justifying these additions to the model without physical evidence is difficult, particularly in the light of our current ignorance of the causes of 'jerks'.

Recent work by Kuang et al. (2008) and Tangborn & Kuang (2008) has attempted to force a dynamo simulation to behave in a manner similar to the geomagnetic field by assimilation of GUFM and CM4 coefficients into the model from 1600AD onwards using a Kalman filtering technique. The results of forecasting from the dynamo model are not clear in Kuang et al. (2008) nor were any fits of predictions to field models shown by Tangborn & Kuang (2008). However, Tangborn & Kuang (2008) stated that 6 dynamo models were run to create an 'ensemble' in an attempt to examine the errors of the dynamo simulation. One obvious issue with the dynamo models used in Kuang et al. (2008) is that they are symmetric about the equator and thus are not full field models. Another issue which they have not justified or explained is their error evolution within the dynamo simulation. I would also contend that their use of the term 'ensemble' is not really in keeping with the meaning as used in weather forecasting where ensembles of at least fifty models are used, not just six. Their approach is promising and remains a potential answer to a fully physical method of forecasting geomagnetic field evolution for short timescales, say less than ten years. Increasing availability of computing power may well lead to better accuracy and certainty in the coming years, as this is currently the primary limiting factor.

In this thesis, the Ensemble Kalman Filter method developed is a truly ensemble method, relying fully on Monte Carlo theory as advocated by Evensen (1994). Although my approach is not as mathematically and computationally sophisticated or complex as the dynamo models of Kuang et al. (2008), the results are more statistically robust,

as up to 1000 models are used to propagate the state forward. The underlying physical bases of the ensemble are derived from observations of SV rather than from first principles of hydrodynamic equations. This simplicity allows a wider range of forecasts to be determined and the accumulation of error and spread of covariance to be better examined. There are also fewer tunable parameters with my approach such as the error associated with measurement. The method has been demostrated to be viable.

However, the Earth's dynamo is an chaotic system which is difficult to forecast due to the inherent non-linearity. Behaviour such as reversals and excursions are poorly understood. In some sense, the magnetic field change can be statistically described, though numerous papers have speculated what this actually implies about the cause of the behaviour (Glatzmaier et al., 1999; Constable, 2000; Jonkers, 2007). I would suggest that interesting questions about core flow and dynamo studies could be investigated from the point of view of dynamical systems and chaos theory.

7.5 Future of Magnetic Field Studies

This is an exciting period for magnetic field research. The next five years promises to be very productive for magnetic satellite studies. The European Space Agency is investing in a state-of-the-art cluster satellite mission known as Swarm (Friis-Christensen et al., 2006). Scheduled to launch in 2010, the cluster will consist of three satellites with instrumentation similar to the CHAMP satellite (Reigber et al., 2002), two of which will orbit in formation at a height of approximately 400km with the third at a higher altitude of 550km. The Swarm mission should improve the recovery of the core, crustal and oceanic magnetic fields.

In particular, it is hoped that measurement of the gradient of the field between satellites will help to resolve the small scale crustal field up to degree 150 (Olsen et al., 2006a, 2007). The satellite pair at lower altitude will also help improve the east-west component of the crustal field, which is poorly resolved in current satellite data (due to their polar orbits). There may be a hiatus of data between the end of the CHAMP mission in late-2009 and the science phase of the Swarm mission in 2010, but this should

not affect the recovery of the SV (up to degree 18) over the lifetime of the mission. Currently SV is reliably recovered up to degree 13 (Nils Olsen, pers. comm., 2009).

The launch of NASA's Juno mission to Jupiter in 2011 (arriving 2016) may offer insights into planetary dynamo behaviour, as the small-scale features of the magnetic field can be observed without the masking effects of a crustal field. Although primarily designed to study the polar regions of the Jovian magnetic field (Connerney & Acuna, 2008), the resulting field models should be of interest to both geomagnetists and dynamo modellers.

Studies of other planets such as Mercury using data from the MESSENGER mission (Purucker et al., 2009; Uno et al., 2009) and Mars (e.g. Whaler & Purucker, 2005; Voorhies, 2008) should bring greater understanding of planetary fields and evolution. For example, the UK currently is involved within the ESA Aurora programme, a framework for development of a European mission to Mars in the future. A surface magnetometer is planned for the ExoMars mission (K. Whaler, pers. comm., 2009).

7.6 Recommendations for Future Work

This research has identified a number of areas of work which could be investigated. I propose that the following topics can be further examined:

- Introduction of alternative minimisation norms: The 'strong' norm of Bloxham (1988) has been used as a minimisation function for the flow model inversion in this study. This norm is based upon finding a minimum value for the squared values of the flow coefficients. As the L_1 norm is based upon the absolute value of the residuals, it should be possible to devise a norm which minimises a more statistically appropriate function.

- Isolation of the internal SV: A number of techniques to further isolate the internal from external field contamination are available. In particular, the use of Slepian functions (e.g. Simons & Dahlen, 2006) to damp or remove unwanted measurements in satellite datasets can be attempted. There are some mathemat-

ical difficulties with applying such functions to magnetic vector data, but these can be overcome (F. Simons, pers. comm, 2008).

- Induced crustal field: With the availability of a decade of high resolution satellite data it may be possible to identify changes in the crustal biases at ground-based observatories using Virtual Observatories, assuming the external and ionospheric contamination can be correctly removed. This may allow the separation of the remanent and induced crustal fields at ground-based observatories (Jackson, 2007). The results from Section 5.2 provide the starting data.

- Improvements in forecasting: Further exploration of the ability to forecast the field based upon better models of core flow and acceleration will be possible in the next few years. In particular, the methods outlined in this thesis could form the basis for producing an IGRF model for the next epoch (2010–2015). An examination of the flow and modelling over the past one hundred years could prove fruitful for better determining how to estimate EnKF covariance e.g. how should the ensemble noise should be driven over time.

- Examination of CM4 correction in satellite data: It is clear from Figures 4.20 and 6.14 that CM4 correction for external and ionospheric field is introducing additional fields and biannual variation into the dataset. This effect may be due to poor values of Dst and F10.7 indices or may indicate that the parameterisation of CM4 is over- or under-compensating for some particular seasonal effects. It might also be possible to suggest better parameterisation for comprehensive modelling.

Chapter 8

Conclusions

This research has studied several features of magnetic secular variation including inversion techniques, data processing techniques and forecasting of magnetic field change over short time periods. The main results are summarised below.

It has been confirmed that the L_1 norm minimisation technique can be applied to flow inversions and consistently produces better fitting flow models to SV data than the more commonly used L_2 norm minimisation. Implementation of the algorithm is straightforward and requires only a small increase in computational time. Thus, it should be employed in flow inversion studies. It has been shown that the use of the SV minimisation norm in flow model inversion must be carefully employed as it does not produce the useful or well-fitted flow models for most purposes.

Using the approach developed by Mandea and Olsen (2006) I created a set of evenly distributed VO at 400km above the Earth's surface in latitude and longitude. I also produced a VO grid of equal area tessera. Both encompassed satellite measurements from the CHAMP satellite over seven years (2001.4-2008.0), inverting the SV calculated at each VO to infer flow along the core-mantle boundary. The SV was globally derived and the L_1 norm used to produce improved core flow models for the period.

However, from direct comparison of the SV generated by the flow model to the SV at individual VO it is evident from residual differences that unwanted internal (to the satellite) and external field effects are still present in the VO. I showed that the binning

and processing of the VO data can also induce artifacts, including sectorial banding, into the residuals.

By employing the core flows from the inversion of SV data it is possible to forecast the change of the present magnetic field (as measured) forwards in time for a short time period (five years) within an acceptable error budget. Using simple advection of steady or non-steady flows to forecast magnetic field change gives a reasonably good match to field models such as GRIMM, POMME or xCHAOS ($<$ 50nT difference after five years).

The forecast of the magnetic field change can be improved by optimally assimilating measurements of the field into the forecast from flow models at discrete points in time (e.g. annually). To achieve this, an Ensemble Kalman Filter (EnKF) can be used to the capture non-linearity of the model and delineate the error bounds by means of a Monte Carlo representation of the field evolution over time.

I demonstrated an implementation of the EnKF for steady and non-steady flows generated from Virtual Observatory field models, and compared the resulting SV to that from the field models GRIMM and xCHAOS over the period 2002 to 2008. Using the EnKF, the maximum difference never exceeds 25nT over the period. This promising approach allows measurements to be included into model predictions to improve the forecast.

Bibliography

Alfvén, H., 1942. On the existence of electromagnetic-hydrodynamic waves, *Nature*, **150**, 405–406.

Amit, H. & Olson, P., 2004. Helical core flow from geomagnetic secular variation, *Phys. Earth Planet. Int.*, **147**, 1–25.

Amit, H. & Olson, P., 2006. Time-average and time-dependent parts of core flow, *Phys. Earth Planet. Int.*, **155**, 120–139.

Amit, H. & Olson, P., 2008. Geomagnetic dipole tilt changes induced by core flow, *Phys. Earth Plan. Int.*, **166**, 226–238.

Asari, S., Shimizu, H., & Utada, H., 2006. Variability of the topographic core-mantle torque calculated from core surface flow models, *Phys. Earth Planet. Int.*, **154**(1), 85–111.

Aubert, J., Amit, H., Hulot, G., & Olson, P., 2008. Thermochemical flows couple the earth's inner core growth to mantle heterogeneity, *Nature*, **454**, 758–761.

Aubert, J., Aurnou, J., & Wicht, J., 2008. The magnetic structure of convection-driven numerical dynamos, *Geophys. J. Int.*, **172**, 945–956.

Backus, G. E., 1968. Kinematics of geomagnetic secular variation in a perfectly conducting core, *Philos. Trans. R. Soc. Lond. Ser A*, **263**, 239–266.

Backus, G. E., 1970. Nonuniqueness of the external geomagnetic field determined by surface intersity measurements, *J. Geophys. Res.*, **75**, 6339–6341.

Beatty, J., Collins Petersen, C., & Chaikin, A., eds., 1999. *The New Solar System*, Cambridge University Press, 4th edn.

Beggan, C. & Whaler, K., 2008. Core flow modelling assumptions, *Phys. Earth Planet. Int.*, **167**, 217–222.

Biggin, A., Strik, H., & Langereis, C., 2008. Evidence for a very-long-term trend in geomagnetic secular variation, *Nature Geoscience*, **1**, 395–398.

Bloxham, J., 1987. Simultaneous stochastic inversion for geomagnetic main field and secular variation 1. A large-scale inverse problem, *J. Geophys. Res.*, **92**(B11), 11,597–11,608.

Bloxham, J., 1988. *The determination of fluid flow at the core surface from geomagnetic observations*, vol. Mathematical Geophysics, chap. 9, pp. 189–208, D. Reidel Publishing Company.

Bloxham, J., 1989. Simple models of fluid flow at the core surface derived from geomagnetic field models, *Geophys. J. Int.*, **99**(1), 173–182.

Bloxham, J. & Gubbins, D., 1985. The secular variation of Earth's magnetic field, *Nature*, **317**, 777–781.

Bloxham, J. & Gubbins, D., 1986. Geomagnetic field analysis - IV: Testing the frozen flux hypothesis, *Geophys. J. R. Astr. Soc.*, **84**, 139–152.

Bloxham, J. & Jackson, A., 1991. Fluid flow near the surface of Earth's outer core, *Reviews of Geophysics*, **29, 1**, 97–120.

Bloxham, J., Gubbins, D., & Jackson, A., 1989. Geomagnetic secular variation, *Philos. Trans. R. Soc. Lond.*, **329**(1606), 415–502.

Braginsky, S. & Le Mouël, J.-L., 1993. Two-scale model of a geomagnetic field variation, *Geophys. J. Int.*, **112**, 147–158.

Breuer, M., Wessling, J., Schmalzl, J., & Hansen, U., 2004. Effect of inertia in Rayleigh-Bérnard convection, *Phys. Rev. E*, **026302**, 1.

Buffett, B., 1999. Role reversal in geomagnetism, *Nature*, **401**, 861–862.

Buffett, B., 2000. Earth's core and the geodynamo, *Science*, **288**, 2007–2012.

Buffett, B. & Christensen, U., 2007. Magnetic and viscous coupling at the core-mantle boundary: inferences from observations of the Earth's nutations, *Geophys. J. Int.*, **171**, 145–152.

Bullard, E. & Gellman, H., 1954. Homogeneous dynamos and terrestrial magnetism, *Phil. Trans. R. Soc. Lond.*, **247**(928), 213–278.

Bullard, E., Freeman, C., Gellman, H., & Nixon, J., 1950. The westard drift of the Earth's magnetic field, *Phil. Trans. R. Soc. Lond. A.*, **243**, 61–92.

Busse, F., 1975. A model of the Geodynamo, *Geophys. J. Roy. Astron. Soc.*, **42**, 437–459.

Butler, S., Peltier, W., & Costin, S., 2005. Numerical models of the Earth's thermal history: Effects of inner-core solidification and core potassium, *Phys. Earth Planet. Int.*, **152**(1-2), 22–42.

Cain, J. & Cain, S., 1971. Derivation of the International Geomagnetic Reference Field [IGFR(1068)], in *The World Magnetic Survey 1957-1969*, edited by A. Zmuda, pp. 163–166; 190–199; 202–203, IAGA Bulletin.

Campbell, W., 2003. *Introduction to Geomagnetic Fields*, Cambridge University Press, 2nd edn.

Cannelli, V., Melini, D., De Michelis, P., Piersanti, A., & Florindo, F., 2007. Core-mantle boundary deformations and J_2 variations resulting from the 2004 Sumatra earthquake, *Geophy. J. Int.*, **170**, 718–724.

Cannelli, V., De Michelis, P., Florindo, F., Melini, D., & Piersanti, A., 2008. A relationship between giant earthquakes and core flow instabilities?, in *Eos Trans. AGU*, vol. 83, pp. GP11A–0688, Fall Meet. Suppl.

Christensen, U. & Tilgner, A., 2004. Power requirement of the geodynamo from ohmic losses in numerical and laboratory dynamos, *Nature*, **249**, 169–171.

Christensen, U. & Wicht, J., 2007. *Treatise on Geophysics*, vol. 8, chap. Numerical dynamo simulations, pp. 254–282, Elsevier.

Coe, R., Glatzmaier, G., Olson, P., & Roberts, P., 2008. Polarity reversals in chaotic geodynamo models, in *Eos Trans. AGU*, vol. 89, pp. DI31A–1787, Fall Meet. Suppl.

Connerney, J. & Acuna, M., 2008. The Juno Magnetic Field Investigation (MAG): Exploration of the polar magnetosphere, in *Eos Trans. AGU*, vol. 89, pp. SM41B–1679, Fall Meet. Suppl.

Constable, C., 2000. On rates of occurrence of geomagnetic reversals, *Phys. Earth Planet. Int.*, **118**, 181–193.

Courtillot, V. & Le Mouël, J.-L., 1984. Geomagnetic secular variation impulses, *Nature*, **311**, 709–716.

Davis, R. & Whaler, K., 1996. Determination of a steady velocity in a rotating frame of reference at the surface of the earths core, *Geophys. J. Int.*, **126**, 92–100.

de Boor, C., 2001. *A Practical Guide to Splines*, Applied Mathematical Sciences 27, Springer, Revised Edition.

de Toma, G. & White, O. R., 2004. Solar Cycle 23: An anomalous cycle?, *Astrophys. J.*, **609**, 11401152.

Dobson, D. & Brodholt, J. P., 2005. Could ultra-low-velocity zones be subducted banded iron formations, in *The Deep Earth: The Structure and Interior of our Planet*, The Geological Society.

Dorf, R. & Bishop, R., 2008. *Modern Control Systems*, Prentice Hall, 11th edn., ISBN 0132270285.

Dormy, E. Valet, J. & Courtillot, V., 2000. Numerical models of the geodynamo and observational constraints, *Geochem. Geophys. Geosyst.*, **1**, 1–42.

Dumberry, M., 2007. Geodynamic constraints on the steady and time-dependent inner core axial rotation, *Geophys. J. Int.*, **170**, 886–895.

Dumberry, M. & Mound, J. E., 2008. Constraints on core-mantle electromagnetic coupling from torsional oscillation normal modes, *J. Geophys. Res.*, **113**, B03102.

Edwards, P., 2000. *A Brief History of Atmospheric General Circulation Modeling*, vol. 70 of **International Geophysics Series**, chap. 2, pp. 67–90, Academic Press.

Eltayeb, I. A., 1999. The stability of compositional plumes in a rotating magnetic fluid, *Phys. Earth Planet. Int.*, **110**, 1–19.

Evensen, G., 1992. Using the extended Kalman Filter with a multi-layer quasi-geostrophic ocean model, *J. Geophys. Res.*, **98**(C9), 16529–16546.

Evensen, G., 1994. Sequential data assimilation with a nonlinear quasi-geostrophic model using Monte Carlo methods to forecast error statistics, *J. Geophys. Res.*, **99**, 1014310162.

Evensen, G., 2004. Sampling strategies and square root analysis schemes for the EnKF, *Ocean Dynamics*, **54**, 539560.

Evensen, G., 2007. *Data Assimilation*, Springer.

Evensen, G. & van Leeuwen, P., 2000. An Ensemble Kalman Smoother for nonlinear dynamics, *Mon. Weather Rev.*, **128**, 1852–1867.

Eymin, C. & Hulot, G., 2005. On core surface flows inferred from satellite magnetic data, *Phys. Earth Planet. Int.*, **152**, 200–220.

Fournier, A., Eymin, C., & Alboussiere, T., 2007. A case for variational geomagnetic data assimilation: insights from a one-dimensional, nonlinear, and sparsely observed MHD system, *Nonlin. Processes Geophys.*,, **14**, 163–180.

Friis-Christensen, E., Lühr, H. L., & Hulot, G., 2006. Swarm: A constellation to study the Earth's magnetic field, *Earth Planets Space*, **58**, 351–358.

Garrick-Bethell, I., Weiss, B. P., Shuster, D. L., & Buz, J., 2009. Early lunar magnetism, *Science*, **323**, 356 – 359.

Gilles, H., Hamel, J., & Charon, B., 2001. Laser pumped ^{4}He magnetometer, *Rev. Sci. Instrum.*, **72**, 2253–2256.

Gillet, N., Pais, A., & Jault, D., 2008. Time resolution of core flow models, in *Eos Trans. AGU*, vol. 89, pp. GP53A–0774, Fall Meet. Suppl.

Glatzmaier, Gary, A., Coe, Roberts, S., Hongre, L., & Roberts, Paul, H., 1999. The role of the Earth's mantle in controlling the frequency of geomagnetic reversals, *Nature*, **401**, 885–890.

Glatzmaier, G. A. & Roberts, P. H., 1995. A three-dimensional self-consistent computer simulation of a geomagnetic field reversal, *Nature*, **377**, 203209.

Glatzmaier, G. A. & Roberts, P. H., 1995. A three-dimensional convective dynamo solution with rotating and finitely conducting inner core and mantle, *Phys. Earth Planet. Int.*, **91**, 63–75.

Glatzmaier, G. A. & Roberts, P. H., 1996. Rotation and magnetism of Earth's Inner Core, *Science*, **274**(5294), 1887–1891.

Goswami, J., 1976. Constraints on the nature of the ancient lunar magnetic field, *Nature*, **261**, 675–677.

Gubbins, D., 1982. Finding core motions from magnetic observations, *Phil. Trans. R. Soc. Lond.*, **306**, 247–254.

Gubbins, D., 1983. Geomagnetic field analysis - I. Stochastic inversion, *Geophys. J. R. Astr. Soc.*, **73**(3), 641–652.

Gubbins, D., 1999. The distinction between geomagnetic excursions and reversals, *Geopys. J. Int.*, **137**, F1–F3.

Gubbins, D., 2004. *Time Series Analysis and Inverse Theory for Geophysicists*, Cambridge University Press.

Gubbins, D., 2007. Geomagnetic constraints on stratification at the top of the Earth's core, *Earth Planets Space*, **59**, 661–664.

Gubbins, D. & Bloxham, J., 1985. Geomagnetic field analysis - III. Magnetic fields on the core-mantle boundary, *Geophys. J. R. Astr. Soc.*, **80**, 695–713.

Gubbins, D. & Herrero-Bervera, E., eds., 2007. *Encyclopedia of Geomagnetism and Paleomagnetism*, Springer.

Gubbins, D., Thomson, C., & Whaler, K., 1982. Stable regions in the Earth's liquid core, *Geophys. J. R. Astr. Soc.*, **68**(1), 241–251.

Gubbins, D., Alfé, D., Masters, G.and Price, G. D., & Gillan, M., 2003. Can the Earth's dynamo run on heat alone?, *Geophys. J. Int.*, **155**, 609–622.

Gubbins, D., Alfè, D., Masters, G., Price, G. D., & Gillan, M., 2004. Gross thermodynamics of two-component core convection, *Geophys. J. Int.*, **157**, 1407–1414.

Gubbins, D., Jones, A., & Findlay, C., 2006. Fall in Earth's magnetic field is erratic, *Science*, **312**, 900–902.

Gubbins, D., Willis, A., & Sreenivasan, B., 2007. Correlation of Earth's magnetic field with lower mantle thermal and seismic structure, *Phys. Earth Planet. Int.*, **162**, 256–260.

Guo, J., Matthews, P., Zhang, Z., & Ning, J., 2004. Impact of inner core rotation on outer core flow: the role of outer core viscosity, *Geophys. J. Int.*, **159**, 372–389.

Gutzwiller, M. C., 1990. *Chaos in Classical and Quantum Mechanics*, Springer-Verlag.

Halley, E., 1692. On the cause of the change in the variation of the magnetic needle; with an hypothesis of the structure of the internal parts of the Earth, *Phil. Trans. R. Soc. Lond.*, **17**, 470–478.

Hansen, J., Sato, M., Ruedy, R., Lacis, A., Asamoah, K., Beckford, K., Borenstein, S., Brown, E., Cairns, B., Carlson, B., Curran, B., de Castro, D., Druyan, L., Etwarrow,

P., Ferede, T., Fox, M., Gaffen, D., Glascoe, J., Gordon, H., Hollandsworth, S., Jiang, X., Johnson, C., Lawrence, N., Lean, J., Lerner, J., Lo, K., Logan, J., Luckett, A., McCormick, M. P., McPeters, R., Miller, R., Minnis, P., Ramberran, I., Russell, G., Russell, P., Stone, P., Tegen, I., Thomas, S., Thomason, L., Thompson, A., Wilder, J., Willson, R., & Zawodny, J., 1997. Forcings and chaos in interannual to decadal climate change, *J. Geophys. Res.*, **102**(D22), 25,679–25,720.

Herrero-Bervera, E. & Valet, J.-P., 1999. Paleosecular variation during sequential geomagnetic reversals from Hawaii, *Earth Planet. Sci. Lett.*, **171**, 139–148.

Hide, R., 1966. Free hydromagnetic oscillations of the Earth's core and the theory of the Geomagnetic Secular Variation, *Phil. Trans. R. Soc. Lond. A*, **259**, 615–647.

Hide, R., McSharry, P., Findlay, C., & Peskett, G., 2004. Quenching Lorenzian chaos, *Int. J. Bifurcat. Chaos*, **14**, 2875–2884.

Hills, R., 1979. *Convection in the Eath's mantle due to viscous shear at the core-mantle interface and due to large-scale bouyancy*, Ph.D. thesis, N.M. State Univ., Las Cruces.

Hollerbach, R., 1996. On the theory of the geodynamo, *Phys. Earth Planet. Int.*, **98**, 163–185.

Holme, R., 1998. Electromagnetic core-mantle coupling - I. Explaining decadal changes in the length of day, *Geophys. J. Int.*, **132**(1), 167–180.

Holme, R., 2000. Electromagnetic core-mantle coupling - III. Laterally varying mantle conductance, *Phys. Earth Planet. Int.*, **117**, 329–344.

Holme, R., 2007. *Treatise on Geophysics*, vol. 8, chap. Large Scale Flow in the Core, pp. 107–130, Elsevier.

Holme, R. & Bloxham, J., 1996. The treatment of attitude errors in satellite geomagnetic data, *Phys. Earth Plan. Int.*, **98**, 221–233.

Holme, R. & Jackson, A., 1997. The cause and treatment of anisotropic errors in near-Earth geomagnetic data, *Phys. Earth Planet. Int.*, **103**, 375–388.

Holme, R. & Olsen, N., 2006. Core surface flow modelling from high-resolution secular variation, *Geophys. J. Int.*, **166**, 518–528.

Holme, R. & Whaler, K., 2001. Steady core flow in an azimuthally drifting reference frame, *Geophys. J. Int.*, **145**(9), 560–569.

Horncastle, E., 2008. Ph.D. thesis, University of Liverpool.

Hulot, G., Eymin, C., Langlais, B., Mandea, M., & Olsen, N., 2002. Small-scale structure of the geodynamo inferred from Oersted and Magsat satellite data, *Nature*, **416**, 620–623.

Irving, J., Duess, A., & Woodhouse, J., 2008. Hemispherical structures in inner core anisotropy, in *Eos Trans. AGU*, vol. 89, pp. DI43A–1759, AGU Fall Meet. Suppl.

Jackson, A., 1997. Time-dependency of tangentially geostrophic core surface motions, *Phys. Earth Plan. Int.*, **103**, 293–311.

Jackson, A., 2007. Studies of crustal magnetic anomalies of the British Isles, *Astron. Geophys.*, **48**, 2.9–2.13.

Jackson, A., Jonkers, A., & Walker, M., 2000. Four centuries of geomagnetic secular variation from historical records, *Philos. Trans. R. Soc. Lond.*, **358**(1768), 957–990.

Jacobs, J., ed., 1987. *Geomagnetism*, Academic Press.

Jault, D., Gire, C., & Le Mouël, J, L., 1988. Westward drift, core motions and exchanges of angular momentum between core and mantle, *Nature*, **333**, 353–356.

Jonkers, A., 2000. *North by Northwest: Science, Seafaring and the Earth's Magnetic Field (1600-1800)*, vol. 1, Academisch Proefschrift.

Jonkers, A., 2007. Discrete scale invariance connects geodynamo timescales, *Geophys. J. Int.*, **171**, 581–593.

Kahle, A., Vestine, E., & Ball, R., 1967. Estimated surface motions of the Earth's core, *J. Geophys. Res.*, **72**, 1095–1108.

Kalman, R., 1960. A new approach to linear filtering and prediction problems, *Transactions of the ASME Journal of Basic Engineering*, **82**, 35–45.

Kerridge, D., 2001. Intermagnet: Worldwide near-real-time geomagnetic observatory data, in *Proceedings of the Workshop on Space Weather*, ESTEC.

Korhonen, J. V., Fairhead, J., Hamoudi, M., Hemant, K., Lesur, V., Mandea, M., Maus, S., Purucker, M., Ravat, D., Sazonova, T., & E., T., 2007. Magnetic anomaly map of the world, Map published by Commission for Geological Map of the World, supported by UNESCO, 1st Edition.

Korte, M. & Constable, C. G., 2006. Centennial to millennial geomagnetic secular variation, *Geophys. J. Int.*, **167**, 43–52.

Kuang, W., Tangborn, A., Jiang, W., Lui, D., Sun, Z., Bloxham, J., & Wei, Z., 2008. MoSST_DAS: The first generation geomagnetic data assimilation framework, *Communications in Computational Physics*, **3**, 85–108.

Labrosse, S., Poirier, J., & Le Mouël, J., 1997. On cooling of the Earth's core, *Phys. Earth Planet. Int.*, **99**, 1–17.

Labrosse, S., Poirier, J., & Le Mouël, J., 2001. The age of the inner core, *Earth Planet. Sci. Lett.*, **190**(3-4), 111–123.

Langel, R. & Estes, R., 1982. A geomagnetic field spectrum, *Geophy. Res. Lett.*, **9**, 250–253.

Langel, R. & Estes, R., 1985. The near-Earth magnetic field at 1980 determined from Magsat data, *J. Geophy. Res.*, **90**, 24952509.

Langel, R. & Hinze, W., 1998. *The Magnetic field of the Earth's Lithosphere*, Cambridge University Press.

Le Mouël, J.-L., 1984. Outer-core geostrophic flow and secular variation of Earth's geomagnetic field, *Nature*, **311**, 734 – 735.

Lehmann, I., 1936. P′, *Publ. Bur. Cent. Seism. Int. Ser. A*, **14**, 3–31.

Leopardi, P., 2006. A partition of the unit sphere into regions of equal area and small diameter, *Electronic Transactions on Numerical Analysis*, **25**, 309–327.

Lesur, V., Macmillan, S., & Thomson, A., 2005. The BGS magnetic field candidate models for the 10th generation IGRF, *Earth Planets Space*, **57**(12), 1157–1163.

Lesur, V., Wardinski, I., Asari, S., & Mandea, M., 2008. Modeling the Earth's core magnetic field under core flow constraints, in *Eos Trans. AGU*, vol. 83, pp. GP53B–05, Fall Meet. Suppl.

Lesur, V., Wardinski, I., Rother, M., & Mandea, M., 2008. GRIMM: the GFZ Reference Internal Magnetic Model based on vector satellite and observatory data, *Geophys. J. Int.*, **173**, 382–394.

Lister, J. & Buffett, B., 1998. Stratification of the outer core at the core-mantle boundary, *Phys. Earth Planet. Int.*, **105**(1), 5–19.

Loper, D., 2007. *Treatise on Geophysics*, vol. 8, chap. Turbulence and Small-Scale Dynamics in the Core, pp. 187–206, Elsevier.

Lorenz, E. N., 1963. Deterministic nonperiodic flow, *J. Atmos. Sci.*, **20**, 130–141.

Love, J., 1999. A critique of frozen-flux inverse modelling of a nearly steady geodynamo, *Geophys. J. Int.*, **138**, 353–365.

Love, J. & Gubbins, D., 1996. Dynamos driven by poloidal flow exist, *Geophys. Res. Lett.*, **23**, 857–860.

Lowes, F., 1966. Mean-square values on a sphere of spherical harmonic vector fields, *J. Geophys. Res.*, **71**, 2179.

Lowes, F., 2007. Measuring magnetic field in the 'diamagnetic' ionosphere, *Geophys. J. Int.*, **171**, 115–118.

Lowrie, W., 1997. *Fundamentals of Geophysics*, Cambridge University Press.

Lühr, H., Maus, S., Rother, M., & Cooke, D., 2002. First in-situ observation of night-time F region currents with the CHAMP satellite, *Geophy. Res. Lett.*, **29(10)**, GL01384.

Mackenzie, D., 2003. Ensemble Kalman Filters bring weather models up to date, *SIAM News*, **36**(8), 1–4.

Macmillan, S., 1996. A geomagnetic jerk for the early 1990's, *Earth Planet. Sci. Lett.*, **137**(1-4), 189–192.

Macmillan, S. & Maus, S., 2005. International Geomagnetic Reference Field: the tenth generation, *Earth Planets Space*, **57**, 1135–1140.

Macmillan, S. & Quinn, J., 2000. The 2000 revision of the joint UK/US geomagnetic field models and an IGRF2000 candidate model, *Earth Planets Space*, **52**, 1149–1162.

Macmillan, S., Maus, S., Bondar, T., Chambodut, A., Golovkov, V., Holme, R., Langlais, B., Lesur, V., Lowes, F., Lühr, H., Mai, W., Mandea, M., Olsen, N., Rother, M., Sabaka, T., Thomson, A., & Wardinski, I., 2003. Ninth generation International Geomagnetic Reference Field released, *Geophys. J. Int.*, **155**, 1051–1056.

Mandea, M. & Olsen, N., 2006. A new approach to directly determine the secular variation from magnetic satellite observations, *Geophys. Res. Lett.*, **33**(15), L15306.

Mandea, M., Olsen, N., Korte, M., Verbanac, G., & Yahiat, Y., 2008. Rapid changes in the geomagnetic field: from global to regional scales, in *Eos Trans. AGU*, vol. 83, pp. GP53A–0772, Fall Meet. Suppl.

Maus, S., Lühr, H. G., Balasis, G., Rother, M., & Mandea, M., 2005. Introducing POMME, the POtsdam Magnetic Model of the Earth, www.geomag.org.

Maus, S., Macmillan, S., Lowes, F., & Bondar, T., 2005. Evaluation of candidate geomagnetic field models for the 10th generation of IGRF, *Earth Planet. Space*, **57**, 1173–1181.

Maus, S., Rother, M., Stolle, C., Mai, W., Choi, S., Lühr, H., Cooke, D., & Roth, C., 2006. Third generation of the Potsdam Magnetic Model of the Earth (POMME), *Geochem. Geophys. Geosyst.*, **7**, Q07008.

Maus, S., Lühr, H., Rother, M., Hemant, K., Balasis, G., Ritter, P., & Stolle, C., 2007. Fifth-generation lithospheric magnetic field model from CHAMP satellite measurements, *Geochem. Geophys. Geosys.*, **8**(5), Q05013.

Maus, S., Silva, L., & Hulot, G., 2008. Can core-surface flow models be used to improve the forecast of the Earth's main magnetic field?, *J. Geophys. Res.*, **113**, B08102.

McElhinny, M. W. & Senanayake, W. E., 1980. Paleomagnetic evidence for the existence of the geomagnetic field 3.5 ga ago, *J. Geophy. Res.*, **85**(B7), 35233528.

McLean, S., Macmillan, S., Maus, S., Lesur, V., Thomson, A., & Dater, D., 2004. The US/UK World Magnetic Model for 2005-2010, Technical Report NESDIS/NGDC-1, NOAA.

Merrill, R., McElhinny, M., & McFadden, P., 1996. *The Magnetic Field of the Earth: Paleomagnetism, the Core and the Deep Mantle*, vol. 63 of **International Geophysics Series**, Academic Press, New York.

Merrill, R. T. & McFadden, P. L., 1990. Paleomagnetism and the nature of the geodynamo, *Science*, **248**, 345–350.

MIL-W-89500, 1993. World Magnetic Model, Tech. rep., Defense Mapping Agency (Department of Defense).

Mound, J. & Dumberry, M., 2008. Timescales of inner core - mantle gravitational locking, in *Eos Trans. AGU*, vol. 89, Fall Meet. Suppl.

Muller, R., 2002. Avalanches at the core-mantle boundary, *Geophys. Res. Lett.*, **29**(19), 41–1–4.

Needham, J., 1978. *The shorter science and civilisation in China : an abridgement of Joseph Needham's original text*, Cambridge University Press.

Neubert, T., Mandea, M., Hulot, G., von Frese, M., Primdahl, F., Jurgensen, J. L., Friis-Christensen, E., Stauning, P., Olsen, N., & Risbo, T., 2001. Oersted satellite captures high-precision geomagnetic field data, *Eos Trans. AGU*, **82(7)**, 87–88.

Nui, F. & Wen, L., 2001. Hemispherical variations in seismic velocity at the top of the Earth's inner core, *Nature*, **410**, 1081–1084.

Oganov, A. & Ono, S., 2004. Theoretical and experimental evidence for a post-perovskite phase of $MgSO_3$ in Earth's D" layer, *Nature*, **430**, 445–448.

Oldham, R., 1906. The constitution of the interior of the Earth, as revealed by earthquakes, *Q. Jl. Geol. Soc. London*, **62**, 456–475.

Olsen, N., 1997. Ionospheric F region currents at middle and low latitudes estimated from Magsat data, *J. Geophy. Res.*, **102**(A3), 4563–4576.

Olsen, N., 2006. The CHAOS model and new methods of estimating SV from satellite data, in *GEOSPACE Consortium Meeting*.

Olsen, N. & Mandea, M., 2007. Investigation of a secular variation impulse using satellite data: The 2003 geomagnetic jerk, *Earth Planet. Sci. Lett.*, **255**, 94–105.

Olsen, N. & Mandea, M., 2008. Rapidly changing flows in the Earth's core, *Nature Geoscience*, **1**, 390–394.

Olsen, N., Haagmans, R., Sabaka, T. J., Kuvshinov, A., Maus, S., Purucker, M., Rother, M. Lesur, V., & Mandea, M., 2006. The swarm end-to-end mission simulator study: A demonstration of separating the various contributions to Earth's magnetic field using synthetic data, *Earth Planets Space*, **58**, 359–370.

Olsen, N., Lühr, H., Sabaka, T., Mandea, M., Rother, M., & Toffner-Clausen, L., 2006. CHAOS: a model of the Earth's magnetic field derived from CHAMP, Oersted, and SAC-C magnetic satellite data, *Geophys. J. Int.*, **166**, 67–75.

Olsen, N., Sabaka, T., & Gaya-Pique, L., 2007. Study of an improved comprehensive magnetic field inversion analysis, Tech. Rep. 1/2007, Danish National Space Centre.

Pais, M. & Hulot, G., 2000. Length of day decade variations, torsional oscillations and inner core superrotation: Evidence from recovered core surface zonal flows, *Phys. Earth Planet. Int.*, **118**, 291–316.

Pais, M. & Jault, D., 2008. Quasi-geostrophic flows responsible for the secular variation of the Earth's magnetic field, *Geophys. J. Int.*, **173**, 421–443.

Pais, M., Oliveira, O., & Nogueira, F., 2004. Nonuniqueness of inverted core-mantle boundary flows and deviations from tangential geostrophy, *J. Geophys. Res.*, **109**, B08105.

Parker, R. L., 1955. Hydromagnetic dynamo models, *Astrophys. J.*, **122**, 293–314.

Parker, R. L., 1994. *Geophysical Inverse Theory*, Princeton University Press.

Parkinson, W., 1983. *Introduction to Geomagnetism*, Scottish Academic Press.

Pinheiro, K. & Jackson, A., 2008. Can a 1-D mantle electrical conductivity model generate magnetic jerk differential time delays?, *Geophys. J. Int.*, **173**, 781–792.

Proudman, J., 1916. On the motion of solids in a liquid possessing vorticity, *Proc. R. Soc. Lond. A*, **92**, 408–242.

Purucker, M., 2008. A global model of the internal magnetic field of the Moon based on Lunar Prospector magnetometer observations, *Icarus*, **196**.

Purucker, M., Sabaka, T., Solomon, S., Anderson, B., Korth, H., Zuber, M., & Neumann, G., 2009. Mercury's internal magnetic field: Constraints on large- and small-scale fields of crustal origin, *Earth Planet. Sci. Lett.*, **in press**.

Randall, D., 2000. *General Circulation Model Development*, vol. 70 of **International Geophysics Series**, Academic Press.

Rau, S., Christensen, U., Jackson, A., & Wicht, J., 2000. Core flow inversion tested with numerical dynamo models, *Geophys. J. Int.*, **141**, 485–497.

Reigber, C., Lühr, H., & Schwintzer, P., 2002. CHAMP mission status, *Adv. Space Res.*, **30**, 129–134.

Roberts, P. & Scott, S., 1965. On the analysis of the secular variation. 1. A hydromagnetic constraint: Theory, *J. Geomag. Geoelec.*, **17**, 137–151.

Runcorn, S., 1978. The ancient lunar core dynamo, *Science*, **199**, 771–773.

Russell, C., 1999. Magnetic stress in solar system plasmas, *Aust. J. Phys.*, **52**, 733–751.

Ryan, D. & Sarson, G., 2007. Are geomagnetic field reversals controlled by turbulence within the Earth's core?, *Geophys. Res. Lett.*, **34**, L02307.

Sabaka, T., Olsen, N., & Langel, R., 2000. A comprehensive model of the near-earth magnetic field: Phase 3, Tech. Rep. TM-2000209894, Goddard Space Flight Center, NASA.

Sabaka, T., Olsen, N., & Purucker, M., 2004. Extending comprehensive models of the Earth's magnetic field with Oersted and CHAMP data, *Geophys. J. Int.*, **159**, 521–547.

Scorer, R. S., 1997. *Dynamics of meteorology and climate*, Wiley.

Shure, L., Parker, R. L., & Langel, R., 1985. A preliminary harmonic spline model from Magsat data, *J. Geophy. Res.*, **90**, 1150511512.

Simons, F. & Dahlen, F., 2006. Spherical Slepian functions and the polar gap in geodesy, *Geophy. J. Int.*, **166**, 1039–1061.

Solomon, S., 2007. Hot news on Mercury's core, *Science*, **316**, 702–703.

Song, X. & Richards, P. G., 1996. Seismological evidence for differential rotation of the Earth's inner core, *Nature*, **382**, 221–224.

Sreenivasan, B. & Jones, C., 2005. Structure and dynamics of the polar vortex in the Earth's core, *Geophys. Res. Lett.*, **32**, L20301.

Stanley, S. & Bloxham, J., 2004. Convective-region geometry as the cause of uranus' and neptunes' unusual magnetic fields, *Nature*, **248**, 151–153.

Stanley, S., Zuber, M., & Bloxham, J., 2007. Using reversed magnetic flux spots to determine a planet's inner core size, *Geophys. Res. Lett.*, **34**, L19205.

Stephenson, F. & Morrison, L., 1990. Long-term fluctuations in the earths rotation: 700 bc to ad 1990, *Philos. Trans. R. Soc. London, Ser. A*, **351**, 165–202.

Stevenson, D., 1987. Origin of the Moon-the collision hypothesis, *Annu. Rev. Earth Planet. Sci.*, **15**, 271–315.

Stevenson, D., 2001. Mars' core and magnetism, *Nature*, **412**, 214–219.

Stevenson, D., 2003. Mission to Earth's core – a modest proposal, *Nature*, **423**, 239–240.

Stevenson, D., 2003. Planetary magnetic fields, *Earth Planet. Sci. Lett.*, **208**, 1–11.

Stevenson, D., 2008. A planetary perspective on the deep Earth, *Nature*, **451**, 261–265.

Sumita, I. & Bergman, M., 2007. *Treatise on Geophysics*, vol. 8, chap. Inner-Core Dynamics, pp. 299–318, Elsevier.

Tangborn, A. & Kuang, W., 2008. Ensemble forecasting of geomagnetic fields, in *Eos Trans. AGU*, vol. 89, pp. GP53B–08, Fall Meet. Suppl.

Tarduno, J. A., Cottrell, R. D., Watkeys, M. K., & Bauch, D., 2007. Geomagnetic field strength 3.2 billion years ago recorded by single silicate crystals, *Nature*, **446**, 657–660.

Taylor, G., 1917. Motion of solids in fluids when the flow is not irrotational, *Proc. R. Soc. Lond. A*, **93**, 99–113.

Thomson, A., 2000. Improving the modelling of the geomagnetic main-field: Isolating the average ionospheric field in satellite data, *Earth Planet. Space Sci.*, **52**, 1199–1206.

Thomson, A. & Lesur, V., 2007. An improved geomagnetic data selection algorithm for global geomagnetic field modelling, *Geophys. J. Int.*, **169**, 951–963.

Tschauner, O., Zerr, A., Specht, S., Rocholl, A., Boehler, R., & Palme, H., 1999. Partitioning of nickel and cobalt between silicate perovskite and metal at pressures up to 80 GPa, *Nature*, **398**, 604–607.

Tyler, R., Maus, S., & Lühr, H., 2003. Satellite observations of magnetic fields due to ocean flow, *Science*, **299**, 239–241.

Uno, H., Johnson, C., Anderson, B., Korth, J., & Solomon, S., 2009. Modelling Mercury's internal magnetic field using smooth inversion, *Earth Planet. Sci. Lett.*, **in press**.

van der Hilst, Rob, D., Bass, J., Matas, J., & Trampert, J., eds., 2005. *Earth's Deep Mantle: Structure, Composition, and Evolution*, no. 160 in Geophysical Monograph Series, American Geophysical Union.

Varadi, F., Ghil, M., & Kuala, W., 1999. Jupiter, Saturn and the edge of chaos, *Icarus*, **139**, 286–294.

Voorhies, C., 2008. Thickness of the magnetic crust of mars, *J. Geophy. Res.*, **113**, E04004.

Voorhies, C. & Backus, G., 1985. Steady flows at the top of the core from geomagnetic field models: The steady motion theorem, *Geophys. Astrophys. Fluid Dynam.*, **32**, 163–173.

Waddington, R., Gubbins, D., & Barber, N., 1995. Geomagnetic field analysis - V. Determining steady core-surface flows directly from geomagnetic observations, *Geophys. J. Int.*, **122**(1), 326–350.

Walker, M. & Jackson, A., 2000. Robust modelling of the Earth's magnetic field, *Geophys. J. Int.*, **143-3**, 799–808.

Wardinski, I., 2005. *Core Surface Flow Models from Decadal and Subdecadal Secular Variation of the Main Geomagnetic Field*, Ph.D. thesis, GeoForschungsZentrum Potsdam.

Wardinski, I. & Holme, R., 2006. A time-dependent model of the Earth's magnetic field and its secular variation for the period 1980-2000, *J. Geophys. Res.*, **111**, B12101.

Wardinski, I., Holme, R., Asari, S., & Mandea, M., 2008. The 2003 geomagnetic jerk and its relation to the core surface flows, *Earth Planet. Sci. Lett.*, **267**, 468–481.

Welch, G. & Bishop, G., 2001. An introduction to the Kalman Filter, in *SIGGRAPH Conference 2001*, ACM.

Wessel, P. & Smith, W. H. F., 1991. Free software helps map and display data, *EOS Trans. AGU*, **72**, 441.

Whaler, K., 1980. Does the whole of the Earth's core convect?, *Nature*, **287**, 528–530.

Whaler, K. & Gubbins, D., 1981. Spherical harmonic analysis of the geomagnetic field: an example of a linear inverse problem, *Geophys. J. R. Astr. Soc.*, **65**, 645–693.

Whaler, K. & Holme, R., 2007. Consistency between the flow at the top of the core and the frozen-flux approximation, *Earth, Planets and Space*, **59**, 12191229.

Whaler, K. & Purucker, M., 2005. A spatially continuous magnetization model for Mars, *Journal of Geophysical Research E: Planets*, **110**(9), 1–11.

Whaler, K., Holme, R., & Jackson, A., 2002. One-norm modelling of flow at the core-mantle boundary, Poster, SEDI Meeting.

Whaler, K. A., 1986. Geomagnetic evidence for fluid upwelling at the core-mantle boundary, *Geophys. J. R. Astr. Soc.*, **86**, 563–588.

Whaler, K. A., 2007. *Encyclopedia of Geomagnetism and Paleomagnetism*, chap. Core Motions, pp. 84–89, Springer, Dordrecht.

Wigner, E. P., 1959. *Group theory and its application to the quantum mechanics of atomic spectra*, New York : Academic Press.

Wookey, J. & Helffrich, G., 2008. Inner-core shear-wave anisotropy and texture from an observation of PKJKP waves, *Nature*, **454**, 873 – 876.

Yu, W. & Wen, L., 2006. Inner core attenuation anisotropy, *Earth Planet. Sci. Lett.*, **245**, 581–594.

Appendix A

Crustal Biases

Biases between the values of the X, Y and Z components of the field as recorded at ground observatories are different to those values derived from satellite models due to the unknown small-scale (high degree) features of the field at the Earth's surface. The difference between field model predictions and the actual value as measured at an observatory is referred to as the crustal anomaly or bias. This varies between field models, depending on the degree and order to which they are calculated. There are few published tables of crustal bias, for example in Sabaka et al. (2000), Bloxham et al. (1989), and Volume 1 of Jacobs (1987), which made direct comparison of the model to the ground observatories difficult. Other satellite models calculated to the same degree (e.g. GRIMM, xCHAOS) showed a similar crustal bias.

Here I present a table of the findings of the crustal anomalies for the field model derived from the VO using All CHAMP data to degree and order $l = 14$. See Section 5.2 for example figures of the offset due to the crustal bias from satellite model minus ground observatory values. The X, Y and Z component biases are given in nT.

Obs Code	**Colatitude**	**Longitude**	**Height (km)**	**X**	**Y**	**Z**
AAA	46.75	76.92	1.30	-432	-10	301
AAE	80.97	38.77	2.44	-584	92	-446
ABK	21.63	18.82	0.38	-220	-101	-234
AIA	155.25	295.74	0.01	-251	86	-507
AQU	47.62	13.32	0.68	-264	-76	144
ARS	33.57	58.57	0.29	-390	233	-585
ASC	97.95	345.62	0.18	532	-319	-100
ASP	113.76	133.88	0.56	-184	53	-385
BDV	40.93	14.02	0.50	-241	-22	61
BEL	38.17	20.80	0.18	-388	-173	-328
BFE	34.37	11.67	0.08	-346	67	126
BFO	41.67	8.32	0.64	-244	-8	-15
BMT	49.70	116.20	0.18	-584	628	62
BOU	49.87	254.77	1.65	-247	-3	364
BRW	18.70	203.25	0.01	-235	73	-269
CBB	20.88	254.97	0.02	-305	136	-365
CLF	41.98	2.27	0.15	-212	-20	-49
CMO	25.13	212.17	0.09	-322	9	-182
CNB	125.32	149.36	0.86	-278	-40	-302
CTA	110.10	146.30	0.37	378	122	-507
CZT	136.43	51.87	0.16	657	-1079	-106
DOB	27.93	9.12	0.66	-151	51	102
DOU	39.90	4.60	0.23	-300	-17	-57
DRV	156.67	140.01	0.03	-80	369	3209
EBR	49.18	0.50	0.05	-261	-37	191
ESA	50.77	141.35	0.40	-734	-505	324
ESK	34.68	356.80	0.25	-293	3	4

EYR	133.40	172.40	0.12	-278	12	-169
FCC	31.23	265.92	0.02	-228	-51	141
FRD	51.80	282.63	0.07	-331	54	150
FRN	52.92	240.28	0.33	-186	45	485
FUR	41.83	11.28	0.57	-267	-29	40
GNA	121.80	116.00	0.06	-265	72	-417
GUA	76.41	144.87	0.14	-38	-76	140
HAD	39.00	355.52	0.10	-251	-49	-55
HER	124.43	19.23	0.03	-74	-14	-36
HLP	35.40	18.82	0.00	-311	134	38
HON	68.68	202.00	0.00	159	-58	540
HRB	42.13	18.18	0.12	-295	-17	123
HRN	13.00	15.55	0.02	-121	-1	-231
HUA	102.05	284.67	3.31	52	29	-77
KAK	53.77	140.18	0.03	-187	-28	356
KDU	102.69	132.47	0.01	41	78	-324
KNZ	54.75	139.97	0.34	-123	-45	328
KOU	84.90	307.40	0.00	-12	-147	90
LER	29.87	358.82	0.09	-134	-198	-163
LRM	112.22	114.10	0.00	-108	6	-537
LRV	25.82	338.30	0.01	27	-618	331
LVV	40.10	23.75	0.40	-420	-163	-140
MAB	39.70	5.68	0.44	-299	-21	-149
MAW	157.61	62.88	0.01	-159	117	-43
MBO	75.62	343.03	0.01	-32	-89	152
MCQ	144.50	158.95	0.01	-631	-54	-176
MEA	35.38	246.65	0.70	-450	-20	112
MIZ	50.88	141.20	0.13	-156	-53	520
MMB	46.08	144.20	0.04	-45	-141	118

NAQ	28.83	314.57	0.00	-6	-278	-605
NCK	42.37	16.72	0.16	-259	-38	113
NGK	37.93	12.68	0.08	-254	-35	65
NUR	29.48	24.65	0.11	-543	71	-238
NVS	34.97	82.90	0.20	-506	103	-128
OTT	44.60	284.45	0.08	-465	138	20
PAG	47.48	24.18	0.56	-95	130	343
PPT	107.57	210.42	0.36	951	1055	145
RES	15.32	265.10	0.03	-211	0	-397
SFS	53.50	353.88	0.08	-205	-43	217
SHU	34.65	199.54	0.08	-668	289	-100
SIT	32.93	224.68	0.02	-360	19	42
SJG	71.88	293.85	0.42	61	-140	208
SOD	22.63	26.63	0.18	-50	67	380
SPT	50.45	355.65	0.92	-253	-44	224
STJ	42.40	307.32	0.10	-378	-62	106
THL	12.52	290.83	0.06	-88	-65	-314
THY	43.10	17.90	0.19	-257	-24	116
TUC	57.75	249.17	0.95	-91	329	-78
UPS	30.10	17.35	0.05	-394	-19	-2
VIC	41.48	236.58	0.20	-339	-4	396
WNG	36.25	9.07	0.05	-335	-82	40

Table A.1: Table of Crustal Bias in the X, Y and Z components of the field as modelled by CHAMP satellite VO minus the values as recorded at ground observatories. Biases are in units of nT.

Appendix B

EnKF MATLAB Code

This appendix gives an example of the implementation in MATLAB of the code for the Ensemble Kalman Filter.

```
% Implementation of a Ensemble Kalman filter for core flow
% forecasting based on the Evensen (2003) paper [Ocean Dynamics, 53, 343-367]
%
% This code runs using the main field (MF) models as the 'true' measurement of the
% system (using spherical harmonic representation). The SV is generated by
% the underlying core flow models. The flow models control the level of
% 'spread' of the Kalman ensemble of models which are propagated forwards
% in time. Thus, the flow models act to control the forward prediction,
% while the MF field model is used as the measurement to 'update' the model
% with. Running the model over several years should help give a feel for
% the errors that build up and the expectation of the allowed deviation
% from the mean.
% Author: Ciaran Beggan
% Date started: 23-09-2008
% Last modified: 24-11-2008

flowfile =  'FlowModel684-1992_CHAMPVOquiet_May08_FlowCoeffs.dat';
```

```
lmax = 14; lsv = 14; lmf = 14;
n = lmax*(lmax+2); nn = 2*n;
ndim = nn*(nn+1)/2; np1 = n+1;
toroidal = 0;  % Set to 0 = toroidal-poloidal; 1 = toroidal only; 2 = poloidal-only

% Time settings
start_epoch = jd2000(2001, 6, 15, 0);
start_year = 2001.53;
time_step = 1/12;                   % Time step in years (i.e. each month)
year = 0; store = [];

% Ensemble of observations
num_months = 68;
num_ensembles = 1000;
num_coeffs = 448;
% Noise correlation for the random walk noise injection into the forward model
alpha = 0.01;

% Ensure time_step decorrelation Eq. 42 in Evensen(2003) using rho
rho = sqrt( (1.0-alpha)^2 / (time_step*((num_ensembles) - 2.0*alpha ...
  - (num_ensembles)*alpha^2 + 2.0*alpha^(num_ensembles+1))) );

% Load in starting field model
% Satellite Field Model
[d, m_SV] = xCHAOScoefficients(start_year, lmax);

[B] = CreateGauntElsasserMatrix(d, lmf, lsv, nn, toroidal);
```

```
% Load in a flow model - give name in apostrophes
[flowtime, flowcoeffs, xknts, answer_store, flowcoeffs_spline] = ...
FitFlowCoeffs_BSplines_function(flowfile);

% Find the std of the observations - this can be used to develop  the allowable
% perturbation of the observation vector. It is assumed from
% prior examintation of the observations that they follow a
% Gaussian normal distribution
flow_model_pertubation_allowed_std = std(flowcoeffs,0,2);

% Begin the forecast and analysis loop
field_ensemble = repmat(d ,1,num_ensembles);

for i = 1:num_months
    % Perturb the flow coeffs with the variance of the allowable range
    flow_forward_model = flowcoeffs(:,i);

    flow_forward_model_perturbations = randn(num_coeffs, num_ensembles)...
      *repmat(flow_model_pertubation_allowed_std*1, 1, num_ensembles);
    % Convert the perturbed flow models to an ensemble of SV models
    SV_perturbations = B * (repmat(flow_forward_model,1,num_ensembles) ...
      + flow_forward_model_perturbations);
    % Calculate the expected variance of the SV pertubations
    SV_observation_perturbation_std = std(SV_perturbations,0,2);


    % Forecast step - forward modelling
    measurement = ones(num_coeffs/2,1)*99;
```

```
% Add the perturbed SV models to the 'observed' field
% The SV per month (1/12 of the year) is added on
% with a small amount of extra noise.
field_ensemble =  field_ensemble + time_step.*SV_perturbations + ...
   sqrt(time_step).* rho.* ...
   repmat(SV_observation_perturbation_std*5, 1, num_ensembles) ...
   .* randn(num_coeffs/2,num_ensembles);

% Output forecast to file
% Assimilation step - Update model once per year
if ~(mod(i,12))

    year = year + 1;
    fprintf(1,'Assimilation step %d \n', year);

    % Analysis - Using the notation from Evensen (2003) now from Eq 44. onwards
    % Now add a measurement in and analyse the data

    A = field_ensemble;

    A_dash = field_ensemble - ...
     ones(num_coeffs/2, num_ensembles).*1/num_ensembles;

    % Satellite Field Model at time (t+1)
    [d] = xCHAOScoefficients(start_year+year, lmax);
    [B] = CreateGauntElsasserMatrix(d, lmf, lsv, nn, toroidal);

    Upsilon = repmat(SV_observation_perturbation_std/10, 1, num_ensembles) ...
     .* rand(num_coeffs/2,num_ensembles);
```

```
        D = repmat(d, 1, num_ensembles) + Upsilon;

        D_dash = D - A;

        A_analysis = A + A_dash * A_dash' * pinv(A_dash * A_dash' + ...
         Upsilon * Upsilon') * D_dash;

        field_ensemble = A_analysis;

    end
   % Record the difference between the measurement and the forecast mean
    %  (from Maus 2008)
     [dn] = xCHAOScoefficients(start_year+(time_step)*i, lmax);
     dPml = sqrt(sum([2:15].*msum((dn - ...
      find_mostlikelycoeff(field_ensemble, 50, num_coeffs/2)).^2, lmax)));

    dPm = sqrt(sum([2:15].*msum((dn - mean(field_ensemble,2)).^2, lmax)));
    dPl = sqrt(sum([2:15].*msum((dn - (mean(field_ensemble,2) ...
     -std(field_ensemble,0,2))).^2, lmax)));
    dPu = sqrt(sum([2:15].*msum((dn - (mean(field_ensemble,2) ...
     +std(field_ensemble,0,2))).^2, lmax)));

    store = [store; i dPm dPu dPl dPml];

end

fclose('all');
```

```
figure, plot(store(:,1), (store(:,2)), 'k-', 'LineWidth', 2)
hold on, plot(store(:,1), (store(:,3)), 'r--', 'LineWidth', 1.5)
plot(store(:,1), (store(:,4)), 'r-.', 'LineWidth', 1.5)
legend('Mean','+1 Std','-1 Std','Location', 'NorthWest')
```

Appendix C

Flow Models and Residuals files

This appendix tabulates the individual Flow Model and Residual images and animations available on the accompanying CD (in wallet).

Directory	Model Description	Section	Flow	Resid.
CHAMP_simulation_nonoise	VO generated from orbital simulation and CHAOS field model	4.5.2	✓	✓
D1_EqLL	VO generated from All CHAMP data	4.4	✓	✓
D1_EqLL_CM4	VO generated from All CHAMP data with CM4 correction	4.6.1	✓	✓
D1_EqLL_CM4_covariancerotated	VO generated from All CHAMP data with CM4 correction and covariance rotation	4.6.3	✓	✓
D1_EqLL_covariancerotated	VO generated from All CHAMP data with covariance rotation	4.6.3	✓	✓
D2_EqLL	VO generated from night-side only data	4.4	✓	✓

D2_EqLL_CM4	VO generated from night-side only data with CM4 correction	4.6.1	✓	✓
D2_EqLL_CM4_covariancerotated	VO generated from night-side only data with CM4 correction and covariance rotation	4.6.3	✓	✓
D2_EqLL_covariancerotated	VO generated from night-side only data with covariance rotation	4.6.3	✓	✓
Oersted_CHAMP_selectedQuiet	VO generated from selected quiet time Ørsted and CHAMP data	4.5.1	✓	✓
SHanalysis_D1_external	Spherical Harmonic Analysis of VO field: External component	4.6.2	✓	✓
SHanalysis_D1_internal	Spherical Harmonic Analysis of VO field: Internal component	4.6.2	✓	✓
SHanalysis_D1_toroidal	Spherical Harmonic Analysis of VO field: Toroidal component	4.6.2	✓	✓
SplineD2_EqLL_44months	B-Spline fit through flow coefficients: Fit through 44 months of VO SV	4.6.5	✓	✓
SplineD2_EqLL_68months	B-Spline fit through flow coefficients: Fit through 68 months of VO SV	4.6.5	✓	–

Table C.1: Table of directories on the accompanying CD. Each directory contains JPEG images and .AVI animations of the monthly flow models and residuals from the processing steps. Further details available in Chapter 4